

**Austrian Contributions to the**

**XXV General Assembly of the  
International Union of Geodesy  
and Geophysics (IUGG)**

**June 27– July 8, 2011, Melbourne, Australia**





## CAPTURE REALITY

- Topcons neue Dimension bei Vermessungsdaten
- Kombination von Messdaten, Punktwolken und photogrammetrischen Informationen
- Automatische Erzeugung von 3D Modellen
- Generieren von Profilen und Konturen
- Flächen- und Volumsberechnungen
- Optimale Messdatendokumentation



### GLS-1500

Laserscanner

### IS

Imaging Totalstation

### Image Master

PC Software



Professionelle Unterstützung und Service - Alleinvertretung für Vermessungsinstrumente von TOPCON in Österreich

**GEODIS AUSTRIA**

GEODIS AUSTRIA GmbH, Campus 21 - BUSINESSZENTRUM WIEN SÜD, Liebermannstr. A01 304, Büro 7, 8, 2345 Brunn am Gebirge, Tel.: +43-2236-315891, Fax: +43-2236-315891-15, Mobil1: +43-699-197 41 833, Mobil2: +43-699-197 41 834, E-Mail: topconbusiness@geodisgroup.at, topconservice@geodisgroup.at, erwin.truttmann@geodisgroup.at, christine.knoetzl@geodisgroup.at



Österreichische Zeitschrift für  
**Vermessung &  
Geoinformation**

**Organ der Österreichischen Gesellschaft für Vermessung und Geoinformation  
und der Österreichischen Geodätischen Kommission**

99. Jahrgang 2011

Heft: 2/2011

ISSN: 1605-1653

Schriftleiter: Dipl.-Ing. Stefan Klotz

Stellvertreter: Dipl.-Ing. Ernst Zahn

Dipl.-Ing. Andreas Pammer

A-1020 Wien, Schiffamtsgasse 1-3

Internet: <http://www.ovg.at>

**Special Issue**

**XXV General Assembly of the International Union of Geodesy  
and Geophysics (IUGG), Melbourne, Australia**

ed. by Johannes Böhm, Alexander Reiterer, Franz Rottensteiner and Helmut Woschitz  
(All Papers of this issue were peer-reviewed.)

<b>Preface to the VGI Special Issue</b>	<b>52</b>
<i>O. Baur, M. Kuhn, W. E. Featherstone:</i> <b>GRACE-derived land-hydrological mass changes and their impact on relative sea-level variations</b>	<b>53</b>
<i>P. Dorninger, B. Székely, A. Zámolyi, A. Roncat:</i> <b>Automated Detection and Interpretation of Geomorphic Features in LiDAR Point Clouds</b>	<b>60</b>
<i>C. Fösleitner, D. Kuçi, B. Hofmann-Wellenhof, H.-P. Ranner, R. Prüller, K. Aichhorn:</i> <b>The Race Against Time In Alpine Regions By Satellite-Based Technologies</b>	<b>70</b>
<i>H. Goiginger, D. Rieser, T. Mayer-Gürr, E. Höck:</i> <b>Global combination gravity field model based on GOCE and GRACE data</b>	<b>79</b>

<i>P. Hafner, M. Wieser, N. Kührtreiber:</i>		
	<b>Quality Assessment of Different GNSS/IMS-Integrations</b>	<b>89</b>
<i>F. Heuberger, D. Rieser:</i>		
	<b>Impact of glacier changes on the local gravity field by numerical forward modelling and applicability studies using GOCE gravity gradients for regional gravity field solutions by Least Squares Collocation</b>	<b>100</b>
<i>F. Hinterberger, F. Blauensteiner, A. Eichhorn, R. Weber:</i>		
	<b>GNSS/IMU integration for the precise determination of highly kinematic flight trajectories</b>	<b>110</b>
<i>K. Huber, P. Berglez, B. Hofmann-Wellenhof, R. Weber, M. Troger:</i>		
	<b>The development of enhanced algorithms for rapid precise point positioning</b>	<b>114</b>
<i>M. Karbon, D. Wijaya, M. Schindelegger, J. Böhm, H. Schuh:</i>		
	<b>Atmospheric effects on the Earth gravity field featured by TU Vienna</b>	<b>122</b>
<i>S. Krauss, A. Maier, G. Stangl:</i>		
	<b>Regional Ionosphere Models for Improving GNSS Navigation</b>	<b>131</b>
<i>G. Möller, E. Brückl, R. Weber:</i>		
	<b>Active tectonic deformation at the transition from the European and Pannonian domain monitored by a local GNSS network.</b>	<b>138</b>
<i>V. Nafisi, M. Madzak, J. Böhm, H. Schuh, A. A. Ardalan:</i>		
	<b>Ray-traced tropospheric slant delays in VLBI analysis</b>	<b>149</b>
<i>D. Ruess, C. Ullrich:</i>		
	<b>20 years of International Comparison of Absolute Gravimeters (ICAG) at the Bureau International des Poids et Mesures (BIPM) in Paris with participation of the BEV</b>	<b>154</b>
<i>S. Schenk, K. Hanke:</i>		
	<b>Automatic Registration of Laser Scanner Point Clouds with Genetic Algorithms</b>	<b>162</b>
<i>G. Thaler, A. Karabatic, R. Weber:</i>		
	<b>Precise Point Positioning – Towards Real-Time Applications</b>	<b>171</b>
<i>A. Wieser, R. Aschauer:</i>		
	<b>Estimating platform kinematics using multi-antenna GNSS</b>	<b>180</b>
<i>H. Woschitz, F. K. Brunner:</i>		
	<b>Dynamic strain measurements using embedded fiber optic sensors</b>	<b>191</b>

# Impressum



## Organ der Österreichischen Gesellschaft für Vermessung und Geoinformation und der Österreichischen Geodätischen Kommission

99. Jahrgang 2011 / ISSN: 1605-1653

**Herausgeber und Medieninhaber:** Österreichische Gesellschaft für Vermessung und Geoinformation (OVG), Austrian Society for Surveying and Geoinformation, Schiffamtsgasse 1-3, A-1020 Wien zur Gänze. Bankverbindung: Österreichische Postsparkasse BLZ 60000, Kontonummer PSK 1190933. ZVR-Zahl 403011926.

**Präsident der Gesellschaft:** Dipl.-Ing Gert Steinkellner, Tel. (01) 21110-2714, Fax (01) 21110-4624, Schiffamtsgasse 1-3, A-1020 Wien.

**Sekretariat der Gesellschaft:** Dipl.-Ing. Karl Haussteiner, Tel. (01) 21110-2311, Fax (01) 2167551, Schiffamtsgasse 1-3, A-1020 Wien.

**Schriftleitung:** Dipl.-Ing. Stefan Klotz, Tel. (01) 21110-3609, Dipl.-Ing. Ernst Zahn, Tel. (01) 21110-3209, Dipl.-Ing. Andreas Pammer, Tel. (01) 21110-5336, Schiffamtsgasse 1-3, A-1020 Wien. Fax (01) 2167551, E-Mail: [vgj@ovg.at](mailto:vgj@ovg.at).

**Manuskripte:** Bitte direkt an die Schriftleitung senden. Es wird dringend ersucht, alle Beiträge in digitaler Form zu übersenden. Genaue Angaben über die Form der Abfassung des Textes sowie der Abbildungen (Autoren-Richtlinien) können bei der Schriftleitung angefordert werden bzw. sind auf <http://www.ovg.at> unter „VGI Richtlinien“ zu ersehen. Beiträge können in Deutsch oder Englisch abgefasst sein; Hauptartikel bitte mit einer deutschsprachigen Kurzfassung und einem englischen Abstract sowie Schlüsselwörter bzw. Keywords einsenden. Auf Wunsch können Hauptartikel einem „Blind-Review“ unterzogen werden. Nach einer formalen Überprüfung durch die Schriftleitung wird der Artikel an ein Mitglied des Redaktionsbeirates weitergeleitet und von diesem an den/die Reviewer verteilt. Artikel, die einen Review-Prozess erfolgreich durchlaufen haben, werden als solche gesondert gekennzeichnet. Namentlich gezeichnete Beiträge geben die Meinung des Autors wieder, die sich nicht mit der des Herausgebers decken muss. Die Verantwortung für den Inhalt des einzelnen Artikels liegt daher beim Autor. Mit der Annahme des Manuskriptes sowie der Veröffentlichung geht das alleinige Recht der Vervielfältigung und Wiedergabe auf den Herausgeber über.

**Redaktionsbeirat für Review:** Univ.-Prof. Dr. Fritz K. Brunner, Univ.-Prof. Dr. Norbert Pfeifer, Univ.-Prof. Dr. Harald Schuh, Dipl.-Ing. Gert Steinkellner, Prof. Dr. Josef Strobl, O.Univ.-Prof.



<http://www.ovg.at>

Dipl.-Ing. Dr. Hans Sünkel und Univ.-Doz. Dipl.-Ing. Dr.iur. Christoph Twaroch

**Copyright:** Jede Vervielfältigung, Übersetzung, Einspeicherung und Verarbeitung in elektronischen Systemen sowie Mikroverfilmung der Zeitschrift oder von in ihr enthaltenen Beiträgen ohne Zustimmung des Herausgebers ist unzulässig und strafbar. Einzelne Photokopien für den persönlichen Gebrauch dürfen nur von einzelnen Beiträgen oder Teilen davon angefertigt werden.

**Anzeigebearbeitung und -beratung:** Dipl.-Ing. Stefan Klotz, Tel. (01) 21110-3609, Schiffamtsgasse 1-3, A-1020 Wien. Unterlagen über Preise und technische Details werden auf Anfrage gerne zugesendet.

**Erscheinungsweise:** Vierteljährlich in zwangloser Reihenfolge (1 Jahrgang = 4 Hefte). Auflage: 1500 Stück.

**Abonnement:** Nur jahrgangswise möglich. Ein Abonnement gilt automatisch um ein Jahr verlängert, sofern nicht bis zum 1.12. des laufenden Jahres eine Kündigung erfolgt. Die Bearbeitung von Abonnementangelegenheiten erfolgt durch das Sekretariat. Adressänderungen sind an das Sekretariat zu richten.

**Verkaufspreise:** Einzelheft: Inland 15 €, Ausland 18 €; Abonnement: Inland 50 €, Ausland 60 €; alle Preise exklusive Mehrwertsteuer. OVG-Mitglieder erhalten die Zeitschrift kostenlos.

**Satz und Druck:** Buchdruckerei Ernst Becvar Ges.m.b.H., A-1150 Wien, Lichtgasse 10.

## Offenlegung gem. § 25 Mediengesetz

**Medieninhaber:** Österreichische Gesellschaft für Vermessung und Geoinformation (OVG), Austrian Society for Surveying and Geoinformation, Schiffamtsgasse 1-3, A-1020 Wien zur Gänze.

**Aufgabe der Gesellschaft:** gem. § 1 Abs. 1 der Statuten (gen. mit Bescheid der Bundespolizeidirektion Wien vom 26.11.2009): a) die Vertretung der fachlichen Belange der Vermessung und Geoinformation auf allen Gebieten der wissenschaftlichen Forschung und der praktischen Anwendung, b) die Vertretung aller Angehörigen des Berufsstandes, c) die Förderung der Zusammenarbeit zwischen den Kollegen der Wissenschaft, des öffentlichen Dienstes, der freien Berufe und der Wirtschaft, d) die Förderung des wissenschaftlichen Nachwuchses, e) die Herausgabe einer Zeitschrift mit dem Namen „Österreichische Zeitschrift für Vermessung und Geoinformation“ (VGI).

**Erklärung über die grundlegende Richtung der Zeitschrift:** Wahrnehmung und Vertretung der fachlichen Belange aller Bereiche der Vermessung und Geoinformation, der Photogrammetrie und Fernerkundung, sowie Information und Weiterbildung der Mitglieder der Gesellschaft hinsichtlich dieser Fachgebiete.



<http://www.oegk-geodesy.at>

## Preface to the VGI Special Issue

The Austrian Geodetic Commission (ÖGK) is the national organisation in Austria related to the International Association of Geodesy (IAG) which is one of the eight associations of the International Union of Geodesy and Geophysics (IUGG).


Every four years IUGG and its associations hold a General Assembly. The IAG uses these general assemblies to present the work performed, to review the structure of IAG, to appoint new officers and to organise a suite of symposia. The XXV General Assembly of IUGG will take place in Melbourne, Australia, June 27 to July 08, 2011 and the ÖGK has decided to contribute with a collection of research papers of Austrian institutions related to geodesy.

The main task of this special issue of the *Österreichische Zeitschrift für Vermessung & Geoinformation (VGI)* is to give the international geodetic research community an idea about the various topics Austrian geodesists are working on. Additionally, this scientific work should be cumulatively shown to those Austrian colleagues who are mainly involved in practical and administrative work. The variety of research topics indicates how closely geodesy is related to its neighbouring disciplines such as geophysics, meteorology, oceanography, space science, and computer science. Joint efforts in different fields are needed to achieve the goals which are common in modern society, such as precise navigation on Earth or a thorough description of the various interactions in 'System Earth' providing important input parameters for research on natural hazards and global change.

With in total 17 papers the present issue can be considered more than a "snapshot" of the geodetic research work carried out in Austria. The authors of this special issue of the VGI represent Vienna University of Technology and Graz University of Technology, both offering the full educational programme in geodesy, as well as the University of Innsbruck, the Federal Office of Metrology and Surveying (BEV), the Space Research Institute (IWF) of the Austrian Academy of Sciences, and their research partners.

I'd like to express particular thanks to the four guest-editors of this issue: Johannes Böhm, Alexander Reiterer, Franz Rottensteiner, and Helmut Woschitz. All four of them were recipients of the Karl Rinner Prize, which is the highest award that the Austrian Geodetic Commission gives once a year to an outstanding young scientist in the field of geodesy.

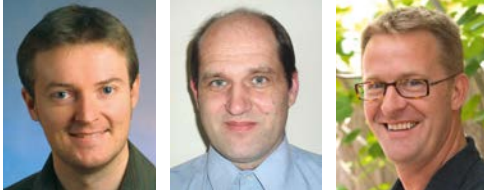
It has to be mentioned that all papers of this issue had to undergo the peer-review process of the VGI to ensure that the quality of the published articles was the same as in a standard issue of the journal. Thus, I also want to thank all reviewers for their useful comments and constructive remarks. On behalf of all authors and the four guest-editors I would like to acknowledge the Austrian Society of Geodesy and Geoinformation (OVG) for providing this platform for the publications. In particular we are grateful to the editor-in-chief of the VGI, Stefan Klotz, and his two deputy editors, Ernst Zahn and Andreas Pammer, for taking care of the layout of the papers and solving all technical problems.



Harald Schuh

(President of the Austrian Geodetic Commission)

## GRACE-derived land-hydrological mass changes and their impact on relative sea-level variations



Oliver Baur, Michael Kuhn and Will E. Featherstone

### Abstract

The GRACE (Gravity Recovery And Climate Experiment) mission allows inference of mass variations on, above and beneath the Earth's surface from gravitational signatures in space. We present a robust and straightforward procedure to derive mass changes from time-variable gravity field estimates. We outline our solution to the leakage problem and shed light on linear versus accelerated secular-change modeling. Based on a six-year gravity field time-series from March 2003 to February 2009, we provide detailed analysis of two selected areas, Greenland and the Orinoco Basin. As a result, annual Greenland mass loss accelerated by  $+21.3 \pm 3 \text{ Gt/yr}^2$  during the six-year period. Furthermore, we show the impact of recent ice melting on global relative sea level. In terms of uniform change, the contributions of Greenland and Antarctica are  $+0.56 \pm 0.01 \text{ mm/yr}$  and  $+0.50 \pm 0.07 \text{ mm/yr}$ , respectively. However, we prove that simplistic uniform modeling of sea-level variations is insufficient as it disregards the gravitational feedback effect caused by mass redistribution.

**Keywords:** Satellite gravimetry, mass balance, trend estimation, sea-level change

### Kurzfassung

Mit dem Start der Satellitenmission GRACE (Gravity Recovery And Climate Experiment) wurde es erstmals möglich, großräumige Massenvariationen im System Erde aus Änderungen in der Erdanziehungskraft zu bestimmen. Im Rahmen der Klimawandeldebatte nimmt dabei der anhaltende Eismassenverlust in den polaren Gebieten der Erde eine besonders bedeutende Stellung ein. Dieser Beitrag präsentiert eine robuste und geradlinige Vorgehensweise zur Bestimmung von Massenänderungen aus zeitvariablen Schwerefeldern. In diesem Zusammenhang spielt der Umgang mit Kriecheffekten (leakage) eine maßgebliche Rolle. Darüber hinaus widmen wir uns der Frage, auf welche Art und Weise der säkulare Trend in den Zeitreihen modelliert werden sollte. Unsere Analyse einer Serie monatlicher Schwerefelder über den Zeitraum März 2003 bis Februar 2009 zeigt, dass sich der jährliche Eismassenschwund über Grönland mit einer Rate von  $+21.3 \pm 3 \text{ Gt/yr}^2$  beschleunigt hat. Das Resultat zunehmender Eisschmelze erweist sich als signifikant im Rahmen der durchgeführten statistischen Tests. Der Zufluss von Schmelzwasser in die Ozeane bedingt naturgemäß einen Anstieg des Meeresspiegels. Ausgedrückt in räumlich gleichförmiger Ausprägung liefern Grönland und die Antarktis mit  $+0.56 \pm 0.01 \text{ mm/yr}$  beziehungsweise  $+0.50 \pm 0.07 \text{ mm/yr}$  derzeit den primären Beitrag. Die Annahme einer auf die Ozeane aufgetragenen konstanten Schicht ist indessen ungenügend. Aufgrund der globalen Massen-Neuverteilung resultiert eine regional sehr unterschiedlich ausgeprägte Variation des relativen Meeresspiegels. Aus diesem Grund müssen sowohl der gravitative Rückkopplungseffekt als auch der Auflasteffekt berücksichtigt werden.

**Schlüsselwörter:** Satellitengravimetrie, Massenbilanz, Trendschätzung, Meeresspiegel

### 1. Introduction

In the context of climate change, the Gravity Recovery And Climate Experiment (GRACE) provides valuable information on mass transport in the system Earth [1]. Range-rate measurements collected by the twin-satellite mission are particularly sensitive to mass variations over large-scale regions. The spacecraft are some nine years in operational mode now. Nevertheless, climate-change forecasts remain a matter of contention. Considering decadal and longer-term variations, the GRACE lifetime is too short to derive statistically meaningful predictions from the data.

GRACE gravity field time-series have often been exploited to determine linear ablation rates in glaciated areas such as Greenland [2], Alaska [3], Antarctica [4] and Patagonia [5]. Hydrological studies typically target seasonal mass-variation characteristics of river basins and water catchments [1,6]. In the recent past, two issues gained increasing interest. Firstly, the more detailed spatial resolution of mass change patterns; [7,8], for instance, subdivided the Greenland area in catchments to improve spatial variability. In [9], point-mass modeling is used to recover the deglaciation geometry. Secondly, it has been shown that linear mass-change trends may in-

adequately represent the temporal progress of secular variations. [10] found that Greenland ice-mass loss accelerated by about 250% between April 2002 to April 2004 and May 2004 to April 2006. This result was supported by [11], analyzing a seven-year period and applying various metric criteria. [12] suggest that over the last 18 years, deglaciation over Greenland and Antarctica accelerated by  $+21.9 \pm 1 \text{ Gt/yr}^2$  and  $+14.5 \pm 2 \text{ Gt/yr}^2$ , respectively.

The motivation of this contribution is twofold. On the one hand, we present a procedure to derive mass-change rates from GRACE gravity field time-series. We (i) shed light on the leakage problem inherent to GRACE analysis, (ii) briefly address glacial isostatic adjustment (GIA) corrections, and (iii) discuss the modeling of secular trends. On the other hand, we translate land-hydrological mass changes to equivalent (relative) sea-level variations. In this framework, we exclusively modeled non-steric changes as GRACE is only sensitive to sea-level variations related to gravitational signatures. [The steric component, mainly driven by thermal expansion, is typically obtained from a combination with satellite altimetry and in-situ observation systems such as Argo. For detailed information, we refer the reader to [13] and the references therein]. Opposed to the simplified assumption of uniform change geometries, regional patterns strongly contradict the constant-layer approximation; we adopted the theory in [14] to take both the gravitational and elastic feedback effects into account.

## 2. GRACE-derived mass changes

Section 2.1 introduces the data used for this study. The methods section 2.2 outlines our algorithms to compute mass-change rates from GRACE gravity fields; we refer the reader to [11] and [15] for a detailed description of the techniques. Finally, exemplary for any region of interest, Sect. 2.3 presents results for Greenland and the Orinoco Basin.

### 2.1 Data

GRACE gravity field time-series are provided by several data processing centers. For our experiments, we used the well-established release RL04 estimates from the Center for Space Research (CSR) at the University of Texas at Austin. Each "monthly" solution consists of a set of fully normalized spherical harmonic coefficients (SHC) complete up to degree ( $l$ ) and order ( $m$ ) 60. The time period for this study covers March 2003 to February 2009, hence six integer years. Satel-

lite gravimetry is insensitive to displacements of the Earth's centre of mass; for this reason, the monthly solutions do not contain degree-1 coefficients. The neglect of secular geocenter motions, such as caused by GIA [16], might introduce a bias to mass-change estimates. As reported by [17], geocenter adjustment over the period July 2003 to June 2007 resulted in approximately  $+0.2 \text{ mm/yr}$  uniform sea-level change equivalent. We replaced GRACE  $c_{20}$  coefficients (representing the Earth's flattening) by values based on satellite laser ranging, which have been proven to be more reliable [18].

### 2.2 Methods

Vertically integrated mass variations, as sensed by GRACE, are commonly approximated by surface mass densities [19]. In terms of equivalent water height (EWH), the changes become

$$\begin{aligned} \Delta \text{EHW}(\lambda, \varphi) &= \\ &= \frac{2\pi a \rho_{\text{ave}}}{3\rho_w} \sum_{l=2}^L \frac{2l+1}{1+k_l} W_l \cdot \\ &\quad \cdot \sum_{m=0}^l P_{lm}(\sin \varphi) [\Delta c_{lm}^{\text{fil}} \cos(m\lambda) + \Delta s_{lm}^{\text{fil}} \sin(m\lambda)] \end{aligned} \quad (1)$$

where  $\Delta c_{lm}^{\text{fil}}$  and  $\Delta s_{lm}^{\text{fil}}$  denote residual SHC taken with respect to the (assumed static) six-year means. The superscript fil indicates that we removed systematic errors by spectral-domain filtering as proposed in [20]. The degree-dependent factors  $W_l$  down-weight short-wavelength features, which are prone to GRACE errors. We selected the factors according to isotropic Gaussian smoothing with a radius of 500 km [21].

In Eq. (1),  $\lambda$  and  $\varphi$  represent longitude and latitude, respectively;  $a$  is the major semi-axis of a reference ellipsoid,  $\rho_{\text{ave}}$  the average mass-density of the solid Earth,  $\rho_w$  the mass-density of freshwater,  $L = l_{\text{max}}$  (here  $L = 60$ ) the maximum spherical harmonic degree and  $k_l$  the load Love numbers. The  $P_{lm}(\sin \varphi)$  are the normalized associated Legendre functions of the first kind.

Based on monthly "snapshots" of residual EWH patterns, Fig. 1 shows global trends from March 2003 to February 2009. The signals over Greenland, Alaska and Antarctica can be attributed to cryospheric processes, whereas the signals over the Canadian Shield and Fennoscandia are mainly subject to GIA. Furthermore, Fig. 1 reveals secular (surface- and ground-water) changes in large river catchments such as the Orinoco Basin and the Mississippi Basin. Noteworthy, it is a delicate matter to separate between real mass-change signals and spurious signals triggered by GRACE errors. Geophysical



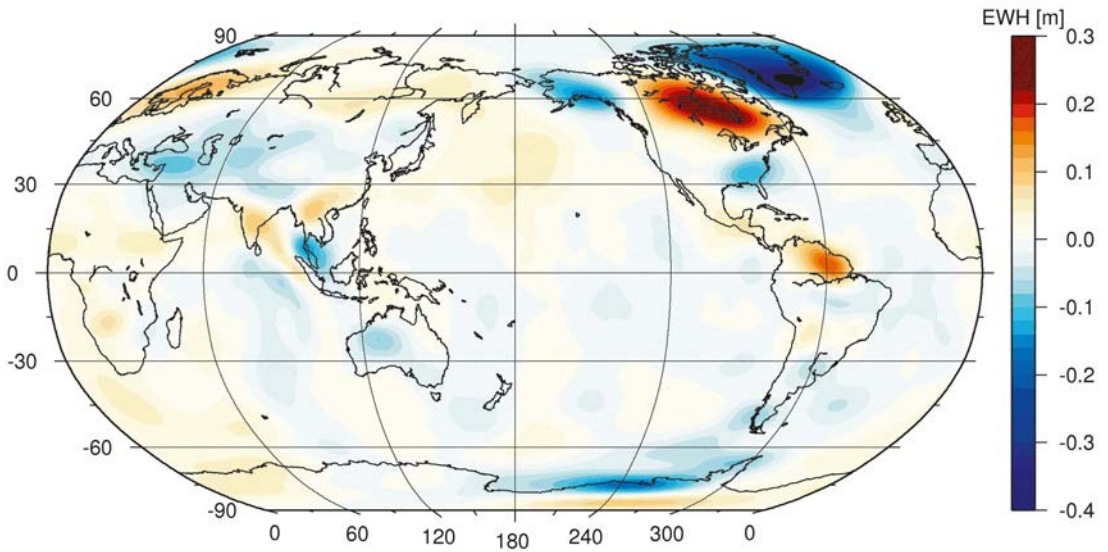


Fig. 1: Secular trends from GRACE gravimetry in terms of EWH. Pattern extracted from the CSR gravity field time-series from March 2003 to February 2009. At each point of a global  $1^\circ \times 1^\circ$  grid a regression line was fit to the time series of residual EWH values, cf. Eq. (1).

interpretation of minor features, hence, has to be done with care.

### 2.2.1 Removing leakage

A major challenge to deriving reliable mass changes from GRACE manifests in the correction for leakage effects. Leakage occurs due to both the restricted spectral resolution ( $L \ll \infty$ ) of gravitational field estimates and spatial averaging in terms of Gaussian smoothing. We demonstrate the situation by means of a simple synthetic example. We assume a disc-shaped mass anomaly of radius  $10^\circ$  located on the Earth's surface (cf. Fig. 2). The disc's gravitational signal is assessed by potential forward modeling (Newton integration). In order to recover the initial mass anomaly from its gravitational attrac-

tion, we truncated the spherical harmonic series at degree and order 60 and applied Gaussian smoothing with a radius of 500 km. Hence, the simulated scenario is consistent with our GRACE analysis.

Only 71% of the initial total mass is located within the disc-shaped area (Fig. 2). From the disc-shaped area point of view, 29% of the signal leaks out. On the other hand, from the perspective of an area outside the disc, signal leaks in. Whereas leakage-out signals have to be restored back into the region of interest, leakage-in signals have to be reduced from it. Although leakage signals strongly attenuate with increasing distance from the source, GRACE mass-change estimates are highly sensitive to these disturbing effects. The signal over Greenland, for instance,

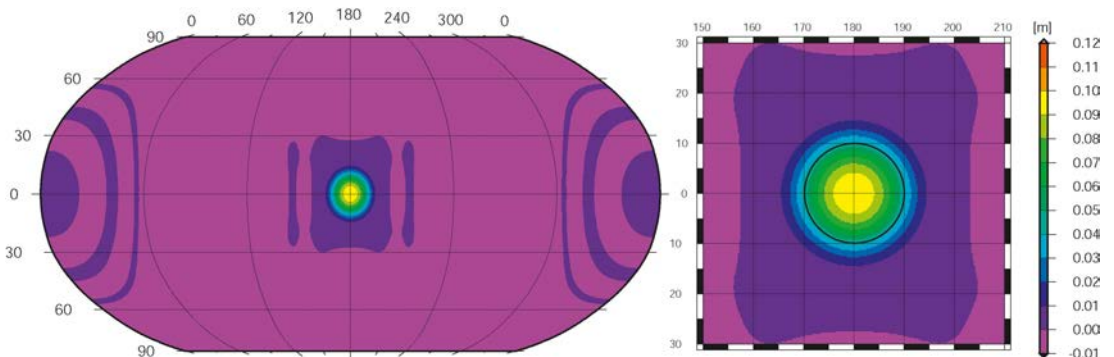


Fig. 2: Signal leakage experiment based on a simulated disc-shaped mass anomaly. The disc with a radius of  $10^\circ$  and 0.1 m EWH value is located on the equator at  $180^\circ$  E. 29% of the gravitational signal leaks out of the initial area.

spreads out over the whole globe. At the same time, signal over the Canadian Shield leaks into the Greenland area (cf. Fig. 1).

We developed and applied a robust four-step procedure to determine mass change from leakage-affected GRACE patterns, cf. [15]. The procedure isolates and quantifies both leakage-out signals and leakage-in signals. The method is a combination of extended spatial filters, followed by “calibration” in terms of comparison with forward gravity field modeling.

### 2.2.2 Glacial isostatic adjustment

GRACE is sensitive to vertically integrated mass variations, hence does not allow for the detection of their vertical (re)distribution. Post glacial rebound signals, in particular, distort conclusions on the magnitudes of contemporary mass transport. GIA modeling is highly subject to assumptions of ice-load history and mantle viscosity. For this reason, independent models differ significantly. As an example, [22] showed that the GIA contribution over Antarctica amounts to  $+100 \pm 67$  Gt/yr. In contrast, [4] quantified the change rate to  $+176 \pm 72$  Gt/yr. Here we used the GIA model according to [23] (Fig. 3), following the recommendation by the GRACE Tellus Team ([grace.jpl.nasa.gov](http://grace.jpl.nasa.gov)).

### 2.2.3 Modeling of secular trends

In order to avoid aliasing effects of strong seasonal signals falsifying our secular-change estimates, we fit basin-averaged residual mass-change time-series with a polynomial and three sinusoids, namely the annual signal, semi-annual signal and a 161-day tidal alias [24]. The model equation is

$$y(t_i) = \sum_{j=0}^n p_j t_i^j + \sum_{k=1}^3 A_k \cos(2\pi f_k t_i) + \sum_{k=1}^3 B_k \sin(2\pi f_k t_i) \quad i = 1, \dots, u. \quad (2)$$

The first term in Eq. (2) represents the secular trend (in terms of polynomial coefficients  $p_j$ ). Here, we investigate linear ( $n=1$ ) versus accelerated ( $n=2$ ) processes.  $y(t_i)$  denote residual mass changes at time  $t_i$ ,  $f_k$  are pre-defined frequencies according to the modeled sinusoids,  $A_k$  and  $B_k$  are the corresponding amplitudes.

We judged appropriate secular-trend modeling on the basis of the statistical significance of the estimated regression parameters. In particular, we balanced the null hypothesis  $H_0: p_j=0$  against the alternative hypothesis  $H_1: p_j \neq 0$ ; results of the Student-test are subject to a 95% confidence interval.

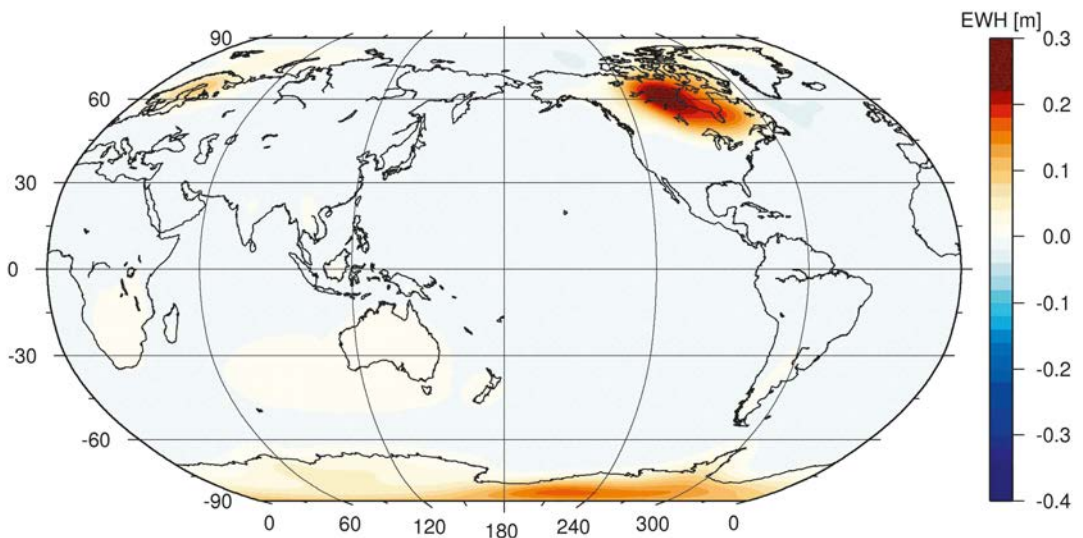
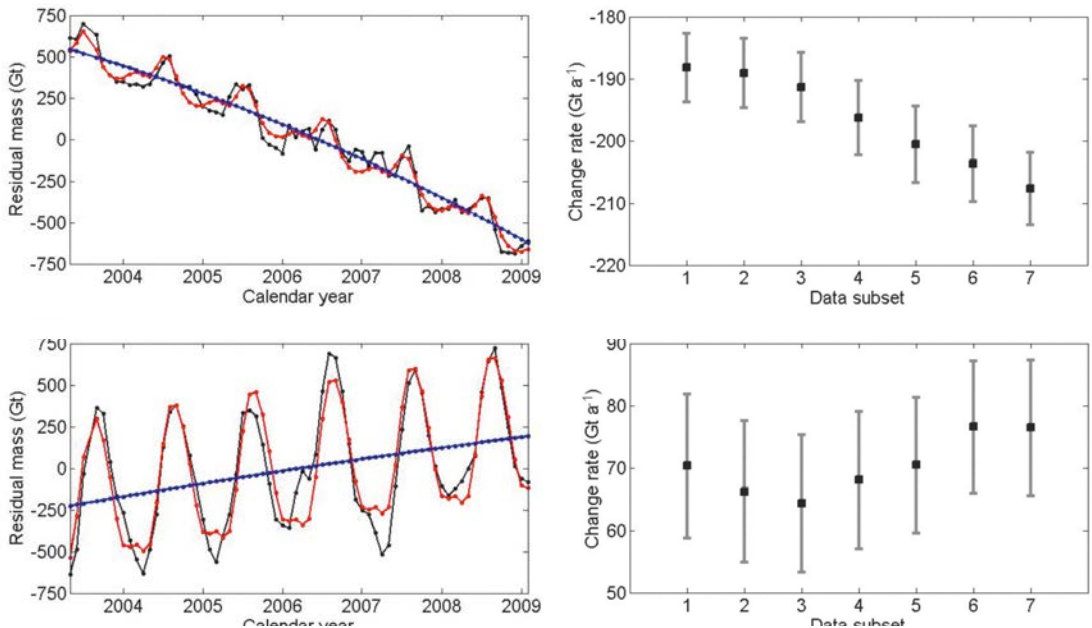


Fig. 3: GIA-induced mass-variation signal in terms of EWH. Pattern extracted from the GIA model in [23] over a six-year period. Within short periods, the GIA signal can be assumed to be linear in time. The same scale as in Fig. 1 applies. A comparison of the patterns reveals that the GRACE signals over the Canadian Shield and Fennoscandia are mainly caused by the rebound effect. Most of the GIA signal over Antarctica is balanced by the deglaciation signal.



**Fig. 4:** Greenland (left panels) and Orinoco Basin (right panels) mass variations from March 2003 to February 2009 (no GIA corrections applied). Top: black lines – monthly residual mass with respect to the temporal mean; red lines – least-squares fit ( $n=2$ ) according to Eq. (2); blue lines – least-squares fit ( $n=2$ ) according to Eq. (2), reduced by seasonal signals. Bottom: linear change rates taken over five-year data subsets. Each subset has an offset of two months to the previous one. Error bars indicate the standard deviation of the estimates.

### 2.3 Results

Fig. 4 (top panels) presents time series of residual mass taken with respect to long-term averages. Whereas Greenland is mainly affected by secular mass loss, in the Orinoco Basin seasonal variations dominate. Most notably, for Greenland we found linear change-rate modeling to be insufficient. Indeed, mass loss increased by  $+21.3 \pm 3 \text{ Gt/yr}^2$ . Greenland, thus, undergoes accelerated ice melting in the six-year time-period considered. Using a second-order polynomial fit, the total loss over the six-year period amounts to  $+1167 \pm 18 \text{ Gt}$ . For the Orinoco Basin, hypothesis testing proved linear regression to be superior to a quadratic fit. Over the period of investigation, the basin gained water at a rate of  $+75 \pm 9 \text{ Gt/yr}$  (i.e., no acceleration).

These findings are supported by the results displayed in the bottom panels in Fig. 4. For Greenland, the slopes of linear regression lines derived over various five-year data subsets increase significantly. Variations of change rates in the Orinoco Basin, on the other hand, are within the error bounds, i.e., not meaningful from a statistical point of view.

### 3. Sea-level change equivalent

Land-hydrological mass variations directly impact global sea-level change (SLC). Eustatic modeling translates mass gain or loss over land area to uniform water changes over the oceans. However, instead of resulting in globally uniform sea-level variations, the (re)distribution of water is spatially variable, which is due to the gravitational and elastic feedback effects caused by the changing surface mass geometries and loads.

Noteworthy, regional patterns subject to specific environmental constraints may significantly deviate from global modeling. For this reason, the conclusions drawn in this section have to be considered in a more general context. In Sect. 3.1, we shed light on the basic methodology of SLC forward modeling, following the theory in [14]. Section 3.2 presents selected results. In particular, we focus on the polar regions of the Earth, which contemporarily show the strongest (GIA-corrected) signals; that is, the secular mass trends as observed by GRACE (cf. Fig. 1) have been corrected by the GIA-signal shown in Fig. 3 so to only represent [assumed] hydrological changes.

### 3.1 Methods

Taking the gravitational and elastic feedback effects into account, the spatial dependency of the new relative sea level  $S(\lambda, \varphi)$  is given by

$$S(\lambda, \varphi) = S_{ii} + [S_{\Delta\Phi}(\lambda, \varphi) - \langle S_{\Delta\Phi}(\lambda, \varphi) \rangle_o] + [U_e(\lambda, \varphi) - \langle U_e(\lambda, \varphi) \rangle_o] \quad (3)$$

where  $S_{ii}$  denotes the global average of all residual water masses. The SLC caused by the gravitational feedback effect of the changing masses is given by  $S_{\Delta\Phi}(\lambda, \varphi) = \Delta\Phi(\lambda, \varphi) / g$ ; therein,  $\Delta\Phi(\lambda, \varphi)$  represents the change in the Earth's gravitational potential (including the elastic feedback) and  $g$  is the gravitational acceleration on the Earth's surface. The vertical surface displacement due to the elastic response is expressed by  $U_e(\lambda, \varphi)$ , i.e., Eq. (3) models sea-level relative to the changing surface of the Earth. The integral-averages  $\langle S_{\Delta\Phi}(\lambda, \varphi) \rangle_o$  and  $\langle U_e(\lambda, \varphi) \rangle_o$  are taken over the global ocean area and have to be subtracted so that the total mass-variation magnitude over the oceans corresponds to the uniform change, i.e.,  $\langle S(\lambda, \varphi) \rangle_o = S_{ii}$ . Equation (3) has to be solved iteratively as both  $\Delta\Phi(\lambda, \varphi)$  and  $U_e(\lambda, \varphi)$  require knowledge of  $S(\lambda, \varphi)$ .

Noteworthy, the new sea-level surface follows that particular equipotential surface in the changed Earth's gravitational field that preserves the eustatic change in a global average sense. Consequently, real sea-level variations are always lower than the eustatic change close to mass-loss areas and higher than the eustatic change further away from them [14,25,26]. Opposite effects hold for mass-accumulation areas.

### 3.2 Results

We applied SLC forward modeling to Greenland and Antarctic mass changes, i.e., to areas with most dominant (GIA-corrected) hydrological signals as detected by GRACE. As such, we shed light on contemporary deglaciation-induced relative sea-level rise. Fig. 5 reveals that relative

sea level does not change in a uniform manner. Most notably, in offshore regions near land ice-mass loss, sea-level fall can be observed. Greenland-induced SLC varies between  $-3$  mm/yr and  $+1$  mm/yr; the average is  $+0.56$  mm/yr. The minimum and maximum values for Antarctica are  $-1.0$  mm/yr and  $+1.0$  mm/yr, respectively; the average amounts to  $+0.50$  mm/yr.

Ice melting in the Arctic mainly causes sea-level rise in the Southern Hemisphere; ice loss over Antarctica dominates sea-level rise in the Northern Hemisphere. As a consequence, the combined pattern is close to the eustatic scenario for vast areas of the world's oceans. However, most regions above 30N and below a 60S are affected less than the eustatic change. The maximum relative sea-level rise is present mostly along a belt covering the tropics and subtropics.

### 4. Conclusions

From our simulation experiments and GRACE results, we claim to have a comprehensive toolkit at hand that allows reliable gravity-related studies on mass transport in the system Earth. Both total mass-change numbers within certain time periods and the temporal progress of these changes are of utmost importance to improve the understanding of present-day phenomena. In this context, we confirm accelerated Greenland ice loss as reported in [12]. Although the numbers are astonishingly close to each other ( $+21.9 \pm 1$  Gt/yr<sup>2</sup> versus  $+21.3 \pm 3$  Gt/yr<sup>2</sup>), the rates refer to different periods, so should not be compared directly.

The error bounds we provide are derived from residuals between the recovered mass-variation time series and the least-squares fit to this series; they do not account for the uncertainties of SHC, and hence GRACE errors. A more rigorous approach would include spectral-to-spatial domain error propagation. In this framework, SHC (co)variance scaling would need to be investigated in order to account for realistic noise levels. Although

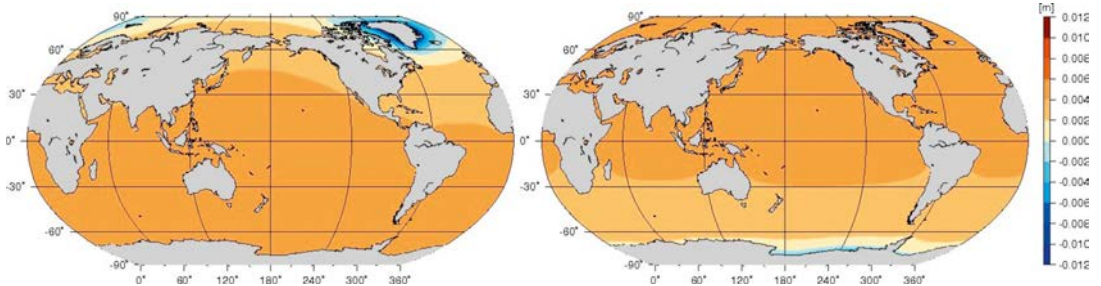


Fig. 5: Global SLC from Greenland (left panel) and Antarctica (right panel) mass-change geometries; GIA corrections applied. Patterns hold for a seven-year period, taking gravitational and elastic feedback effects into account.

we are aware of the fact that our error bounds tend to be overoptimistic, we expect our main conclusions on the statistical significance of the estimated regression parameters to be still valid taking the full error budget into consideration.

Relative SLC patterns induced by mass variations in the Earth's system depend on (i) mass-change magnitudes, (ii) mass-change geometries, and (iii) global ice/water mass redistribution. Uniform modeling of sea-level variations is insufficient for meaningful geophysical interpretation. As such, gravitational and elastic feedback effects should always be considered. Apart from present scientific and socio-economic significance, they allow a more realistic outlook for future mid-term SLC patterns as opposed to the simplistic uniform SLC model. Our mass-balance studies over Greenland and Antarctica result in a relative SLC equivalent of  $+1.06 \pm 0.07$  mm/yr; the contribution from Antarctica is highly subject to GIA modeling.

## References

- [1] Tapley, B. D., Bettadpur, D., Ries, J. C., Thompson, P. F., Watkins, M. M. (2004): GRACE Measurements of Mass Variability in the Earth System. *Science* 305: 503-505.
- [2] Luthcke, S. B., Zwally, H. J., Abdalati, W., Rowlands, D. D., Ray, R. D., Nerem, R. S., Lemoine, F. G., McCarthy, J. J., Chinn, D. S. (2006): Recent Greenland ice mass loss by drainage system from satellite gravity observations. *Science* 314: 1286-1289.
- [3] Chen, J. L., Tapley, B. D., Wilson, C. R. (2006): Alaskan mountain glacial melting observed by satellite gravimetry. *Earth Plan. Sci. Lett.* 248: 368-378.
- [4] Velicogna, I., Wahr, J. (2006): Measurements of time-variable gravity show mass loss in Antarctica. *Science* 311: 1754-1756.
- [5] Chen, J. L., Wilson, C. R., Tapley, B. D., Blankenship, D. D., Ivins, E. R. (2007): Patagonia Icefield melting observed by Gravity Recovery and Climate Experiment (GRACE). *Geophys. Res. Lett.* 34, L22501.
- [6] Schmidt, R., Petrovic, S., Güntner, A., Barthelmes, F., Wunsch, J., Kusche, J. (2008): Periodic components of water storage changes from GRACE and global hydrology models. *J. Geophys. Res.* 113, B08419.
- [7] Wouters, B., Chambers, D., Schrama, E. J. O. (2008): GRACE observes small-scale mass loss in Greenland. *Geophys. Res. Lett.* 35, L20501.
- [8] Broeke van den, M., Bamber, J., Ettema, J., Rignot, E., Schrama, E., Berg van de, W. J., Meijgaard van, E., Velicogna, I., Wouters, B. (2009): Partitioning recent Greenland mass loss. *Science* 326: 984-986.
- [9] Baur, O., Sneeuw, N. (2011): Assessing Greenland ice mass loss by means of point-mass modeling: a viable methodology. *J. Geod.*, online first.
- [10] Velicogna, I., Wahr, J. (2006): Acceleration of Greenland ice mass loss in spring 2004. *Nature* 443: 329-331.
- [11] Baur, O., Kuhn, M., Featherstone, W. E. (2010): Linear and non-linear secular mass variations over Greenland. *Proc. VII Hotine-Marussi Symposium*, Springer, in press.
- [12] Rignot, E., Velicogna, I., Broeke van den, M., Monaghan, A., Lenaerts, J. (2011): Acceleration of the contribution of the Greenland and Antarctic ice sheets to sea level rise. *Geophys. Res. Lett.*, in press.
- [13] Lombard, A., Garcia, D., Ramillien, G., Cazenave, A., Biancale, R., Lemoine, J. M., Flechtner, F., Schmidt, R., Ishii, M. (2007): Estimation of steric sea level variations from combined GRACE and Jason-1 data. *Earth Plan. Sci. Lett.* 254: 194-202.
- [14] Farrell, W. E., Clark, J. A. (1976): On postglacial sea level. *Geophys. J. R. astr. Soc.* 46: 647-667.
- [15] Baur, O., Kuhn, M., Featherstone, W. E. (2009): GRACE-derived ice-mass variations over Greenland by accounting for leakage effects. *J. Geophys. Res.* 114, B06407.
- [16] Klemann, V., Martinec, Z. (2009): Contribution of glacial-isostatic adjustment to the geocenter. *Tectonophysics*, in press.
- [17] Quinn, K. J., Ponte, R. M. (2010): Uncertainty in ocean mass trends from GRACE. *Geophys. J. Int.* 181: 762-768.
- [18] Cheng, M., Tapley, B. D. (2004): Variations in the Earth's oblateness during the past 28 years. *J. Geophys. Res.* 109, B09402.
- [19] Wahr, J., Molenaar, M., Bryan, F. (1998): Time variability of the Earth's gravity field: Hydrological and oceanic effects and their possible detection using GRACE. *J. Geophys. Res.* 103: 30,05-30,29.
- [20] Swenson, S., Wahr, J. (2006): Post-processing removal of correlated errors in GRACE data. *Geophys. Res. Lett.* 33, L08402.
- [21] Jekeli, C. (1981): Alternative methods to smooth the Earth's gravity field. Report 327, Dept. of Geod. Sci. and Surv., Ohio State University, Columbus.
- [22] Riva, R. E. M., Gunter, B. C., Urban, T. J., Vermeersen, B. L. A., Lindenbergh, R. C., Helsen, M. M., Bamber, J. L., Wal van de, R. S. W., Broeke van den, M. R., Schutz, B. E. (2009): Glacial Isostatic Adjustment over Antarctica from combined ICESat and GRACE satellite data. *Earth Plan. Sci. Lett.* 288: 516-523.
- [23] Paulson, A., Zhong, S., Wahr, J. (2007): Inference of mantle viscosity from GRACE and relative sea level data. *Geophys. J. Int.* 171: 497-508.
- [24] Chen, J. L., Wilson, C. R., Seo, K.-W. (2009): S2 tide aliasing in GRACE time-variable gravity solutions. *J. Geod.* 83: 679-687.
- [25] Mitrova, J. X., Tamisiea, M. E., Davis, J. L., Milne, G. A. (2001): Recent mass balance of polar ice sheets inferred from patterns of global sea-level change. *Nature* 209: 1026-1029.
- [26] Kuhn, M., Featherstone, W. E., Makarynsky, O., Keller, W. (2010): Deglaciation-induced spatially variable sea level change: a simple-model case study for the Greenland and Antarctic ice sheets. *Int. J. Ocean Climate Sys.* 1(2): 67-83.

## Contacts

**Dr.-Ing. Oliver Baur**, Space Research Institute, Austrian Academy of Sciences, Schmiedlstraße 6, 8042 Graz, Austria.  
E-mail: oliver.baur@oeaw.ac.at

**Dr.-Ing. Michael Kuhn**, Western Australian Centre for Geodesy and The Institute for Geoscience Research, Curtin University of Technology, GPO Box U1987, Perth, WA 6845, Australia.  
E-mail: m.kuhn@curtin.edu.au

**Prof. Will E. Featherstone**, Western Australian Centre for Geodesy and The Institute for Geoscience Research, Curtin University of Technology, GPO Box U1987, Perth, WA 6845, Australia.  
E-mail: w.featherstone@curtin.edu.au

## Automated Detection and Interpretation of Geomorphic Features in LiDAR Point Clouds



*Peter Dorninger, Balázs Székely,  
András Zámolyi and Andreas Roncat*

### Abstract

Laser scanning has proven to be an adequate tool for the acquisition of topographic data. For large scale or even country-wide campaigns, airborne platforms (ALS) are suited, while for small areas, terrestrial laser scanners (TLS) are commonly used. According to the instrument type and the measurement principle applied, more than one million points may be acquired per second. This allows for dense and accurate acquisition of the topography. Unfortunately, the amount of data becomes a considerable challenge for the user of such data. Therefore, often products derived from the original point clouds are provided. For topographic modeling, digital terrain models are commonly used. Such models may be derived by means of robust filtering strategies for separating ground surface points from others representing, for example, vegetation, buildings, etc. Within this contribution, the application of a point-based segmentation algorithm for reducing the amount of data for the purpose of subsequent geomorphological topography analysis is presented. For this, the raw point data is subdivided into planar faces, allowing reducing the amount of data by a factor of up to 3,000 without a significant reduction in the level of detail of the terrain representation. The application of this approach is proven on a series of ALS and TLS data sets acquired at the landslide in Doren, Vorarlberg. By means of additionally recorded geological in-situ measurements it could be demonstrated that geomorphological primary directions can be properly determined within the reduced laser scanning data.

**Keywords:** Segmentation, Laserscanning, Doren, Geomorphology, Landslide

### Kurzfassung

Zur Erfassung topographischer Daten haben sich Laserscanning basierte Methoden etabliert. Für großflächige bzw. landesweite Messkampagnen eignen sich flugzeug- bzw. helikoptergestützte Plattformen (ALS), zur kleinräumigen Erfassung kommen häufig sogenannte Terrestrische Laserscanner (TLS) zum Einsatz. Abhängig vom Gerätetyp und dem verwendeten Messprinzip können mehr als eine Million Punkte pro Sekunde erfasst werden. Dem damit offenkundig verbundenen Nutzen einer äußerst dichten und genauen Erfassung des Geländes stehen aber auch meist enorme Datenmengen gegenüber. Dies stellt den Anwender derartiger Daten häufig vor nahezu unüberwindbare Probleme. Daher werden im Allgemeinen aus den Rohdaten (Punktwolken) abgeleitete Produkte zur Verfügung gestellt. Im Bereich der Topographiemodellierung finden häufig digitale Geländemodelle Verwendung. Diese können mit Hilfe robuster Filtermethoden aus den Originalpunkten abgeleitet werden. Dieser Beitrag demonstriert die Anwendung einer punktwolken-basierten Segmentierungsmethode zur Reduktion der zu verarbeitenden Daten für weiterführende, geomorphologische Geländeanalysen. Dabei wird das erfasste Gelände auf Basis der Rohdaten in ebene Flächen unterteilt. So kann eine Datenreduktion um den Faktor 3.000 erzielt werden, ohne signifikante Einbußen in Bezug auf die Detailliertheit der Geländebeschreibung hinnehmen zu müssen. Die Anwendung dieses Ansatzes wird an Hand einer Serie von ALS und TLS Aufnahmen der Hangrutschung in Doren, Vorarlberg, demonstriert. Mit Hilfe zusätzlich erfasster geologischer Geländemessungen konnte gezeigt werden, dass geomorphologische Hauptrichtungen auch in den stark reduzierten Laserscanning Daten erfolgreich bestimmt werden können.

**Schlüsselwörter:** Segmentierung, Laser Scanning, Doren, Geomorphologie, Massenbewegung

### 1. Introduction

LiDAR (light detection and ranging), also referred to as laser scanning, has proven to be an adequate tool for the acquisition of high-density and accurate topographic data (e.g. [1], [2], [3]). If the sensor is carried by airborne platforms (e.g. airplanes or helicopters), it is commonly referred to as Airborne Laser Scanning (ALS). ALS allows for the acquisition of topographic data of large

scale areas or even country-wide with decimeter accuracy. Depending on the acquisition geometry (i.e. accessibility and visibility of the area to be captured), for smaller areas Terrestrial Laser Scanning (TLS) is a preferable alternative to ALS. In this case, the scanner is mounted on a tripod allowing, in general, for capturing the panoramic surroundings of the scanning position with centimeter accuracy or even better, dependent on

the measurement distance and the surface structure. Current instruments applying the phase-shift measurement principle for distance measurement allow for sampling up to one million points per second [4].

Despite the above mentioned advantages of laser scanning technology, a great number of potential users are limited in its use. A major problem in the application of laser scanning is the enormous amount of data. Up to one million points are captured per second meaning a considerable challenge for the end user of the data even for smaller areas and becoming more and more insuperable with an increasing size of the areas to be investigated. Hence, the experimenter has to have a high degree of data-specific knowledge and experience in order to manage the acquired dataset and to derive the relevant information from raw or intermediate data products. By the way, a considerable processing infrastructure may be required for processing the data within acceptable time. From this, the key research question of this contribution can be defined as the following hypothesis: "Applying an automated plane detection algorithm on large scale LiDAR datasets enables reducing the amount of data for further interpretation significantly without loss of information".

Within the Christian Doppler Laboratory "Spatial Data from Laser Scanning and Remote Sensing", assigned to the Institute of Photogrammetry and Remote Sensing of the Vienna University of Technology, a variety of aspects with respect to laser scanning have been investigated for seven years from end of 2003 to end of 2010 including potential solutions to the aforementioned problems. A team of up to ten researchers was financed by all together eleven commercial partners and funded by the Christian Doppler Research Association (CDG). The fields of business activities of the partner companies covered instrument manufacturing, surveying and photogrammetry, geo-data services, cultural heritage management, and stone masonry. Correspondingly, a variety of topics was investigated covering instrument calibration (ALS: [5], TLS: [4]), object extraction [6], geometric modeling [7], and analysis. The produced results exceeded the current industry standards in quality and in quantity, and therefore proved to be suitable to carry out various experiments for future applications.

Among others, a key product delivering possibilities for geomorphologically relevant topics proved to be the digital terrain model (DTM) rep-

resenting the bare surface of a given area [8]. DTM generation may be based on applying adequate filtering techniques on the original points (e.g. [9]). This allows for separating terrain points from other objects such as vegetation or buildings and subsequently the generation of a DTM. Alternatively, the amount of data may be reduced by aggregating points with similar properties to distinct objects representing the attributes of the original points, i.e. a segmentation of the point cloud. An example for such an application is the derivation of building models from point clouds. In this case, points belonging to planar features are assigned to roof planes as the foundation for the subsequent geometrical modeling process. The assumptions made when assigning points to the plane (i.e. similar aspect and slope, neighborhood, etc.) guarantee that the respective attributes of the plane are similar to those of the belonging points hence representing the information of the original points properly, without significant loss of information. As a matter of fact, the number of objects (in this case the plane faces) is significantly smaller than the number of original points. Therefore, the amount of data to be processed for further interpretation and analysis is reduced significantly, so it becomes usable for most end users.

The segmentation into planes described above, was developed for the analysis of roofs and other man-made surfaces. In this article we study, if and how this segmentation can be used in analysis of natural surfaces. In close cooperation with earth sciences, geomorphologic analysis of the topography at the very high resolution of laser scanning data and derived products provided new and detailed results in assessing micro-topographic features and also changes of these features in time (e.g. [10], [11]). A prominent study area is the landslide of Doren in Western Austria (Vorarlberg). Here, both object extraction and time-series analysis of the extracted geomorphic features could be tested.

## 2. Theoretical Aspects

The progress made in automated extraction and modeling of buildings from ALS data serves as a promising originator for testing these algorithms for detection and generalization of geomorphic features. Our aim is to recognize automatically as many features as possible from airborne and terrestrial laser scanning point clouds, in order to reduce the amount of data significantly for further geomorphological interpretation. For this, we propose to apply a segmentation process allow-

ing determining planar structures within a surface represented by a point cloud. This allows processing the original point cloud directly without the prior computation of a DTM.

The segmentation is based on a robust calculation of local tangential planes for all recorded points. For this, a set of neighboring points is taken and, by means of a robust plane fit, the fifty percent of points fulfilling best a locally estimated planarity criterion are used to determine the local tangential plane for each point ([12]). For the determination of planar structures in the point cloud it is assumed that similar tangential planes were determined for points belonging to the same planar structure.

Based on checking the quality parameters describing the planarity behavior of such a point set (i.e. the ratio of the axis of the covariance ellipsoid circumscribing the points accepted for the locale plane fit), points acquired at non-continuous surfaces (e.g. vegetation) can be identified and excluded from subsequent analysis. Hence, a prior filtering of the point cloud as necessary for DTM computation as described in [9] is not required in this case. The procedure of segmenting an ALS point cloud representing a house is demonstrated for two planes in Fig. 1 (plane 1: a&b, plane 2: c&d). First, seed regions are determined globally in a feature space defined by the parameters of the local regression planes and using a 4D distance threshold for distinguishing different planes (red circles). Afterwards, all points possibly belonging to this seed plane are assigned using a 3D distance threshold within the object space (orange and light green). Points that do not fulfill the planarity criterion of the seed plane are subsequently rejected applying the feature space threshold again (orange) and finally, a robust plane is fitted into the selected points (dark green). The final segmentation result is shown in Fig. 1 e.

Owing to the design of the algorithm, millions of input points can be processed with acceptable processing time on standard computer systems [7]. For each segment, numerous parameters are derived which can be used for further exploration. These are, for example, location, area, aspect, slope, and roughness. For processing large scale areas with low variety in surface structure with respect to its global extension it turned out to be advisable to apply the segmentation using a tiling structure. Although the feature space distance measure used for investigating the identity of individual planes is scale independent (i.e., the size of the investigated area is normalized by its extension), it turned out that especially the globally applied seed region determination tends to geometrically correct but geomorphologically unreliable results if being applied to large scale areas, especially in areas with low geometrical variety.

### 3. Data and Methodology

The study area, the Doren landslide, is located in Bregenzer Wald in Vorarlberg, Western Austria in the Foreland Molasse Zone. It can be classified as a deep-seated rotational landslide [13]. The landslide itself has shown several active periods in the last decades, endangering settlements and land property. Geologic units of the area mainly comprise sediments of the freshwater molasses. This area formed a depression zone in front of the over thrusting and northwards propagating Alpine nappe stack. The molasse units consist lithologically of variegated sediments such as sandstones, marls and clays that are mixed up and interbedded. The landscape was subject to glaciation leaving remnants of Würmian moraines. Regional and local topography is highly dissected by river incision. Several watercourses cut into the host rock; the most important of them is the Weißbach River, since its incision forms the valley

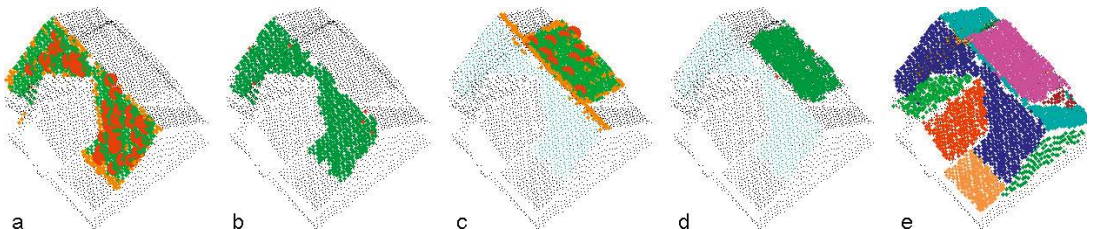


**Fig. 1:** Detecting planar faces from a point cloud by segmentation, demonstrated on man-made surfaces like roof facets. (a)-(d): Determination of segments 1 and 2. (a) and (c): Seed cluster points (red circles), points accepted in object space (orange and green), points accepted in feature space (green). (b) and (d): Result of robust plane fit (dark green: accepted, red: rejected). Small cyan dots in (c) and (d): points assigned to segment 1. (e): result of the segmentation; black: points of the rejection class not assigned to planes.



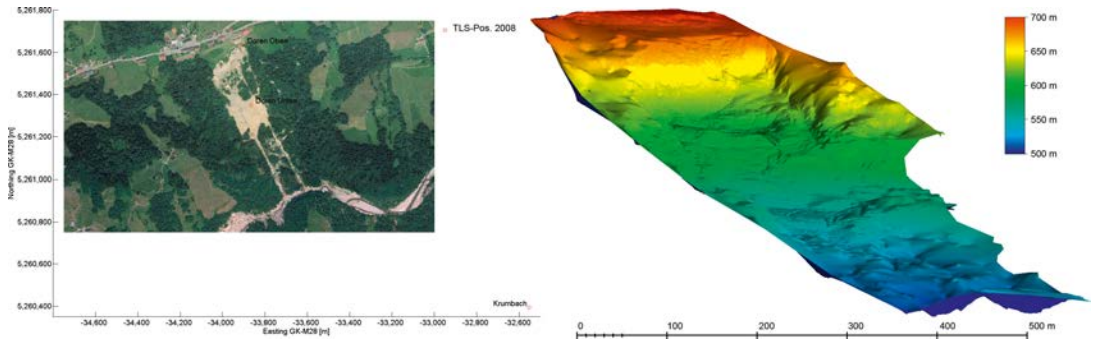


Fig. 2: Orthophoto of the Doren landslide in 2006 and scanning positions of TLS campaign 2008 (left); perspective view of a height coded DTM derived from the TLS data of the September 2008 campaign (right).

containing the Doren landslide. The discharge of the river varies highly. Due to the incision of the valleys, the valley slopes show bimodality in slope angles, resulting in steep slopes towards the thalweg. Consequently, settlement areas are located on the valley slopes in the upper areas. Additionally, major parts of the valley slopes, primarily the steepest ones, are covered with forest or shrubs. Fig. 2 shows an orthoimage of the study area (left) and a height coded DTM (right).

In the following, we investigate ALS data from 2003, 2006 and 2007. The mean point density

varies slightly; it is approximately 2 points per square-meter. The height accuracy is about 15 cm. Additionally, two TLS campaigns were realized in 2008 and 2009. For both TLS campaigns, artificial retroreflective targets were used to support the subsequent registration process.

In September 2008, a terrestrial full-waveform scanner *Riegl LPM-321* was used. This instrument allows for a maximum measurement distance of 6 km with an accuracy of approximately 10 cm, depending on the measurement distance. Using the on-board point extraction algorithm,

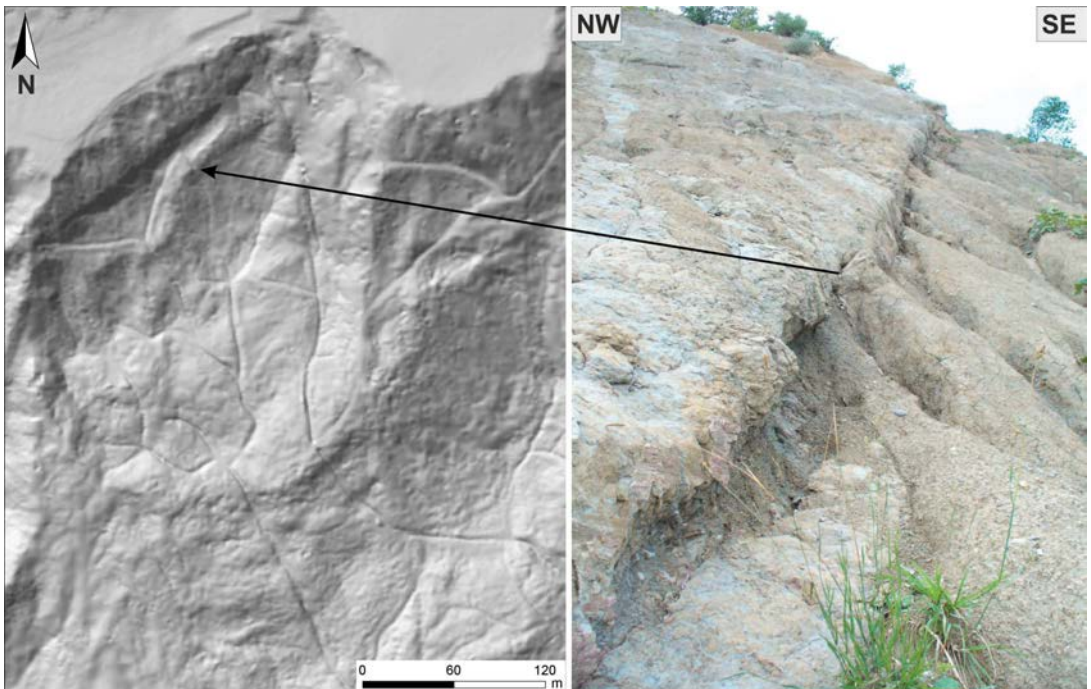


Fig. 3: Hillshade of a DTM derived from ALS-data of the year 2003 (left). A major fault observed in the field is dissecting the main scarp; black arrow shows its location on the hillshaded DTM (right). The height of the terrain scarp along the fault is approximately 50 cm.

the instrument determines up to three echoes per shot. Unfortunately, the internally sampled waveform could not be processed properly with "standard" wave-form processing approaches (e.g. [5], [14], [15]) and was therefore not used further. All together, approximately two million echoes were recorded from three scanning positions (see Fig. 2, left) resulting in a mean point density of approximately 20 cm.

In August 2009, a terrestrial scanner *Riegl LMS-Z420i* was used. This instrument records one echo per shot only. However, it enables faster sampling rates and hence higher point densities. Seven scans from five scanning positions were realized and 2.5 million points were captured.

During the TLS field campaigns the local geologic and geomorphic setting was documented, too. Structural geologic field measurements were taken close to the mass movement for characterization of the host rock. Field observations revealed a large number of cracks and faults within the interbedded marls and sandstones surrounding the landslide. Fig. 3 shows a prominent fault cutting the main scarp and its appearance in the hillshaded DTM derived from ALS data in 2003. In the area affected by the mass movement itself, orientation, length and position of cracks were recorded using GPS. These cracks were open and not filled with any kind of material. The results of the field measurements were visualized using Schmidt's net lower hemisphere plots (Fig. 4), a common technique in structural geology. The fault shown in Fig. 3 has an orientation of NNW-SSE. This is in accordance with the linear feature observed in the hillshaded DTM of 2003. Other linear features detected in the ALS and TLS data using the described processing techniques (i.e. segmentation) were verified or rejected by means of field measurements.

#### 4. Experiment and Discussion

We applied the described segmentation approach to the ALS and TLS point clouds. The investigated region covers approximately 600 by 1,000 meters. In Fig. 5, four different parameters (i.e. slope, aspect, number of points per plane, standard deviation of plane fit) as determined for each segmentation plane are shown for a selected region of the 2007 ALS data set. This point cloud originally consisted of 700,000 points. Of that, 225 planes were determined using a distance tolerance of 50 cm and excluding small planes with less than 500 defining points. These parameters were determined

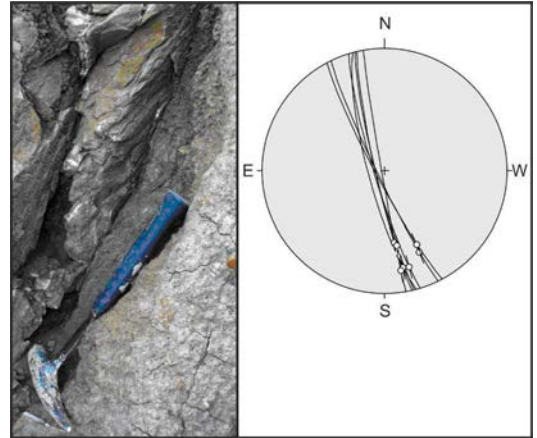


*Fig. 4: Structural geologic field measurements of the faults shown in Fig. 3 indicate a NNW-SSE orientation. The field measurements were plotted using Schmidt's net plots. It is important to note that many linear features in the host rock surrounding the mass movement have similar orientation.*

empirically. Decreasing the tolerances resulted in an over-segmentation with numerous very small faces and numerous points not assigned to planar structures. Increasing the tolerances led to under-segmentation or erroneous results. The local normal vector was determined from 16 points, hence the local regression plane is fitted to those 9 out of the closest 16 neighbors of each point which are most likely to represent a planar structure. The proper neighborhood-size was selected empirically by evaluating color-coded plots of the resulting normal vectors and of the local roughness which was determined from the circumscribing covariance ellipsoid.

Color coded visualizations of the respective parameters are shown in the left column. The center column shows the distribution of the parameters with respect to the number of planes and the right column with respect to the number of points. These two histograms may vary for the same parameter due to the fact that having a large segment with many points assigned to, this segment is counted only once for the "number of planes" histogram while many points with the same parameter do exist. Hence, the segment-based analysis gives the global trend (i.e., how many regions with a certain parameter are found) while the point-based analysis gives a hint to the total area if a homogeneous point distribution is given. Therefore, in order to equalize the two histograms, a normalization of the plane-based parameter considering the area covered by the plane would be necessary.

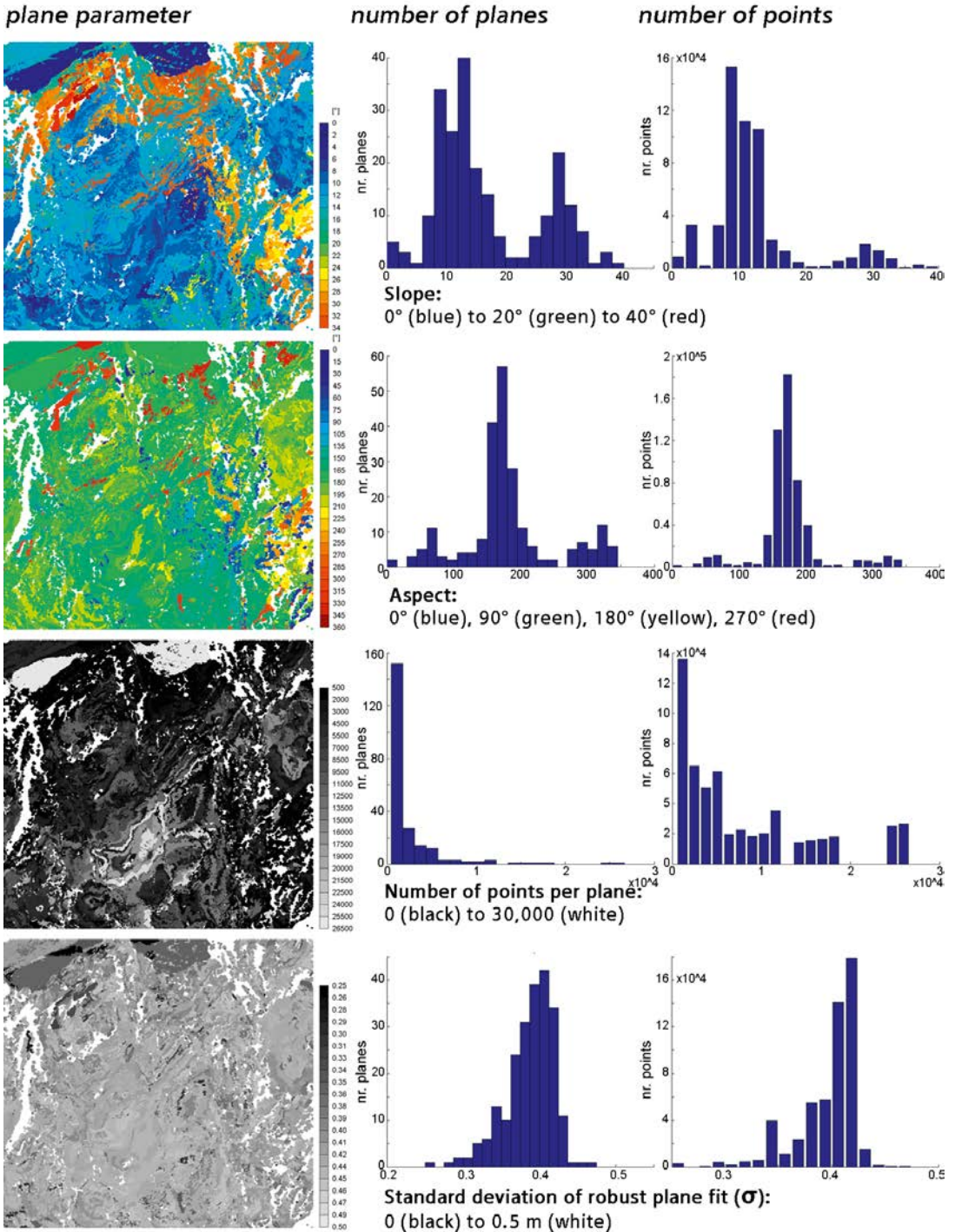
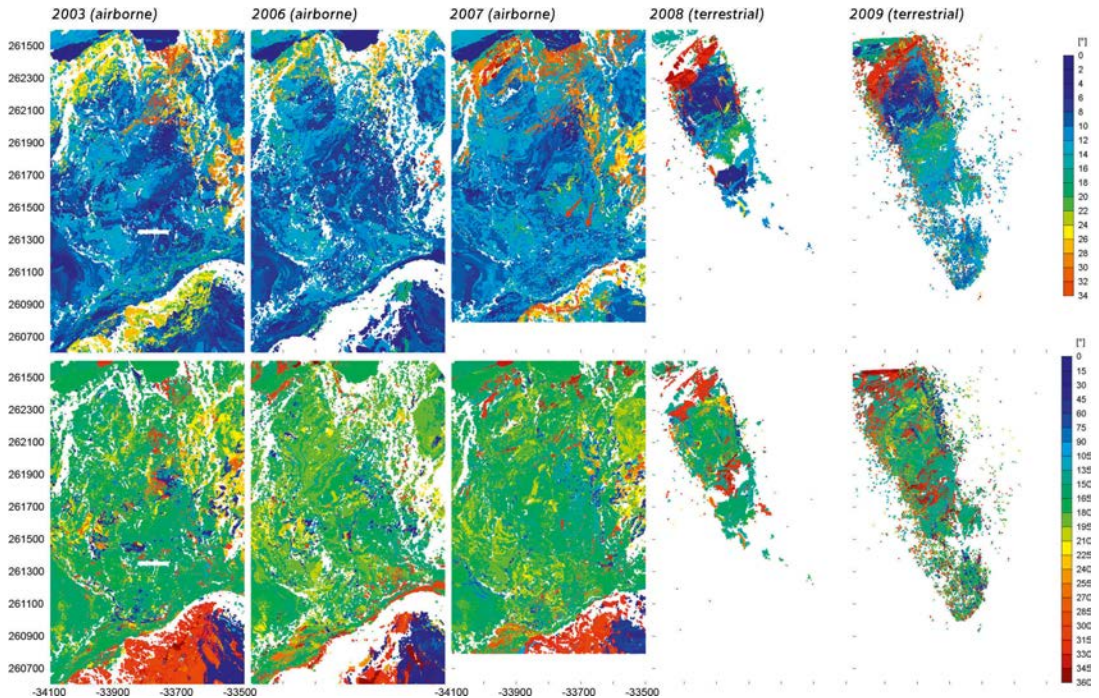


Fig. 5: Analysis of plane parameters derived from the ALS 2007 dataset. The left column shows the parameters “slope”, “aspect”, “number of points per plane”, and “standard deviation of plane fit” as determined for each plane. Color codes are indicated on the right hand side of each parameter map. The histograms show the distribution of these parameters with respect to the number of detected planes (center column) and the number of points (right column).



**Fig. 6:** Time series of the Doren landslide region from 2003 to 2009. The upper image series shows the slope angles of the fitted planes, the lower one shows their aspect angles. On both types of maps changes in the shape of the landslide can be observed. On the slope map, the progressive denudation of the main sliding plane is clearly indicated by the on-going steepening along the main scarp, whereas on the aspect map of the ALS data, the change in shape of the landslide toe can be documented.

For the two parameters slope and aspect, a time series of the five available datasets from 2003 to 2009 was generated as shown in Fig. 6. Although the amount of data was reduced approximately by a factor of 3,000, the major differences in the surface caused by the landslide can be seen clearly. Especially the increasing slope angle in the north-western region (i.e. the upper main scarp) is visible, and dynamic changes are discernible within the whole region.

For all ALS point clouds, the parameters as described above were applied. For the TLS data, the neighborhood for normal vector estimation was increased to 32 in order to cope with the higher point density and the vegetation points. Therefore, vegetation points do not influence the result significantly, although large areas of the investigated region are covered by vegetation. This is enabled by the implicit elimination of those points during the determination of planar structures. As mentioned in the theory-section, the robust estimation of the local tangential planes, allows for eliminating points representing non planar structures. A shortcoming of the current implementation of the segmentation is the

fact that for large point clouds – like those presented – a connected component analysis can not be applied due to memory restrictions. Such a connected component analysis should enable separating disconnected regions with identical plane parameter. If this is not performed – as it is the case for the presented results – originally disconnected regions are assigned to the same planar structure. This has no influence on the analysis of local surface parameter like slope, aspect, or sigma. However, some of the vegetation points may be assigned to planar regions (see Fig. 6, right), especially if numerous vegetation points are in the point cloud (e.g. TLS 2009). What is clearly visible on the slope maps of Fig. 6, is the progressive denudation of the main sliding plane and thus a steady increase in slope angles.

According to field observations and the analysis of the ALS and TLS data, the landslide of Doren in its present form shows features similar to those of a complex rotational landslide as described by [16]. Material on the unstable slopes starts moving along a convex main scarp the geometry of which is influenced by

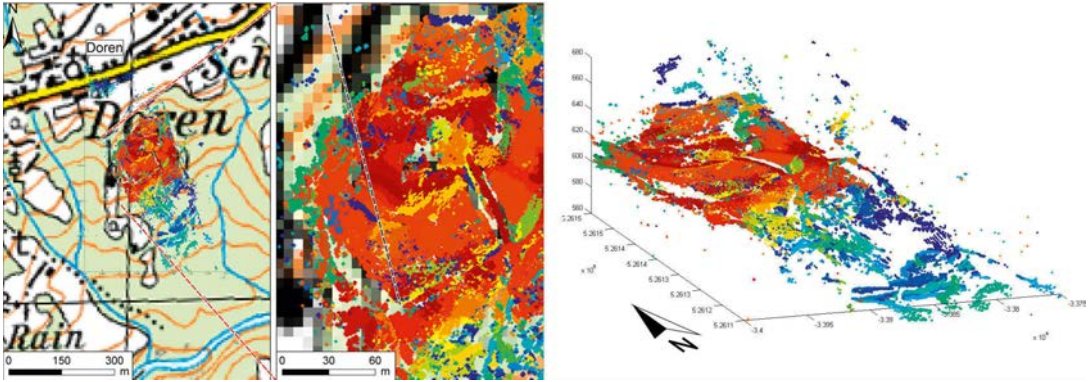


Fig. 7: Fitted planes of the TLS data from 2008 on the background of the Austrian topographic map (BEV, ÖK 50-BMN, Blatt 112 Bezau, scale: 1:50,000). The center image is an enlargement of the overview map shown left and the right image shows a perspective view of the segmentation. Each patch with a given color represents a different plane. The best approach for the analysis of such plane-maps would be the pattern analysis of the plane boundaries. If plane margins do line up in a certain pattern, a geological or geomorphological meaning should be verified in the field. The dashed black line in the right hand image, for instance denotes the location of the fault dissecting the main scarp also shown in Fig 3. Note that some man-made structures are also outlined: these belong to the drainage system that had been initiated after the major landslide movement in 2007.

the lithology of the host rock. The margins of the Doren landslide are sharp and reveal the host rock forming a steep slope on either side. Downwards, the convex main scarp rises underneath the gravitatively moving mass and induces the formation of a tongue-shaped landslide toe (see also: [13], [17]). The main driving force inside the mass movement is gravity. Transverse cracks form, as the material migrates down the convex main scarp and its lower rise. Accordingly, linear or planar features derived by segmentation outside the area affected by the mass movement, may show a certain pattern linked to faulting within a regional stress field with  $\sigma_1$  oriented NW-SE and  $\sigma_3$  oriented NE-SW ( $\sigma_1 > \sigma_2 > \sigma_3$ , see also: [18]). On the mass movement itself, however, a different pattern related to gravitational sliding should be dominant (e.g. transverse linear features, see [16]).

Comparing the images of the time series (Fig. 6), the main scarp is clearly visible, as well as the margins of the landslide. Other features include the transverse zones of lower slope angles within the mass movement area. What is only visible after a thorough evaluation is the fact that the main toe in the center of the landslide evolved during 2007 (as indicated by red arrows on the slope map in Fig 6). Prior to that date, an area more to the west seems to have been active. At the same time, starting in 2007, slope angles along the main scarp increase constantly up to 2009 indicating denudation and erosion on the main scarp.

From a geomorphological point of view, classic surface derivatives such as slope and aspect provide a necessary and generally good overview on the state of the studied area. However, fitted planes derived by the segmentation algorithms can deliver a higher level of detail, especially at the boundaries between planes (Fig. 6). The segmentation algorithm is able to show distance offsets of 50 cm and bigger. Due to the additional consideration of the plane parameter, even small differences between neighboring planar structures may be determined if the planes are tilted.

Analysis of the processed ALS and TLS data, along with geologic field measurements and geomorphological field observations indicate the major role of the incision of the Weißbach River in creating unstable slopes. Due to its highly variable discharge (mean annual  $Q = 38 \text{ m}^3/\text{s}$ , minimum annual  $Q = 11 \text{ m}^3/\text{s}$ , maximum annual  $Q = 440 \text{ m}^3/\text{s}$ , measured at the station at Bozenau, directly at the confluence of the Weißbach with the Bregenzerach river; values derived from the homepage of the State of Vorarlberg, [19]), the evacuation of sediment from the Weißbach valley occurs intermittently. Structural geologic measurements indicate the existence of deep-seated faults formed within a regional stress field. These faults are not active, but surface processes are mainly influenced by their orientation. The most recent geomorphic process identified is gravitational mass movement on the slopes and at places, where the host rock has been dissected

by older faults. The area surrounding the landslide and the landslide itself are continuously evolving with occasional peak events of mass movement (e.g. 1980s and 2005).

## 5. Conclusions

It could be demonstrated that a topographic surface can be properly represented by a set of automatically determined planar structures for subsequent interpretation with respect to geomorphic characteristics. The amount of data was reduced up to a factor of 3,000. Additional geological in-situ measurements verified some of our findings in the sense that similar primary directions could be found that were derived from the LiDAR data. Since planar segments robustly represent the surface at a given scale, the results are typically suitable for further analysis that implies trend characteristics. The appropriate selection of input parameters is a key issue in this processing: it determines the size and character of the resulting surface facets, and how far they estimate the real surface. Higher tolerance values (i.e. a threshold on the standard deviation of the residuals) may lead to more generalized surfaces, however the experimenter should ascertain that the resulting trend surface is still geomorphologically sound, and shows the major characteristics of the original surface. If this property can be ascertained, the geomorphic-geological analysis of the trend surface becomes feasible and the resulting parameters of the planar facets can be compared to other spatial data like drainage pattern, geological layering, schistosity, structural geological features.

## Acknowledgements

The Doren project has been supported by the Austrian Academy of Sciences (ÖAW) within the framework of scheme "Geophysics of the Earth's crust". Riegl GmbH ([www.riegl.com](http://www.riegl.com)) generously provided a full-waveform terrestrial laser scanning device; Thomas Gaisecker, Gábor Molnár, and Hubert Lehner are thanked for their help in data acquisition in 2008. Airborne Laser Scanning and EO data acquired prior to 2008 are provided by the Surveying Office (Landesvermessungsamt) of the Federal State of Vorarlberg, Austria; Peter Drexel is acknowledged for his close cooperation. The development of the segmentation algorithm was supported by Vermessung Schmid ZT GmbH and funded by the Christian Doppler Research Association (CDG). András Zámolyi received substantial support from Project 536001 Karpatian Tectonics, funded by the Österreichische Mineralölverwaltungsgesellschaft (OMV). Andreas Roncat has been supported by a Karl Neumaier Ph.D. scholarship.

## References

- [1] Lan, H., Martin, C.D., Chenghu, Z., Chang Ho, L.: "Rockfall hazard analysis using LiDAR and spatial modeling"; *Geomorphology*, 118 (2010), pp. 213 – 223.
- [2] Baldo, M., Bicocchi, C., Chiocchini, U., Giordan, D., Lollino, G.: "LiDAR monitoring of mass wasting processes: The Radicofani landslide, Province of Siena, Central Italy"; *Geomorphology*, 105 (2009), pp. 193 – 201.
- [3] Kasai, M., Ikeda, M., Asahina, T., Fujisawa, K.: "LiDAR-derived DEM evaluation of deep-seated landslides in a steep and rocky region of Japan"; *Geomorphology*, 113 (2009), pp. 57 – 69.
- [4] Dorninger, P., Nothegger, C., Pfeifer, N., Molnár, G.: "On-the-job detection and correction of systematic cyclic distance measurement errors of terrestrial laser scanners"; *Journal of Applied Geodesy*, 2 (2008), 4; 191 - 204.
- [5] Wagner, W., Ullrich, A., Ducic, V., Melzer, T., Studnicka, N.: "Gaussian Decomposition and Calibration of a Novel Small-Footprint Full-Waveform Digitising Airborne Laser Scanner"; *ISPRS Journal of Photogrammetry and Remote Sensing*, 60 (2006), 2; 100 - 112.
- [6] Höfle, B., Mücke, W., Dutter, M., Rutzinger, M., Dorninger, P.: "Detection of building regions using airborne LiDAR - A new combination of raster and point cloud based GIS methods"; in: "Geospatial Crossroads @ GI\_Form '09 - Proceedings of the Geoinformatics Forum Salzburg", (2009), 66 - 75.
- [7] Dorninger, P., Pfeifer, N.: "A Comprehensive Automated 3D Approach for Building Extraction, Reconstruction, and Regularization from Airborne Laser Scanning Point Clouds"; *Sensors*, 8 (2008), 11; 7323 - 7343.
- [8] McKean, J., Roering, J.: "Objective landslide detection and surface morphology mapping using high-resolution airborne laser altimetry"; *Geomorphology*, 57 (2004), pp. 331 – 351.
- [9] Kraus, K., Pfeifer, N.: "Determination of terrain models in wooded areas with airborne laser scanner data"; *ISPRS Journal*, 53 (1998), pp. 193 – 203.
- [10] Székely, B., Zámolyi, A., Draganits, E., Briese, C.: "Geomorphic expression of neotectonic activity in a low relief area in an Airborne Laser Scanning DTM: A case study of the Little Hungarian Plain (Pannonian Basin)"; *Tectonophysics*, 474 (2009), 1-2, pp. 353 – 366.
- [11] Pocsai A., Zámolyi A., Székely B., Molnár G., Roncat A., Drexel P.: Change detection on the Doren landslide, using geological field measurements and laser-scanned data (Vorarlberg, Austria); *Geophysical Research Abstracts* 13 (2011), EGU2011-938.
- [12] Nothegger, C., Dorninger, P.: "3D Filtering of High-Resolution Terrestrial Laser Scanner Point Clouds for Cultural Heritage Documentation"; *Photogrammetrie, Fernerkundung, Geoinformation*, 1 (2009), 53 - 63.
- [13] Highland, L.M., Bobrowsky, P.: "The Landslide Handbook – A Guide to Understanding Landslides"; U.S. Geological Survey Circular 1325 (2008), Reston, Virginia, pp.129.
- [14] Jutzi, B., Stilla, U.: "Range determination with waveform recording laser systems using a Wiener filter."; *ISPRS Journal of Photogrammetry and Remote Sensing*, 61 (2006), No. 1, pp. 95–107.

- [15] Roncat, A., Wagner, W., Melzer, T., Ulrich, A.: "Echo detection and localization in full-waveform airborne laser scanner data using the averaged square difference function estimator"; *The Photogrammetric Journal of Finland*, 21 (2008), No. 1, pp. 62–75.
- [16] Dikau, R., Brunsdon, D., Schrott, L., Ibsen, M.L.: "Landslide recognition –identification, Movement and Causes"; *International Association of Geomorphologists*, Publication No. 5, Wiley & Sons (1996), Chichester, pp. 247.
- [17] Persaud M., Pfiffner O.A.: "Active deformation in the eastern Swiss Alps: post-glacial faults, seismicity and surface uplift"; *Tectonophysics*, 385 (2004), 59-84.
- [18] Kastrup, U., Zoback, M.L., Deichmann, N., Evans, K.F., Giardini, D., Michael, A.J.: "Stress field variations in the Swiss Alps and the northern Alpine foreland derived from inversion of fault plane solutions"; *Journal of Geophysical Research*, 109 (2004), B01402.
- [19] *Homepage of the State of Vorarlberg, discharge values per year*, URL: [http://www.vorarlberg.at/abfluss/Bozenau\\_dia1\\_Q.gif](http://www.vorarlberg.at/abfluss/Bozenau_dia1_Q.gif), last accessed: 27.04.2011

## Contacts

**Peter Dorninger**, Vienna University of Technology, Institute of Photogrammetry and Remote Sensing, Gußhausstraße 27-29, 1040 Vienna, Austria.  
E-mail: pdo@ipf.tuwien.ac.at

**Habil. Dr.rer.nat. Balázs Székely**, Vienna University of Technology, Institute of Photogrammetry and Remote Sensing, Gußhausstraße 27-29, A-1040 Vienna, Austria. Eötvös University, Department of Geophysics and Space Science, Pázmány Péter sétány 1/C, H-1117 Budapest, Hungary.  
E-mail: bs@ipf.tuwien.ac.at

**Mag. Andras Zamolyi**, Universität Wien, Department for Geodynamics and Sedimentology, Althanstrasse 14, A-1090 Vienna, Austria. Eötvös University, Department of Geophysics and Space Science, Pázmány Péter sétány 1/C, H-1117 Budapest, Hungary.  
E-mail: andras@zamolyi.info

**Andreas Roncat**, Vienna University of Technology, Institute of Photogrammetry and Remote Sensing, Gußhausstraße 27-29, 1040 Vienna, Austria.  
E-mail: ar@ipf.tuwien.ac.at

# The Race Against Time In Alpine Regions By Satellite-Based Technologies



*Claudia Fösleitner, Driton Kuçi, Bernhard Hofmann-Wellenhof, Hans-Peter Ranner, Rainer Prüller and Klaus Aichhorn*

## Abstract

More than 300 persons per year die in the Austrian Alps. The increasing skiing, hiking, and climbing tourism implies a variety of high risks. In case of accidents, the race against time is crucial and needs to be supported as much as possible.

Integrating positioning, navigation, geoinformation, and communication techniques, an innovative system has been developed and is ready for use to improve the assistance and coordination of rescue forces in case of Alpine accidents such as avalanches and hiking or climbing accidents.

**Keywords:** Search and rescue, GNSS, Geographic information systems, Communication

## Kurzfassung

In den Österreichischen Alpen verunglücken jährlich mehr als 300 Menschen tödlich. Der steigende Wander-, Kletter- und Schitourentourismus birgt viele unterschiedliche Gefahren. Bei Alpinunfällen ist der Wettlauf gegen die Zeit kritisch und muss daher so weit wie möglich unterstützt werden.

Durch die Integration der Technologien Positionierung, Navigation, Geoinformation und Kommunikation wurde ein innovatives Gesamtsystem entwickelt, das die Unterstützung und Koordination der Rettungskräfte bei Unfällen im alpinen Raum – wie zum Beispiel Lawinenabgängen, Wander- oder Kletterunfällen – erheblich verbessert.

**Schlüsselwörter:** Such- und Rettungseinsatz, GNSS, Geografische Informationssysteme, Kommunikation

## 1. Introduction

Based on a project named SARONTAR (Search And Rescue Optimization by satellite Navigation Technologies in Alpine Regions), first a functional demonstrator has been developed comprising the system components mobile terminal, mission control center, and communication link [1] as shown in Fig. 1. Then the focus was put on achieving the technology readiness level of a mission-proved prototype. The system consists of three segments: a portable mission control center, a regional data center and several mobile terminals. The mission control center assists the leadership to obtain a visual overview of the current situation. This helps to analyze the situation rapidly and to forward precise instructions to the search and rescue teams. At the regional data center, the entire data set is stored, which enables a post-mission reconstruction and documentation of the operation. The search and rescue teams are supported by mobile terminals, which operate as combined communication and navigation tools. These provide current mission-related information and positioning data

by Global Navigation Satellite Systems (GNSS). Due to the rough climatic conditions in the Alps, rugged hardware components as well as sophisticated software design are necessary to fulfill the demanding user requirements, especially for the mobile system components. The mobile terminals and the portable mission control center are connected to the regional data center by a hybrid communication link. Considering possible terrestrial communication outages, satellite communication systems are also utilized.

The chosen open architecture allows for the extension of further rescue organizations, e.g., air emergency and fire brigades, and provides the basis for a regional disaster management system in the near future.

## 2. Components of the System

### 2.1 Mobile Terminal

The search and rescue teams are supported by mobile terminals. Generally, positioning data is provided by Global Navigation Satellite Systems [2], at present GPS (Global Positioning System)



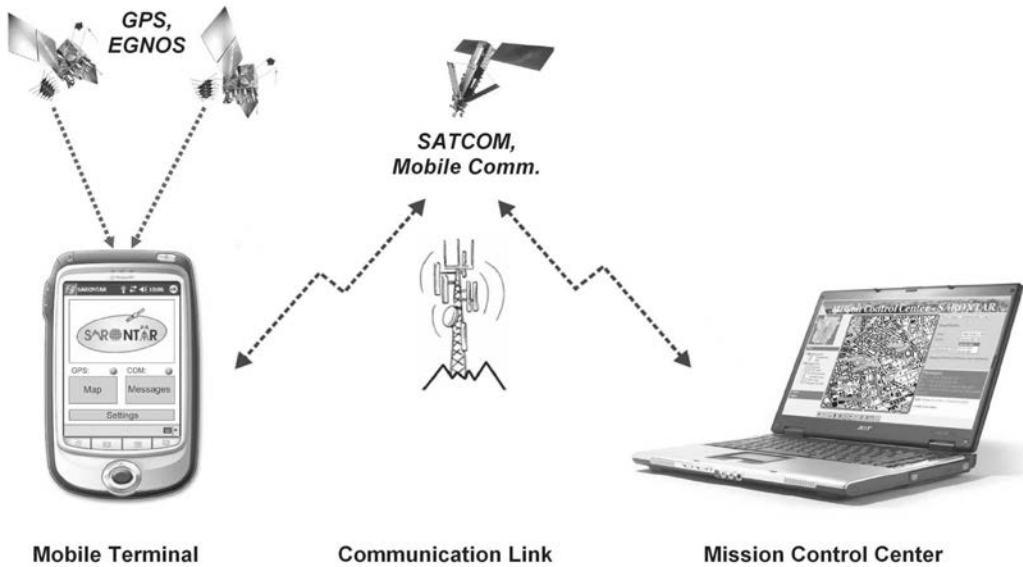


Fig. 1: System architecture of the functional demonstrator with the components mobile terminal, communication link, and mission control center

and EGNOS (European Geostationary Navigation Overlay Service). Positioning data including time stamps are transmitted automatically to the mission control center in constant intervals; however, due to the challenging Alpine topography and vegetation, signal obstructions are possible. This effect may cause short-time outages of positioning data. Due to the rough climatic conditions in the Alps, rugged hardware components and sophisticated user interface design are necessary to fulfill the demanding user requirements [3]. Ease of use and range of function as well as clear arrangement and information content, have been taken into account within software development.

The main window of the graphical user interface consists of two red/green signal indicators for navigation and communication, a message protocol list box and three buttons for displaying a map, sending messages and setting various system parameters, see Fig. 2. An extra large button design with sufficient displacement is required to enable easy handling even when using gloves in winter season. With the button “Map” a mobile GIS (Geographic Information System) is invoked. The current position and the track of the mobile team are mapped on an Austrian Map raster image. Additionally, mission-related information received from the control center can be displayed, including search areas and points of interests (POIs). In case of search and rescue

applications, POIs include, e.g., helicopter landing sites, meeting points, and locations of lost equipment or injured persons. The button “Mes-



Fig. 2: User interface for the mobile search and rescue teams

sages" calls a dialog window, where different predefined messages can be selected and sent to the control center, e.g., an SOS alarm message. Furthermore, the user is able to type additional keywords on a sophisticated touch screen keyboard. The message including keywords, time stamp and positioning data is transmitted to the mission control center via the communication link. When receiving a message from the mission control center, the user will be informed by an acoustic signal. A message box including text message and time stamp is invoked. In this case, the user is immediately prompted to return "ok", "later" or "negative". The protocol on the main window allows an overview of all sent and received messages. In summary, the search and rescue teams in Alpine regions are supported by the mobile terminals, providing positioning data, a continuous communication link and current mission-related geoinformation.

After several experiences in reality, some additional features were formulated by the rescue teams, e.g., replacing the Personal Digital Assistant (PDA) by a smartphone. Therefore, further investigations have been performed mainly in 2010/11. Now each mobile team is equipped with two mobile devices, a smartphone (on which the application is installed and runs), and a satellite handheld mobile. The smartphone supports touch-screen, Bluetooth technology, data transfer (e.g., GPRS or UMTS service), virtual serial ports, different display orientation (landscape and portrait). In addition, it is equipped with a GPS receiver and a camera. The smartphone runs in Windows Mobile OS. The satellite handheld mobile is used as a gateway for the smartphone to connect to the server if the connection cannot be established via the Mobile Network (MN). This happens in areas being not covered by the MN or due to possible disaster cases where the MN does not work at all. The application of mobile terminal attempts to connect with the server via MN and tries to avoid the connection via the satellite mobile because of the high costs and the battery life of both devices since the Bluetooth radio has to be used as well.

The star topology is used where the server is in the center and all other clients (mobile terminals and mission control center) around it. Each connection is totally independent from the others. In cases where a specific connection is dropped only that specific team loses the connection with the server, the others remain connected. Communication between the mobile terminals and the mission control center is based on messages

and is realized only through the server. These messages are used to register all teams as active, send the current position of the team, send and receive text messages, inform the teams about POIs (meeting place, injured people found, helicopter landing place, etc.) as well as any search sector (area that a team has to cover by its search). For terminating the application, a special message is sent in order to inform the mission control center that the application is voluntarily terminated. Some of these messages are sent automatically and periodically and the teams do not have to pay any attention to them. To detect errors occurred in the message, the XOR checksum (two-character hexadecimal number) added at the end of each message is used. There is no error correction algorithm implemented, thus, errors can only be detected but not corrected. The whole communication traffic between the teams during the intervention is stored in a database being located in the server computer. When the connection with the server is operable, either via the mobile network or via the satellite mobile, every message is sent immediately upon creation; however, if the connection is lost for any reason, the messages are saved in appropriate buffers in order to be sent when the connection is re-established.

The mobile terminal application has been tested with the most popular mobile network providers in Austria: A1, Drei, T-Mobile, Teling, Orange, Yesss and Bob. It works correctly with all of them. In different areas, where rescue operations can take place, different providers can be used, depending on their signal quality. Furthermore, it depends on the user which provider will be used.

GPS is used to determine the actual position of the teams, the track they followed, and the position of important objects in the terrain. The GPS data are based on the standard NMEA-0183.

The mobile terminal can also send photos taken of the terrain. Supported formats are: JPG, JPEG, JFIF, PNG. Just one photo can be sent at a time which is transmitted only when the connection is established via the mobile network and not via satellite. Some text of description can be added which is hidden inside the photo by using Steganography. The required time to send a photo depends on the size of the photo and the connection quality. A notification is displayed in the Mission Control Center immediately upon reception of the photo.

As perspective for the future, this application should be available for smartphones running in other OS such as Android and iOS, as well as using other satellite networks (Iridium) and other global navigation systems (Galileo, GLONASS, COMPASS).

## 2.2 Mission Control Center

The search and rescue operation can be coordinated in the mission control center by using the viewer shown in Fig. 3. The coordinator is informed about the positions of the search and rescue teams during the operation and is able to communicate with them using this WebGIS application. The implemented viewer can be run by a common internet browser (e.g., Microsoft Internet Explorer or Mozilla Firefox) without being connected to the World Wide Web. In the center of the viewer, a map which can be adapted by the user is shown. An overview map of the whole rescue area in the upper left corner shows the current map section. As background, a high resolution orthophoto or the official Austrian Map can be chosen. The primary information is mission-related and displayed in the foreground:

- Position of mission control center, current position and track of each search and rescue team,
- POIs created by the mission control center and by the mobile teams,
- search sectors created by the mission control center.

These elements can be combined and shown in the map. The search sectors and POIs are created by a digitizing tool on the left side of the viewer. Search sectors define dedicated search areas for each mobile team. This information is stored in the central database and can be transmitted to the teams on demand. Further tools for adjusting the map are in the toolbar below the map. They allow zooming and panning, returning to earlier map views and other operations. Moreover, the symbols shown on the map are explained in a legend.

The main technology for generating the maps is the open source mapserver of the University of Minnesota (UMN MapServer), see [4]. Geodata such as orthophotos and the Austrian Map as well as mission-related information from the central database are merged by the UMN MapServer to a raster image which can be implemented in a web application. For every new map view, the client sends a request via the webserver to the mapserver. The mapserver accepts this request, calculates a new map view according to the requested parameters and responds on demand with a map, an overview, a legend and a scalebar. The skeletal structure of the viewer is based on the open source software Mapbender running under General Public License (GPL). It offers graphical user interfaces for orchestrating, viewing, navigating and querying geographic information.



Fig. 3: Web-based viewer of the Mission Control Center

Communication with the search and rescue teams in the field can be handled with tools on the right side of the viewer. The operation manager is able to send messages, POIs and search sectors stored in the central database. The process of sending a message to a team in the field, starts for example with writing the message and storing it in the database. Then, the communication tool is able to use this information to transmit it via the communication link. The process of sending POIs or search sectors works in a similar way. The operation manager digitizes POIs or search sectors within the viewer, adds an optional description and stores the objects in the database. Within the communication tool, these digitized elements can be used for sending information to the mobile search and rescue teams. In the other direction – when a mobile team sends information to the mission control center – the reaction depends on the type of message. In principle, the operation manager is informed when a new message arrives. After confirmation, the message is added to the list of received messages shown in the mid-right part of the viewer. Below this list, an integrity message is displayed. It shows the availability of the communication and GPS connection of the

search and rescue teams in order to assess the actuality of the displayed positions. In general, all information exchanged between the mission control center and the mobile teams is stored in the central database realized by the freely available object-relational database management system PostgreSQL with the spatial extension PostGIS. This central database is the basis for the documentation and reconstruction of the entire search and rescue mission. Thus, debriefing is supported and a mission report can be created automatically after the search and rescue operation.

### 2.3 Communication Link

As briefly described in the previous section, the data transfer between the mobile terminals and the mission control center is performed by a hybrid communication link. Depending on availability, terrestrial mobile networks – data services like GPRS (General Packet Radio Service) and UMTS (Universal Mobile Telecommunications System) – and satellite communication systems are used (Fig. 4). In future, TETRA (Terrestrial Trunked Radio) might also be taken into account if available.

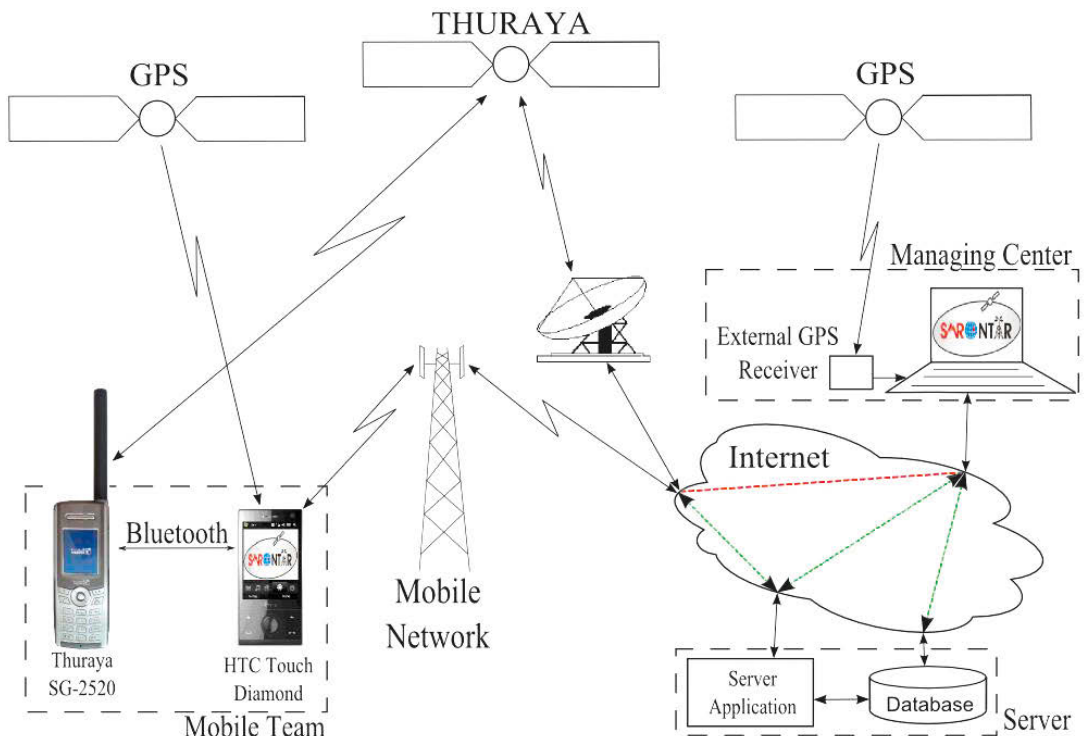


Fig. 4: Communication components in the context of the SARONTAR system

Within the development of the functional demonstrator, two mobile Thuraya satellite phones were used. The Arabian satellite communication system Thuraya comprises three components: ground segment, space segment, and user segment. The ground segment includes terrestrial gateway stations, which connect the Thuraya network to other telephone and data networks. The space segment consists of geostationary satellites with extra large antennas including hundreds of spot beams for a supply that is similar to mobile communication systems. The user segment comprises hybrid mobile satellite phones which can be used for satellite and mobile communication as well. The supply area of Thuraya ranges from Europe and North Africa to Central Asia. In the Alpine states, e.g., Austria, a minimal southern elevation angle of 30 – 35 degrees is necessary for using Thuraya services. The reasons to select the Thuraya system are the rather low operating costs – in comparison

to other satellite communication systems – and the interoperability with mobile communication standards.

**3. Practical Tests in Alpine Regions**

The usability of the system was tested under real conditions several times. As an examples, consider the training exercise of the Austrian mountain rescue service on 13th March 2010 (Figures 5 and 6). The assumption for this training was that a group of ski mountaineers lost its way in the “Dachstein” mountains – a massif in Styria, Austria – due to a sudden change in weather and a following snowstorm. Six search and rescue teams of the Austrian mountain rescue service took part in this training. Through accompanying the training exercise with modern navigation and communication technologies, the innovative aspects of a satellite based rescue operation system became apparent compared to the current rescue organization (Table 1).

Current situation	Improvement through SARONTAR
Search paths for the respective teams are created via desktop GIS and afterwards transmitted via cable to mobile GPS devices.	Search paths can be created via the SARONTAR mission control centre and transmitted wireless to the mobile terminals.
Current positions of the rescue teams are recorded by the mobile GPS devices but not transmitted to the mission control centre. After finishing the rescue operation, the tracks of the teams are collected via cable connection and visualized on the desktop GIS for debriefing.	The positions recorded by the mobile terminals are sent to the mission control centre periodically in real-time and automatically visualized on the web-based map.
Current coordinates of the rescue teams are requested in different intervals via mobile phone or radio and thereafter recorded via the desktop GIS as point. Additionally, the current position of each team is marked in an analogue map.	The positions of the mobile teams are visualized as track on the web-based map of the mission control centre. On receiving a current position, the track is updated automatically.
Mobile and radio services are not permanently available in the alpine regions throughout the rescue operation. In case of missing voice communication, there is absolutely no information about the rescue progress.	The availability of communication is significantly improved through the SARONTAR satellite communication backup.
Operation-relevant spatial information is exchanged via voice communication between mission control centre and mobile teams.	Operation-relevant spatial data is recorded via map and sent to the communication partner automatically. Received spatial information is visualised on the map in turn. Therefore, the complex exchange of coordinates via voice is eliminated.

Tab. 1: Demonstrating the innovations and improvements achieved by SARONTAR



Fig. 5: The system under real conditions [[www.bergrettung-groebming.at](http://www.bergrettung-groebming.at)]

In summary, the developed system may significantly speed up the search and rescue operation. Through up-to-date information, the current status of the rescue operation can be distributed to all members of the rescue mission. Thus, an appropriate management of the rescue operation is assured from the very beginning.

The participants of the training exercise identified the following innovative aspects of the described system:

- The mission control centre improves the coordination of the rescue operation considerably.
- The whole rescue operation can be coordinated via a single control centre.
- Coordination and documentation of the rescue operation can be handled through the same system.
- The protocol of the rescue operation is prepared automatically and is instantly available after the operation.
- The rescue operation can be continuously supervised through up-to-date information. Therefore, the mission control centre is able to react quickly to unpredicted events.
- The user interfaces is simple and intuitive.
- Many advantages come along with the replacement of voice communication through text communication: higher availability; text communication is more unambiguous due to no interruptions (further inquiries or discus-



Fig. 6: Mission control centre during training exercise [[www.bergrettung-groebming.at](http://www.bergrettung-groebming.at)]

sions unnecessary); information transfer via text is kept short and concise; the mission control centre is able to prioritize incoming information (voice communication requires immediate reaction); no more overlaps like simultaneously incoming radio messages and/or phone calls; text communication is more neutral than voice communication (less emotions)

**4. Outlook**

One possible improvement is the additional use of autonomous sensors, e.g., accelerometers, magnetometers, gyroscopes and barometers [5]. Generally, the combination of GNSS and augmentation sensors will improve the navigation parameters accuracy, availability, reliability and integrity [6]. However, the main drawback of sensor augmentation is the need for extra hardware components.

As an alternative method without needing additional hardware, a step-by-step improvement of single frequency GPS positioning is discussed [7]:

- Step 1ab: Broadcast ephemerides and broadcast ionosphere model
- Step 1c: Troposphere model

- Step 2: Precise ephemerides
- Step 3: Differential code biases
- Step 4: Global ionosphere maps
- Step 5: Code pseudorange smoothing

The positioning accuracies in steps 1ab and 1c are consistent with the declaration of GPS Standard Positioning Service (SPS) for C/A-code (Coarse/Acquisition) receivers [8]. In step 2, precise ephemerides processed and provided by the International GNSS Service (IGS) are used instead of the predicted broadcast ephemerides [9]. For consistency reasons, the precise ephemerides refer to the ionosphere-free linear combination of the carriers L1 and L2. In case of received C/A-code pseudoranges, in step 3 differential code bias values are taken into account for achieving data consistency and thereby, improved positioning accuracy [10]. In step 4, broadcast ionosphere models are displaced by more accurate global ionosphere maps [11]. Finally in step 5, the noise level can be reduced by combining C/A-code data with carrier phase measurements.

The results of a static 24 hour data set with 30 seconds interval in Fig. 7, show the significant improvement of horizontal positioning accuracy

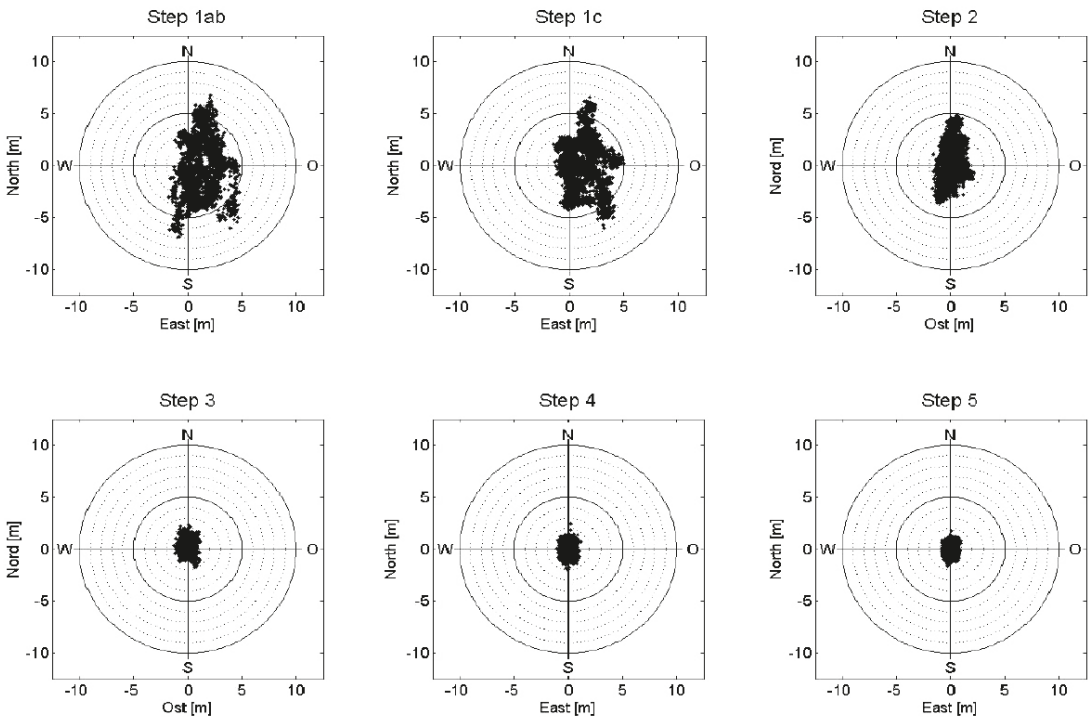


Fig. 7: Static 24 hour data set with 30 seconds interval

from 5-10 m (steps 1a and 1c) to meter and even sub-meter level (steps 4 and 5). Also the vertical position component can be improved through this step-by-step approach of single frequency GPS positioning. The method described belongs to Precise Point Positioning (PPP) which currently is a topic of international research.

Another general goal for the future is to adapt the developed system for other emergency services like police, fire department or the Red Cross. Thereby, the cooperation between different emergency services would be enormously facilitated in the case of disasters.

### Acknowledgements

(1) The development of the system has been funded by the Zukunftsfonds of the Federal State of Styria. Furthermore, the research activities have been supported by Senator h.c. Günter Bauknecht, a generous sponsor of the Universitätszentrum Rottenmann.

(2) Parts of this paper have been extracted and adapted from "Search and rescue optimization in alpine regions by satellite-based technologies". In: CD-Proceedings of the 1st GNSS Vulnerabilities and Solutions Conference, Baska, Croatia, September 7-9, 2008. Authors: H.P. Ranner, R. Prüller, K. Aichhorn, B. Hofmann-Wellenhof.

### References

- [1] Aichhorn K., Hofmann-Wellenhof B., Ranner H.-P., Ofenheimer A., Schardt M., Prüller R., Bartelme N., Koudelka O., Schrotter P. (2007): SARONTAR I Final Report. Graz University of Technology, Institute of Navigation and Satellite Geodesy, October 2007.
- [2] Hofmann-Wellenhof B., Lichtenegger H., Wasle E. (2008): GNSS Global Navigation Satellite Systems – GPS, GLONASS, Galileo & more. Springer, Wien New York.
- [3] Berglez P., Hofmann-Wellenhof B., Plank G., Schiffer S., Matl H., Ranner H.-P., Vallant J., Schardt M., Prüller R., Bartelme N., Rautz K., Schrotter P., Vössner S., Brandstätter H. (2006): SARONTAR I Midterm Report. Graz University of Technology, Institute of Navigation and Satellite Geodesy, September 2006.
- [4] Prüller R. (2006): Visualisierung von Geodaten mit dem UMN Mapserver. Master thesis, Graz University of Technology, Institute of Geoinformation.
- [5] Weimann F., Abwerzger G., Hofmann-Wellenhof B. (2007): Let's Go Downtown! Let's Go Indoors! Pedestrian Navigation in Obstructed Environments. GPS World, 18(11): 26-34.
- [6] Hofmann-Wellenhof B., Legat K., Wieser M. (2003): Navigation – principles of positioning and guidance. Springer, Wien New York.
- [7] Le A.Q. (2004): Achieving Decimetre Accuracy with Single Frequency Standalone GPS Positioning. In: Proceedings of ION GNSS 17th International Technical Meeting of the Satellite Division, Long Beach, California, 21-24 Sept. 2004, 1881-1892.
- [8] Department Of Defense (2001): Global Positioning System standard positioning service performance standard. Available from the US Assistant for GPS, Positioning and Navigation, Defense Pentagon, Washington DC.
- [9] Kouba J. & Heroux P. (2001): Precise point positioning using IGS orbit products. GPS Solutions, 5(2): 12-28.
- [10] Schaer S. & Steigenberger P. (2006): Determination and Use of GPS Differential Code Bias Values. IGS Workshop Darmstadt, Germany, 08-11 May 2006. Available at <http://nng.esoc.esa.de/ws2006> (29.01.2008).
- [11] Schaer S. (1997): How to use CODE's global ionosphere maps. Astronomical Institute, University of Berne. Available at <http://www.aiub-download.unibe.ch/ionosphere/doc> (29.01.2008).

### Contacts

**Mag. Claudia Fösleitner**, TeleConsult Austria GmbH, Rettenbacherstraße 22, 8043 Graz, Austria.  
E-Mail: [cfoesleitner@teleconsult-austria.at](mailto:cfoesleitner@teleconsult-austria.at)

**Driton Kuçi**, TeleConsult Austria GmbH, Rettenbacherstraße 22, 8043 Graz, Austria.  
E-Mail: [dkuci@teleconsult-austria.at](mailto:dkuci@teleconsult-austria.at)

**Univ.-Prof. Dr. Dr.h.c.mult. Bernhard Hofmann-Wellenhof**, Technische Universität, Institut für Navigation, Steyrergasse 30, 8010 Graz, Austria.  
E-Mail: [hofmann-wellenhof@tugraz.at](mailto:hofmann-wellenhof@tugraz.at)

**Dipl.-Ing. Hans-Peter Ranner**, Goldbichl 12a, 8786 Rottenmann, Austria.  
E-Mail: [hp.ranner@gmx.at](mailto:hp.ranner@gmx.at)

**Dipl.-Ing. Mag. Rainer Prüller**, Technische Universität, Institut für Fernerkundung und Photogrammetrie, Steyrergasse 30, 8010 Graz, Austria.  
E-Mail: [rainer.prueller@tugraz.at](mailto:rainer.prueller@tugraz.at)

**Dipl.-Ing. Klaus Aichhorn**, Universitätszentrum Rottenmann, Technologiepark 2, 8786 Rottenmann, Austria.  
E-Mail: [aichhorn.klaus@uzr.at](mailto:aichhorn.klaus@uzr.at)



## Global combination gravity field model based on GOCE and GRACE data



*Helmut Goiginger, Daniel Rieser,  
Torsten Mayer-Gürr and Eduard Höck*

### Abstract

A high-accuracy and detailed global map of the Earth's gravity field is an essential product in many branches of Earth system sciences. A main research interest at the Institute of Theoretical Geodesy and Satellite Geodesy, TU Graz, is the generation of high-resolution global gravity field models by combining data from the satellite gravity missions GOCE, GRACE and CHAMP with complementary gravity field information represented by terrestrial and air-borne data, satellite altimetry, and satellite laser ranging (SLR). These different data types are complementary with respect to their measurement principle, accuracy, spatial distribution and resolution, and spectral (error) characteristics. By means of data combination, benefit can be taken from their individual strengths and favourable features, and in parallel specific deficiencies can be reduced. The combination is performed by means of the weighted addition of the normal equation system of each data type. Within a simulation scenario it could be demonstrated that the method of variance components estimation is well suited for weights estimation. The models are parameterized in terms of coefficients of a spherical harmonic expansion including a proper error description in terms of a variance-covariance matrix. Together with our partners within the international GOCO (Gravity Observation Combination) consortium, the first satellite-only gravity field model GOCO01S was released in July 2010. The model is a combination solution based on 2 months of GOCE data, and 7 years of GRACE data, resolved up to degree and order 224 of a harmonic series expansion. GOCO01S has been validated against external global gravity models and regional GPS-levelling observations. The comparison to existing models revealed improvements especially in mountainous regions and in areas where only a few or less accurate terrestrial observations are available. With the continuously increasing availability of GOCE and GRACE data further improvements in global gravity field recovery will be achieved.

**Keywords:** Combination gravity field models, GOCE, GRACE

### Kurzfassung

Die genaue Kenntnis über das Schwerefeld der Erde bildet die Basis für verschiedene Forschungsgebiete, wie Ozeanographie, Geophysik, Meeresspiegeländerung und Klimaveränderung. In der Geophysik können damit geodynamische Prozesse im Erdinneren besser modelliert und verstanden werden. Auf dem Gebiet der Ozeanographie dient das Erdschwerefeldmodell zusammen mit Beobachtungen von Satellitenaltimetrie-Missionen der Bestimmung von Meeresströmungen, welche wesentlich für den Energietransport auf der Erde verantwortlich sind. Gleichzeitig können auch Meeresspiegeländerungen erfasst werden, die u.a. aufgrund von Abschmelzvorgängen in den Polregionen hervorgerufen werden. Auch die Geodäsie profitiert von einem hochauflösenden Schwerefeldmodell, z.B. in der globalen Vereinheitlichung von Höhensystemen.

Terrestrische Schwerefeldmessungen wurden schon seit jeher durchgeführt. Vorteil dieser Beobachtungen ist die hohe erreichbare Messgenauigkeit. Nachteile sind jedoch, dass zum einen ein homogenes und globales Beobachtungsnetz kaum realisierbar ist und zum anderen, dass aufgrund des Einsatzes unterschiedlichster Messinstrumente die Beobachtungen entsprechend unterschiedliche Messgenauigkeiten aufweisen. Der Start der Satellitenmissionen CHAMP (2000), GRACE (2002) und GOCE (2009) im letzten Jahrzehnt revolutionierte die Modellierung des Erdschwerefeldes. Aufgrund der kontinuierlichen Beobachtung aus dem Weltraum kann eine globale Abdeckung mit homogener Messgenauigkeit erzielt werden. Die Missionen unterscheiden sich prinzipiell anhand des individuellen Orbitdesigns und des Messkonzepts. Somit erhält man komplementäre und voneinander komplett unabhängige Beobachtungstypen, welche sich hinsichtlich räumlicher Verteilung, Auflösung und spektraler Eigenschaften ergänzen. Ein weiterer Beobachtungstyp stellt das Konzept des Satellite Laser Ranging (SLR) dar. Hierbei kann die vom Gravitationsfeld der Erde beeinflusste Trajektorie von Satelliten mittels Entfernungsmessung von der Erde aus im cm-Bereich ermittelt werden. Eine genaue Kenntnis über die Bahn ermöglicht in einem weiteren Schritt die Bestimmung des auf den Satelliten wirkenden Erdschwerefeldes.

Mittels Datenkombination können nun die individuellen Stärken und Vorteile der einzelnen Datentypen genutzt und gleichzeitig etwaige Defizite reduziert werden. Daraus sollen letztlich hochgenaue, hochauflösende globale Modelle des Gravitationsfeldes der Erde, parametrisiert durch sphärisch harmonische Koeffizienten einer Kugelfunktionsreihe und eine zugehörige Beschreibung der Genauigkeit mittels Varianz-Kovarianz-Matrix resultieren. Mathematisch erfolgt

diese Kombination auf Basis einer gewichteten Summation der Normalgleichungssysteme eines jeden Datentyps. Zur Berechnung der individuellen Gewichte bietet sich z.B. die Methode der Varianzkomponentenschätzung an, welche aus den gerechneten Residuen und der Redundanz einer jeden Beobachtungsgruppe in einem iterativen Vorgang einen Gewichtungsfaktor ableitet.

Im Juli 2010 wurde zusammen mit unseren Partnern innerhalb des GOCO (Gravity Observation Combination) Konsortiums das erste Kombinationsmodell aus Satellitenbeobachtungen veröffentlicht und trägt den Namen GOCO01S. Dieses Modell beruht auf sieben Jahren GRACE Daten und zwei Monaten GOCE Daten und hat eine Auflösung bis sphärisch-harmonischem Grad 224, was einer halben Wellenlänge von ca. 90 km entspricht. Die Kombination erfolgte auf Basis der Normalgleichungssysteme. Aufgrund einer angemessenen stochastischen Modellierung der GRACE und GOCE Beobachtungen gingen die beiden Komponenten mit einem Einheitsgewicht in die Kombination ein. Vergleiche zu bereits existierenden Modellen zeigen Verbesserungen speziell in gebirgigen Regionen und in Regionen in denen nur wenige und ungenaue terrestrische Messungen vorliegen. Durch die kontinuierlich zunehmende Beobachtungsdauer von GOCE und GRACE kann eine ständige Verbesserung der Schwerefeldmodelle erwartet werden. Derzeit arbeiten wir bereits an Nachfolgemodellen, welche sechs Monate an GOCE Daten, SLR Beobachtungen und terrestrische Datensätze beinhalten werden.

**Schlüsselwörter:** Schwerefeldmodelle, Kombinationsmodell, GOCE, GRACE

## 1. Introduction

The knowledge about the Earth's gravity field essentially supports research activities in oceanography, geophysics, geodesy and sea-level research, and further contributes to studies about climate change. In geophysics it is an important product to improve the modeling of the Earth's interior and of geodynamic processes. In oceanography gravity information is merged with satellite radar altimetry to derive models about ocean circulations, which are important for a better understanding of the global energy transport and climate regulation. It also contributes to observe sea-level change as a result of melting ice sheets. Finally, various fields of geodesy benefit from a unified definition of physical height systems. For these reasons the science and application communities are interested in a high-accuracy and detailed global map of the gravity field.

In the last century models of the Earth's gravity field were mainly derived based on satellite orbit perturbations and in-situ terrestrial observations. Major drawbacks of this type of observation are the inhomogenous data distribution and the varying measurement accuracy. In the last decade satellite gravity missions have been launched (CHAMP [13], GRACE [15], GOCE [14]) and are dedicated to provide a uniform picture of the gravity field. Depending on the individual mission design the derived models are limited to a certain spatial resolution and accuracy. Therefore, the objective of global gravity field modeling is the combination of all observation types to overcome the individual deficiencies and exploit the individual advantages.

Large efforts are made by different teams to compute combination models like the well-known EGM2008 ([12]) or EIGEN-5C ([3]) mod-

els. In 2009 the GOCO (Gravity Observation Combination) consortium was established, comprised by the Institute of Theoretical Geodesy and Satellite Geodesy at TU Graz (Austria), the Institute of Astronomical and Physical Geodesy at Technical University of Munich (Germany), the Institute of Geodesy and Geoinformation at University of Bonn (Germany), the Astronomical Institute of the University of Bern (Switzerland), and the Space Research Institute of the Austrian Academy of Sciences in Graz (Austria). The objective of the GOCO consortium is to provide global gravity field models with high accuracy and spatial resolution together with a consistent and reliable error description in terms of a covariance matrix to the user community. In this context the satellite-only model GOCO01S ([11]) was released in July 2010 which is the first combination model incorporating data of the GOCE satellite.

The model is represented by a spherical harmonic series expansion of the gravitational potential  $V$  at spherical coordinates with radius  $r$ , co-latitude  $\vartheta$ , and longitude  $\lambda$  according to

$$V(r, \vartheta, \lambda) = \frac{GM}{R} \sum_{l=0}^{l_{\max}} \left( \frac{R}{r} \right)^{l+1} \sum_{m=0}^l \bar{P}_{lm}(\cos \vartheta) \cdot \left[ \bar{C}_{lm} \cos(m\lambda) + \bar{S}_{lm} \sin(m\lambda) \right] \quad (1)$$

where  $G$  is the gravitational constant,  $M$  the mass of the Earth,  $R$  the mean Earth radius,  $\bar{P}_{lm}$  the fully normalized Legendre polynomials of degree  $l$  and order  $m$ , and  $\{\bar{C}_{lm}, \bar{S}_{lm}\}$  the spherical harmonic coefficients which should be determined up to a maximum degree  $l_{\max}$ .

## 2. Data combination procedure

The combination concept is based on the fusion of the normal equation systems of each data set

which are assembled according to a standard Gauß-Markov model. The resulting combined normal equation system is then solved for the unknown spherical harmonic coefficients (indicated by  $\hat{x}$ ) in terms of

$$\hat{x} = N^{-1}\mathbf{n} \quad (2)$$

where the combined normal equation matrices  $N$  and the right-hand sides  $\mathbf{n}$  are composed of the individual components according to

$$N = \sum_i w_i N_i \quad (3)$$

$$\mathbf{n} = \sum_i w_i \mathbf{n}_i$$

where  $i$  denotes the individual data set. The determination of the optimum weights  $w_i$  of the individual components is one of the major issues when computing combination gravity field models. There are several methods to deal with this task. Two common strategies are the so-called variance components estimation (VCE, [6]) and the calibration procedure based on subset solutions described by Lerch et al. ([8]). The method of VCE is based on the calculated least squares residuals whereas the latter one is based on the differences between the parameters of the individual solution and the combined solution, and the differences of the variances, respectively. In the next section the two weighting schemes are assessed within a test environment.

### 3. Simulation scenario

The present test environment was implemented on a single computer to perform basic experiments with focus on the combination methodology. The used test data sets are based on GOCE orbit data and on surface data, respectively. Due to the memory limitation of a single processor only small dimensioned normal equation systems were assembled. Nevertheless, the scenario demonstrates and compares the weights computation based on VCE and on the method of Lerch, respectively.

#### 3.1 Assembling of normal equation systems

##### GOCE kinematic orbit data

The used satellite-to-satellite tracking (SST) measurements (illustrated in Fig. 1) provided by the GPS receiver are from an end-to-end simulated data set generated by ESA which is based on the reference gravity field model EGM96 ([7]). The resulting GOCE SST-only model is based on 59 days of precise orbit data and accelerometer measurements representing the non-gravitational forces acting on the low orbiting satellite.

To assemble and process the normal equation system the energy balance approach ([5]) was utilized. The system is parameterized up to degree and order 70 for this test scenario which corresponds to a normal equation matrix with a dimension of 5041. Note: In the processing of real GOCE data, the SST observations are used to recover the long wavelengths structure of the gravity signal whereas the GOCE satellite gravity gradients (SGG) are able to measure the short wavelengths. Finally, both observation groups are combined to compute a GOCE-only model.

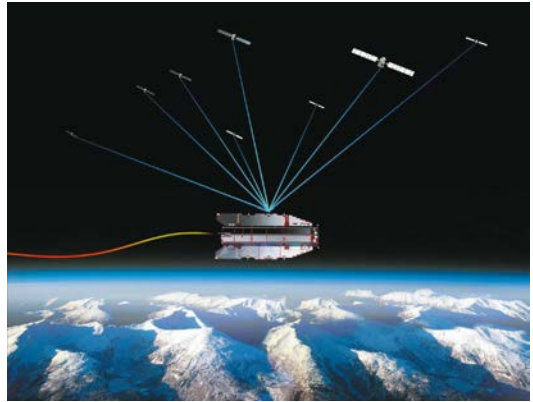


Fig. 1: Satellite-to-satellite tracking concept to determine the GPS position of GOCE and to obtain low-resolution gravity-field data (© ESA – AOES Medialab).

##### Terrestrial gravity data

To simulate terrestrial measurements covering the whole globe, gravity anomalies are computed based on spherical harmonic coefficients. A special issue of combining different data types is the definition of common reference parameters and numerical standards. For the processing of the gravity anomalies, the global gravity model EGM96 was used. Since the simulated GOCE data described above is also based on this model the issue on homogenization of standards and reference parameters can be circumvented. The processing steps of calculating synthetic gravity anomaly observations are briefly explained in the following. Based on the spherical harmonic coefficients of the EGM96 model, gravity anomalies on a  $2^\circ \times 2^\circ$  global grid were derived by series expansion of the gravitational potential complete to degree and order 70 according to Equation 1. In the next step random noise of 0.5 mGal was superposed to the derived grid values which then served as simulated gravity anomaly measurements. Finally, the inverse process was performed to recover the

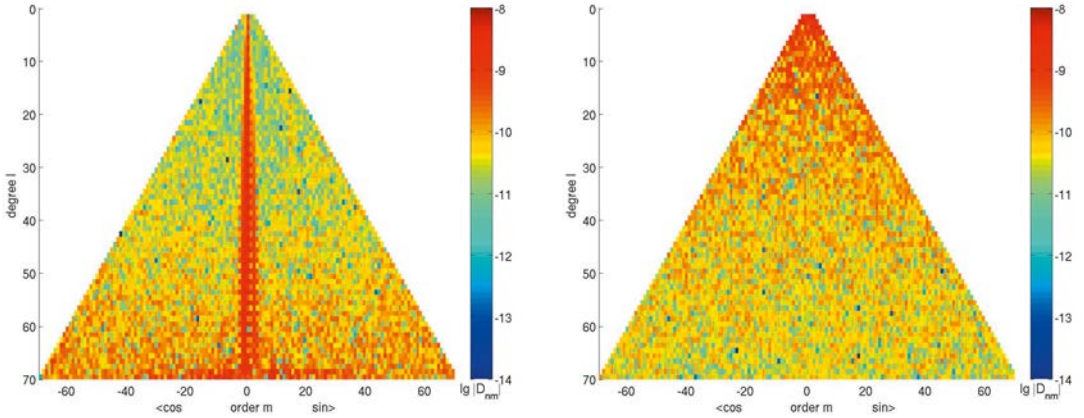


Fig. 2: Coefficient differences of models derived from simulated GOCE SST data (left) and from synthetic terrestrial data (right) w.r.t. EGM96. The colorbar refers to a logarithmic scale.

spherical harmonic coefficients from the noisy observations. In this step the normal equation system was assembled at the same time for the subsequent combination procedure.

### 3.2 Results of the simulation scenario

The benefit of such a combination is clearly demonstrated by the so-called spectral triangle plots. Fig. 2 (left) illustrates the coefficient differences based on the model computed only from GOCE SST observations with respect to the reference model EGM96. The large differences of the zonal and near-zonal degrees originate from the polar caps which cannot be observed by GOCE because of the particular orbit inclination. However, this is not true for the model based on the

terrestrial data (Fig. 2 (right)) since grid values are computed covering the whole globe.

Although the characteristics of the test data sets play only a minor role for this simulation study it can be seen that the coefficients based on terrestrial observations perform worse in the low degrees and become better with increasing degree. For GOCE SST exactly the opposite behaviour can be observed. Now, the task of data combination is to join the strengths of each data type. Fig. 3 (left) displays the coefficient differences of the combination solution based on weights computed by VCE (cf. Table 1).

Obviously, the polar cap problem of GOCE is covered by the terrestrial observations on the one hand, and on the other hand the coefficient differences are very homogeneous over

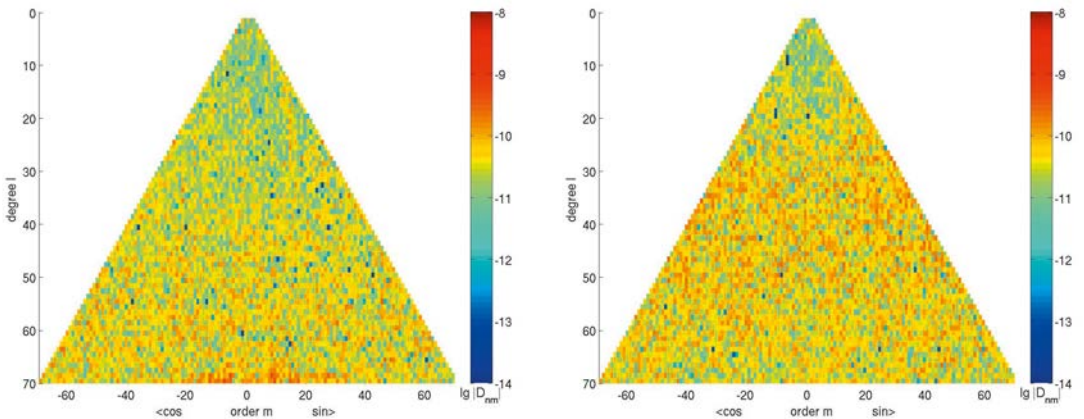


Fig. 3: Coefficient differences of combination models based on weights computed by variance component estimation (left) and on the method of Lerch (right) w.r.t. EGM96. The colorbar refers to a logarithmic scale.

the whole spectral range due to the favourable observations of GOCE SST in the low degrees and the high-quality terrestrial measurements in the higher degrees. The transition of the influence from one data type to the other is rather smooth which should also be a criterion for the quality of the combination. A different picture is shown by the combination solution based on weights computed by the Lerch method (Fig. 3 (right)). The weak estimation of the (near-)zonal coefficients by GOCE also causes strong correlations between these coefficients. Since the approach of Lerch only considers the variances but not the correlations the determined weight of GOCE SST (cf. Table 1) is distorted, whereas VCE computes reliable weights due to the consideration of these correlations.

	VCE	Lerch
GOCE SST	1.00	0.02
Terr. data	0.83	0.74

**Tab. 1:** Estimated weights for synthetic GOCE SST and terrestrial data sets based on the variance components estimation (VCE) and the Lerch method.

The simulation scenario revealed that the approach of Lerch is not qualified when working with GOCE data. In contrast VCE computed an optimum solution and thus is further used in the combination of real data.

#### 4. Satellite-only gravity field model GOCO01S

GOCO01S is the first combination gravity field model where GOCE observations are incorporated. The model is comprised by seven years of GRACE data and two months of GOCE satellite gravity gradients (SGG) data.

##### 4.1 GRACE

GRACE (Gravity Recovery and Climate Experiment) is a twin-satellite gravity field mission (cf. Fig. 4) which was launched in March 2002 ([15]). It is a joint project between the University of Texas Center for Space Research, GFZ Potsdam, NASA and Deutsches Zentrum für Luft- und Raumfahrt with the aim to determine the low to medium wavelengths of the Earth's gravity signal and its variability. The basic observations are the range and range rates between the spacecrafts. These measurements are performed by the satellites' key instrument, the K-band Ranging System, which is capable of resolving the one-way distances between the satellites with a high precision of about 1  $\mu\text{m}$  based on microwave technology. The absolute orbit positions at cm-level

are derived from GPS-measurements using the onboard GPS receiver assembly mounted on each satellite. The non-conservative forces acting on the satellites are determined by accelerometers, while a Star Camera Assembly is used to derive the actual satellite attitude in space.

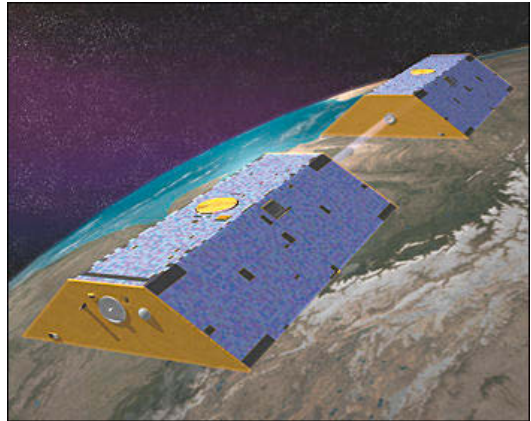


**Fig. 4:** GRACE tandem configuration with the ranging link between the two spacecrafts (© NASA).

The Institute of Geodesy and Geoinformation at the University of Bonn, our partner within the GOCO consortium, is computing static and time-variable gravity field models from GRACE. GRACE normal equations of the ITG-Grace2010s model ([10]) up to degree and order 180 have been used in the combination procedure which are based on the observation period from August 2002 to August 2009. The model is computed by the integral equation approach using short arcs with a maximum length of 60 minutes based on K-band range rates and kinematic orbits. Additionally, an adequate stochastic model for each short arc was introduced.

##### 4.2 GOCE

The Gravity field and steady-state Ocean Circulation Explorer (GOCE, [2]) is the first Earth Explorer Core mission as part of ESA's Living Planet Programme and is – after the satellite missions CHAMP and GRACE – the third dedicated gravity satellite. The satellite was launched in March 2009. After an in-orbit-calibration phase of 7 months GOCE started to record science data. Integral part of the mission concept and payload is the Electrostatic Gravity Gradiometer (Fig. 5) consisting of three pairs of orthogonally mounted accelerometers. The gradiometer is able to sense short-wavelength structures of the gravity field with unprecedented precision. The measurement principle is based on the analysis

of accelerations acting on a proof mass. Each pair is separated by about 50 cm on the gradiometer arm. For the very first time, the principle of satellite gravity gradiometry (SGG) comes into operation.

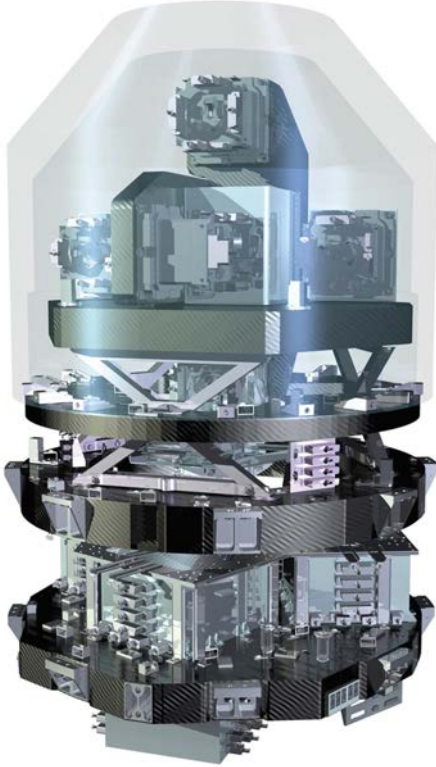


Fig. 5: Electrostatic Gravity Gradiometer carried by GOCE (© ESA – AOES Medialab).

The scientific data processing (Level 1b to Level 2) is performed by the “European GOCE Gravity Consortium” (EGG-C), a consortium of 10 European universities and research institutes, within the ESA-funded project “GOCE HPF”. In the frame of this project the Institute of Theoretical Geodesy and Satellite Geodesy together with partners from the Austrian Academy of Sciences, University of Bonn, and Technical University Munich, is responsible for the processing of an Earth’s gravity field model and the corresponding variance-covariance matrix from the precise GOCE orbit and SGG data.

The GOCE contribution to the GOCO01S model is based on two months of satellite gravity gradients (SGG) covering the time span of November 1, 2009, until December 31, 2009. The observed gravity gradients are the second order derivative of the gravitational potential

and are directly related to the spherical harmonic coefficients to be estimated. The gradiometer measurements are affected by colored noise and perform best within the measurement bandwidth of 5 to 100 mHz. Thus one key issue is the correct stochastic modeling of the spectral behaviour of the observations ([1]). This is realised by the application of digital auto-regressive moving average filters to the full observation equation, i.e., both to the columns of the design matrix and the observations. Finally the GOCE SGG normal equation system was assembled up to degree and order 224 on a PC cluster.

### 4.3 Constraints

The third component incorporated in GOCO01S is a Kaula regularization to improve the signal-to-noise ratio in degrees larger than 170. One main objective of the GOCO models is to be completely independent from existing gravity field models. Thus the solution is Kaula constrained towards zero and not towards any a-priori geopotential coefficients.

### 4.4 Combination solution

The calculation of the final combination solution was performed by the fusion of the individual normal equation systems according to Equations 2 and 3. The weights for the GRACE and GOCE components as well as for the Kaula constraints applied to the high degrees were calculated by means of variance component estimation. The resulting estimated weights for GRACE and GOCE were close to one. This is an indicator for the realistic and correct stochastic modeling of the errors for both, GRACE and GOCE data. The final normal equation system was rigorously solved up to degree and order 224 using the in-house implemented parallel software.

## 5. Results and validation of GOCO01S

Fig. 6 illustrates the comparison of the GOCO01S model with the well-known EGM2008 model which is also a combination model based on ITG-Grace03s ([9]), terrestrial and altimetry-derived gravity data. As already mentioned, the lack of GOCE observations over polar regions causes a poor determination of the (near-)zonal coefficients. Therefore, to enable a representative comparison the figure displays the robust median difference per spherical harmonic degree.

The black curve indicates the median of the absolute signal per degree whereas the colored curves represent the median of the coefficient

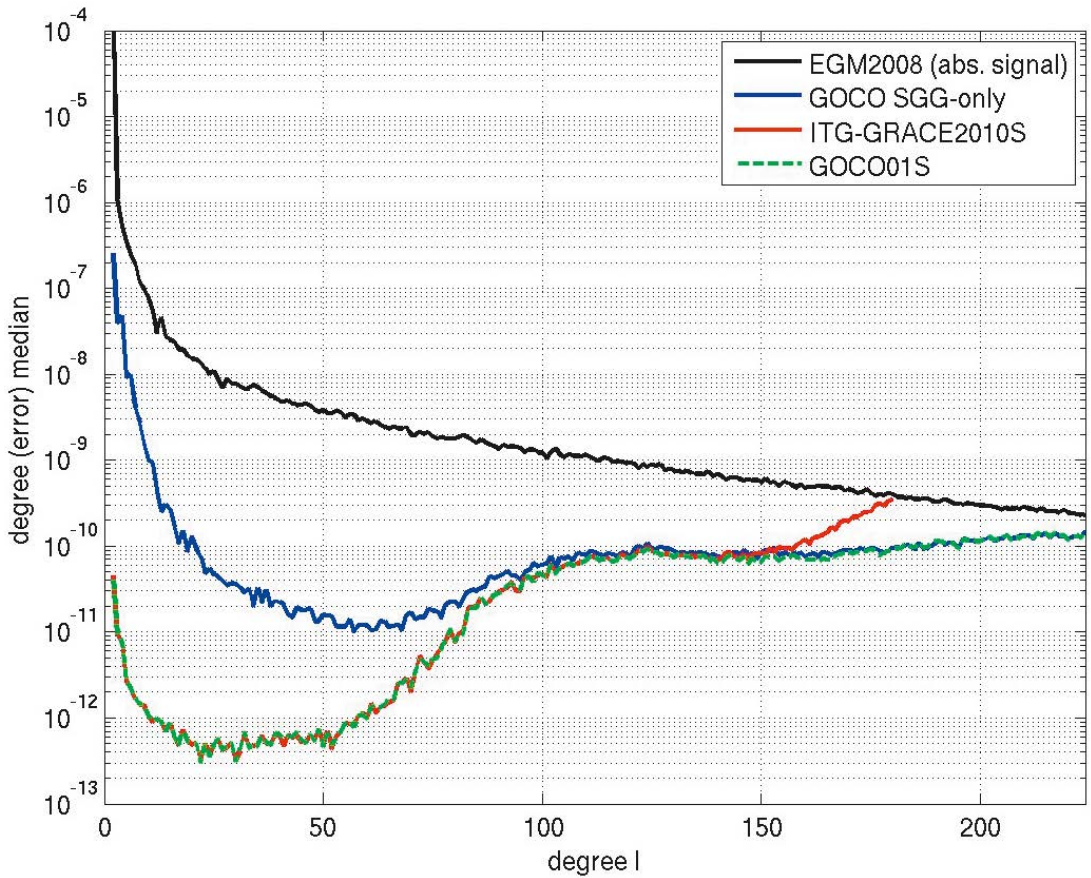


Fig. 6: Degree error medians of the GOCE SGG-only component (blue curve), the GRACE component (red), and the combination solution GOCO01S (green dashed) w.r.t. to the EGM2008 model. The black curve represents the median of the absolute coefficients signal per degree.

deviations per degree of the single solutions and the combination solution w.r.t. EGM2008. The GOCE solution (blue curve) is only based on gravity gradients. Thus the low degree coefficients are poorly estimated because of the limited measurement bandwidth of the gradiometer. As a consequence the combination solution (green dashed curve) clearly demonstrates that the low to medium degrees are mainly determined by GRACE (red curve). The contribution of GOCE SGG starts at about degree 100. Beyond degree 150, GOCE is the dominant contributor.

Fig. 7 displays the geoid height differences of GOCO01S (top) and ITG-Grace2010s (bottom) w.r.t. EGM2008 up to d/o 180. Both plots demonstrate that satellite data deliver additional information especially in mountainous regions (e.g. Himalayas, Andes) and in regions where only a few and less accurate terrestrial measurements are available (e.g. Africa, Antarctica). This benefit is most underlined by the GOCO01S

model. Furthermore, the along-track pattern differences, which are typical GRACE errors, disappear when using GOCE data.

For a completely independent validation a comparison of geoid heights derived from GOCO01S and other gravity models with geoid heights determined by GPS and levelling observations was performed (a description of the methodology can be found in [4]). Here, the models were truncated at different degrees  $N_{max}$ . The RMS of the geoid height differences are listed in Table 2. As can be noticed, there are regional offsets in the given values because of inconsistencies in the height system definitions. However, compared to the ESA GOCE-only model the GOCO01S model benefits from multi-year GRACE observations in the degrees up to 150. Beyond degree 150 the differences from GOCO01S model are smaller than from ITG-Grace2010s due to the dominant contribution from GOCE.

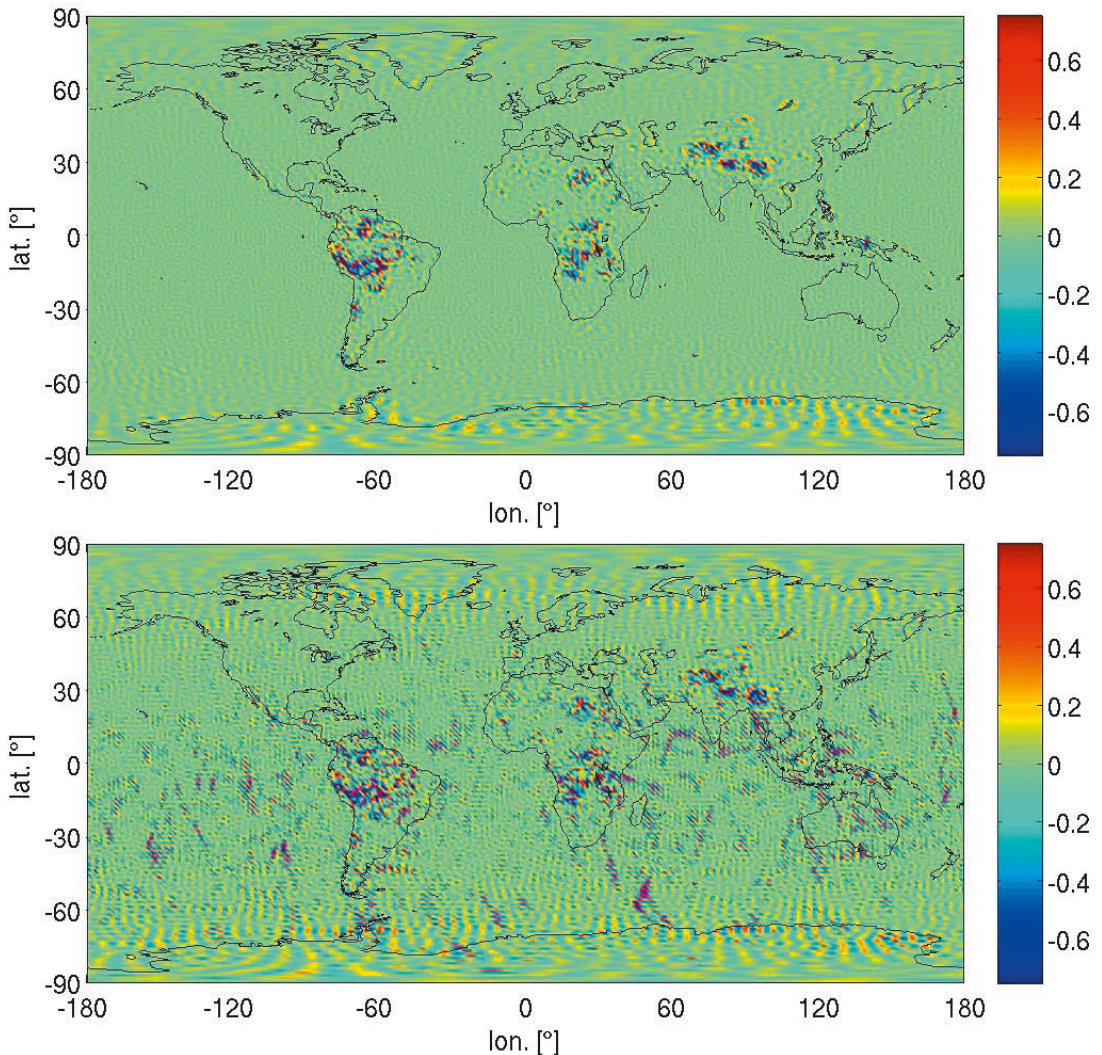


Fig. 7: Geoid height differences [m] of GOCO01S (top) and ITG-Grace2010s (bottom) w.r.t. EGM2008.

## 6. Conclusions and outlook

The combination procedure is based on the weighted fusion of normal equation systems. Two methods for weights estimation have been implemented and assessed within a test environment. The result based on the variance components estimation has delivered an optimum solution in the sense of a minimum achievable error throughout the whole spectrum. In contrast, the weights estimated by the approach of Lerch has been distorted due to the degraded determination of the zonal and near-zonal coefficients by GOCE. The principle difference between these two weighting procedures is the consideration of the covariances of the coefficients in the case of the variance components estimation method

whereas only the variances are used in the case of the Lerch method.

One objective of the GOCO consortium is to process complementary data sets without the use of any prior gravity information to finally provide a consistent combination model to the users. The GOCO01S is the first satellite-only combination model computed by the GOCO consortium. The benefit of a pure satellite-only model is that it is independent of altimetry data and thus it can be used e.g. to derive the dynamic ocean topography. Currently the next generation model GOCO02S is being processed which contains more than 6 months of GOCE data. GOCO02S will have a resolution of up to degree and order 250. Furthermore Satellite Laser Rang-



Model	Germany	Japan	Canada
	RMS [cm]	RMS [cm]	RMS [cm]
$N_{\max} = 100$			
GOCO01S	4.0	9.9	14.0
ITG-Grace2010s	4.1	10.2	14.6
ESA GOCE-only	4.2	10.8	14.6
EIGEN-5C	4.1	10.4	14.5
$N_{\max} = 150$			
GOCO01S	4.6	9.9	14.0
ITG-Grace2010s	4.8	10.5	14.7
ESA GOCE-only	5.3	11.2	14.7
EIGEN-5C	6.3	12.7	16.4
$N_{\max} = 170$			
GOCO01S	4.9	9.7	14.3
ITG-Grace2010s	7.5	13.9	17.7
ESA GOCE-only	5.7	10.7	15.4
EIGEN-5C	5.7	14.4	16.8
$N_{\max} = 200$			
GOCO01S	14.3	13.0	17.0
ITG-Grace2010s	26.5	34.9	30.3
ESA GOCE-only	15.1	13.9	18.2
EIGEN-5C	6.6	17.8	16.6

**Tab. 2:** RMS of geoid height differences [cm] between gravity field models and GPS-levelling observations for Germany (675 points), Japan (873 points), and Canada (430 points) truncated at degree and order  $N_{\max}$ .

ing (SLR) data will be used to recover the very low degree coefficients. With the approval of the extension of the GOCE mission until the end of 2012 further improvements of combination models can be expected. In the near future a combination model using also terrestrial and altimetry observations will be processed and published. The GOCO01S model (and the follow-on models) can be downloaded from <http://itsg.tugraz.at/goco> or from <http://icgem.gfz-potsdam.de/ICGEM/ICGEM.html>.

#### Acknowledgements

The project work performed by the Institute of Theoretical Geodesy and Satellite Geodesy at TU Graz and the Space Research Institute of the Austrian Academy of Sciences is funded by the Austrian Space Application Programme No. 6 of FFG, charged by BMVIT (project ID 819685). The authors are grateful to the European Space Agency for providing the GOCE data. The collaboration with Roland Pail, Thomas Fecher, and Thomas Gruber from the Institute of Astronomical and Physical Geodesy at Technical University Munich, Adrian Jäggi from the Astronomical Institute at University of Bern, Wolf-Dieter Schuh and Jan Martin Brockmann from the Institute of Geodesy and Geo-

information at University of Bonn, Andrea Maier, Sandro Krauss, Walter Hausleitner and Oliver Baur from the Space Research Institute of the Austrian Academy of Sciences within the GOCO Consortium is gratefully acknowledged.

#### References

- [1] Brockmann J.M., B. Kargoll, I. Krasbutter, W.-D. Schuh, M. Wermuth: GOCE Data Analysis: From Calibrated Measurements to the Global Earth Gravity Field. In: Flechtner, F. et al. (eds.) System Earth via Geodetic-Geophysical Space Techniques, pp 213-229, doi: 10.1007/978-3-642-10228-8\_17, 2010.
- [2] Drinkwater M., R. Floberghagen, R. Haagmans, D. Muzi, A. Popescu: GOCE: ESA's First Earth Explorer Core Mission. Space Sciences Series of ISSI, 18, p 419-432, 2003.
- [3] Foerste C., F. Flechtner, R. Schmidt, R. Stubenvoll, M. Rothacher, J. Kusche, K.-H. Neumayer, R. Biancale, J. M. Lemoine, F. Barthelmes, S. Bruinsma, R. Koenig, U. Meyer: EIGEN-GL05C - A new global combined high-resolution GRACE-based gravity field model of the GFZ-GRGS cooperation. General Assembly European Geosciences Union, Geophysical Research Abstracts, 10, Vienna, Austria, 2008.
- [4] Gruber T.: Evaluation of the EGM2008 gravity field by means of GPS-levelling and sea surface topogra-

- phy solutions; External quality evaluation reports of EGM08. Newton's Bulletin, International Association of Geodesy and International Gravity Field Service, 4th April 2009.
- [5] *Jekeli, C.*: The determination of gravitational potential differences from satellite-to-satellite tracking. *Celestial Mechanics and Dynamical Astronomy* 75, p 85-101, 1999.
- [6] *Koch K.R., J. Kusche*: Regularization of geopotential determination from satellite data by variance components. *Journal of Geodesy*, 76 (5), p 641-652, 2001.
- [7] *Lemoine F.G., S.C. Kenyon, J.K. Factor, R.G. Trimmer, N.K. Pavlis, D.S. Chinn, C.M. Cox, S.M. Klosko, S.B. Luthcke, M.H. Torrence, Y.M. Wang, R.G. Williamson, E.C. Pavlis, R.H. Rapp, T.R. Olson*: The Development of the Joint NASA GSFC and the National Imagery and Mapping Agency (NIMA) Geopotential Model EGM96. National Aeronautics and Space Administration, Goddard Space Flight Center, Greenbelt, Maryland, 1998.
- [8] *Lerch F.J.*: Optimum Data Weighting and Error Calibration for Estimation of Gravitational Parameters. NASA TM 100737, 1989.
- [9] *Mayer-Guerr T.*: Gravitationsfeldbestimmung aus der Analyse kurzer Bahnbögen am Beispiel der Satellitenmissionen CHAMP und GRACE, Dissertation, University of Bonn, 2006.
- [10] *Mayer-Guerr T., A. Eicker, E. Kurtenbach and K.-H. Ilk*: Global Static and Temporal Gravity Field Models from GRACE Data. *System Earth via Geodetic-Geophysical Space Techniques*, p 159-168, ISBN 978-3-642-10228-8, Springer Berlin Heidelberg, 2010.
- [11] *Pail R., H. Goiginger, W.-D. Schuh, E. Höck, J. M. Brockmann, T. Fecher, T. Gruber, T. Mayer-Guerr, J. Kusche, A. Jäggi, D. Rieser*: Combined satellite gravity field model GOCO01S derived from GOCE and GRACE, *Geophys. Res. Lett.*, 37, L20314, doi: 10.1029/2010GL044906, 2010.
- [12] *Pavlis N.K., S. A. Holmes, S. C. Kenyon, J. K. Factor*: An Earth Gravitational Model to Degree 2160: EGM2008. General Assembly European Geosciences Union, *Geophysical Research Abstracts*, 10, Vienna, Austria, 2008.
- [13] *Reigber C., H. Luehr, P. Schwintzer*: CHAMP mission status. *Advances in Space Research*, 30, p 129-134, 2002.
- [14] *Rummel R., T. Gruber, R. Koop*: High Level Processing Facility for GOCE: Products and Processing Strategy. Proceedings 2nd International GOCE User Workshop, Frascati 2004, European Space Agency, Noordwijk, The Netherlands, 2004.
- [15] *Tapley B.D., S. Bettadpur, M. Watkins and C. Reigber*: The Gravity Recovery and Climate Experiment: Mission Overview and Early Results. *Geophysical Research Letters*, 31(9), 2004.

### Contacts

**Dipl.-Ing. Helmut Goiginger**, Institut für Theoretische Geodäsie und Satellitengeodäsie, TU Graz, Steyrergasse 30, 8010 Graz, Austria.

E-mail: [h.goiginger@tugraz.at](mailto:h.goiginger@tugraz.at)

**Dipl.-Ing. Daniel Rieser**, Institut für Theoretische Geodäsie und Satellitengeodäsie, TU Graz, Steyrergasse 30, 8010 Graz, Austria.

E-mail: [daniel.rieser@tugraz.at](mailto:daniel.rieser@tugraz.at)

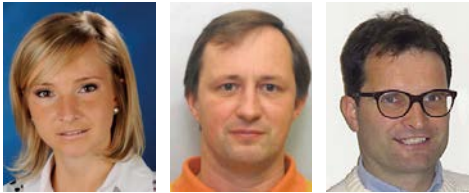
**Univ.-Prof. Dr.-Ing. Torsten Mayer-Gürr**, Institut für Theoretische Geodäsie und Satellitengeodäsie, TU Graz, Steyrergasse 30, 8010 Graz, Austria.

E-mail: [mayer-guerr@tugraz.at](mailto:mayer-guerr@tugraz.at)

**Dipl.-Ing. Eduard Höck**, Space Research Institute, Austrian Academy of Sciences, Schmiedlstrasse 6, 8042 Graz, Austria

E-mail: [hoeck@geomatrics.tu-graz.ac.at](mailto:hoeck@geomatrics.tu-graz.ac.at)

## Quality Assessment of Different GNSS/IMS-Integrations



*Petra Hafner, Manfred Wieser and Norbert Kühtreiber*

### Abstract

In the field of navigation, integrated navigation is an upcoming technique. This means that trajectory determination of a moving object is performed via sensor fusion. Complementary multi-sensor systems are used to compensate the disadvantages of the one sensor by the advantages of the other and vice versa. In case of the project VarloNav, different integration methods based on satellite-based positioning and inertial measurement systems (IMS) are investigated and compared under varying circumstances. The goal of the project is the comparison of three distinct categories of sensors in terms of accuracy and quality on the one hand and the comparison of three different coupling methods (uncoupled, loosely coupled and tightly coupled) on the other hand. For these investigations, a platform was developed to enable terrestrial field tests with a car. This measurement platform can be mounted on the roof rack of a car and carries four GNSS (Global Navigation Satellite System) antennas and three types of IMS. This construction allows an optimal comparison of the measurement data of the different onboard sensor systems and their integration. The comparison of the integration results demonstrates that the surrounding of the trajectory strongly influences the choice of the used sensors and the type of integration. The worse the measurement conditions the higher are the requirements concerning the sensor quality and their integration.

**Keywords:** Kalman Filter, Sensor Integration, GNSS, IMS

### Kurzfassung

Die integrierte Positionsbestimmung spielt heutzutage im Bereich der Navigation eine immer größere Rolle. Um die Trajektorie eines sich bewegenden Objektes zu bestimmen, werden verschiedenste Sensoren gekoppelt. Die Sensoren werden so gewählt, dass die Nachteile des einen Sensors durch die Vorzüge des anderen Sensors ausgeglichen werden. Im Fall von mobilen Plattformen ist es sehr gebräuchlich, satellitengestützte Positionierungsverfahren in Kombination mit inertialen Messsystemen (IMS) zu verwenden. Die Vorteile dieser Sensorfusion liegen darin, dass einerseits mit Hilfe von IMS Signalabschattungen von GNSS (Global Navigation Satellite System) überbrückt werden können und andererseits GNSS das für IMS typische Driftverhalten kompensiert.

Das Institut für Navigation der TU Graz untersuchte im Rahmen des Projektes VarloNav einerseits verschiedenste Sensorkombinationen und andererseits unterschiedliche Integrationsmethoden. Die Analysen basieren auf terrestrischen Testmessungen, bei denen unterschiedliche Bedingungen (teilweise bis komplette GNSS Signalabschattung) untersucht wurden. Um eine einheitliche Basis für die Analysen zu schaffen, wurde eine Messplattform für ein Auto entwickelt, auf der vier GNSS Antennen und drei IMS Sensoren montiert werden können. Mit Hilfe dieser Plattform ist es möglich, das Verhalten der Sensoren und die verschiedenen Sensorkombinationen während einer Messfahrt miteinander zu vergleichen.

Im Rahmen dieser Untersuchungen wurden zunächst detaillierte Analysen hinsichtlich der drei unterschiedlichen Kopplungsmethoden – ungekoppelte, lose gekoppelte und eng gekoppelte Integration – durchgeführt. Die eng gekoppelte Integration basiert im Unterschied zu den zwei anderen Kopplungsmethoden auf rohen Messdaten, welche mit Hilfe des Kalman-Filters miteinander kombiniert werden. Der Vorteil der eng gekoppelten Integration besteht darin, dass bei weniger als vier sichtbaren Satelliten die GNSS Messungen nicht verworfen werden müssen, sondern als Stützung der IMU-Messungen (Inertial Measurement Unit) einen Beitrag zur Trajektorienbestimmung liefern. Für die ungekoppelte als auch lose gekoppelte Integration ist eine Vorprozessierung der Messdaten erforderlich, da die Integration auf prozessierten Trajektorien basiert.

In einem weiteren Schritt wurden die Integrationsmethoden vor dem Hintergrund der Qualitäts- und Preisklassen der Sensoren untersucht. Für diese Analysen wurden drei verschiedene GNSS-Empfänger (Xsens MTiG, Novatel ProPak V3 und Javad Sigma) und drei verschiedene IMS Produkte (Xsens MTiG, iMAR FSAS und iMAR RQH) verwendet, die jeweils niedrig-, mittel- und hochpreisige Sensoren repräsentieren.

Das Hauptaugenmerk sämtlicher Analysen liegt hierbei auf den erreichbaren Genauigkeiten der Positions- und Attitudelösung. Als Ergebnis liegt eine Klassifizierung der untersuchten Integrationsmethoden als auch Sensorsysteme vor und die Qualitätsparameter wie Einsatzfähigkeit, Genauigkeit und Zuverlässigkeit werden anhand der Integrationsergebnisse hinterfragt.

Die Analysen zeigen, dass die Wahl der Sensoren sehr stark von den Messbedingungen entlang der Trajektorie abhängen. Wenn die Anzahl der verfügbaren Satelliten unter vier sinkt, kann man sehr große Unterschiede in den

Ergebnissen der unterschiedlichen Integrationen erkennen. Die eng gekoppelte Integration liefert hierbei die besten Ergebnisse. Kommt es zu einem vollständigen GNSS-Signalausfall basiert die Lösung nur mehr auf der Qualität des inertialen Sensors. Nach einem GNSS-Ausfall von 50 s weicht die Sigma/iNAV-RQH Lösung nur 20 cm von der Referenztrajektorie ab, hingegen treten bereits bei der ProPak/FSAS Kombination viel größere Differenzen auf (5,3 m).

**Schlüsselwörter:** Kalman Filter, Sensor Integration, GNSS, IMS

## 1. Introduction

In the field of navigation, integrated navigation is an upcoming technique. This means that the trajectory determination of a moving object is performed by a sensor fusion: for a discrete sequence of epochs, the object-specific state vector and its components (position, velocity and attitude) are derived by an integration of several sensors. In most cases, complementary multi-sensor systems are used. Therefore, sensors with different operation principles and characteristics complement each other in such a way that disadvantages of the one sensor are compensated by the advantages of the other and vice versa [7, 8]. In the case of mobile platforms, the integration of satellite-based positioning and inertial measurement systems is gaining importance today [3]. Global Navigation Satellite Systems (GNSS), such as GPS or the future Galileo, yield absolute positions, but in the sense of radio navigation, they are non-autonomous systems. In contrast, inertial navigation (use of gyroscopes and accelerometers) is self-contained, but provides relative positions [4]. Therefore, the importance of the sensor integration is obvious: an inertial measurement system (IMS) overcomes outages of GNSS, while GNSS compensates the IMS-typical drift behavior. In Table 1 the characteristics of GNSS are opposed to the characteristics of IMS.

Within the scope of the project VarloNav [5], a science-based and comprehensive investigation of different types of GNSS-IMS integration was performed by the Institute of Navigation, Graz University of Technology. The goal of the project was a classification of different integration methods based on different sensor combinations in the frame of the trajectory determination for a mobile exploration system (imaging sensors)

operated by DIGITAL (department Remote Sensing and Geoinformation), an institute of JOANNEUM RESEARCH, Graz. The investigation should be a basis for investment decisions – are additional costs for high quality sensors really necessary to achieve the desired accuracy?

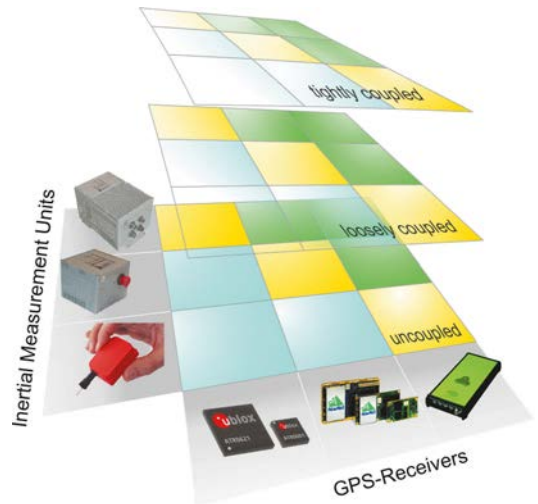


*Fig. 1: Different coupling methods to integrate GNSS-receivers and inertial measurement units of various categories*

Several integrations of all possible combinations of GNSS-receivers and inertial measurement units (IMU) of three different quality classes (low, medium and high) are compared with regard to accuracy and reliability of the results (position, attitude) as well as applicability for different tasks of navigation, see Fig. 1. Besides the quality of the involved sensors, the results of the integration (position, velocity, attitude, and their estimated accuracy) depend also on the applied coupling method. Due to the used filtering technique (Kalman filter), an uncoupled,

	GNSS	IMS
measurement principle	distances from time delays	accelerations and angular rates
system operation	reliance on space segment	autonomous
output variables	position, velocity, time	position, velocity, orientation angles
stability	long-term	short-term
typical data rate	1-100 Hz	≥ 50 Hz

*Tab. 1: Complementary characteristics of GNSS and IMS [2]*

loosely coupled, and tightly coupled integration of GNSS-receivers and IMUs are performed [2]. Depending on the chosen coupling method, either pre-processed data (in the uncoupled and loosely coupled cases) or raw data (for tight coupling) are introduced in the Kalman filter. The comparison of the performance of the different coupling methods and sensor combinations are based on the behavior of the estimated state vector (position, attitude) and its accuracy.

To guarantee the comparability of the results, a measurement platform, carrying four GNSS antennas and three IMUs, was designed. This platform can be mounted on the roof rack of a car and enables consistent measurement scenarios. The different integrations based on the collected observations have been processed, on the one hand, with the commercial software Inertial Explorer [7] (loosely and tightly coupled integration), also used by DIGITAL, and on the other hand, by a self-implemented software tool (uncoupled and loosely coupled integration).

In section 2 the theoretical background of the integration methods based on Kalman filtering is summarized, followed by a description of the terrestrial field tests performed within this study in section 3. Finally the results and comparisons are presented in section 4, while section 5 contains the conclusions.

## 2. Integration Methods

For the integration of the GNSS and IMS measurement data, a Kalman filter is used. Kalman filtering enables the determination of the state vector comprising the non-stationary position, velocity, and attitude of a moving object. The Kalman

filter represents a general form of a recursive least-squares adjustment where time updates of the state vector and its variance-covariance matrix are estimated every epoch [3, 4, 8]. These time updates are based on the prediction of the present into the future state which is realized by a dynamical model. By using a dynamical model, the knowledge of the movement of the object can be integrated as well as the behavior of sensor and model parameters (receiver clock error, drift of the gyros, offset of the accelerometers etc.). The fact that the Kalman filter and its dynamical model include a time-variant observation and system noise declares the Kalman filter as an optimum filter for integrated navigation [4].

The dynamic behavior can be derived by the relationship of two consecutive state vectors ( $x_k, x_{k-1}$ ) at discrete time epochs  $t_k$  and  $t_{k-1}$  by

$$x_k = \Phi_{k-1}x_{k-1} + w_{k-1}, \tag{1}$$

where matrix  $\Phi_{k-1}$  is the transition matrix modeling the dynamic characteristics. The matrix  $w_{k-1}$  corresponds to the system noise which specifies the uncertainties of the dynamical model. Additional to the dynamic model, a functional model is needed to describe the relationship between the observations  $z_k$  and the estimated state vector  $x_k$ . This is done by the design matrix  $H_k$ :

$$z_k = H_kx_k + v_k. \tag{2}$$

The accuracy of the measurements are summarized within the noise vector  $v_k$ . The interaction of these two models is realized by the Kalman filter which consists of three main steps, Fig. 2. Within the first step the Kalman gain matrix is computed. This matrix  $K_k$  determines

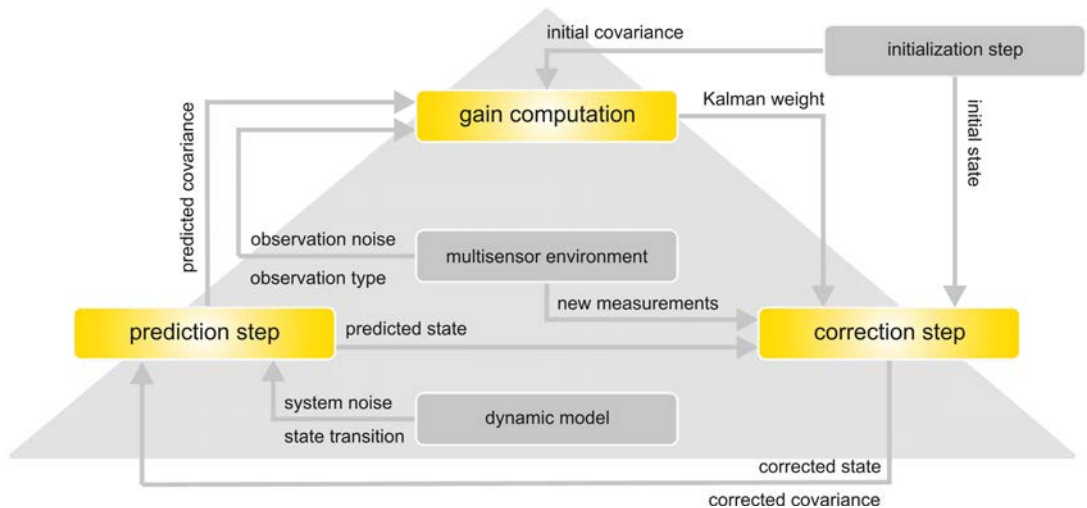


Fig. 2: Concept of the Kalman filter algorithm [4]

the influence of the new measurements  $z_k$  on the predicted state  $\tilde{x}_k$  and covariance  $\tilde{P}_k$  (step 2). In the last step the state and the covariance for the next epoch are predicted.

Step 1: Gain computation

$$K_k = \tilde{P}_k H_k^T (H_k \tilde{P}_k H_k^T + R_k)^{-1} \quad (3)$$

Step 2: Correction Step

$$\hat{x}_k = \tilde{x}_k + K_k (z_k - H_k \tilde{x}_k) \quad (4)$$

$$P_k = (I - K_k H_k) \tilde{P}_k$$

Step 3: Prediction Step

$$\tilde{x}_k = \Phi_k \hat{x}_k \quad (5)$$

$$\tilde{P}_{k+1} = \Phi_k P_k \Phi_k^T + Q_k$$

As shown in Fig. 2, for the practical realization of the three steps external information is needed (measurement data of the multisensor environment for every epoch, information about the dynamic behavior and an initialization of the state vector  $\tilde{x}_k$  and the covariance matrix  $\tilde{P}_k$ ).

Concerning the implementation of the Kalman filter, three different types of sensor coupling can be distinguished [6]: the uncoupled, the loosely coupled, and the tightly coupled integration. In the following, the differences of the different coupling methods are explained.

### 2.1 Uncoupled sensor integration

In the case of an uncoupled Kalman filter, the GNSS as well as the IMS trajectory have to be computed separately in a pre-processing step. As shown in Fig. 3, on the one hand, the input of the Kalman filter is the position, the velocity and the time based on GNSS measurements; and on the other hand, it is the position, the velocity, and the attitude resulting from IMS measurements. The result of the integration depends, besides

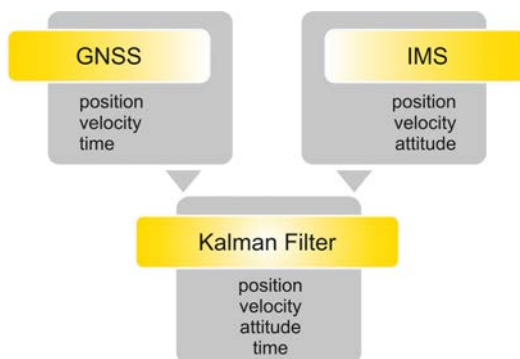


Fig. 3: Concept of uncoupled sensor integration

the types of measurements, on the accuracy of the computed GNSS and IMS trajectories determined in the pre-processing step and the performance of the dynamical model. The output of the filter are the integrated positions and velocities, while the attitude parameters and the time are not combined within the filter.

### 2.2 Loosely coupled sensor integration

In contrast to the uncoupled Kalman filter, the output of the loosely coupled integration is used to support the determination of the IMS trajectory, see Fig. 4. Similar to the uncoupled Kalman filter, the integration is not performed on the raw measurement level. The computation of the GNSS and the IMS trajectory is executed in an iterative way, which means that the output of the Kalman filter (position, velocity, attitude) of the previous epoch is introduced as additional information for the determination of the IMS trajectory. However, the GNSS position and velocity are computed independently. This method enables the correction of the drift of the IMS-based trajectory which is the limiting factor of inertial measurement systems.

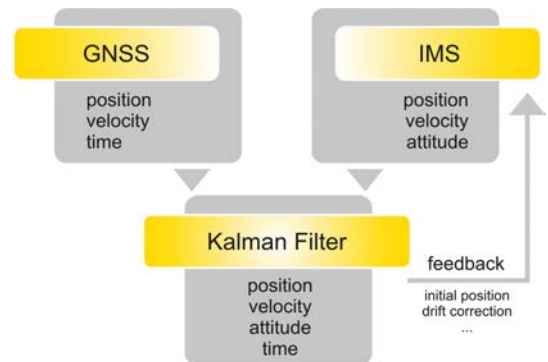


Fig. 4: Concept of loosely coupled sensor integration

### 2.3 Tightly coupled sensor integration

In the case of the tightly coupled Kalman filter, no separated evaluation of the GNSS and IMS measurement data is performed. As demonstrated in the scheme in Fig. 5, for the integration within the Kalman filter, the unprocessed measurement data of GNSS (code, phase and Doppler observations; in case of relative positioning of the rover as well as of the reference station) and IMS (accelerations, range rates) are used to estimate the position, velocity and attitude on the one hand and the sensor errors to optimize the trajectory determination on the other hand. This method requires an adequate relation between the GNSS and IMS observations which has to be modeled within the Kalman filter. The advantage of the tightly cou-

pled sensor integration is that the output of the filter (estimated parameters) and the Kalman filter model itself support the trajectory determination by means of solving the phase ambiguities and applying the estimated IMU sensor errors (gyro drift [9], accelerometer biases, misalignment ...). The modeling of all correlations and relations between the GNSS and IMS data results in a very complex filter design.

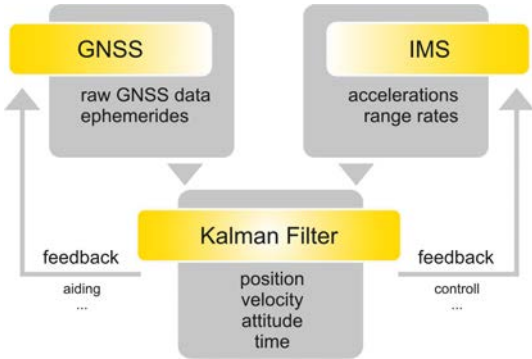


Fig. 5: Concept of tightly coupled sensor integration

The tightly coupled integration has, among others, the essential advantage that also absolute position solutions with less than four observable satellites can be computed, since the absent observations are compensated by the complementary measurement system (IMS).

### 3. Terrestrial field tests

The goal of the investigations was the accuracy estimation of the navigation components (position, velocity and attitude) with regard to the various measurement sensor combinations and the different coupling methods. The analysis of the results and their estimated accuracy should give information about the applicability of the different sensors and integration methods for mobile mapping systems. These analyses are based on terrestrial field tests which were performed under varying circumstances (partly and complete GNSS outage). For a consistent comparison of the used GNSS receivers and IMS sensors, a platform had to be designed to realize the same sensor configuration for every test measurement. The equipment is fixed to a stiff and light-weighted carbon-fiber frame which can be mounted on the roof rack of a car. The mounting of the GNSS-antennas and IMUs is shown in Fig. 6. The lever arms between the GNSS and IMU reference points have to be determined as good as possible. This is done with an accuracy in the sub millimeter range by terrestrial measurements with a theodolite.

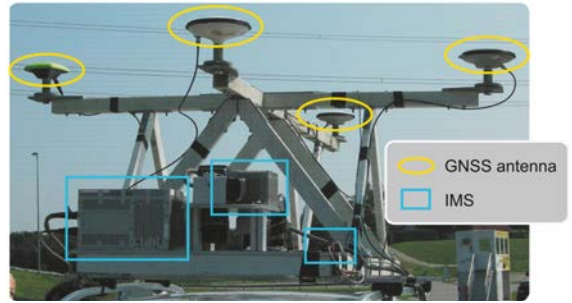


Fig. 6: Measurement platform mounted on the roof rack of a car

### 3.1 Sensors and observables

For the quality analysis of the sensors, GNSS receivers and IMUs of three different quality classes have been used and integrated via different coupling methods (see Fig. 7). The GNSS receivers are Sigma (Javad), ProPak-V3 (Novatel) and MTi-G (Xsens). In general, the GNSS receivers differ in the recorded measurement types (code, carrier phase) and their measurement frequency (4 Hz – 100 Hz). The Sigma and the ProPak-V3 receivers are both dual frequency GNSS receivers, however they differ in the update rate (Sigma offers up to 100 Hz, ProPak-V3 up to 50 Hz). The MTi-G measures C/A-Code with a frequency of 4 Hz.

The iNav-RQH (iMAR), the FSAS (iMAR) and the MTi-G (Xsens) are representing the IMU sensors. The drift behavior of the gyros, the offset of the accelerometers and the measurement frequency are among other parameters responsible for the classification of the IMUs. iNav-RQH is a very precise measurement system, whose RLGs (ring laser gyros) possess a high bias stability with a gyro-drift of 0.003°/h. It is one of the best available sensors on the IMU market. The IMU FSAS consists of three fiber optical gyros (FOG) and three servo-accelerometers. The gyro-drift is less than 0.75°/h, the offset of the accelerometers is about 1 mg (compared to iNav-RQH which shows an offset of 0.06 mg). MTi-G represents a low-cost system which is based on MEMS technology (Micro Electro Mechanical System). The gyro-drift (1°/h) and the offset of the accelerometers (100 mg) are much worse than the parameters of the other two IMUs.

For the integration of the GNSS and IMU sensors, different types of GNSS positioning methods are involved. Single point positioning based on code measurements is used for the combination of the MTi-G sensors. In case of the dual frequency receivers ProPak-V3 and Sigma relative

positioning is performed. As reference station for relative positioning, two dual frequency GNSS receivers of type Z-Xtreme (Ashtech) have been used in addition to the above mentioned GNSS receivers.

The IMU observables are accelerations and angular rates of three input axes. The MTi-G also includes three magnetometers to compensate the worse drift behavior of the low quality gyros [10].

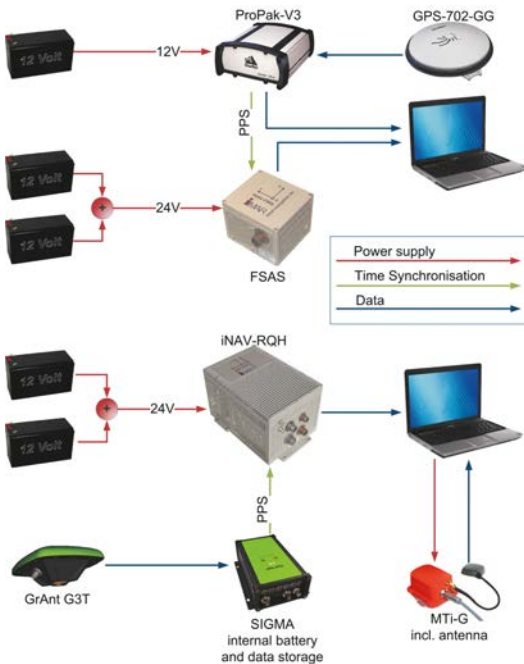


Fig. 7: Field test on a 7.5 km track close to Graz

### 3.2 Trajectory

The results analyzed in this paper are based on a 7.5 km track in Stainz (in the southwest of Graz, Austria). The choice of the observation time was based on the optimum conditions for GNSS measurements. During 80% of the track more than six satellites were logged. Additionally, it was important that at the beginning and at the end of the trajectory a static and a kinematic alignment was possible (many satellites in view, space for driving circles). The static alignment is necessary to determine the initial orientation of the sensor axes relative to the local level system [11]. The concept of the static alignment takes advantage of the fact that while the object is not moving, the accelerometers and gyros measure only the known gravity and the earth rotation. This method is called zero velocity update (ZUPT). The alignment phase is very important, since the whole trajectory is based on the initial attitude solution [12]. The kine-

matic alignment is used to determine the biases of the IMU sensor components which is mathematically realized by Kalman filtering [6]. As illustrated in Fig. 8, a static alignment of ten minutes was done at the beginning but also at the end of the trajectory to enable a forward and a reverse computation of the track.

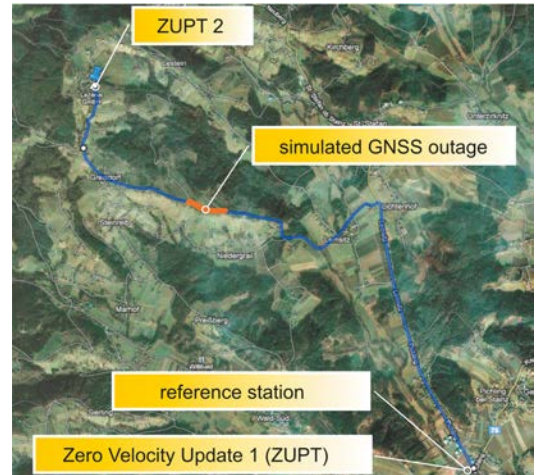


Fig. 8: GNSS receivers and IMUs of various categories can be integrated via different coupling methods

## 4. Results

The evaluation of the measured trajectory was mainly done with the commercial software module Inertial Explorer 8.3 (Waypoint Products Group, NovAtel [7]). For the visualization and comparison of the results, a user interface has been implemented in Matlab. The Inertial Explorer enables the evaluation and integration of GNSS and IMS measurements in the sense of loosely and tightly coupling. The uncoupled integration was realized by evaluating the GNSS and IMS trajectory separately in a pre-processing step followed by an integration step based on a self-implemented Kalman filter.

With the Inertial Explorer, the evaluation of the trajectory can be done in both directions (with increasing and decreasing time) which is called 'forward' and 'reverse' processing. By combining both results, the accuracy of the trajectory can be upgraded especially in the case of the absence of GNSS measurement data (tunnel, shadowing effects). However, for the comparison of the results just the forward or reverse solution has been used, since systematic effects can be detected and interpreted more easily. The combination of the solutions would falsify the scientific analysis of the results, but for practical use the combination should be favored.



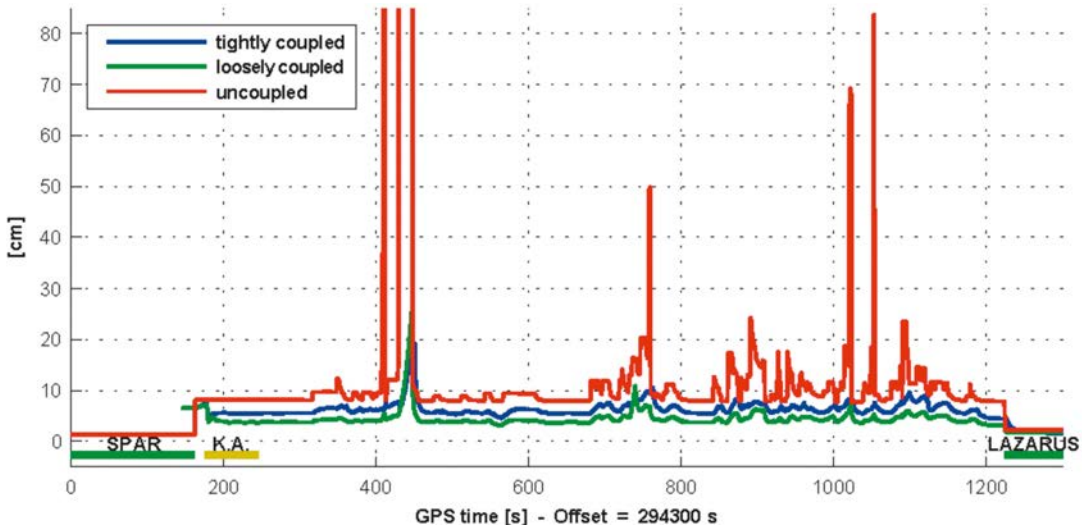


Fig. 9: Estimated  $1\sigma$ -accuracy of the computed position based on uncoupled, loosely coupled and tightly coupled integration

For a better comparison of the different IMU sensors, a GNSS signal outage was simulated (see Fig. 8), since in the case of the absence of a GNSS measurement, the quality of the IMU has a very strong impact on the determined trajectory.

#### 4.1 Comparison of the coupling methods

The FSAS and the ProPak-V3 have been selected for the evaluation of the different coupling methods. For the comparison of the integration results the  $1\sigma$ -accuracy values of the computed positions along the trajectory have been analyzed. The accuracy values of the uncoupled, loosely and tightly coupled integrations are shown in Fig. 9. For a better visualization of the differences of the integration results, the worse accuracy in the area of the GPS outage (~400 - 450s) is cut off.

Surprisingly, the loosely coupled integration leads to better accuracies than the tightly coupled method, see Fig. 9. The median and max-

imum values of the positions and the attitude angles in Table 2 emphasize this fact. The implementation of an incorrect model for the observation noise within the Inertial Explorer might be the explanation for the unexpected better results of the loosely coupled solution. If correlations between GNSS and IMS are not considered correctly or the IMS error model is not representative, the tightly coupled solution delivers suboptimal results.

In Fig. 10 and Fig. 11 the solutions for the roll and yaw angle are presented (pitch is not shown here, since the solution is very similar to roll). The graphic on top of Fig. 10 shows the  $1\sigma$ -accuracy of the roll angle for every type of integration. While the loosely coupled and the tightly coupled solution show nearly the same behaviour, the uncoupled values are much worse. The kinematic alignment phase is utilized by the loosely and tightly coupled algorithm to determine the sensor errors. Consequently, the accu-

		$\sigma_{HZ}^*$	$\sigma_{roll} \sim \sigma_{pitch}$	$\sigma_{yaw}$
uncoupled	median	4,4 cm	0,024°	0,956°
	max	35,2 cm	0,056°	0,963°
loosely coupled	median	2,4 cm	0,004°	0,022°
	max	22,6 cm	0,005°	0,094°
tightly coupled	median	3,4 cm	0,004°	0,024°
	max	16,0 cm	0,005°	0,049°

\*HZ ... horizontal

Tab. 2: Summary of the median and maximum values of the  $1\sigma$ -accuracy of the attitude angles and the positions resulting from an uncoupled, a loosely and a tightly coupled integration based on the terrestrial field test data

racy is much better. In the area of 260 s there is a short static phase after the kinematic alignment which is used as ZUPT. This phase is used by the uncoupled algorithm to correct the trajectory. Since there is no further ZUPT till the end of the trajectory the accuracy of the uncoupled integration is decreasing. This behaviour can also be observed in the bottom of Fig. 10 which represents the differences of the roll angle between the tightly coupled solution and the two others.

The behaviour of the yaw angle is different to the roll and pitch angle which is illustrated in Fig. 11. The accuracy for the uncoupled solution is up to 60' while the accuracy of roll is between 0.3' and 5.5'. In addition, no improvement can be recognized in the static phase (~260 s). Just

the ZUPT at the end of the trajectory causes an increasing accuracy. The loosely coupled and tightly coupled integration is again very similar. At the bottom of Fig. 11 a smaller scale of these two methods is depicted to illustrate the better performance of the tightly coupled integration in the kinematic alignment phase. For the rest of the trajectory, the results of the loosely coupled method are little bit more accurate.

Since the GNSS signal is recorded nearly continuously, the benefit of the tightly coupled integration can not be exploited, see Fig. 9, 10 and 11. In areas, where less than four GNSS signals are available, the tightly coupled integration yields better results. In order to proof this fact, a short and partly GNSS signal outage has been

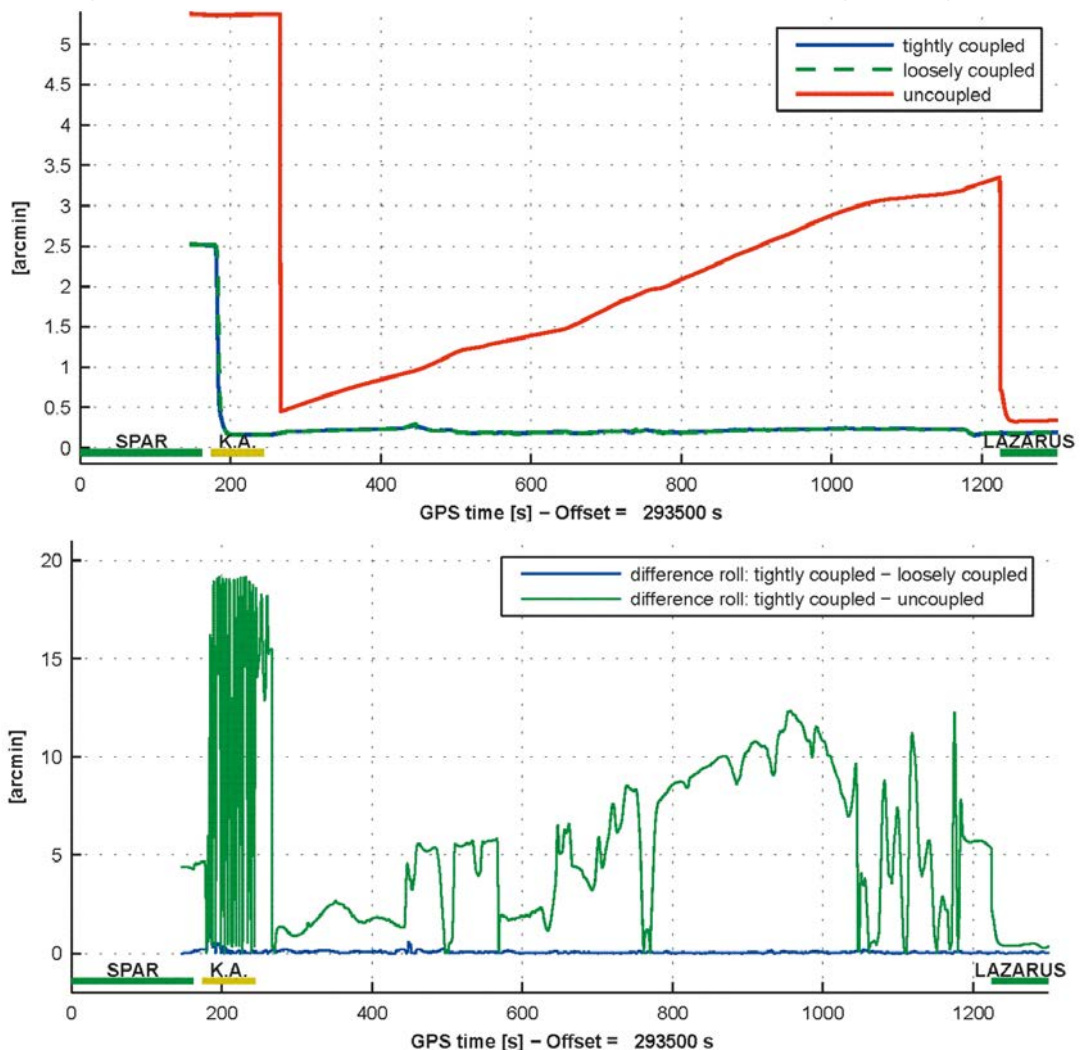


Fig. 10: Top:  $1\sigma$ -accuracy of roll based on uncoupled, loosely coupled and tightly coupled integration; Bottom: Differences of the loosely coupled and uncoupled solution with respect to the tightly coupled solution

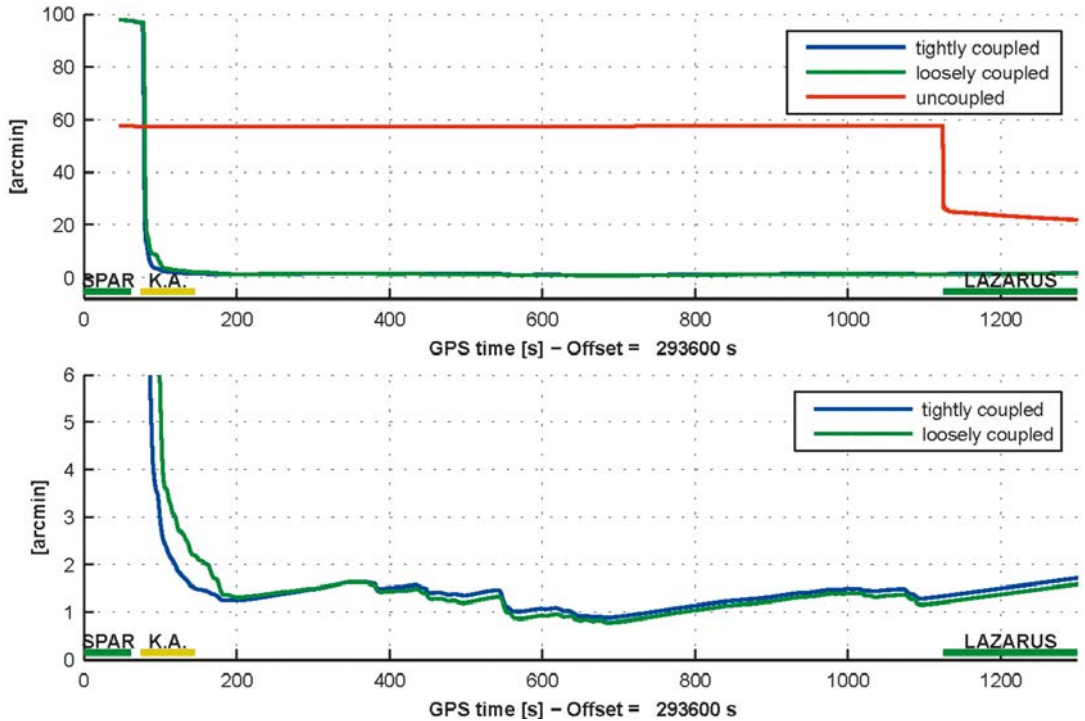


Fig. 11: Top:  $1\sigma$ -accuracy of yaw based on uncoupled, loosely coupled and tightly coupled integration; Bottom: Comparison of the  $1\sigma$ -accuracy of yaw based on a loosely coupled and tightly coupled integration

simulated (compare the marked 'simulated GNSS outage' in Fig. 8), which means that all satellites except three (with the highest elevation angle to simulate obstacles) have been eliminated. Now, the loosely coupled integration misses the GNSS position solution (for the computation of a GNSS based position at least four GNSS measurements are needed) and therefore just depends on the quality of the IMS data. Since the tightly coupled Kalman filter design is based on the raw measurement data, this method can benefit from the three remaining GNSS signals to support the IMS solution. Fig. 12 shows the differences between the loosely and tightly coupled integration within the short and partly GNSS signal outage. The tightly coupled solution is much better than the output of the loose coupling and deviates less from the reference trajectory (best solution without GNSS outage). This shows clearly that the use of tight coupling is unavoidable in case of bad GNSS conditions.

#### 4.2 Comparison of the sensors

The different sensors have been categorized into three quality (price) classes:

- Low quality: The Xsens MTi-G is a combined GPS-IMU system (price  $\approx$  3.500 €).

- Medium quality: The combination of the GNSS receiver ProPak-V3 and the IMU FSAS has been defined as the medium quality representative (price  $\approx$  57.000 €).
- High quality: For a high quality sensor fusion the GNSS receiver Javad Sigma and the IMS iNAV-RQH are involved. The IMS is the main component of the costs (price  $\approx$  187.000 €).

quality	$\sigma_{\text{HZ}}$ *	$\sigma_{\text{roll}} \sim \sigma_{\text{pitch}}$
low	90,0 cm	1,2°
medium	2,4 cm	0,004°
high	2,0 cm	0,002°

\*HZ ... horizontal

Tab. 3: Median of the  $1\sigma$ -accuracy of the horizontal position, the roll and pitch angles based on the terrestrial field test data

Table 3 shows the results for the  $1\sigma$ -accuracy levels of the horizontal position as well as for the roll and pitch angles. The accuracy of the low quality combination is poor compared to the results of the other two combinations.

For a deeper investigation of the integration results of the medium and high quality sensor

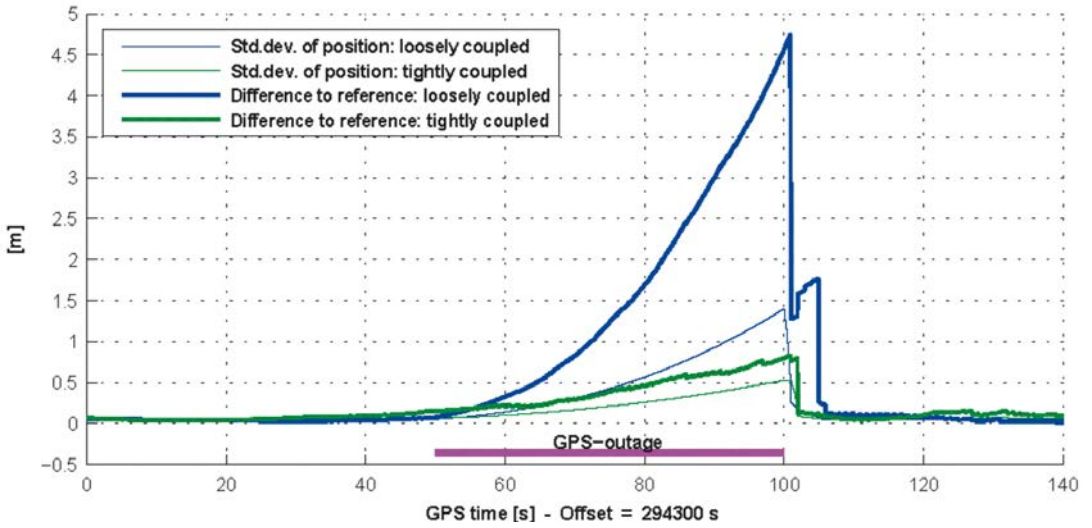


Fig. 12: Differences with respect to the reference trajectory and standard deviations of the position based on loose and tight coupling

fusions, a complete GNSS signal outage has been simulated, see Fig. 7. By simulating a GNSS outage, the quality of the IMS sensors can be analyzed. This is very important, since the large difference in the costs is caused by the different IMS sensors. In Fig. 13, the solutions of the integrations of the FSAS/ProPak-V3 and Sigma/iNAV-RQH are shown and compared to the reference trajectory (best integration result without GNSS outage). The low quality combination is not shown in Fig. 13, because of the bad performance of the IMU and the use of GNSS code measurements. The graphical representation of

the MTi-G position errors would make a comparison of the other two combinations impossible (the difference exceeds the scale already after a few seconds). Since there is no GNSS signal available in the outage, the graphic can be interpreted as the performance of the IMS. Obviously, the high quality IMU (iNAV-RQH) indicates a much better drift behaviour. While the differences to the reference trajectory for the IMU FSAS are up to 5.3 m which is much more than the largest estimated standard deviation (1.5 m), for the IMU iNAV RQH the opposite is true. At the end of the GNSS outage (after 50 seconds), the

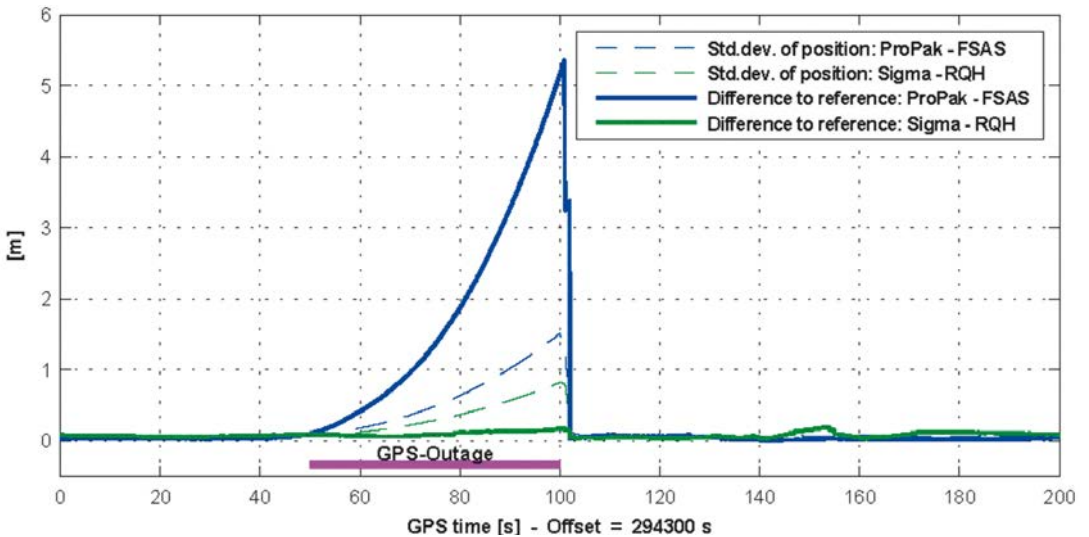


Fig. 13: Differences with respect to the reference trajectory and standard deviations of the position based on sensor fusions with the medium and high quality equipments

difference to the reference trajectory for the IMU iNAV RQH is 0.2 m although the estimated accuracy reaches a value of 0.8 m.

## 5. Conclusion

Within these investigations, the performance of different GNSS and IMU sensor integrations has been tested and analyzed. On the one hand, three different categories of sensors in terms of accuracy and quality have been compared. On the other hand, the efficiency of an uncoupled, loosely coupled and tightly coupled integration has been examined. For the investigations, a measurement platform was designed to guarantee consistent measurement data of all sensors. The processing of the observed data showed that the choice of the sensor combination and their integration strongly depends on the surroundings of the trajectory. If no GNSS signal outages occur, the loosely coupled integration of the GNSS receiver Sigma and the IMU iNAV-RQH leads to the best results in terms of position and attitude accuracy. However, the investigations have demonstrated, that the integration method has a strong impact on the result, if less than four satellites are available (in particular three satellites are observed). In this case, the performance of the tightly coupled integration is best, since this method uses the IMU data to compensate the missing satellites. All other integration methods use solely IMU data for the trajectory determination, since no independent GNSS position can be computed with less than four satellites. If a complete GNSS outage occurs, the integration result depends on the quality of the IMU only. After a GNSS outage of 50 s the Sigma/iNAV-RQH solution differs just 20 cm from the reference trajectory, while the differences based on the ProPak/FSAS combination were much higher (5.3 m). The bad performance of the low quality IMU results in a difference of several tens of meters already after a few epochs. In case of the GNSS outage, the trajectory benefits from the performance of the high quality IMU.

At the moment the Institute of Navigation is working on the implementation of a software which is capable of performing all kinds of integrations. Since the Inertial Explorer is a commercial software and a blackbox for the user, it is impossible to analyse the internal settings and models. By using the self-implemented software, a quality analysis on a higher scientific level can be done.

## References

- [1] Gordon, G.S. (1998): Navigation systems integration. *Airborne Navigation Systems Workshop (Ref. No. 1998/275)*, IEE, vol., no., pp. 4/1- 4/16, 10 Feb 1998. doi: 10.1049/ic:19980390
- [2] Zhao, X., Syed, Z., Wright, D.B. and El-Sheimy, N. (2009): An Economical and Effective Multi-sensor Integration for Portable Navigation System. Proceedings of the 22nd International Technical Meeting of The Satellite Division of the Institute of Navigation (ION GNSS 2009).
- [3] Grewal, M. S., Weill, L. R. and Andrews, A. P. (2001): *Global Positioning Systems, Inertial Navigation and Integration*. John Wiley & Sons, Inc.
- [4] Hofmann-Wellenhof, B., Legat, K. and Wieser, M. (2003): *Navigation – Principles of Positioning and Guidance*. Springer-Verlag Wien.
- [5] Hafner, P., Längauer, K., Wasle, B., Wieser, M. and Kührtreiber, N. (2010): Analyse verschiedener Integrationsvarianten von GPS und Inertialnavigation in Hinblick auf unterschiedliche Georeferenzierungsszenarien (VarIoNav). Final Report, FFG, Austrian Space Applications Programme.
- [6] Jekeli, C. (2001): *Inertial Navigation System with Geodetic Applications*. Walter de Gruyter.
- [7] NovAtel (2010): *Inertial Explorer User Guide*. NovAtel Inc.
- [8] Zarchan, P. and Musoff, H. (2005): *Fundamentals of Kalman Filtering: A Practical Approach*. Progress in Astronautics and Aeronautics. Volume 208. American Institute of Aeronautics and Astronautics, Inc., USA.
- [9] Wei, G.; Qi, N.; Guofu, Z. and Hui, J. (2007): Gyroscope Drift Estimation in Tightly-coupled INS/GPS Navigation System. 2nd IEEE Conference on Industrial Electronics and Applications, 2007. pp.391-396, 23-25 May 2007. doi: 10.1109/ICIEA.2007.4318437.
- [10] MTI-G – miniature AHRS with integrated GPS (2011): MTI-G leaflet. Xsens Technologies B.V. [http://www.xsens.com/images/stories/products/PDF\\_Brochures/mti-g%20leaflet.pdf](http://www.xsens.com/images/stories/products/PDF_Brochures/mti-g%20leaflet.pdf)
- [11] Titterton, D. H. and Weston, J. L. (2004): *Strapdown Inertial Navigation Technology*. MPG Books Limited.
- [12] Hong, S., Lee, M. H., Kwon, S. H. and Chun, H. H. (2004): A Car Test for the Estimation of GPS/INS Alignment Errors. *IEEE Transactions on Intelligent Transportation Systems*, vol.5, no.3, pp. 208- 218, Sept. 2004. doi: 10.1109/TITS.2004.833771.

## Contacts

Dipl.-Ing. Petra Hafner, Graz University of Technology, Institute of Navigation, Steyrergasse 30/III, 8010 Graz, Austria.

E-mail: [petra.hafner@tugraz.at](mailto:petra.hafner@tugraz.at)

Ao.-Univ.-Prof. Dipl.-Ing. Dr.techn. Manfred Wieser, Graz University of Technology, Institute of Navigation, Steyrergasse 30/III, 8010 Graz, Austria.

E-mail: [wieser@geomatics.tu-graz.ac.at](mailto:wieser@geomatics.tu-graz.ac.at)

Ao.-Univ.-Prof. Dipl.-Ing. Dr.techn. Norbert Kührtreiber, Graz University of Technology, Institute of Navigation, Steyrergasse 30/III, 8010 Graz, Austria.

E-mail: [norbert.kuehtreiber@TUGraz.at](mailto:norbert.kuehtreiber@TUGraz.at)

## Impact of glacier changes on the local gravity field by numerical forward modelling and applicability studies using GOCE gravity gradients for regional gravity field solutions by Least Squares Collocation



*Florian Heuberger and Daniel Rieser*

### Abstract

A numerical approach to gravity forward modelling is developed and introduced in order to investigate the effects of ice mass changes on the local gravity field. These studies are based on a synthetic glacier model of the northern island of Novaya Zemlya, which incorporates geometrical as well as 3D-density information. By modifying the model parameters like ice thickness and the density distribution in the interior of the ice body, the changes that can be expected in the gravity signal are estimated. Furthermore, different assumptions on the underlying bedrock topography can also be evaluated with respect to the resulting gravity signal. Simulations with realistic model parameters yield to gravity attraction differences in the order of a few mGal. Based on given digital elevation models featuring ice mass changes within the last 60 years, the forward modelling approach allows the investigation of the impact of ice change on the gravity field. The estimated effect on the gravity field reaches a maximum amplitude of 6 mGal over the whole period, implying an average change of 1 mGal per decade. In addition, a concept for using gradient observations of ESA's satellite mission GOCE for regional gravity field determination is introduced in this paper. In contrast to the official objectives, i.e. the generation of a global static gravity field based on the entirety of observations, here the measurements are introduced as in situ observations over a spatially restricted area and the gravity field is determined by means of Least Squares Collocation. For this purpose the noisy gradient data are filtered using the Wiener approach and the covariance functions required for collocation are derived. Furthermore, the problematic issue of the coordinate frame is discussed and a possible solution is presented. Finally, a gravity field solution based on real GOCE gradient data for November 2009 is generated for the above mentioned study area in terms of gravity anomalies. With this method and the chosen data configuration it is possible to determine the gravity field with an estimated accuracy of 4 mGal. The difficult comparison of gravity attractions from numerical forward modelling and gravity anomalies from the space-borne gradiometry is discussed.

**Keywords:** Numerical forward modelling, gravity field, ice mass change, least squares collocation, GOCE

### Kurzfassung

Um die Auswirkungen von Eismassenvariationen auf das lokale Schwerfeld zu untersuchen, wird ein numerischer Ansatz zur Schwere-Vorwärtsmodellierung entwickelt und vorgestellt. Diese Untersuchungen bauen auf einem synthetisch generierten Gletschermodell für die Nordinsel der Novaya Zemlya Inselgruppe auf, das sowohl die geometrische Struktur als auch die 3D-Dichteverteilung beinhaltet. Durch Modifikationen der Modellparameter wie Eisdicke und Dichteverteilung im Eiskörper werden die zu erwartenden Veränderungen im Schweresignal untersucht. Die modellierte Topographie des Felsuntergrundes kann ebenfalls hinsichtlich unterschiedlicher Annahmen auf Differenzen im resultierenden Schweresignal betrachtet werden. Die Simulationen mit realistisch angenommenen Modellparametern ergeben Gravitationsunterschiede von wenigen mGal. Weiters wird mit Hilfe des Vorwärtsmodellierungsansatzes die Auswirkung der Eismassenveränderungen der letzten 60 Jahre untersucht, die in Form von zwei digitalen Geländemodellen gegeben sind. Der abgeschätzte Effekt auf das Schwerfeld erreicht eine maximale Amplitude von 6 mGal über den gesamten Zeitraum, bzw. eine durchschnittliche Veränderung von ca. 1 mGal pro Jahrzehnt. In weiterer Folge wird in diesem Beitrag ein Konzept vorgestellt, wie Gradientenbeobachtungen der ESA Satellitenmission GOCE für eine regionale Schwerfeldlösung verwendet werden können. Im Gegensatz zur offiziellen Zielsetzung, der Bestimmung eines globalen statischen Schwerfelds basierend auf der Gesamtheit aller Beobachtungen, werden hier die Messungen als Direktbeobachtungen über einem räumlich begrenzten Gebiet eingeführt und die Schwerfeldlösung über die Methode der Kollokation nach kleinsten Quadraten errechnet. Dazu werden die rauschbehafteten Gradientendaten nach dem Wiener-Ansatz gefiltert und die für die Kollokation notwendigen Kovarianzfunktionen abgeleitet. Weiters wird die Problematik des Koordinatenrahmens diskutiert und ein möglicher Lösungsansatz vorgestellt. Mit einem realen GOCE Gradienten Datensatz für November 2009 wird eine Schwerfeldlösung in Form von Schwereanomalien für das oben genannte Untersuchungsgebiet berechnet. Mit der verwendeten Meth-

ode und Datenkonfiguration kann das Schwerefeld mit einer geschätzten Genauigkeit von 4 mGal bestimmt werden. Die schwierige Gegenüberstellung der beiden Ansätze (Gravitation aus Vorwärtsmodellierung und Schwereanomalien aus Satellitengradiometrie) wird diskutiert.

**Schlüsselwörter:** Numerische Vorwärtsmodellierung, Schwerefeld, Eismassenveränderung, Kollokation nach kleinsten Quadraten, GOCE

## 1. Introduction

The knowledge of the (regional) gravity field is an important factor for the observation and interpretation of ice mass changes in the context of climate change. The ice mass balance is commonly derived from geometrical information of the ice bodies, which is observed and mapped by different methods [1]. Amongst those are space-borne altimetric missions like ICESat, CryoSat-2 as well as interferometric concepts like ERS-ENVISAT, TanDEM-X or TerraSAR-X. For such remote sensing and mapping methods a precise static gravity field expressed in terms of geoid heights provides a common solid height datum which is aimed to be known with highest accuracy.

Additionally, mass changes like those of the snow and ice resources also have a direct impact on the gravity field, since gravity is related to mass distribution within the Earth and at its surface. With the launch of the satellite mission Gravity Recovery and Climate Experiment (GRACE) [2] in 2002, the gravity field can also be observed with respect to its temporal variations. These can inversely be related to the mass transports from geodynamic processes [3, 4]. However, the separation of the gravity effect caused by a distinct source of mass change like ice cover variations from the overall gravity signal still poses a scientific problem, which is amplified by the so called leakage effect, explained e.g. in [5, 6].

In this context two aspects of the gravity field are investigated and presented in this paper: on the one hand (section 2), local changes in the gravity field caused by variations of ice masses can be modelled by numerical forward modelling. Based on a realistic simulation of an ice body's structure, the gravity field effects are estimated. Also, temporally changing mass distributions, e.g. variations in the snow-ice cover, are treated. Thus, also the gravity field accuracy required to sense such (temporally varying) signals can be estimated.

On the other hand, the ESA satellite mission Gravity field and steady state Ocean Circulation Explorer (GOCE) [7] offers new opportunities for accurate static gravity field solutions. The objective of GOCE is the determination of a global

gravity field. However, such a global approach might smooth local or regional features of the gravity field to some extent. Furthermore, satellite gravity missions can only deliver gravity information limited in spectral and spatial resolution (about 80 km are expected from GOCE). Therefore, a combination of terrestrial, air-borne and satellite gravity data is commonly performed [8] for regional gravity field determinations to overcome these limitations. The method of Least Squares Collocation (LSC) offers such an opportunity for data combination. In section 3, an approach for the inclusion of the novel gravity gradient data type of the GOCE mission in a LSC process is introduced and a regional gravity field on solely gradient data is computed.

For the research presented in this paper, Novaya Zemlya has been selected as principal study region (Fig. 1). The northern part of the island is covered by the world's third largest ice body of about 22 000 km<sup>2</sup> (cf. [9]). The main causes for selecting this region were the availability of detailed digital elevation models for the forward modelling as well as the dense GOCE ground tracks (high spatial density of gravity gradient observations) at this high geographical latitude.

Section 4 of this paper includes a discussion of the intermediate results of both approaches and their comparison. Section 5 contains the conclusions, and an outlook is given on possible applications and further studies.



Fig. 1: The study region Novaya Zemlya (Source: Marble).

## 2. Numerical Forward Modelling

### 2.1 Mathematical Background

A closed formula for a rectangular prism's gravity effect on an arbitrarily defined computation point can be derived from Newton's integral formula describing the attraction exerted by a solid body, as described in [10]. The formula for the gravity anomaly  $\Delta g$  depending on the relative density  $\Delta\rho$  is based on using all eight prism corners ( $x_{1,2}$ ,  $y_{1,2}$ ,  $z_{1,2}$  in a local horizontal system with its origin at the computation point) for the integral solution, as described in [11]

$$\Delta g = -G\Delta\rho \left[ x \ln(y+r) + y \ln(x+r) - \right. \quad (1)$$

$$\left. - z \arctan \frac{xy}{zr} \right] \Bigg|_{x_1}^{x_2} \Bigg|_{y_1}^{y_2} \Bigg|_{z_1}^{z_2}$$

where  $G$  denotes the Newton gravitational constant and  $r$  is the distance between the computation point and the currently evaluated corner of the prism.

By summing up the resulting gravity anomalies  $\Delta g$  of all individual prism elements of a digital terrain model (DTM) for one particular computation point, the sum yields the model's gravity effect on this point. This process is of course well known in remove-restore techniques for gravity field computation (cf. [12]). However, usually a constant density value  $2.67 \text{ g/cm}^3$  is applied. In this paper, we use a three-dimensional density distribution, i.e. prisms of different density (Fig. 2) leading to an absolute synthetic gravity field effect instead of terrain reduction. This modelling strategy will allow computing the contributions of bedrock and (changing) ice separately. Due to combination of DTM and 3D-density, we speak of a digital terrain density model (DTDM).

By defining a whole grid of computation points situated on the prism tops or on a constant level above, a synthetic gravity field can be calculated representing the gravitational effect (gravity attraction) of the underlying DTDM

The model itself is defined in a WGS-84 based geographic grid with homogeneous spacing in both directions. In order to meet the requirements of the Cartesian coordinate based Eq. (1), a transformation of relevant model parts (mass selection radius 167 km) to a local level frame (North, East, Up) originating at the actual computation point is carried out. This ensures that all the masses are placed correctly during each calculation loop, with regard to the Earth's curvature

and the meridian convergence as "seen" from individual computation points.

### 2.2 Model Composition

As described above, numerical forward modelling relies on the surface geometry and a three-dimensional density distribution. The geometrical representation of Novaya Zemlya is a combination of different data sources: synthetic aperture radar, altimetry and various maps were compiled by Joanneum Research (cf. [13]), yielding a digital terrain model of the island. Additionally, the International Bathymetric Chart of the Atlantic Ocean (IBCAO) [14] was used for modelling the surrounding underwater topography. By merging both data sets, a detailed geometric model of Novaya Zemlya and its surroundings could be generated. Forward modelling can only reflect a relative part of the gravity signal (cf. discussions in section 4). While this would not pose a problem in classical remove-restore techniques, more masses had to be included in the computations in order to obtain realistic mGal-ranges for the comparison with (absolute) gravity data from the LSC-solution. Accordingly, the digital terrain and density model (DTDM) was expanded and incorporates masses down to a depth of 600 meters.

In order to combine geometry and density information, a 3D-separation into ice, bedrock and ocean, which are treated individually during the model compilation process, is performed. One example of a final DTDM is shown in Fig. 2. The 3D-separation procedure has several interfaces that can be used to customize the parameters of bedrock and ice regarding both geometry and density in order to simulate different model states. These different models allow the analysis of every individual parameter change in terms of gravity field changes. Due to the primary focus

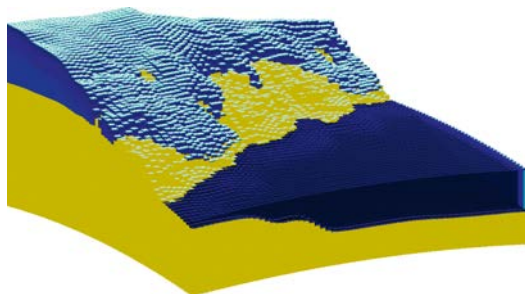


Fig. 2: Schematic close-up view of the digital terrain density model as "seen" from a computation point during numerical forward modelling, representing different densities for ice (cyan), bedrock (brown) and ocean (dark blue).



on ice mass change, the densities of bedrock and ocean were set to common constant values, whereas the ice density distribution relies on an empirical depth-density relation described more extensively in section 2.3 and [15].

**2.3 Investigation of model parameters**

The spatial resolution of the models used in this section is 0.5 km. A computation point for the gravity field forward modelling is situated directly on top of every (stacked) prism in the DTDM. All results in this section are gravity attractions  $g$  expressed in mGal. In the following paragraphs differences with respect to an “absolute” solution at epoch 2008 with default parameters are shown in the course of tuning the model parameters.

**2.3.1 Changes in Ice Geometry**

First, we simulated an ice loss of 10 % at the main ice cap which would result in a gravity field change in the range of 3 mGal (Fig. 3). This relative ice loss corresponds to about 40 to 50 m at the thickest parts of the ice sheet. Note that the ice thickness and therefore the underlying bedrock topography in this modelling process are based on the generic lookup table (LUT) described below. The positive changes in the gravity attractions are due to the fact that the computation points – in these forward modelling differences – are located directly on the surface of the DTDMs to asses the observable signal change, e.g. with terrestrial measurements that might be executed in situ. The computed ice mass loss results in lower altitudes on the second model and therefore in increased gravity attractions.

**2.3.2 Bedrock Height**

A LUT is used to model the bedrock height below the ice cap depending on the surface height given in the DTM. Two different LUT settings were compared in Fig. 4 to analyze the impact

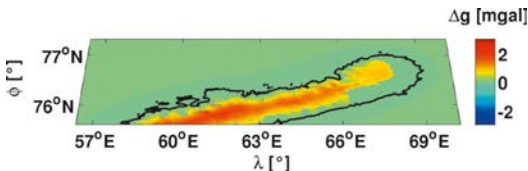


Fig. 3: Gravity attraction differences (in mGal) to be expected from an assumed ice mass loss of 10 % over the whole study area simulated via numerical forward modelling. Positive values (differences) are due to the lower altitude of computation points, where the surface height is decreasing due to the ice loss.

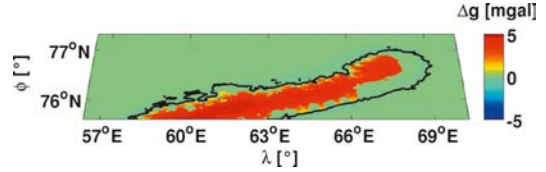


Fig. 4: Gravity attraction differences (in mGal) to be expected between different models for the bedrock topography below the ice caps simulated via numerical forward modelling (computed on the model surface).

of the LUT-parameters on the gravity field computation. In both cases a second order polynomial was used to compute the height of bedrock below a given surface height. These assumptions are based on observations performed by Joanneum Research ([17]). The impact on the computed gravity field amplitude is caused by the different bedrock height settings (differences of about 50 m at the areas with maximum DTM elevation) via the LUTs.

**2.3.3 Ice Density Model**

In order to achieve a realistic density distribution within the ice body, the empirical relation for a density  $\rho$  at a depth  $z$ , published by [16] is used

$$\rho(z) = \rho_i - (\rho_i - \rho_s) \exp\left(-\frac{1.9}{z_i} z\right). \tag{2}$$

The different parameters were defined in accordance with in situ measurements carried out by Joanneum Research in 2008 in the study region: the mean density of ice  $\rho_i$  (empirically determined), the surface snow density  $\rho_s$ , and the site dependent firn-ice transition depth  $z_i$ . The underlying measurements are described in [17]. Quantization into six bins allowed the top down density modelling by means of stacked prisms.

Due to its low firn-ice transition depth, the model has only a thin hull of lighter snow and ice above a solid ice core with constant density. The negligible impact of less than 1 mGal caused by different firn ice transition depths for the Schytt model is analyzed in [15].

**2.4 Ice Change during the past 60 years**

A combination of maps dated around 1950 and present remote sensing data allowed Joanneum Research [18] the mapping of spatially distributed ice change during the past 60 years (Fig. 5). Of course this map cannot be regarded as completely error free due to the large time span covered (with few historical datasets available) and might overestimate certain surface changes.

The implementation of this geometry variation within our numerical forward modelling frame-

work allows the computation of this surface elevation change interpreted as ice mass gain/loss in terms of gravity attractions (Fig. 6). The maximum signal amplitude change of about 6 mGal can be observed at the northern ice cap. This corresponds to about 1 mGal signal variation per decade. Regarding the spatial extent of the northern ice cap's signal change, a region of roughly 800 km<sup>2</sup> is mainly affected by these significant amplitudes.

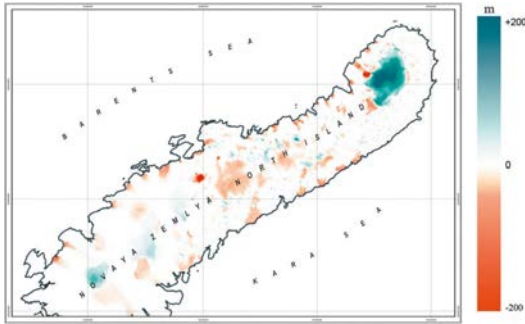


Fig. 5: Differences between elevation models of 1950s and 2008 in meters (Joanneum Research).

Note that the stations for these computations were held at an ellipsoidal height of 1500 m. This height was kept constant in order to avoid misinterpretations due to local gravitational effects acting on computation points directly at the surface of the different DTDMs. Additionally, the smaller absolute differences compared to Fig. 3 are also due to the smaller lateral extent of the observed surface changes opposed to a simulated melting over the whole study region.

### 3. Gravity field determination using GOCE gradients with Least Squares Collocation

The numerical forward modelling approach described in the previous sections allows a computation of gravitational effects based on a known or assumed topography and density distribution in the upper lithosphere. However, this reflects only a subset constituent of the actual gravity signal, which is a product of all masses inside the Earth and on its surface according to New-

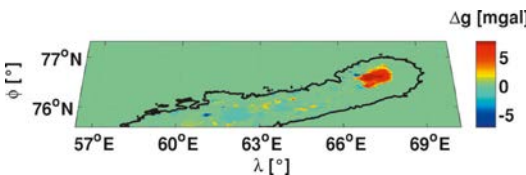


Fig. 6: Gravity attraction differences (in mGal) corresponding to the observed surface elevation changes since 1950 (computed using numerical forward modeling at a constant computation height of 1500 m).

ton's law of gravitation. The overall gravity signal can only be observed by terrestrial, air-borne or space-borne gravimetric measurements. As direct observations of the actual gravity are rare in remote regions, a space-borne technique like GOCE [7], launched in March 2009, offers a possibility to obtain information about the actual gravity field also in our study area. This mission is dedicated to determine the static global gravity field, which is accomplished by the European GOCE Gravity Consortium in the frame of the ESA project 'GOCE HPP' [19]. In this context the GOCE mission is expected to provide accurate gravity information, which is superior to other data types, especially in the medium wavelength spectrum of about degree and order 100 to 250 in terms of a spherical harmonic series expansion, which corresponds to 200 km to 80 km half wavelength of the gravity signal. The key instrument of the GOCE mission is the gradiometer. This assembly allows to measure gravity gradients, i.e. second order derivatives of the gravitational potential, from space. In contrast to the GOCE HPP solution strategies for deriving a global gravity field, the methods and concepts for the use of GOCE gradient data as in situ observations in the frame of local geoid computations are presented in this section.

### 3.1 Least Squares Collocation (LSC)

At regional scale, LSC [20] is a standard method for the computation of the Earth's gravity field. Its ability to combine various kinds of gravity field observations, e.g. geoid undulations, gravity anomalies or gravity gradients as measured by GOCE, is the major strength of this approach.

According to the theory of LSC, any arbitrary gravity field signal  $s$  can be predicted, if the linear functional which relates the signal to the basic disturbing potential  $T$  is applied to the covariance model of  $T$  in terms of a covariance propagation. The basic formula of LSC is given by

$$s = C_{sl}(C_{ll} + C_{nn})^{-1}l \tag{3}$$

where  $C_{sl}$  consists of the cross-covariances between the signal  $s$  and the observation  $l$ , while  $C_{ll}$  is the auto-covariance matrix of the signal content of the observations. The error structure of the observations is introduced by the noise-covariance matrix  $C_{nn}$ . The entries of  $C_{sl}$  and  $C_{ll}$  can be calculated from a covariance function of the anomalous potential

$$C(r_i, r_j, \psi_{ij}) = \sum_{n=N_{min}}^{N_{max}} k_n \left( \frac{R^2}{r_i r_j} \right)^{n+1} P_n(\cos \psi_{ij}). \tag{4}$$

It depends on the radius  $R$  of a sphere completely enclosed by the Earth, the distances  $r_i$ ,  $r_j$  from the geocenter to the observation stations, and the Legendre polynomials  $P_n$  of degree  $n$ , which are functions of the cosine of the spherical distance  $\psi_{ij}$  between the stations. The signal variances  $k_n$  can for instance be obtained from the fully normalized harmonic coefficients of an a-priori gravity field model via the relation

$$k_n = \sum_{m=0}^n \left( \bar{C}_{nm}^2 + \bar{S}_{nm}^2 \right). \quad (5)$$

While the functional that relates the vertical gravity gradient  $T_{ZZ}$  to the anomalous potential  $T$  is simply given by the second order radial derivative, the functionals for all other gradients are more complex. For instance, the  $T_{XX}$  gradient can be expressed in terms of spherical coordinates by

$$T_{XX} = \left( \frac{1}{r} \frac{\partial}{\partial r} + \frac{1}{r^2} \frac{\partial^2}{\partial \varphi^2} \right) T. \quad (6)$$

To derive the covariance between gradients  $T_{XX}$  at different positions, the functional of Eq. 6 has to be applied twice to the covariance function in Eq. 4, once for each position, leading to

$$\text{cov}(T_{XX}, T_{XX'}) = \left( \frac{1}{r} \frac{\partial}{\partial r} + \frac{1}{r^2} \frac{\partial^2}{\partial \varphi^2} \right) \left( \frac{1}{r'} \frac{\partial C}{\partial r'} + \frac{1}{r'^2} \frac{\partial^2 C}{\partial \varphi'^2} \right). \quad (7)$$

It can be seen, that the covariance propagation for gravity gradients requires partial derivatives of the basic covariance model  $C$  up to a maximum order of four. To calculate all necessary covariances of derivatives of  $T$ , an approach as in [21] can provide a convenient solution of the problem. An advantage of this approach is the possibility to perform covariance propagation to another reference frame quite easily. This fact is of great importance and will be applied in the next section.

### 3.2 Methodological restrictions and their solutions

Before GOCE gradient data can be used in LSC, it has to be considered that the six accelerometers of the gradiometers only show good performance in the measurement bandwidth between 5 and 100 mHz. The gradient data comprise measurement errors in terms of coloured noise in particular in the long-wavelength fraction of the gravity signal. To reduce these effects a filtering step has to be introduced. Here the standard Wiener filter method for filtering GOCE gravity gradients, explained in detail in [22] and [23], is adapted for the data set within the investigated region. It should be mentioned that this

approach requires a signal that is stationary in time, which has to be considered next.

A further major issue when dealing with GOCE data is the fact that the GOCE mission observes gravity gradients in the sensor frame called Gradiometer Reference Frame (GRF), where stationarity is not given in strict sense. However, this requirement would be fulfilled in the Local Orbit Reference Frame (LORF), which is defined by the actual flight direction of the satellite. GRF is deviating from LORF by several degrees (cf. [24]), so a preceding frame transformation would be necessary before filtering the gradient data.

Furthermore, gravity field quantities are derived with LSC in a Local North Oriented Frame (LNOF), defining a local geographical coordinate frame. In the case of the GOCE gradiometer, unfortunately not all of the gravity gradient components can be measured with the same level of accuracy. In fact, the accuracy of the off-diagonal elements  $T_{XY}$  and  $T_{YZ}$  is degraded by a factor of 100 to 1000 [25]. Hence, a rotation of the gradient tensor from GRF to LORF or GRF to LNOF must be avoided. Otherwise the large errors of the off-diagonal elements would be propagated to all other components and drastically deteriorate the well-measured gradients [26]. Alternatively, the base functions (i.e. the covariance matrices) of LSC given in LNOF have to be rotated to the GRF or LORF, which can be performed as outlined in section 3.1.

As a consequence of the problems discussed above, different solution strategies can be considered [27]. For this study, the GRF is defined as the computational reference frame, while the theoretical requirement of a stationary gradient time series is neglected, cf. Fig. 7. This means, that the covariance matrix entries of  $C_{ll}$  and  $C_{sl}$  of the LSC procedure (cf. Eq. 3) related to gradient observations have to be rotated to GRF, while the Wiener filter is directly applied to the observed gradient time series. If one further assumes that the gradient components are uncorrelated amongst each other, the noise-covariance matrix  $C_{nm}$  can be set up by using the corresponding error covariance function, which can be derived via the filter error of the Wiener filter process [28].

### 3.3 Gravity field computation

In this study the GOCE Level-1b data set for November 2009 is used. GOCE is expected to improve the gravity field especially in the medium-wavelength. Therefore, in accordance to the remove-restore concept [12], long wave-length gravity signals are computed from the EGM2008

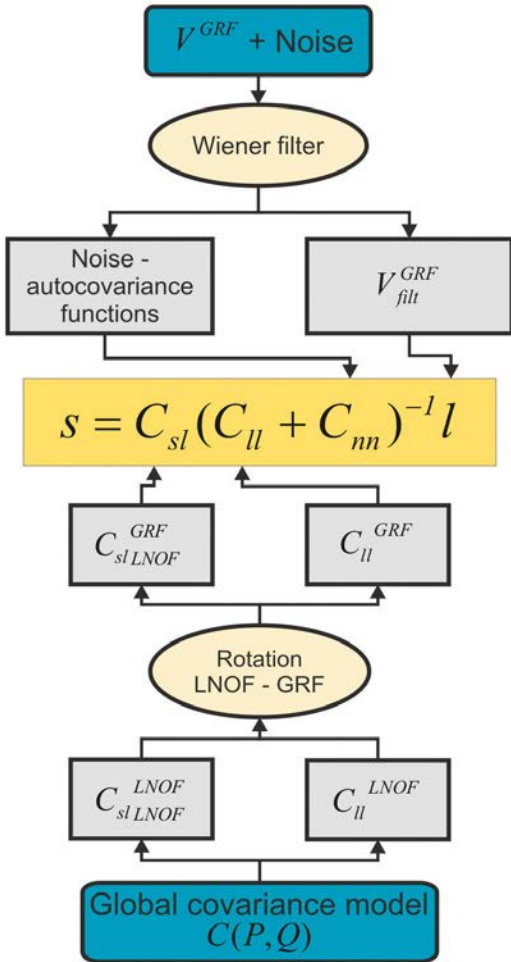


Fig. 7: Solution strategy for LSC applied in this study.

[29] gravity model up to degree and order (D/O) 49 in terms of spherical harmonics representation, and subtracted from the GOCE data beforehand. Thus it is implicitly assumed that the very long-wavelength component can be reduced by external gravity field information, e.g. derived by GRACE (which is integrated in EGM2008) very precisely in the low degrees. This assumption has been made since for this regional collocation study, the gravity data given in an area of such limited extent do not adequately represent the very long wavelength signal. Although GOCE will be superior to other data types only at higher degree and orders from around D/O 100 to maximum 250 (which corresponds to a spatial resolution of 80 km), in this case spectral information starting at D/O 50 is used. Hence, using GOCE data at these low degrees may not be an optimal

choice, but guarantees that most of the detectable gravity signal is used in this investigation.

The gravity field solutions are generated from GOCE gradient data of the main diagonal tensor components  $T_{xx}$ ,  $T_{yy}$  and  $T_{zz}$ . Following the solution strategy introduced in the preceding section, each gradient time series is first filtered in the GRF by applying the Wiener filter method. The resulting Power Spectral Densities (PSDs) reflecting the signal content per frequency are exemplarily depicted for the  $T_{zz}$  gradient in Fig. 8. The noise-free reference gradient signals (blue), which are required for Wiener filtering, are simulated from EGM2008, D/O 50 to 250, while the noise PSDs (green) are an adaptation of the ones used in [25]. The resulting spectral content of the filtered signal (magenta curve) is very close to the one of the noise free reference in the measurement bandwidth.

To reduce computational efforts, the gradient data is thinned out from a sampling rate of originally 1 second to 5 seconds, and the test area is restricted to 53°–69°E and 73°–78°N, covering the Northern island of Novaya Zemlya, which is displayed in Fig. 9, bottom.

For the derivation of the covariance matrices  $C_{sl}$  and  $C_{ll}$  degree variances of EGM2008 consistent to the spectral information content of the observations from D/O 50 to 250 are used. The noise covariance matrix  $C_{mm}$  is set up in GRF using the error covariance functions of the Wiener filtering.

The gravity field solution based on this input data configuration is shown in Fig. 9, top, in terms of gravity anomalies. Note that the preliminary removed long-wavelength gravity constituent is not restored in this plot, thus the result depicts the impact of GOCE gradient data within the measurement bandwidth of the gradiometer instrument only. The result shows a strong gravity signal over the island with maximum val-

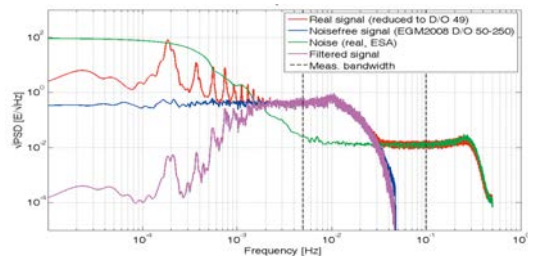


Fig. 8: PSD of GOCE  $T_{zz}$  gradients in GRF from D/O 50 to 250: real GOCE data (red), simulated from EGM2008 (blue), noise from ESA (green) and filtered (magenta).

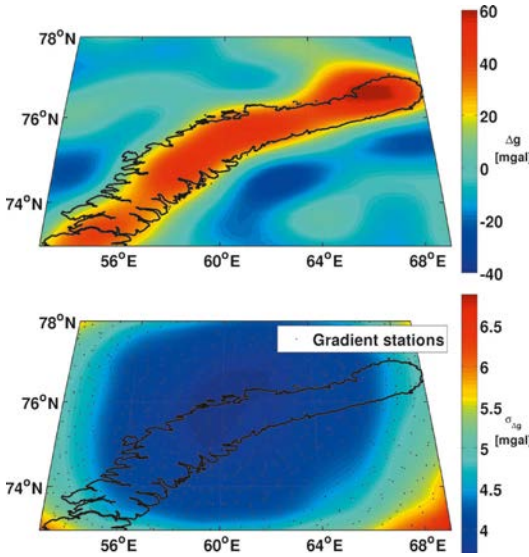


Fig. 9: top, Gravity field solution in terms of gravity anomalies (in mGal) from GOCE main diagonal gradient tensor components (November 2009) representing the spectral content from D/O 50 to 250; bottom, Corresponding standard deviation in mGal and data distribution of observations over the test area.

ues on the northern ice cap. The standard deviations (Fig. 9, bottom) are in the order of about 4 mGal, in the central region of the study area. The decreasing accuracy towards the borders of the test region can be explained with windowing effects of the LSC computation and is therefore not distressing.

4. Discussion of the results

In section 2, different model parameters of the forward modelling approach were investigated separately. Different assumptions for the bedrock structures beneath the ice body only have a negligible effect on the resulting gravity field (especially when looking at relative changes between two epochs). Even different parameter settings for the ice density model do not influence the computations (not shown in this paper), due to the shallow firn-ice transition depth in the study region. As the investigations with numerical forward modelling in section 2.3 have shown, a total ice mass loss in Novaya Zemlya of about 10 % would induce a gravity change in the order less than 3 mGal. The true ice change at the northern ice cap within the last 60 years (cf. section 2.4) has a gravity response of about 1 mGal/decade. This is by no means detectable by today’s gravity satellite missions for such small areas. For GRACE the temporally varying signals can

be resolved up to spectral degree and order 40 or 50, while higher frequency signals cannot be recovered due to the degrading signal-to-noise ratio of the mission with increasing degree [3]. Thus, only large mass variations can be detected by GRACE in e.g. Greenland, Alaska or Antarctica (cf. [27] and [28]) with a spatial resolution of several hundred kilometres.

The static regional gravity field solution with LSC is based on solely gravity gradient data from GOCE. The resulting achievable accuracy of 4 mGal (Fig. 9, bottom) is in correspondence with the accuracy of current official global GOCE HPF gravity field solutions [29]. Taking into account that the computation is only based on a very limited number of observations, this result can be regarded as very promising. However, despite GOCE is continuously (in contrast to the initial mission plans) observing gravity gradients with high precision in the spectral range between degree and order 50 and 250, this will not aid to improve the recovery of time variable signals. It has been shown in [30] and [31] that time variable signals from sources like ice mass variations are below the gradiometer error level. Recent studies conclude that only GOCE satellite-to-satellite tracking data will help to stabilize temporal GRACE solutions to some extent [32].

Finally, a coarse comparison between the gravity signal of the study area Novaya Zemlya resulting from the forward modelling approach (Fig. 10) and the computed gravity anomalies from LSC using GOCE gradients (Fig. 9, top) is performed. Beforehand, the results of numerical forward modelling had to be spatially filtered in order to allow a comparison despite the different spatial resolutions – while the high spatial resolution of the used DTDM (0.5 km posting) surpasses even the currently highest-degree model EGM2008 (maximum degree 2190, corresponding to 10 km), the LSC solution is limited to a spatial resolution of about 80 km. The filtered gravity field is slightly affected by the windowing effects of the Gaussian filter that was applied

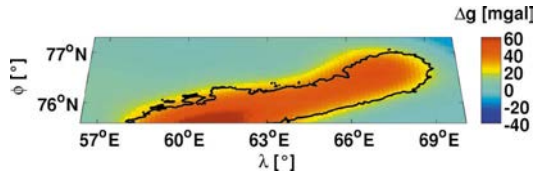


Fig. 10: Low-pass filtered gravity solution (gravity attractions  $g$  in mGal) computed by numerical forward modelling of ice (density model according to Schytt) and topographic masses down to a level of  $-600$  m (constant density of  $2.67$  g/cm<sup>3</sup>).

to adapt the resolutions of the two computed gravity fields. Nevertheless, the general structures – in form of two distinct bulges with maximum amplitude along the main elevations of the ice body – are clearly discernible in both figures.

However, interpretations have to be done with care as several aspects have to be considered. First, the local modelling of mass prisms is mainly based on relative density contrasts in the upper lithosphere. Also, the modelled area is just a finite part of the whole Earth's mass and is therefore neglecting the influence of masses lying outside and underneath this region. In contrast, the LSC solution incorporates the integral gravity field, but only in the spectral range of degree and order 50 to 250. Thus, this is only a plausibility consideration of the results of both methods.

## 5. Conclusions and Outlook

For the estimation of the gravitational effects that can be caused by changing ice masses, a numerical forward modelling approach has been implemented and tested for the island of Novaya Zemlya. The investigated glacier model incorporates the 3D-geometry and assumed density distribution of the ice body and its surrounding topography. Simulations of mass change within the modelling process enable a better understanding of the impacts of ice mass variations on the gravity field. The amplitudes of these effects on the gravity field are – as expected – very small, especially with respect to their small spatial extent. Therefore, ice mass changes of the magnitude currently observed on Novaya Zemlya will be hard to detect by multi-temporal (mainly space-borne) gravity field solutions working on lower spatial resolutions. Nevertheless, numerical forward modelling can still be a valuable tool to aid the separation of ice-related gravity signals from the integral gravity variations as observed by GRACE, where it can help in isolating leakage effects.

In the second part of this paper the novel gravity gradient data type of the GOCE mission is integrated in the LSC process for regional gravity field determination independent of the reference frame. It is shown that a Wiener filter can reduce the coloured noise from gradient data on the one hand, and on the other hand delivers an adequate stochastic model of the measurement errors in terms of covariance functions. A regional gravity field solution with LSC based on solely real GOCE gradient data achieves an accuracy level similar to that of the current offi-

cial global gravity field solutions of GOCE HPF. Currently ESA is carrying out investigations to further refine the quality of the gravity gradient data. Hence, some potential improvements for the approach presented here might be expected. In future, GOCE gravity gradients shall be combined with other (terrestrial) data sources via LSC. First studies (not shown in this paper) have already stated the favourable impact of GOCE gradients on the accuracy of combined regional gravity field solutions.

## Acknowledgments

The presented studies were part of the project Modelling Snow-Ice cover Evolution and Associated Gravitational Effects with GOCE constraints (ICEAGE) which was performed in the frame of the Austrian Space Application Programme (ASAP), Phase 5, funded by the Austrian Research Promotion Agency (FFG), project number 817106.

Without the help of our project partners and colleagues Aleksey Sharov (Joanneum Research), Prof. Roland Pail (now TU München), and Christoph Gisinger, these results would not have been achievable.

## References

- [1] *Rignot E., Thomas R.H. (2002).* Mass Balance of Polar Ice Sheets. *Science* 297, 1502, doi: 10.1126/science.1073888
- [2] *Tapley, B. D., Bettadpur S., Watkins M., Reigber C. (2004a).* The Gravity Recovery and Climate Experiment: Mission Overview and Early Results. *Geophys. Res. Lett.*, Vol. 31, L09607
- [3] *Wahr J., Molenaar M., Bryan F. (1998).* Time variability of the Earth's gravity field: Hydrological and oceanic effects and their possible detection using GRACE. *Journal of Geophysical Research*, Vol. 103, no. B12, pp 30,205-30,229
- [4] *Tapley, B. D., Bettadpur S., Ries J. C., Thompson P. F., Watkins M. M. (2004b).* GRACE measurements of Mass Variability in the Earth System. *Science*, Vol. 305, no. 5683, 503-505
- [5] *Baur O., Kuhn M., Featherstone W. E. (2009).* GRACE-derived ice-mass variations over Greenland by accounting for leakage effects. *Journal of Geophysical Research*, Vol. 114, B06407, doi:10.1029/2008JB006239
- [6] *Swenson S., Wahr J. (2003).* Estimated accuracies of regional water storage variations inferred from the Gravity Recovery and Climate Experiment (GRACE). *Water Resources Research*, Vol. 39, No. 8, 1223, doi:10.1029/2002WR001808
- [7] *Drinkwater M., Foberghagen R., Haagmans R., Muzi D., Popescu A. (2003).* GOCE: ESA's First Earth Explorer Core Mission. *Space Sciences Series of ISSI*, 18, p 419-432
- [8] *Pail R., Kührtreiber N., Wiesenhofer B., Hofmann-Wellenhof B., Of G., Steinbach O., Höggerl N., Imrek E., Ruess D., Ullrich C. (2008).* The Austrian Geoid 2007. *VGI, Jahrgang 98, Heft 1/10*
- [9] *Sharov A.I. (2005).* Studying changes of ice coasts in the European Arctic, *Geo-Marine Letters* 25, Springer,

- New York, 153–166, DOI 10.1007/s00367-004-0197-7
- [10] Hofmann-Wellenhof B., Moritz H. (2005). *Physical Geodesy*. Springer, Wien, New, York
- [11] Mader, K. (1951). Das Newtonsche Raumpotential prismatischer Körper und seine Ableitungen bis zur dritten Ordnung. Österreichische Zeitschrift für Vermessungswesen, Österreichischer Verein für Vermessungswesen. Sonderheft 11
- [12] Forsberg, R. (1984). A study of terrain reductions, density anomalies and geophysical inversion methods in gravity field modelling, Tech. Rep. 355, The Ohio State University, Columbus
- [13] Pail R., Sharov A., Rieser D., Heuberger F., Gisinger C. (2010). Modelling snow-ice cover evolution and associated gravitational effects with GOCE constraints (ICEAGE), Final Report. Technical report, FFG, Austrian Space Applications Programme
- [14] Jakobsson M., Macnab R., Mayer M., Anderson R., Edwards M., Hatzky J., Schenke H-W., Johnson P. (2008). An improved bathymetric portrayal of the Arctic Ocean: Implications for ocean modeling and geological, geophysical and oceanographic analyses, v. 35, L07602, Geophysical Research Letters, doi:10.1029/2008GL033520
- [15] Gisinger C., Heuberger F., Rieser D., Pail R., and Sharov A. (2010). Ice Mass Change versus Gravity – Local Models and GOCE's Contribution. In Living Planet Symposium Conference Proceedings, ESA
- [16] Schytt V. (1956). Summary of the glaciological work. In Report on glaciological investigations during the Norwegian-British-Swedish Antarctic Expedition, 1949-1952, Assn. Intern. Hydrologic, Vol. 4, IUGG, Rome, 236–243
- [17] Sharov A. I. (Ed., 2010). SMARAGD – Satellite Monitoring and Regional Analysis of Glacier Dynamics in the Barents-Kara Region, Joanneum Research, Printshop, Graz
- [18] Sharov A.I., Nikolskiy D. B. (2007). Semi-controlled interferometric mosaic of the largest European glacier, in Proceedings ENVISAT Symposium Montreux, 7, European Space Agency, SP-636
- [19] Rummel R., Gruber T., Koop R. (2004). High Level Processing Facility for GOCE: Products and Processing Strategy. In Proceedings 2nd International GOCE User Workshop, Frascati 2004, European Space Agency, Noordwijk, The Netherlands
- [20] Moritz H. (1980). *Advanced Physical Geodesy*. Wichmann Verlag, Karlsruhe
- [21] Tscherning C.C. (1993). Computation of covariances of derivatives of the anomalous gravity potential in a rotated reference frame. *Manuscripta Geodetica*, Vol. 18, no. 3, pp 115-123
- [22] Albertella A., Migliaccio F., Reguzzoni M., Sansò F. (2004). Wiener filters and collocation in satellite gradiometry. In International Association of Geodesy Symposia, '5th Hotine-Marussi Symposium on Mathematical Geodesy', (Ed. F. Sansò), vol. 127, Springer-Verlag, Berlin, 32-38
- [23] Papoulis A. (1984). *Signal analysis*. McGraw Hill, New York
- [24] Pail R. (2005). A parametric study on the impact of satellite attitude errors on GOCE gravity field recovery. *Journal of Geodesy*, 79, 231-241
- [25] Catastini G., Cesare S., De Sanctis S., Dumontel M., Parisch M., Sechi G. (2006). Predictions of the GOCE in-flight performance with the end-to-end system simulator. In Proc. 3rd International GOCE User Workshop, November 2006 Frascati, Italy, ESA SP-627, pp9-16
- [26] Müller J. (2003). GOCE gradients in various reference frames and their accuracies. *Advances in Geosciences*, 1, 33–38, doi:10.5194/adgeo-1-33-2003
- [27] Rieser D., Pail R. (2009). Using GOCE Gravity Gradients For A Combined Regional Gravity Field Solution With Least Squares Collocation, Poster presented at the IAG 2010, Buenos Aires
- [27] Velicogna, I., Wahr J. (2005). Greenland mass balance from GRACE. *Geophys. Res. Lett.*, 32, L18505, doi:10.1029/2005GL023955
- [28] Migliaccio F., Reguzzoni M., Sansò F. (2004). Space-wise approach to satellite gravity field determination in the presence of coloured noise. *Journal of Geodesy*, 78, 304-313
- [28] Velicogna, I., Wahr J. (2006). Measurements of time-variable gravity show mass loss in Antarctica. *Science*, 311, 1754–1756, doi:10.1126/science.1123785
- [29] Gruber T. (2011). GOCE Gravity Field and Orbit Results: The HPF Experience. Presentation at: 4th International GOCE User Workshop, 31 March – 1 April 2011, Munich, Germany
- [29] Pavlis N. K., Holmes S., Kenyon S., Factor J. (2008). An Earth Gravitational Model to Degree 2160: EGM2008, Poster presented at the 2008 General Assembly of the European Geosciences Union, Vienna
- [30] Abrikosov O., Jarecki F., Müller J., Petrovic S., Schwintzer P. (2006). The impact of temporal gravity variations on GOCE gravity field recovery. In: Flury J., Rummel R., Reigber C., Rothacher M., Boedecker G, Schreiber U (eds.), *Observation of the Earth system from space*. Springer, Heidelberg, pp 255–269
- [31] Bouman J., Rispens S., Gruber T., Koop R., Schrama E., Visser P., Tscherning C. C., Veicherts M. (2009). Preprocessing of gravity gradients at the GOCE high-level processing facility; *Journal of Geodesy*, Vol. 83, Nr. 7, pp 659-678, Springer, ISSN 0949-7714, DOI: 10.1007/s00190-008-0279-9
- [32] Pail R., Fecher T., Jäggi A., Goiginger H. (2011). Can GOCE help to improve temporal gravity field models? Presentation at: EGU General Assembly 2011, 04 -- 08 April 2011, Vienna, Austria

## Contacts

Dipl.-Ing. Florian Heuberger, Institute of Theoretical Geodesy and Satellite Geodesy, TU Graz, Steyrergasse 30/III, 8010 Graz, Austria.

E-mail: florian.heuberger@tugraz.at

Dipl.-Ing. Daniel Rieser, Institute of Theoretical Geodesy and Satellite Geodesy, TU Graz, Steyrergasse 30/III, 8010 Graz, Austria.

E-mail: daniel.rieser@tugraz.at

## GNSS/IMU integration for the precise determination of highly kinematic flight trajectories



*Fabian Hinterberger, Franz Blauensteiner, Andreas Eichhorn and Robert Weber*

### Abstract

An indispensable prerequisite for operating an airborne laserscanner for point determination on or close to the earth's surface is the knowledge about the precise spatial position and orientation of the laserscanner. These parameters of the aircraft's (respectively scanner) trajectory can be determined using a multi-sensor system which consists of a GNSS receiver and an inertial navigation system. This article focuses on the basic principles of IMU/GNSS integration and the comparison of a combination software, developed at TU Vienna, with the commercial software Waypoint. Further investigations cover the implementation and modelling of the IMU sensor errors.

**Keywords:** aircraft trajectory, GNSS, IMU, Kalman-filtering, dead reckoning

### Kurzfassung

Eine Voraussetzung für die Bestimmung von Punkten auf und nahe der Erdoberfläche unter Verwendung eines luftfahrzeuggestützten Laserscanners ist die Kenntnis der räumlichen Position und der räumlichen Orientierung des Laserscanners während des Fluges. Die Bestimmung dieser Parameter erfolgt aus Messungen eines Multisensorsystems, bestehend aus einem GNSS Empfänger und einem Trägheitsnavigationssystem. Dieser Artikel beinhaltet die Grundprinzipien der IMU/GNSS Integration sowie den Vergleich einer Integrations-Software, entwickelt an der TU Wien, mit der kommerziellen Software Waypoint. Weitere Untersuchungen befassen sich mit der Modellierung und Implementierung der systematischen Fehler der IMU.

**Schlüsselwörter:** Flugzeugtrajektorie, GNSS (Globales Navigationssatellitensystem), IMU (Inertiale Messeinheit), Kalmanfilterung, Koppelnavigation

### 1. Motivation

To measure points on or close to the earth's surface by laserscanning, it is necessary to have precise knowledge about the current position and spatial orientation of the scanner. To obtain decimetre accuracy at points on the earth's surface, the parameters of the trajectory must be determined with an accuracy of a few centimetres for the position and a few mgon for the spatial orientation.

This article summarizes the results of the diploma thesis [1], which was carried out at TU Vienna, Institute of Geodesy und Geophysics in collaboration with the Austrian laserscan data provider GeoService. It describes the basics in GNSS/IMU integration, highlights the implemented model and presents first results of a developed combination software.

In the following the design and structure of the developed Kalman-filter algorithm are presented. The filter is tested by using GNSS and IMU measurements of a 2 hours test flight, which has been carried out by GeoService. This flight

was performed by means of a helicopter. The helicopter was equipped with a Topcon GNSS receiver and a navigation grade IMU (iNAV-FJI-AIRSURV-001) which is one of the most accurate inertial systems for non-military applications. The GNSS receiver operates with a data rate of 5 Hz. The IMU comprises three coaxially arranged pendulous accelerometers, three optical gyroscopes and operates with a data rate of 1000 Hz.

The results of the test flight are compared with a reference trajectory, which is calculated with the commercial software Waypoint. In comparison to Waypoint the new algorithm is developed in an open and transparent manner. Thus extensions like modelling and estimation of systematic sensor errors can be easily implemented.

### 2. GNSS and IMU processing

There are several options for integrating GNSS and IMU data by Kalman-filtering, whereas the loosely coupled approach is very common. This means the combination is based on the individual results of GNSS and IMU processing.



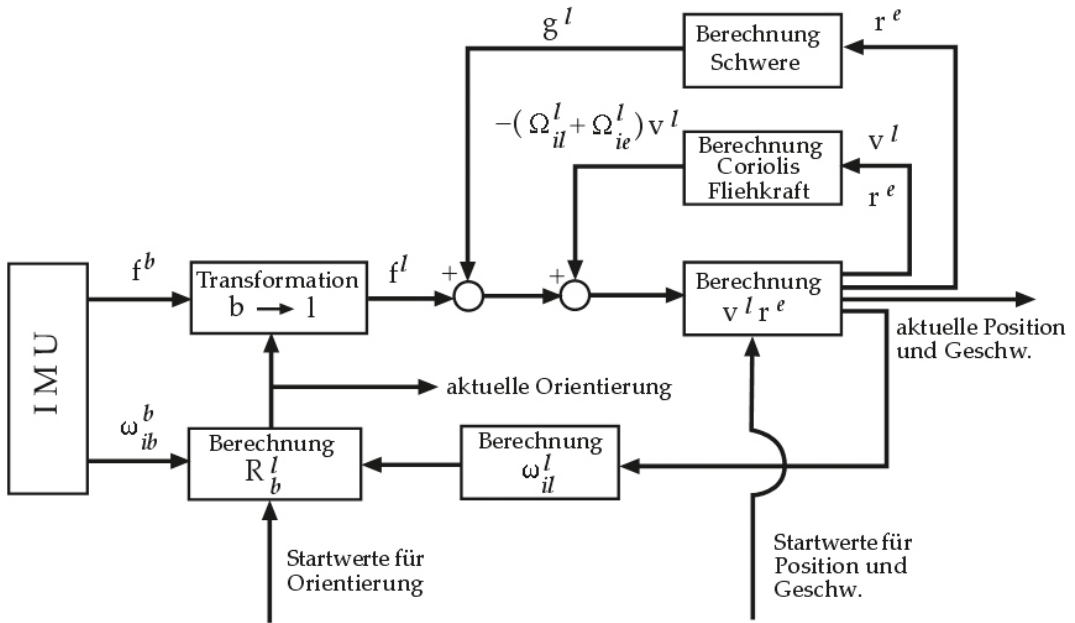


Fig. 1: Procedure for solving the navigation equations

To reach the aspired accuracy of a few centimetres from GNSS processing, relative kinematic positioning is used. For IMU processing the relation between the measured quantities  $f^b$  (accelerations) and  $\omega_{ib}^b$  (angular velocities), accelerations and angular velocities, and desired quantities has to be built. The desired quantities are the position  $r^e$ , velocity  $v^l$  and spatial orientation  $R_b^l$  of the sensor at each epoch during the flight. The superscript  $e$  denotes the earth-fixed coordinate frame (e.g. ITRF), in which the positions are computed.  $l$  labels the local level frame, in which the obtained velocities are orientated. The spatial orientation is described by the attitude matrix  $R_b^l$ , which represents the rotation between body frame and local level frame. The relation is represented by a set of differential equations (1.a-c), which are called 'navigation equations' [2].

$$\dot{r}^e = D^{-1}v^l \tag{1a}$$

$$\dot{v}^l = \dot{R}_b^l f^b - (\Omega_{il}^l - \Omega_{ie}^l)v^l + g^l \tag{1b}$$

$$\dot{R}_b^l = R_b^l (\Omega_{ib}^b - \Omega_{il}^l) \tag{1c}$$

The basis for the derivation of the navigation equations is Newton's Law, which enables the description of a moving object in inertial space. The matrix  $D$  in (1a) performs the transformation between the local frame and the earth fixed frame. For navigation applications on or close to the earth's surface, the measured quantities are superimposed by earth gravity. To obtain the accelerations, which are responsible for the transla-

tion of the helicopter, the measured accelerations need to be corrected by the gravity vector  $g^l$  (eq. 1b). The second term of (1b) describes the Coriolis acceleration, which occurs due to the motion of the helicopter relative to the rotating earth.  $\Omega_{il}^l$  is the skew-symmetric form of  $\omega_{il}^l$  which is the rotation rate of the local level frame with respect to the inertial frame and  $\Omega_{ie}^l$  is the skew-symmetric form of  $\omega_{ie}^l$  which is the rotation rate of the earth-fixed frame with respect to the inertial frame. Equation (1c) combines the attitude matrix  $R_b^l$  with the gyro measurements  $\Omega_{ib}^b$ . As we only need the angular velocities between the local and the body frame, the gyro measurements are compensated by  $\Omega_{ib}^b$  (thus, the angular rate between the local level frame with respect to the inertial frame, represented in the body frame). The position, velocity and orientation can be obtained by numerical integration of the measured IMU quantities  $f^b$  and  $\omega_{ib}^b$ . This is known as *free-inertial navigation* [2]. According to [3], the procedure is shown in Figure 1.

### GNSS / IMU integration

For the integration of GNSS and IMU data a Kalman-filter is used. The Kalman-filtering was developed in the late 50's by Rudolf Kalman. It is especially suitable for the estimation of non-stationary random processes [4]. Besides the measurements the Kalman-filter uses additional information about the time dependent behaviour of the system. This behaviour may be mod-

elled by differential equations. The fundamental relations for many time dependent processes are shown in eq. (2).

$$\dot{\mathbf{x}}(t) = \mathbf{F}(t)\mathbf{x}(t) + \mathbf{C}(t)\boldsymbol{\omega}(t) \quad (2a)$$

$$\mathbf{l}(t) = \mathbf{A}(t)\mathbf{x}(t) + \mathbf{v}(t) \quad (2b)$$

In the system equations (2a)  $\mathbf{x}(t)$  is the time dependent state vector.  $\mathbf{F}(t)$  is called 'system matrix', which describes the time dependent behaviour. The system error vector  $\boldsymbol{\omega}(t)$  describes the uncertainties of the model referring to reality.  $\mathbf{C}(t)$  is the corresponding noise matrix. Using the design matrix  $\mathbf{A}(t)$ , the measurement equations (2b) combine the state vector with the measurement vector  $\mathbf{l}(t)$ , whereas  $\mathbf{v}(t)$  denotes the measurement noise. The quantities  $\boldsymbol{\omega}(t)$  and  $\mathbf{v}(t)$  describe Gaussian distributed, white noise processes [2]. The state vector has the following form.

$$\mathbf{x}(t) = \underbrace{(\delta\varphi \ \delta\lambda \ \delta h)}_{\delta\mathbf{r}^e} \underbrace{(\delta v_n \ \delta v_e \ \delta v_d)}_{\delta\mathbf{v}^l} \underbrace{(\varepsilon_n \ \varepsilon_e \ \varepsilon_d)}_{\boldsymbol{\varepsilon}} \quad (3)$$

The state vector (3) is typical for the loose coupling strategy, where  $\delta\varphi$ ,  $\delta\lambda$  and  $\delta h$  are the deviations between the IMU's computed and the true position. Furthermore,  $\delta v_n$ ,  $\delta v_e$  and  $\delta v_d$  are the deviations in velocity, orientated in north, east and down direction,  $\varepsilon_n$ ,  $\varepsilon_e$  and  $\varepsilon_d$  are small rotation angles, which describe the deviations in the attitude matrix  $\mathbf{R}_b^l$ .

The system equations of the Kalman-filter are derived from (1) by linearisation using either a Taylor series expansion or perturbation analysis. According to [5], the results of the perturbation analysis are shown in (4.a-c).

$$\delta\dot{\mathbf{r}}^e = \mathbf{F}_{rr}\delta\mathbf{r}^e + \mathbf{F}_{rv}\delta\mathbf{v}^l \quad (4a)$$

$$\delta\dot{\mathbf{v}}^l = \mathbf{F}_{vr}\delta\mathbf{r}^e + \mathbf{F}_{vv}\delta\mathbf{v}^l + \boldsymbol{\varepsilon}^l \times \mathbf{f}^l + \mathbf{R}_b^l\delta\mathbf{f}^b + \delta\mathbf{g}^l \quad (4b)$$

$$\dot{\boldsymbol{\varepsilon}}^l = \mathbf{F}_{\varepsilon r}\delta\mathbf{r}^e + \mathbf{F}_{\varepsilon v}\delta\mathbf{v}^l - \boldsymbol{\omega}_{il}^l \times \boldsymbol{\varepsilon}^l - \mathbf{R}_b^l\delta\boldsymbol{\omega}^b \quad (4c)$$

$\mathbf{F}_{ij}$  are submatrices of the system matrix  $\mathbf{F}$ . The elements of these matrices can be deduced by partial derivation of the Navigation equations with respect to the desired quantities of the flight trajectory. The quantities  $\delta\mathbf{f}^b$  and  $\delta\boldsymbol{\omega}^b$  describe the errors of the accelerometer and gyroscope measurements. In the first realisation of the combination tool those errors were not taken into account. Uncertainties in the gravity vector  $\mathbf{g}^l$  are represented by  $\delta\mathbf{g}^l$ . This quantity is required in case that the deflection of vertical is not explicitly considered. As a consequence, systematic errors are treated as uncertainties.

In Figure 2 the differences of the combined GNSS/IMU trajectory to a reference trajectory are shown. The reference trajectory was computed with the commercial software Waypoint. This software also uses a loose coupling strategy for Kalman-filtering but additionally estimates the systematic IMU errors. These errors can be specified as three accelerometer biases and three gyro drifts (see [6]). In Figure 2 the deviations in latitude, longitude and height are plotted over time. The test flight includes rest periods of approximately 10 minutes at the beginning and at the end of the flight. Those periods where used for zero updates.

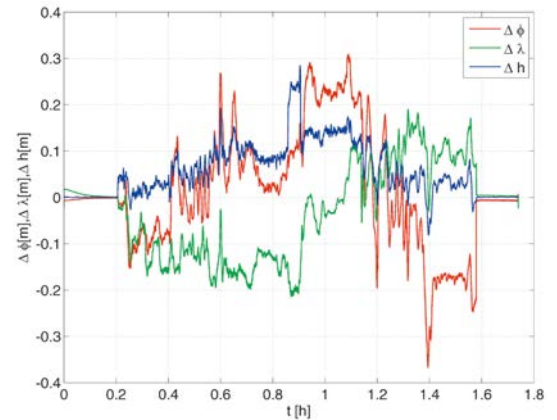


Fig. 2: Deviations between new Kalman-filter and Waypoint trajectory

The deviations between the new filter and the Waypoint solution are rather small – within a range of a few decimetres only. The main reason for the remaining residuals is that the systematic IMU errors are still neglected in the new Kalman-filter. Consequently, the further improvement to the 'cum-range' requires the implementation of realistic IMU error models.

Therefore the residual sensor errors are modelled as Gauß-Markov process of first order, which is defined by the following first-order differential equation:

$$\dot{b} = \beta b + \sqrt{2\beta\sigma_b^2} \quad (5)$$

where  $\beta$  is the reciprocal of the process correlation time and  $\sigma$  is the sensor measurement standard deviation. The new extended state vector has the following form:

$$\mathbf{x}(t) = \underbrace{(\delta\varphi \ \delta\lambda \ \delta h)}_{\delta\mathbf{r}^e} \underbrace{(\delta v_n \ \delta v_e \ \delta v_d)}_{\delta\mathbf{v}^l} \underbrace{(\varepsilon_n \ \varepsilon_e \ \varepsilon_d)}_{\boldsymbol{\varepsilon}} \underbrace{(fb_x \ fb_y \ fb_z)}_{\delta\mathbf{f}^b} \underbrace{(\omega d_x \ \omega d_y \ \omega d_z)}_{\delta\boldsymbol{\omega}^b} \quad (6)$$

Where  $fb_x$ ,  $fb_y$  and  $fb_z$  denote the residual bias errors of the accelerometers and  $\omega d_x$ ,  $\omega d_y$ ,  $\omega d_z$  the residual gyro drift errors. Furthermore the terms  $+R_b^l \delta f^b$  in equation (4b) and  $-R_b^l \delta \omega^b$  in (4c) are now taken into account. The estimation of the Gauß-Markov parameters of each accelerometer and gyroscope and further analysis of the sensors are described in [7]. Representative values for the parameters for the accelerometers are  $\beta = 5.3986 \cdot 10^{-4}$  [1/s],  $\sigma_b^2 = 3.82 \cdot 10^{-10}$  [m<sup>2</sup>/s<sup>4</sup>] and for the gyros  $\beta = 3.494 \cdot 10^{-4}$  [1/s],  $\sigma_b^2 = 8.56 \cdot 10^{-18}$  [rad<sup>2</sup>/s<sup>2</sup>].

One important question is how modelling the sensor errors, affects the results of the new Kalman-filter. In Figure 3 the comparison between the new extended Kalman-filter and the Waypoint trajectory is shown.

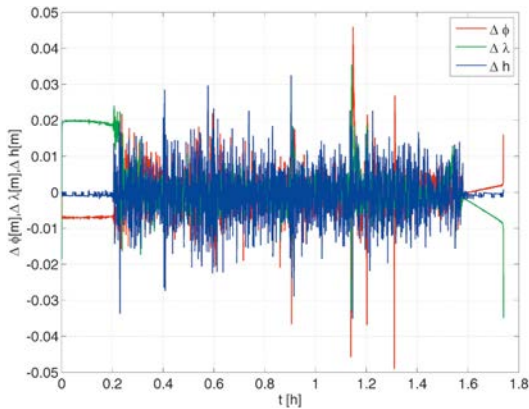


Fig. 3: Deviations between new extended Kalman-filter and Waypoint trajectory

As expected the deviations between the two trajectories decrease. Now the deviations are within a range of a few centimetres. This result shows very clear, that the consideration of the systematic IMU errors is necessary when cm accuracy must be obtained.

### 3. Conclusions and outlook

A first Kalman-filter approach for the integration of GNSS an IMU data has been established in an open and transparent form. In comparison with the results obtained by the commercial Waypoint solution it can be noticed that Waypoint still shows a little better performance than our new Kalman-Filter approach. Nevertheless, the new algorithm and the Waypoint solution already

match within a range of a few centimetres. This is a very promising basis for future investigations, which are already carried within the Project: "Integrierte bordautonome und bodengestützte Georeferenzierung für luftgestützte Multisensorsysteme mit cm-Genauigkeit" which was approved and funded by FFG (Austrian Research Promotion Agency) in December 2009.

### References

- [1] Blauensteiner, F. (2009). *GPS/IMU Integration für die präzise Bestimmung von hoch-kinematischen Flugtrajektorien*, Diploma thesis, Vienna University of Technology, Institute of Geodesy and Geophysics.
- [2] Jekeli, C. (2001). *Inertial Navigation Systems with Geodetic Applications*, Berlin New York: Walter de Gruyter.
- [3] Legat, K. (2005). *Untersuchungen zur GPS/INS-Integration*, Österreichische Zeitschrift für Vermessung und Geoinformation, Heft 2 / 2005, 72–82.
- [4] Schrick, K.-W. (1977). *Anwendungen der Kalman-Filter-Technik*, R. Oldenbourg, München/Wien
- [5] Chiang, K.-W. (2004). *INS/GPS Integration Using Neural Networks for Land Vehicular Navigation*, Doctoral thesis, University of Calgary. Department of Geomatics Engineering.
- [6] *Inertial Explorer User Manual (2006)*. NovAtel Inc.
- [7] Blank, D. (2010). *Statische und kinematische Untersuchung eines Inertialmesssystems zur hochgenauen Ortung eines Hubschraubers*, Diploma thesis, Darmstadt University of Technology, Institute of Geodesy, Department Geodetic Measurements Systems and Sensors.

### Contacts

Dipl.-Ing. Fabian Hinterberger, Projektassistent: TU Wien, Institut für Geodäsie und Geophysik, Forschungsgruppe Höhere Geodäsie, Gußhausstraße 27-29, 1040 Wien, Austria.

E-mail: fabian.hinterberger@tuwien.ac.at

Dipl.-Ing. Franz Blauensteiner, Projektassistent: TU Wien, Institut für Photogrammetrie und Fernerkundung, Gußhausstraße 27-29, 1040 Wien, Austria.

E-mail: franz.blauensteiner@tuwien.ac.at

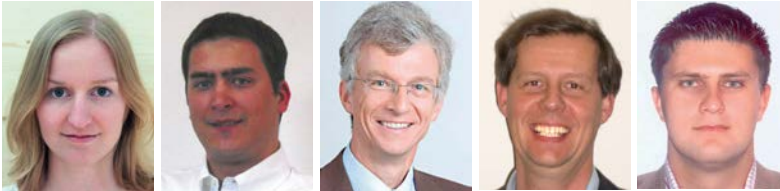
Prof. Dr.-Ing. Andreas Eichhorn: TU Darmstadt, Geodetic Institute, Dept. Geodetic Measurement Systems and Sensors, Petersenstr. 13, 64287 Darmstadt, Germany.

E-mail: eichhorn@geod.tu-darmstadt.de

a.o. Prof. Dipl.-Ing. Dr. Robert Weber: TU Wien, Institut für Geodäsie und Geophysik, Forschungsgruppe Höhere Geodäsie, Gußhausstraße 27-29, 1040 Wien, Austria.

E-mail: robert.weber@tuwien.ac.at

## The development of enhanced algorithms for rapid precise point positioning



*Katrin Huber, Philipp Berglez, Bernhard Hofmann-Wellenhof, Robert Weber and Markus Troger*

### Abstract

Within the last decade, Precise Point Positioning (PPP) has been discussed by GNSS (Global Navigation Satellite System) experts and research groups all over the world. PPP uses code or phase observations on zero-difference level in combination with precise orbits and clock corrections to achieve highly accurate point coordinates. PPP in comparison to Differential GPS (DGPS) and Real-Time Kinematic (RTK) based techniques has no need for nearby reference stations, since the corrections used for PPP are globally valid. Still, PPP is suffering from long convergence times, which makes it rarely used for real-time applications.

Therefore, the project RA-PPP (Rapid Precise Point Positioning) was started in 2009 to conduct detailed investigations on new algorithms for PPP. Several techniques to reduce the convergence time and to increase the accuracies were developed and finally implemented into a PPP client for evaluation purposes. This paper will present the investigations and results of the project, as well as the developed PPP client. Finally, a first glance on a PPP real-time implementation is provided.

**Keywords:** GNSS, Precise Point Positioning, convergence time, software module

### Kurzfassung

Seit einigen Jahren beschäftigt sich eine Vielzahl von GNSS (Globales Navigations satellitensystem) Experten und Forschungsgruppen mit dem Thema Precise Point Positioning (PPP). Diese Positionierungstechnik verwendet undifferenzierte Phasen- und Codebeobachtungen in Kombination mit präzisen Orbits und Uhrkorrekturen, um hochgenaue Positionslösungen zu erhalten. Dabei benötigt PPP im Vergleich zu differentiellen und relativen Positionierungstechniken keine Referenzstation, da global gültige Korrekturdaten von diversen Organisationen angeboten werden. Jedoch wird PPP derzeit aufgrund relativ langer Konvergenzzeiten noch selten für Echtzeitanwendungen eingesetzt.

Aus diesem Grund wurde 2009 ein Projekt namens RA-PPP (Rapid Precise Point Positioning) gestartet, dessen Hauptaugenmerk auf der Erforschung und Evaluierung neuer Algorithmen und Methoden für PPP lag. Einige Ansätze zur Verringerung der Konvergenzzeit als auch zur Verbesserung der Positionsgenauigkeit wurden untersucht und entwickelt, um schließlich im Rahmen eines PPP Software Clients evaluiert zu werden. Dieser Artikel präsentiert einige Aspekte dieser Projektarbeit sowie den Aufbau und die Ergebnisse der entwickelten Software. Am Ende des Papers wird ein Ausblick auf eine derzeit laufende Echtzeit-Implementierung gegeben.

**Schlüsselwörter:** GNSS, Precise Point Positioning, Konvergenzzeit, Software Modul

## 1. Fundamentals

### 1.1 The principle of PPP

Compared to the lifetime of Global Navigation Satellite Systems (GNSS), Precise Point Positioning (PPP) is a relatively new positioning technique aiming at high accuracies by processing data of only one receiver. While the concept of PPP was first mentioned in the 1970's, the theoretical foundation of PPP has not been published until 1997. At that time, the Jet Propulsion Laboratory (JPL) presented its first investigations on positioning within a few cm level using dual-frequency data from single GPS receivers in post-processing [1]. Since then PPP has become a well-known technique to process data of isolated GPS receivers.

In contrast to the Single Point Positioning (SPP) technique, for PPP code and phase measurements are supported by precise orbits and precise clock corrections to compute precise positions on zero-difference level. In the case of dual-frequency observations, an ionosphere-free linear combination is used to remove influences of the ionosphere. Single-frequency users need additional information on the ionosphere, since neglecting its influence could result in errors in the range of some meters. Therefore, ionospheric maps as well as precise orbits and clocks are provided by organizations like the IGS (International GNSS Service), which is a voluntary federation of more than 200 agencies worldwide pooling re-

sources and permanent GPS (Global Positioning System) and GLONASS (Globalnaja Nawigazionnaja Sputnikowaja Sistema) station data to generate precise GPS and GLONASS products. IGS products comprise GPS ephemerides, satellite and station clock corrections, earth rotation parameters, and atmospheric parameters. Detailed information on IGS products and services can be found on the IGS website [2].

### 1.2 Mathematical Model

Figure 1 visualizes the main error contributions to undifferenced GNSS observables relevant for PPP processing.

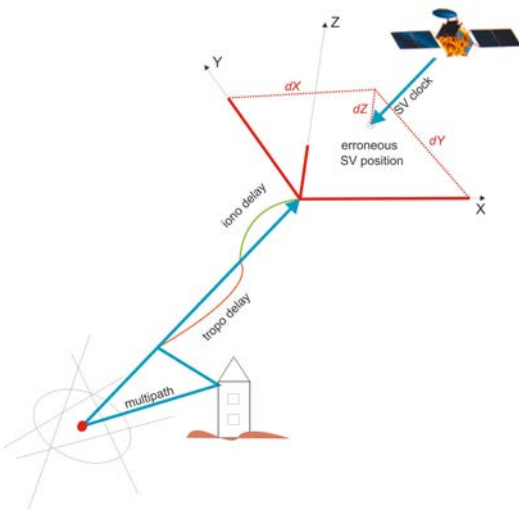


Fig. 1: Overview of the main GPS errors sources

After virtually eliminating satellite clock and orbit errors by using precise orbits and clock products, the standard mathematical model underlying PPP is defined by the ionosphere-free combination of code pseudoranges  $R_i$  (1) and phase measurements  $\Phi_i$  (2) according to [3].

$$\frac{R_1 f_1^2}{f_1^2 - f_2^2} - \frac{R_2 f_2^2}{f_1^2 - f_2^2} = \rho + cdt_r + \Delta_{trp} \tag{1}$$

$$\begin{aligned} \frac{\lambda_1 \Phi_1 f_1^2}{f_1^2 - f_2^2} - \frac{\lambda_2 \Phi_2 f_2^2}{f_1^2 - f_2^2} &= \\ &= \rho + cdt_r + \Delta_{trp} + \frac{\lambda_1 N_1 f_1^2}{f_1^2 - f_2^2} - \frac{\lambda_2 N_2 f_2^2}{f_1^2 - f_2^2} \end{aligned} \tag{2}$$

The term  $c$  stands for the speed of light,  $f_i$  is the frequency on carrier  $i$  and  $\lambda_i$  is the respective wavelength. The unknown parameters to be determined are the point position contained in  $\rho$ , the receiver clock error denoted by  $dt_r$ , the

tropospheric delay  $\Delta_{trp}$ , and a phase bias term including the ambiguities  $N$  and calibration biases. To solve the equations for these parameters, several strategies are possible, relying on least-squares adjustment or Kalman filtering. The receiver clock solution contains further error terms like noise and multipath, which cannot be accessed individually. The determined geocentric coordinates are directly linked to the reference frame of the precise orbits.

It can be further distinguished between static PPP where the coordinates are assumed to be stable over the whole observation period and kinematic PPP where the coordinates are estimated every epoch. Today's PPP systems can provide accuracies up to centimeter level after long observation periods with static dual-frequency approaches. Decimeter accuracy, which is sufficient for many applications, is achieved after an initialization time of some 15 to 30 minutes. These accuracies mainly depend on the quality of the orbit and the clock data. Orbit predictions by the IGS, being available within real-time, are reported to have dm accuracy within the first hours of prediction. Further information on IGS products can be found in [4].

### 1.3 Constraints and Limitations

On the one hand, PPP can be considered as a rather cost-efficient technique compared to common techniques like RTK or DGPS, since it is based on observations of single GNSS receivers. Due to globally valid correction data being freely provided by analysis centers, there is no need for simultaneous observations of a nearby reference station and, thus, there is no restriction in operational range.

On the other hand, PPP is a zero-difference technique being influenced by errors cancelling in double-difference approaches. Examples of effects degrading PPP accuracy are the quality of orbit and clock products, the tie to the appropriate reference frame, the noise amplification of the ionosphere-free combination used and the inability to fix integer phase ambiguities due to non-integer calibration phase biases that vanish in difference-mode. Furthermore, the quality of single-frequency PPP strongly depends on the quality of information on the ionospheric activity to account for the signal delay within this dispersive part of the atmosphere. Due to long convergence times and the limited quality of real-time PPP products, the technique is rarely used for real-time positioning by now.

## 2. Project work

As already stated, there is still a need for further developments on the PPP technique and its algorithms. Therefore, a research project called 'Innovating Algorithms for Rapid Precise Point Positioning' (RA-PPP) was started in 2009 concentrating on the development and improvement of PPP algorithms and techniques to reduce convergence times and to increase position accuracy. The Graz University of Technology, Institute of Navigation (lead), the Vienna University of Technology, Institute of Geodesy and Geophysics, as well as the companies TeleConsult Austria GmbH and Wien-Energie Stromnetz GmbH contributed to this research which has been successfully completed in 2010.

### 2.1 Aims and goals

RA-PPP stands for the need of faster and more accurate algorithms for PPP and, therefore, comprises the refinement of this technique towards real-time capability. Thus, in a first step the strengths and deficiencies of currently used PPP processing algorithms and products were identified. Based on this pre-information, the following four approaches were considered to be the most promising enhancements for the PPP technique:

- The derivation of improved Total Electronic Content (TEC) models for single-frequency users,
- the use of so called 'regional clocks', which will be explained later,
- the use of new ionosphere-free linear combinations with reduced phase noise, and
- the simulation to solve for ambiguities under special conditions.

To establish a basis for the evaluation of the algorithms, a PPP client was developed enabling the processing of single- and dual-frequency measurements. The client's output parameters consist of positions and quality parameters for static and kinematic users. Finally, a test environment was set up to evaluate the user module and the algorithms' performance concerning convergence time, accuracy, and availability. The relevant concepts are shortly presented.

### 2.2 Concepts

Derivation of improved TEC models for single-frequency users

If only single-frequency observations are available, the user needs additional information on ionospheric refraction, since the ionospheric influence cannot be eliminated as in the case

of dual-frequency measurements. Hence, the derivation of accurate TEC models is required to achieve enhanced position accuracy for single-frequency PPP. In the context of the RA-PPP project, various TEC models were evaluated. The global models are based on high resolution spherical harmonics while the local models are obtained by Taylor series expansion of the electron content from local reference station networks. The spherical harmonics are of degree and order 15 to 30 resulting in a wavelength > 1500 km. This is still too sparse to cover high resolution features of the ionosphere but allows for catching a time varying scale factor for extended regions. The local models based on Taylor series expansion are able to catch smaller features of the ionospheric delay such as ionospheric disturbances, but are representative for small areas only. A detailed description of global and local ionospheric modeling can be found in [5].

### 'Regional clocks'

The 'regional clocks' (also denoted as 'pseudo clocks') concept was first introduced by Leandro [6], and provides a possibility to add corrections accounting for regional effects like troposphere to clock corrections to improve the convergence time of a PPP solution.

Assuming at least two successfully tracked signals at different carrier frequencies, we start with the ionosphere-free linear combination  $\Phi_{if}$ . After linearization and a slight reformulation of formula (2),

$$\begin{aligned} \Phi_{if} - \rho^0 - \Delta_{trp}^0 - \lambda_{if} N_{if}^0 &= \\ &= c(dt_s - dt_r) + \delta G + \delta \Delta_{trp} + \lambda_{if} \delta N_{if} + m + n \end{aligned} \quad (3)$$

is obtained where, on the left-hand side of the equation, the superscript <sup>0</sup> indicates approximate values for geometric effects like orbits and tropospheric delay as well as an initial bias parameter  $N$  per individual satellite. On the right-hand side we solve for the satellite clock  $dt_s$  with respect to the receiver clock  $dt_r$ . Residual effects are the orbit errors  $\delta G$ , the remaining tropospheric delay  $\delta \Delta_{trp}$  and a residual bias parameter  $\delta N_{if}$  as well as the environmental multipath  $m$  and the noise  $n$ . Since the only parameters to solve for are the clocks, all further effects on the right hand side map onto these parameters. This procedure produces a kind of virtual clock differences covering regional effects and being clearly correlated with clocks at nearby stations (see Figure 2). Therefore, we call these clock differences 'regional clocks', which are different from clock solutions provided for instance by

the IGS. When introducing the ‘regional clocks’ via a PPP solution to process the coordinates of a nearby isolated station (rover station), we remove the impact of the remaining master station clock which will be absorbed by the rover station clock. The satellite-specific bias at the master station will be absorbed as well by the ambiguity parameter at the rover station. This concept differs from DGPS techniques concerning the calculation model, since for DGPS differences between simultaneous observations at master station and rover are calculated and passed to the user, while ‘regional clock’ corrections are manipulated clock differences calculated independently at the master station.

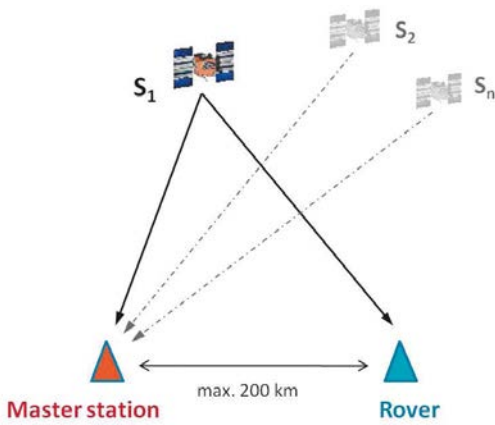


Fig. 2: Spatial correlation of atmospheric and orbit effects

The convergence time will be reduced in any case down to 30 minutes or less which demonstrates the strength of this procedure. The accuracy reaches dm level which is quite comparable with state-of-the-art PPP procedures. Nevertheless, this approach cannot compete in fixing times with double-difference approaches; however, the correlation holds over hundreds of kilometers distance to the master station and the clock differences can easily be obtained, even in real-time.

This approach was evaluated by feeding the PPP algorithm with ‘regional satellite clocks’ recovered from a master station with observation data of well-known rover stations in the vicinity (50 km up to 150 km distance) of the master station. On the one hand, the ‘regional clocks’ approach was tested with the Bernese software using a least-squares adjustment, on the other hand, the same tests were performed with the RA-PPP client based on a Kalman filter (cf. [7]).

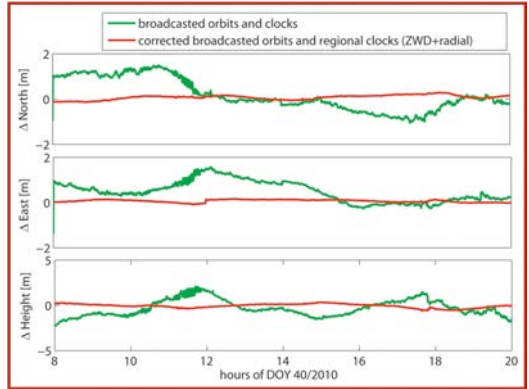


Fig. 3: Comparison of pseudorange PPP solutions with broadcast orbits and clocks and broadcast orbits and ‘regional clocks’

Figure 3 shows the effect of ‘regional clock corrections’ with a tropospheric zenith wet delay correction calculated at a nearby reference station and orbit corrections in the radial component. It is shown, that the PPP solution can be dramatically improved with ‘regional clocks’ if only broadcast ephemerides are available to the user. These types of corrections can be applied especially in situations, where the bandwidth for data communication is low, or if communication is too expensive to forward standard RTCM range and phase corrections. The validity span of ‘regional clock corrections’ is quite long due to medium term variation of orbital errors and ZWD. Regional Clock corrections might therefore be interpolated and extrapolated (in case of stable satellite clocks). Further information on the ‘regional clocks’ concept can be found in [8].

**Use of new ionosphere-free linear combinations with reduced phase noise**

It is well known that the use of the ionosphere-free combination (equations (2) and (3)) for dual-frequency observations significantly increases the noise of code and phase observations compared to isolated signals. Due to new carrier bands and signals being available in the near future, advantages for the data processing are expected. It is obvious that the use of new Galileo signals or the new civil signal at GPS L5 will allow for the formation of additional linear combinations with phase and code based on three to five individual frequencies. This will enable a better ambiguity resolution as well as reduced noise amplification within the combination of different signals. Unfortunately, the Galileo system will not become fully operational until 2015 (see [9]). Concerning GPS L5, the number of satellites in orbit, emitting the L5 signal, is insufficient to evaluate the noise

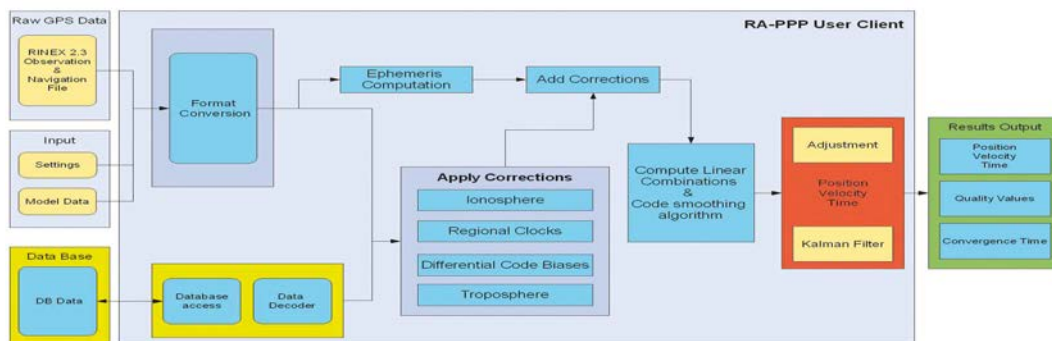


Fig. 4: Architectural Design of the RA-PPP user client

behavior of the new linear combinations with real data. Further considerations concerning new linear combinations can be found in [10] and [11].

### Simulation to solve for ambiguities under special conditions

The probably most effective approach to improve convergence time of PPP solutions is to determine the initial satellite and station bias parameters and to subsequently fix the remaining integer ambiguities as described in [12]. So far, this approach was investigated only from a theoretical point of view, but not yet implemented in the PPP user-client.

### 3. RA-PPP client

Based on the previously described concepts a PPP user client for post-processing was developed by TeleConsult Austria GmbH. This client obtains the necessary correction data from a data base on a correction data server which contains not only publicly available corrections (precise ephemerides, global ionospheric maps, differential code biases) from providers like IGS or CODE (Center for Orbit Determination in Europe) but also local ionospheric maps and 'regional clocks' calculated in a correction data computation module.

The actual position computation is carried out in the PPP client. RINEX files are used as raw data input source for the client. The key element of the RA-PPP user client is the processing module which includes the previously designed algorithms. The module is capable of calculating the user's positions as well as quality parameters by means of Kalman filtering. An overview of the processing module is given in Figure 4.

The RA-PPP client is implemented in C/C++, since a real-time capability is envisaged for the

future. The processing module consists of two core modules – the correction computation and the PVT (Position, Velocity and Time) module. Before the actual computation occurs, all incoming data are converted into an internal format and plausibility checks are performed. The correction module accesses the data server and requests the necessary correction parameters in dependence on the user input. The corrections to each observation are calculated. Then the corrected observations together with the computed satellite positions are forwarded to the PVT module. Within this module the actual position calculation is carried out. For evaluation purposes, either a least-squares adjustment or a Kalman filter algorithm can be used. In case of pseudorange and phase observations, a time-dependent code smoothing by means of phase observations, in order to reduce the measurement noise, is applied. Along with the processed position of the rover, also accuracy and quality parameters as well as the convergence time are provided to the user.

Apart from general tests on the user client, also the performance of the algorithms was investigated. Two different groups of data sets were used during the tests. The first group was generated by a GNSS constellation and performance simulator (cf. [13]) in order to evaluate the positioning algorithm itself. The second group represents real data recorded by a Javad Sigma receiver, capable of receiving GPS L1, L2, and L5 signals. The receiver, as well as the GNSS constellation simulator, provided the raw observation data (pseudoranges and phases, as well as ephemeris data) in the RINEX format.

As mentioned before, no linear combinations with the new GPS L5 carrier could be tested within the RA-PPP client due to a lack of L5 ca-



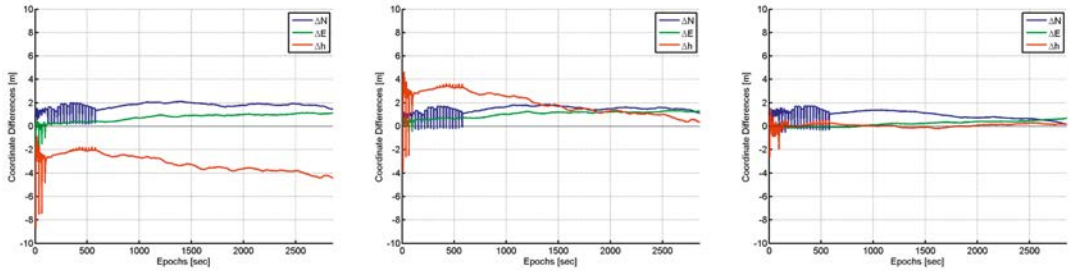


Fig. 5a-c: UTM coordinate differences for single-frequency solution (a) with code-smoothing, Klobuchar ionosphere model and Hopfield troposphere model applied (b) with code-smoothing, global ionosphere model and Hopfield troposphere model applied (c) with code-smoothing, precise ephemeris and ‘regional clock’ data

pable satellites. Nevertheless, tests in December 2009, January, March and July 2010 showed a maximum number of five L2C observations (new civil code on L2) out of up to twelve visible satellites. This is sufficient for position computation, but tests would have been more significant with a higher number of L2C measurements. For a critical investigation of the performance of the linear combinations the P2 (precise code on L2) measurements were used instead. Comparing P2 with L2C showed the same performance, when all satellites transmitted dual-frequency data.

All real data were recorded at the roof of the Geodesy building in Graz on geodetic pillars with known coordinates in WGS84. The algorithms’ performance was evaluated by comparing the calculated coordinates with the reference coordinates of the pillar.

Figure 5a shows the coordinate differences with respect to the reference coordinates when applying the broadcast ionospheric model (Klobuchar) and a Hopfield tropospheric model to the phase-smoothed code observations. The blunders, which are visible during the first 500 seconds, mainly result from rapid changing satellite geometry. This causes the smoothing algorithm for the specific satellites to restart. The height offset is caused by the coarse ionospheric model, which obviously overcompensates for the ionospheric delay during calm phases.

As an alternative to the broadcast ionosphere model, the user can choose either a global or a local ionospheric map model. Figure 5b shows the coordinate differences with respect to the reference coordinates when using code-smoothed single-frequency data with a Hopfield model for troposphere, but now, with a global ionosphere map model. It is obvious that the calculated model parameters fit much better than the broadcast model before.

		Mean [m]	Median [m]	Std [m]
Figure 5a	dN	1.769	1.827	0.293
	dE	0.749	0.905	0.339
	dh	-3.165	-3.302	0.736
Figure 5b	dN	1.479	1.532	0.313
	dE	1.014	1.166	0.299
	dh	1.936	1.781	0.950
Figure 5c	dN	1.000	1.078	0.393
	dE	0.213	0.242	0.246
	dh	0.070	0.096	0.187

Tab. 1: Statistical mean, median and standard deviation of time series in Figure 5a-c

One main goal of RA-PPP was the development and implementation of so called ‘regional clocks’. The use of ‘regional clocks’ within the user client is very similar to the use of precise clocks. Again, the clock biases are given in a certain time interval and a cubic interpolation is used to obtain the corrections for a specific time. Due to fact that regional effects are taken into account, a benefit within the obtained coordinates is visible. Figure 5c shows the coordinate differences with respect to the reference coordinates when using precise orbits, precise clock corrections and on top regional effects converted to further clock information. As expected the statistical values of the presented time series (see Table 1) reflect the benefit of using ‘regional clocks’ especially in the height component. All further results of the RA-PPP client can be found in [7].

Within the RA-PPP project, a PPP user client was successfully developed. The client is able to use RINEX files as input and has the ability to automatically connect to a correction data base, which provides several models for correcting different error sources. The user client is able to use different models for compensating atmospheric

effects (e.g. Klobuchar model, global VTEC (Vertical Total Electron Content) model, local VTEC model, Hopfield model, Saastamoinen model, Modified Hopfield model). The client uses precise clock and orbit data in order to account for the satellite specific errors as well as 'regional clock' corrections. In case of dual-frequency observations, a linear combination is used to eliminate the ionospheric error.

Currently the software is not capable of processing real-time data. Nevertheless modules have already been established which can handle real-time correction data transfer in future. Tests and evaluations show the performance of the developed algorithms. Especially the 'regional clocks' provide a benefit to the accuracy.

#### 4. Future Work

While within the last years the demand for real-time PPP tailored to the needs of various applications increased, also a handful of commercial and free services providing real-time correction products were brought to life.

Currently, the IGS real-time working group is providing a real-time pilot project to be prepared for the trend towards real-time GNSS data and derived products such as precise clock corrections and orbits. Organizations or reference stations producing real-time GNSS data can participate in the working group to provide their data-streams via a central service (cf. [14]).

Recently, the commercial positioning service called G2, providing real-time orbits and clocks, was initiated. Operated by Fugro, it mainly addresses the vessel navigation market. Using G2, for the first time also GLONASS integration within PPP (see [15]) is possible.

Nevertheless, real-time PPP is only in its starting phase and only few applications make use of the technique. There are still many unsolved problems left, e.g., the integer ambiguity resolution during PPP processing and the insufficient availability of real-time correction data, which again directly influences the position accuracy.

Based on the outcome of the project RA-PPP, the same consortium is currently investigating the adaptation of the developed algorithms to the new challenges within a follow-up project called 'Development of a real-time PPP processing facility' (short title RT-PPP) which started at the beginning of 2011. Within this work, we plan to develop appropriate algorithms for real-time PPP and to modify existing algorithms to comply with

the requirements of modern applications. It is planned to estimate the gain and deficiencies of using GLONASS observations within PPP as a response to the recovered constellation and modernization of the Russian satellite system. Based on an increasing number of GNSS satellites, improvements in accuracy and availability due to a better geometric constellation can be expected. Since a lot of applications are safety or liability critical, it will also be necessary to include investigations on integrity monitoring algorithms, appropriate for PPP.

Enabling real-time PPP processing requires producing and distributing real-time correction data fulfilling the accuracy needs depending on the addressed applications. Therefore, the project consortium plans to strongly focus on that task. Thereby the calculation and application of the 'regional clock' corrections within real-time will be one of the challenges of RT-PPP.

A so called data streamer will concentrate on the dissemination of orbit, clock and atmospheric corrections that will be provided via RTCM data messages. 'Regional clocks' will be calculated for a set of GNSS stations for adequate time intervals and forwarded to a data conversion unit together with the other correction data. The data will be sent to a stream encoder to convert the correction terms for PPP into appropriate RTCM data messages, which will be broadcasted via Ntrip. An Ntrip client within the rover requests and receives the RTCM messages and forwards them to the processing unit of the built in user-client, where the RTCM corrections can be applied to the observations to improve the PPP solution.

For our current project the post-processing software produced in RA-PPP serves as a base platform for the implementations of a real-time processing facility. It will be adapted and upgraded not only with a module enabling the reception of real-time corrections but also with new algorithms and modules in order to serve as a real-time processing device.

#### Acknowledgements

The work was performed within the RA-PPP (Innovative Algorithms for Rapid Precise Point Positioning – RA-PPP) project. RA-PPP was carried out under the responsibility of the Austrian Research Promotion Agency (FFG) and was funded through the Federal Ministry for Transport, Innovation and Technology (BMVIT) in the course of their 6th Space Applications Programme (ASAP6).

## References

- [1] Zumberge J. F., Heflin M. B., Jefferson D. C., Watkins M. M., Webb F. H. (1997): Precise Point Positioning for the efficient and robust analysis of GPS data from large networks, *J. Geophys. Res.*, 102(B3), 5005–5017.
- [2] IGS: <http://igs.cb.jpl.nasa.gov/>, February 2011.
- [3] Hofmann-Wellenhof B., Lichtenegger H., Wasle E. (2007): *Global Navigation Satellite Systems – GPS, Glonass, Galileo and more*, Springer, Wien New York.
- [4] Kouba J. (2009): A guide to using International GNSS Service (IGS), Geodetic Survey Division, Natural Resources Canada, 615 Booth Street, Ottawa, Ontario K1A 0E9, May 2009, [http://igs.cb.jpl.nasa.gov/igs\\_cb\\_resource/pubs/UsingIGSProductsVer21.pdf](http://igs.cb.jpl.nasa.gov/igs_cb_resource/pubs/UsingIGSProductsVer21.pdf).
- [5] Dach R., Hugentobler U., Fridez P., Meindl M. (2007): *Bernese Software Version 5.0*, Astronomical Institute, University of Bern, Switzerland, <http://www.bernese.unibe.ch/docs/DOCU50.pdf>.
- [6] Leandro R. (2009): *Precise Point Positioning with GPS: A New Approach for Positioning, Atmospheric Studies, and Signal Analysis*. Ph.D. dissertation, Department of Geodesy and Geomatics Engineering, University of New Brunswick, Canada, April 2009.
- [7] Huber K., Ranner H.-P., Abart C., Heuberger F., Karabatić A., Weber R., Berglez P., Klug C. (2010): *Final Report of RA-PPP, Innovative Algorithms for Rapid Precise Point Positioning*, Technical Report for Austrian Research Promotion Agency, (contact the main-author).
- [8] Karabatic A., Weber R., Huber K., Abart C., Heuberger F., Berglez P., Seybold J., Klug Ch. (2010): *Concepts to limit convergence time of GPS-based Precise Point Positioning (PPP)*, Proceedings of the 23rd International Technical Meeting of The Satellite Division of the Institute of Navigation (ION GNSS 2010), Portland, OR, September 2010, pp. 1533-1539.
- [9] *ESA Galileo Information*: [http://www.esa.int/esaNA/SEM4986SXIG\\_galileo\\_0.html](http://www.esa.int/esaNA/SEM4986SXIG_galileo_0.html), February 2011.
- [10] Cocard, M., Bourgon, S., Kamali, O., Collins, P. (2008). *A systematic investigation of optimal carrier-phase combinations for modernized triple-frequency GPS*, *Journal of Geodesy*, Vol. 82, pp. 555-564, DOI: 10.1007/s00190-007-0201-x.
- [11] Urquhart L. (2009): *An analysis of multi-frequency carrier phase linear combinations for GNSS*, Techn. Report No. 263, Department of Geodesy and Geomatics Engineering University of New Brunswick, Canada.
- [12] Ge M., Gendt G., Rothacher M. (2006): *Integer ambiguity resolution for Precise Point Positioning*, Proceedings of the VI Hotine Marussi Symposium of Theoretical and Computational geodesy: Challenge and Role of Modern Geodesy, May 29 – June 2 2006, Wuhan, China.
- [13] Berglez P., Wasle E., Seybold J., Hofmann-Wellenhof B. (2009): *GNSS Constellation and Performance Simulator for Testing and Certification*, Proceedings of the 22nd International Technical Meeting of The Satellite Division of the Institute of Navigation (ION GNSS 2009), Savannah, GA, September 2009, pp. 2220-2228.
- [14] *IGS Real-Time Pilot Project*: <http://www.rtigs.net/>, February 2011.
- [15] Melgard T., Vigen E., Ørpen O., Zandbergen R., Sanchez J. F., Agratis L. (2009): *First real time GPS/GLONASS orbit/clock decimetre level precise positioning service*, European Navigation Conference, ENC-GNSS 2009, 3-6 May 2009, Naples, Italy.

## Contacts

Dipl.-Ing. Katrin Huber, Institute of Navigation, Graz University of Technology, Steyrergasse 30, 8010 Graz, Austria.

E-mail: [katrin.huber@tugraz.at](mailto:katrin.huber@tugraz.at)

Dipl.-Ing. Philipp Berglez, TeleConsult Austria GmbH, Schwarzbauerweg 3, 8043 Graz, Austria.

E-mail: [pberglez@tca.at](mailto:pberglez@tca.at)

Univ.-Prof. Dipl.-Ing. Dr.h.c.mult. Dr.techn. Bernhard Hofmann-Wellenhof, Institute of Navigation, Graz University of Technology, Steyrergasse 30, 8010 Graz, Austria.

E-mail: [hofmann-wellenhof@tugraz.at](mailto:hofmann-wellenhof@tugraz.at)

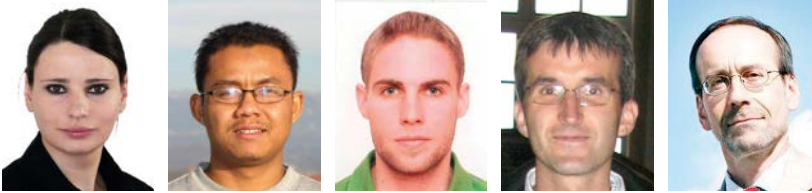
A.o. Prof. Dipl. Ing. Dr. techn. Robert Weber, Institute of Geodesy and Geophysics, Vienna University of Technology, Gusshausstrasse 27-29, 1040 Vienna, Austria.

E-mail: [rweber@mars.hg.tuwien.ac.at](mailto:rweber@mars.hg.tuwien.ac.at)

Dipl.-Ing. Markus Troger, TeleConsult Austria GmbH, Schwarzbauerweg 3, 8043 Graz, Austria.

E-mail: [markus.troger@tca.at](mailto:markus.troger@tca.at)

## Atmospheric effects on the Earth gravity field featured by TU Vienna



*Maria Karbon,  
Dudy Wijaya,  
Michael  
Schindelegger,  
Johannes Böhm and  
Harald Schuh*

### Abstract

Satellite missions like GRACE (Gravity Recovery and Climate Experiment) and GOCE (Gravity field and steady-state Ocean Circulation Explorer) which explore the Earth gravity field observe the instantaneous distribution of mass in the Earth, including all solid, liquid and gaseous components. Due to the fluctuation of those masses at various temporal and spatial scales, a long observation period does not guarantee that the introduced variations in the gravity field are cancelled out. Therefore, to avoid aliasing effects, the mass variations have to be modeled and corrected with respect to the mean state. Within project GGOS Atmosphere, funded by the Austrian Science Fund (FWF) at the Institute of Geodesy and Geophysics (IGG) of the Vienna University of Technology, different methods for the determination of Atmospheric Gravity field Coefficients (AGC) are evaluated. Results indicate that for a proper modelling the vertical structure of the atmosphere has to be taken into account, as already applied for GRACE data processing. Further, atmosphere loading adds a significant signal to the gravity change which has to be considered, in particular at longer wavelengths. The choice of different data structures of the ECMWF (European Centre for Medium-range Weather Forecasts), i.e. model or pressure level data, does not have a significant impact on the final AGC. All findings confirm the data processing strategy of the GRACE Science Data System ([4] Flechtner, 2007), providing the operational GRACE AOD1B (level 1B atmosphere and ocean de-aliasing) product.

**Keywords:** Gravity field, atmosphere, GRACE, de-aliasing

### Kurzfassung

Satelliten-Missionen wie GRACE (Gravity Recovery and Climate Experiment) und GOCE (Gravity Field and steady-state Ocean Circulation Explorer), die das Erdschwerefeld erkunden, beobachten die momentane Verteilung der Massen im System Erde, einschließlich aller festen, flüssigen und gasförmigen Bestandteile. Aufgrund der Fluktuation dieser Massen auf verschiedenen räumlichen und zeitlichen Skalen garantiert eine lange Beobachtungszeit nicht, dass die durch sie verursachten Variationen des Schwerefeldes eliminiert werden. Um so genannte Aliasing-Effekte zu vermeiden, muss deshalb der bekannte Teil der Massenvariationen modelliert und bezüglich eines mittleren Zustandes korrigiert werden. Innerhalb des Projekts „GGOS Atmosphäre“, finanziert vom Österreichischen Wissenschaftsfonds (FWF) am Institut für Geodäsie und Geophysik (IGG) der TU Wien, werden verschiedene Methoden zur Bestimmung der atmosphärischen Schwerefeldkoeffizienten (AGC) ausgewertet. Die Ergebnisse zeigen, dass für eine adäquate Modellierung die vertikale Struktur der Atmosphäre zu berücksichtigen ist. Außerdem hat die Auflast der Atmosphäre einen signifikanten Einfluss auf die Schwerkraftvariation und ist somit ebenfalls zu berücksichtigen. Die Wahl unterschiedlicher Datenstrukturen des ECMWF (European Centre for Medium-range Weather Forecasts), nämlich „model“ oder „pressure level“ Daten, hat keinen entscheidenden Einfluss auf die AGC. Alle Ergebnisse bestätigen die Strategie zur Datenverarbeitung des GRACE Science Data Systems ([4] Flechtner, 2007), welches das GRACE AOD1B (Stufe 1B Atmosphäre und Ozean de-Aliasing) Produkt bereitstellt.

**Schlüsselwörter:** Schwerefeld, Atmosphäre, GRACE, de-aliasing

### 1. Introduction

Exploring the Earth gravity field requires the removal of short term (sub-daily) mass variations in the system Earth, including all solid, liquid and atmospheric particles. Due to the fluctuation of those masses at various temporal and spatial scales (like high and low atmospheric pressure systems) as well as due to a strong dependency on the sampling rate of the ground track of the satellite, a long observation time does not guar-

antee that the introduced variations in the gravity field are cancelled out by the mean operator. De-aliasing then denotes incorporating such instantaneous variations in the atmospheric masses with respect to a static mean state of the atmosphere, either during the preprocessing of observations or during the estimation procedure of the gravity field solution. The same holds for all other mass variation effects inside the system Earth; only that within the atmosphere also the centre of mass of the atmospheric column is varying,

which interferes again on the satellite observations ([5] Gruber et.al,2009).

To eliminate the aliasing signals the determination of accurate Atmospheric Gravity field Coefficients (AGC) is indispensable. For the determination of AGC it has become state of the art to use high resolution Numerical Weather Models (NWM), which take into account the three-dimensional distribution of the atmospheric mass. By subtracting the gravity spherical harmonics of the instantaneous atmosphere from the ones of the mean atmospheric field, the residual gravity spherical harmonic series are obtained. These describe the deviation of the actual gravity field from the mean gravity field due to atmospheric mass variations.

In Section 2 we contrast the formulation of the AGC under different hypotheses, i.e. the thin layer assumption and the 3D approach. Section 3 is devoted to the different data structures, the pre-processing of the NWM data, and the strategy used for the computation of the AGC. The computational results are given in Section 4.

## 2. From mass to gravity

The atmosphere is nearly in a hydrostatic equilibrium, which means that the change in atmospheric pressure on the surface is proportional to the change of mass in the corresponding atmospheric column, including variations in water vapour mass as well as in the dry air mass.  $\rho$  describes the density along the column which can be expressed in terms of surface load  $\sigma$  ([2] Boy et al. 2002, [4] Flechtner, 2007) and which is linked directly to the surface pressure variation  $\Delta p$ .

$$\Delta p = g_0 \int_{r_s}^{\infty} \Delta \rho dr = g_0 \Delta \sigma, \quad (1)$$

$$\Delta \sigma = \frac{\Delta p}{g_0}, \quad (2)$$

where  $g_0$  is the mean gravity acceleration at the Earth surface,  $\Delta p$  the pressure variation and  $r_s$  denotes the Earth surface.

The atmosphere affects the Earth gravity field in two different ways: a direct attraction of the atmospheric masses acting on the orbiting satellite and a much smaller indirect effect introduced by the deformation of the Earth's surface due to elastic loading. Both effects are always evaluated with respect to a mean atmosphere model. This approach is described in detail by [8] Torge (1989).

This section is exclusively devoted to the direct effect, whereas Section 4.2 will deal with the indirect effect. A mathematical description of the gravitational potential can be given in terms of a spherical harmonic expansion (see [8] Torge, 1989):

$$V = \frac{GM}{r} \sum_{n=0}^{\infty} \sum_{m=0}^n \left( \frac{a}{r} \right)^n P_{nm}(\cos \theta) (C_{nm} \cos m\lambda + S_{nm} \sin m\lambda), \quad (3)$$

$$\begin{cases} C_{nm} \\ S_{nm} \end{cases} = \frac{1}{(2n+1)Ma^n} \cdot \iiint_{Earth} r^n P_{nm}(\cos \theta) \begin{cases} \cos m\lambda \\ \sin m\lambda \end{cases} dM, \quad (4)$$

$$\text{where } dM = \rho r^2 dr \sin \theta d\theta d\lambda. \quad (5)$$

$GM$  is the geocentric gravitational constant multiplied with the Earth's mass (solid Earth + oceans + atmosphere),  $a$  denotes the radius of a spherical Earth,  $r$  is the distance to the centre of mass of the Earth,  $\theta$  and  $\lambda$  are co-latitude and longitude,  $C_{nm}$  and  $S_{nm}$  are dimensionless coefficients and  $P_{nm}$  are the fully normalized associated Legendre functions, both depending on degree  $n$  and order  $m$ .

Due to mass redistribution in the atmosphere the potential  $V$  changes with time. This time-dependency of atmospheric density  $\Delta \rho$  can be represented in terms of time-dependent  $\Delta C_{nm}$  and  $\Delta S_{nm}$  coefficients, taking into account Equations (4) and (5), as follows:

$$\begin{cases} \Delta C_{nm} \\ \Delta S_{nm} \end{cases} = \frac{1}{(2n+1)Ma^n} \cdot \iiint_{Earth} \left[ \int_{r_s}^{\infty} \Delta \rho r^{n+2} dr \right] P_{nm}(\cos \theta) \begin{cases} \cos m\lambda \\ \sin m\lambda \end{cases} \sin \theta d\theta d\lambda \quad (6)$$

### 2.1 Thin layer approximation

In the simplest approach the vertical extent of the atmosphere is neglected and all the atmospheric masses are concentrated in a thin layer at the Earth surface. This can be done under the assumption that most of the mass changes occur in the lower 10 km of the atmosphere and act as variable loading effects on the solid Earth's surface ([1] Boy et al., 2005).

Surface loads are defined as mass per surface element; therefore the density change in the atmosphere can be expressed in terms of surface load as follows:

$$\begin{cases} \Delta C_{nm} \\ \Delta S_{nm} \end{cases} = \frac{a^2}{(2n+1)M} \cdot \iint_{Earth} \Delta \sigma P_{nm}(\cos \theta) \begin{cases} \cos m\lambda \\ \sin m\lambda \end{cases} dS, \quad (7)$$

considering that the mass element.

$$\begin{aligned} dM &= \rho r^2 dr \sin \theta d\theta d\lambda = \\ &= r^2 \sigma \sin \theta d\theta d\lambda = r^2 \sigma dS. \end{aligned}$$

Following the definition of the surface load  $\sigma$  in Equation (2), the surface pressure  $p_s$  can be introduced, whereas a mean pressure field  $\underline{p}_s$ , representing a static mean state of the atmosphere, has to be subtracted to obtain the mass variation:

$$\begin{cases} \Delta C_{nm} \\ \Delta S_{nm} \end{cases} = \frac{a^2}{(2n+1)Mg_0} \cdot \iint_{Earth} (p_s - \underline{p}_s) P_{nm}(\cos \theta) \begin{cases} \cos m\lambda \\ \sin m\lambda \end{cases} dS \quad (8)$$

## 2.2 Vertical integration of the atmospheric column

As mentioned in the introduction, also the change of the centre of mass of the atmospheric column has an impact on the orbiting satellite, not only the mass change itself. This variation of the centre of mass is not addressed in the thin layer approximation but has to be taken into account for satellite gravity missions such as GRACE (Gravity Recovery and Climate Experiment) ([4] Flechtner, 2007; [7] Swenson and Wahr, 2002; [11] Velicogna et al., 2001).

This deficiency can be overcome by considering the whole vertical structure of the atmosphere by performing a vertical integration of the atmospheric masses. To do so, Numerical Weather Models (NWM) which describe the vertical structure by introducing various numbers of pressure or model levels are needed. The structure and the processing of these data will be explained in Section 3.

To formulate the vertical integration (VI) we start from the basic Equations (3) and (4), introducing the volume element from Equation (5) (for details see [4] Flechtner, 2007; [9] Zenner et al., 2010; [10] Zenner et al., 2011).

$$\begin{cases} C_{nm} \\ S_{nm} \end{cases} = -\frac{1}{(2n+1)Ma^n} \cdot \iint_{Earth} \left[ \int_{r_s}^{\infty} r^{n+2} \rho dr \right] P_{nm}(\cos \theta) \begin{cases} \cos m\lambda \\ \sin m\lambda \end{cases} \sin \theta d\theta d\lambda \quad (9)$$

Adopting the hydrostatic equation  $\rho dr = -\frac{dp}{g_r}$ , where  $g_r$  is the gravity acceleration at each level, we get:

$$\begin{cases} C_{nm} \\ S_{nm} \end{cases} = -\frac{1}{(2n+1)Ma^n} \cdot \iint_{Earth} \left[ \int_{p_s}^0 \frac{r^{n+2}}{g_r} dp \right] P_{nm}(\cos \theta) \begin{cases} \cos m\lambda \\ \sin m\lambda \end{cases} \sin \theta d\theta d\lambda \quad (10)$$

Again, to analyze gravity field variations caused by atmospheric effects, a quantity  $\underline{p}_{VI}$  representing the mean state of the atmosphere, has to be subtracted from the inner integral, leading to:

$$\begin{cases} \Delta C_{nm} \\ \Delta S_{nm} \end{cases} = -\frac{1}{(2n+1)Ma^{n+2}g_0} \cdot \iint_{Earth} \left( \left[ \int_{p_s}^0 r^{n+2} dp \right] - \underline{p}_{VI} \right) P_{nm}(\cos \theta) \begin{cases} \cos m\lambda \\ \sin m\lambda \end{cases} \sin \theta d\theta d\lambda \quad (11)$$

## 3 Data and processing

### 3.1 Numerical Weather Models

For this work NWM data from the European Centre for Medium-range Weather Forecasts (EC-MWF) are used. Generally, the results of the EC-MWF analysis are provided on individual layers, realized as model or pressure level data. The model level data presently consist of 91 model levels. The concept of model levels addresses the problem of discontinuities in the atmosphere, for example mountains, by creating atmospheric levels that follow the contours of the Earth's surface in the lower and mid-troposphere, the so-called orography. In high altitude the effect of the orography diminishes until the layers in the upper atmosphere become parallel to layers of constant pressure.

From the model level data the so-called pressure levels are retrieved, where the vertical discretization is implemented through 25 levels instead of 91, following continuous surfaces of equal pressure from 1000 hPa to 1 hPa, which can also lie underneath the topography. At each level, among other parameters, the temperature, the specific humidity, and the geopotential height are available. For this paper, pressure level data on global equidistant grids with a horizontal resolution of  $1^\circ \times 1^\circ$  and a temporal resolution of 6 hours (00, 06, 12, 18 UTC) were used.

### 3.2 Pre-processing: from geopotential height to the topography

As can be seen in Equation (10), not the geopotential height of each level is needed but the

geocentric radius, which is not delivered by ECMWF. Equations and approximations for the usage of the geopotential height can be found in [4] Flechtner (2007). Otherwise, the radii of the individual levels as well as the gravitational acceleration at each level have to be calculated in the pre-processing.

At TU Vienna, the data from the ECMWF are downloaded daily as rectangular, three-dimensional grids in the grib-format, containing the geopotential  $Z$ , the specific humidity  $Q$ , and the temperature  $T$  at discrete points on each pressure level and at each epoch (00, 06, 12, 18 UTC). Further meta-data like time and date, spatial resolution and number of nodes are included.

In the pre-processing the following steps are performed:

1. The geographical co-latitude  $\theta$  given by ECMWF is transformed to the WGS84 ellipsoid by setting it equal to the geocentric latitude  $\psi$ .
2. In order to get the longitude and latitude dependent gravity acceleration at each level, it is necessary to introduce a gravity model. We used the fully normalized degree 2 coefficients and the corresponding gravity acceleration of the tide-free EGM96 model. Further, the geoid undulation is needed to retrieve exact ellipsoidal heights. At this point the EGM96 geoid as given by the IGFS (International Gravity Field Service) on a  $1^\circ \times 1^\circ$  ellipsoidal grid is used. The differences to geocentric latitudes are again neglected. Finally, the geocentric radii, the corresponding gravity acceleration and the ellipsoidal height of all layer grid points are computed. Additionally, the density and the virtual temperature  $T_v$  ([4] Flechtner, 2007) are calculated and stored.
3. The ECMWF model level data are not based on topography but on orography, i.e., an envelope of the actual topography, with the consequence that smaller details or rapid height changes are not represented. To overcome this deficiency we reduce all the parameters retrieved during step 2 to the topography of the ETOPO5 model (<http://www.ngdc.noaa.gov/mgg/global/etopo5.HTML>).
4. For all layers and all nodes block-mean values are calculated to be consistent with the theory of spherical harmonic expansions.

Although we introduce longitude and latitude dependent radii and gravity acceleration for the Earth surface instead of the constant  $a$  and  $g_0$  in Equations (8) and (10), investigations have

shown, that at the current accuracy levels of the GRACE processing, this alteration has no significant influence.

### 3.3 Calculation strategy for the Atmospheric Gravity Coefficients (AGC)

For both approaches, the thin layer approach as well as the vertical integration, a reference (pressure) field is needed. In the first case as a 2D field at the surface, and for VI approach it has to represent the three-dimensional structure of the atmosphere. For the thin layer approach we use the Global Reference Pressure model GRP developed at our institute (Schuh et al., 2010). It is a 2D surface pressure field computed from the atmospheric data of ECMWF ERA-40 and referenced to the ETOPO5 topography. Given its nature, GRP cannot be used for VI, where a 3D model corresponding to the calculation model has to be used. For this purpose, Equation (10) was evaluated for the years 2008 and 2009 and a mean was formed. Consequently, this mean field is not a surface pressure field, but consists of mean Atmospheric Gravity Coefficients (AGC).

#### 3.3.1 Thin layer approach

Starting from the block-mean value obtained in the pre-processing of the ECMWF data, the mean pressure field GRP is subtracted from the actual surface pressure to get the pressure variation. Those differential values are then entered in Equation (8) and integrated numerically over the entire Earth's surface. The obtained integral value is then transformed into the actual potential by multiplication with the expression in front of the surface integral. This procedure is repeated for each degree and order.

#### 3.3.2 Vertical Integration (VI)

For the VI approach we evaluate Equation (10) for the actual epoch. The inner integral is computed first, starting from the highest level, down to the topography. This value is then entered in the same procedure as used for the thin layer approach. Unlike the thin layer approach, we do not calculate the difference of the 3D-pressure beforehand but afterwards by subtracting the coefficients of the mean 3D field from the ones just calculated for the actual epoch.

All the coefficients are derived up to degree and order 100 and stored as text file in  $(n, m, C_{nm}, S_{nm})$  format on our central server (<http://ggosatm.hg.tuwien.ac.at/GRAVITY/>). The GRP model can be downloaded from there as well.

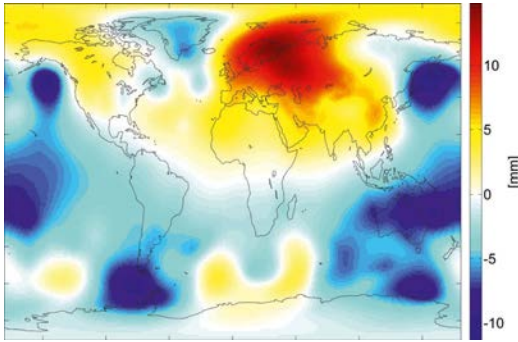


**Fig. 1a:** Geoid height variation (VI approach) with respect to the mean field (over 2008 and 2009) in mm on January 1<sup>st</sup>, 2008, 00 UTC (min: -11.35 mm, max: 14.81 mm, rms: 2.9 mm).

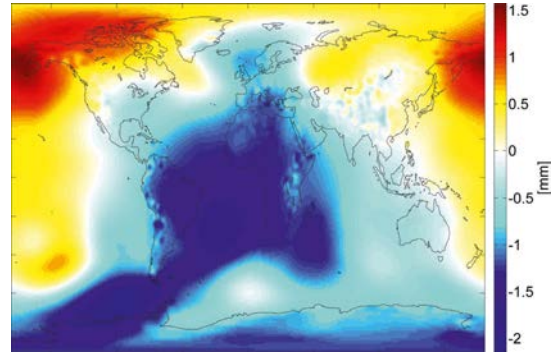


**Fig. 1b:** Difference between the AOD1B "atm" product and our (TU Vienna) VI approach in geoid height (min: -2.25 mm, max: 1.77 mm, rms: 0.7 mm).

#### 4. Results

The real impact of aliasing effects and other miss-modelling of the atmosphere cannot be estimated straight forwardly. Therefore, we rely on comparisons of degree standard deviations in geoid height and global plots of the geoid heights.

All the results presented here base on the 6-hourly pressure information of the year 2008. (Mind that the mean field for the VI approach was determined for 2008 and 2009.) As an example the first epoch (00 UTC) of January 1<sup>st</sup> 2008 is selected. Figure 1a (left plot) depicts the geoid height variation following the VI approach and Fig. 1b (right plot) the difference between the official AOD1B "atm" product and our (TU Vienna) VI approach is shown, also expressed in geoid height.

Both solutions, AOD1B and TU Vienna, show a good agreement, also in terms of degree standard deviation (Figure 2) or distinct coefficients (Figure 3). The differences are most prominent at long wavelengths and can be attributed to the different definition of the static mean field of the atmosphere (AOD1B: mean over 2001+2002, VI approach by TU Vienna: mean over 2008+2009) and to the fact that in the VI approach by TU Vienna the S1 tide is still included.

To evaluate the significance of the vertical structure of the atmospheric column, the spherical harmonic series resulting from the thin layer approach and the ones of the VI approach are compared. In Figure 2 the degree standard deviations of the coefficients for the year 2008 up to degree 100 are compared to the AOD1B co-

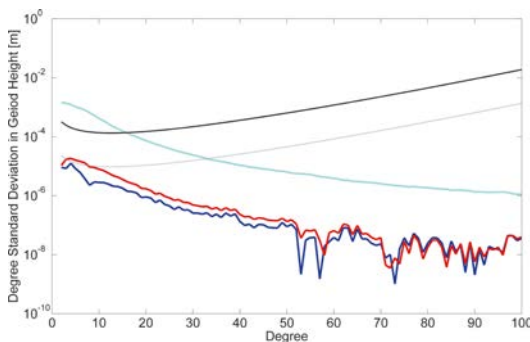


**Fig. 2:** Degree standard deviation in terms of geoid height for the year 2008, in cyan for the AOD1B product for the atmosphere, in blue the difference of the VI approach by TU Vienna with respect to the AOD1B product, in red the corresponding difference of our thin layer approach w.r.t. AOD1B. The black line marks the actual error level of GRACE, the grey one the theoretical error as obtained by pre-launch simulations.

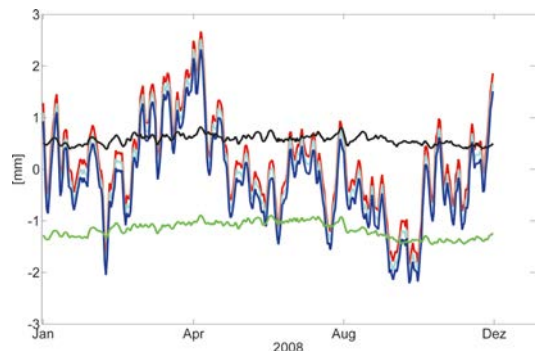


**Fig. 3:** Time variation of the  $C_{20}$  coefficient in geoid height for the year 2008, in blue for the VI approach by TU Vienna, in red the thin layer approach, in cyan for the AOD1B product. The difference between the VI approach by TU Vienna and AOD1B is shown in black, the difference between the thin layer approach and AOD1B in green, both differences multiplied by a factor of 10.



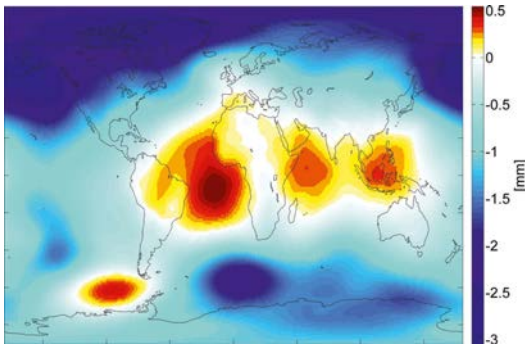


Fig. 4a: Difference of the geoid height variation between the VI approach and the thin layer approach for January 1<sup>st</sup> 2008, 00 UTC (min: -3.05 mm, max: 0.54 mm, rms: 1.2mm).

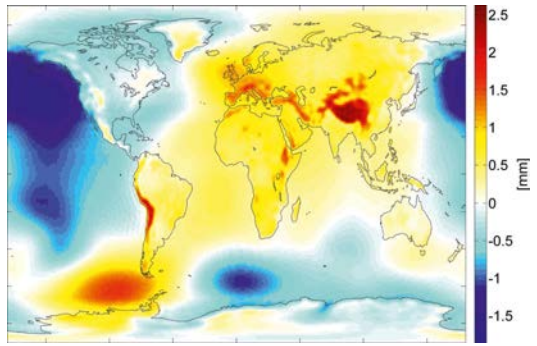


Fig. 4b: Difference of the reference fields for the VI and the thin layer approach, expressed in geoid height (min: -2.62 mm, max: 1.86 mm, rms: 0.52 mm).

efficients. Figure 3 exemplarily shows the geoid height variability for the  $C_{20}$  coefficients. The results indicate that at the current error level the differences between the two approaches by TU Vienna and the official product are negligible, thus also confirming the approach by the GRACE science team.

In a second step, the resulting potential fields obtained from the two different approaches (thin layer and VI, both from TU Vienna) for January 1<sup>st</sup>, 2008, 0 UTC and the two corresponding mean fields are compared, always in terms of geoid height. Figure 4a on the left shows the difference between the thin layer approach and the vertical integration approach, and for both approaches the respective mean fields are subtracted. Figure 4b shows the discrepancy between the two mean fields (average per latitude band was removed). In Figure 5 the absolute values (no mean field subtracted) for the two methods at the actual epoch are plotted. In order not to have a dominating effect of the topog-

raphy, a land-sea mask was applied. If the different approaches (thin layer vs. VI) would be the cause of the differences in Figure 4a, similar structures should appear also in the discrepancy of the total atmosphere in Figure 5; however this is not the case. Therefore those signals are introduced somewhere else, probably due to the different definition of the mean fields mentioned in Section 3.3. Obviously, besides topographical signals due to the different reference height, i.e. surface and centre of mass, also some signals coming from the atmosphere are still present in Figure 4b, showing some correlation with the artefacts in Figure 4a. This leads to the conclusion that those signals are introduced and then propagated to the final AGC.

This discrepancy can be overcome, if a consistent mean pressure field would be calculated (from Equation (10)). However, due to the enormous computational expense to process the full ERA-40 dataset in 3D, this task was abandoned for now. Although the effect is too small to have a significant influence on the resulting AGC for the actual GRACE mission, improved versions of reprocessed gravity solutions might demand to take this factor into account.

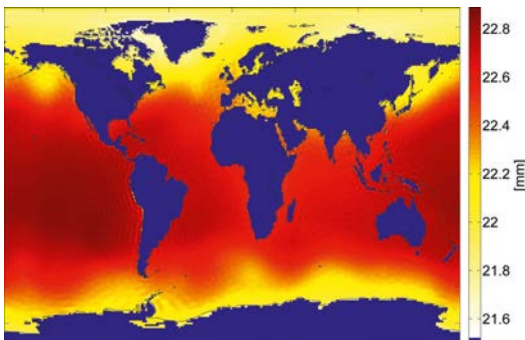


Fig. 5: Difference of the total atmosphere between VI and the thin layer approach, expressed in geoid height for January 1<sup>st</sup> 2008, 0 UTC (min: 21.34 mm, max: 22.89 mm, rms: 22.44 mm).

#### 4.2 Loading

In all the calculations up to now the indirect effect, i.e. the elastic deformation of the solid Earth due to atmospheric loading was not considered. This effect is counteracting the direct effect due to the deformation towards the geocentre. In general, for small deformations the additional change in the potential  $\Delta V$  depends linearly on the potential (Equation (3)), following [3] Farrell (1972):

$$\Delta V_n^{ind} = k_n \Delta V, \tag{12}$$

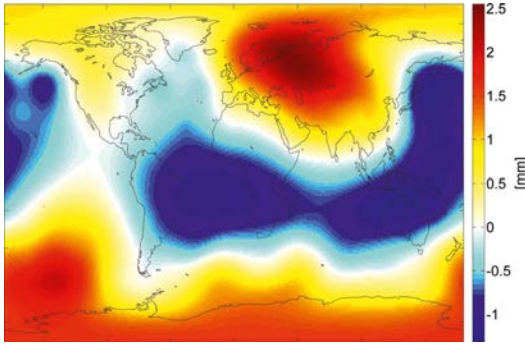


Fig. 6: Difference of the geoid height variation for the thin layer approach between the variants with and without loading for January 1<sup>st</sup>, 2008, 0 UTC; (min: -1.32 mm, max: 2.45 mm, rms: 0.78 mm).

$$\Delta V_n^{tot} = \Delta V + k_n \Delta V = (1 + k_n) \Delta V. \quad (13)$$

$k_n$  denote the degree dependent Load Love numbers and represent the deformational behaviour based on the rheology of the Earth. For our processing, we use Load Love numbers defined in the centre of mass frame calculated by Pascal Gegout, provided by Jean-Paul Boy, and downloaded from [http://astrogeo.org/agra/Load\\_Love2\\_CM.dat](http://astrogeo.org/agra/Load_Love2_CM.dat).

Figure 6 shows the difference between a solution without considering loading and one which includes loading, both for the thin layer approximation. As expected only differences at a big spatial scale appear since Earth's elastic surface deformation due to mass redistribution is sensitive to large scale pressure variations with wave-

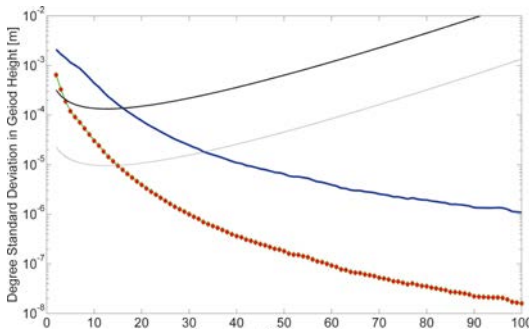


Fig. 7: Degree standard deviation in terms of geoid height for the year 2008, in blue for the VI approach with loading, in green the corresponding difference of the VI approach without loading, in red the corresponding difference of the thin layer approach without loading. The black line marks the actual error level of GRACE, the grey one the theoretical error as obtained by pre-launch simulations.

lengths greater than 2000 km, corresponding to  $n < 10$  (Boy et al. 2002). This result is confirmed by the degree standard deviation expressed in geoid height calculated for the year 2008 (Figure 7).

Given the fact that the differences up to degree 4 lie above the actual error level and up to degree 15 above the predicted error level, the indirect effect has to be accounted for, as it is of course done for the AOD1B product. The same conclusion is drawn looking at the difference between with and without loading in terms of geoid height variability for low degrees (Figure 8), considering the aimed precision of GRACE to be a few micrometers for degrees 3 to 5.

### 4.3 Pressure and model level data

As mentioned before, the ECMWF data can be downloaded as pressure or model level data. The biggest difference between those two representations is the method of discretisation of the vertical structure of the atmosphere. Whereas the model level data reach up to approximately 80 km, the pressure level search up to a height of about 46 km. The lowest model level, i.e. the one nearest to the surface, follows the orography used by the ECMWF; the lowest pressure level is at 1000 hPa. In Figure 9a (left plot) the difference between topography and orography is shown; the majority of the differences appear in mountainous regions like the Himalaya or the Andes, but the most prominent anomalies (more than 1 km) can be found in the Antarctica.

To determine the influence of the data structure on the AGC results, the difference between the VI solutions computed with pressure level data and model level data was calculated and plotted in Figure 9b in terms of geoid height. Small non-zero features over the continents appear, most prominent in the Himalaya region.

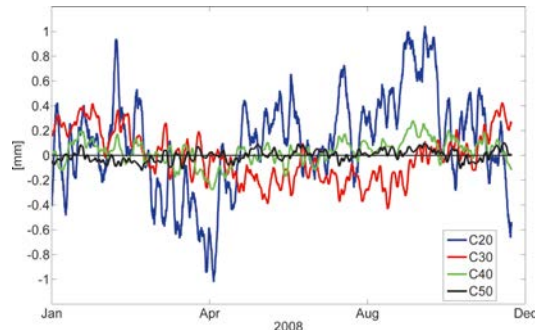
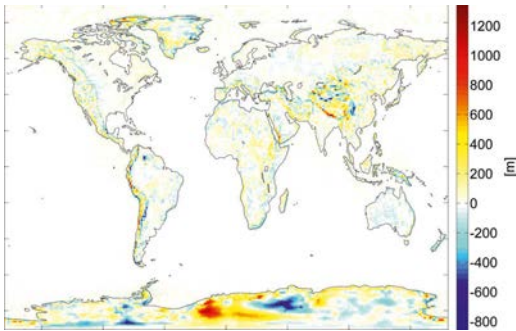
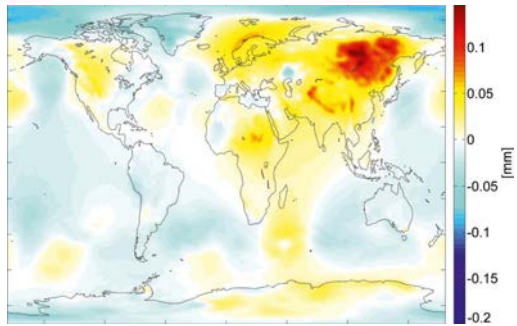


Fig. 8: Time variations for low degree coefficients, calculated with and without loading, expressed in geoid height.



**Fig. 9a:** Difference of the geocentric surface radii for the orography used by the ECMWF and ETOPO5 (min: -855.76 m, max: 1350.18 m, rms: 51m).



**Fig. 9b:** Difference of the geoid height variation between the VI approaches with pressure level and model level data for January 1<sup>st</sup> 2008, 00 UTC (min: -0.09 mm, max: 0.15 mm, rms: 0.018 mm).

Although some features propagate into the final results, their impact is small. This leads to the conclusion that the definition of the Earth surface and the method of vertical discretisation of the atmosphere do not have a significant impact on the actual GRACE processing. Although the differences in height, especially in the Antarctica are huge, those features do not show up in the AGC.

## 5. Conclusion and outlook

Our de-aliasing product shows good agreement with the official AOD1B product provided by GFZ ([4] Flechtner, 2007), the source for the discrepancies seems to be the different definition of the static mean field of the atmosphere. The current and future space gravity missions demand a very high accuracy in modelling atmospheric effects, both the direct and the indirect effects. We have confirmed that for the actual GRACE mission, in order to reach the predicted error level, the 3D structure of the atmosphere must not be neglected. Also the indirect effect, i.e. loading, has to be modelled, at least for wavelengths longer than 2000 km. Therefore both are applied for the operational GRACE short-term atmosphere and ocean de-aliasing product. Concerning the data sets provided by the ECMWF, the differences between model and pressure level data can be neglected.

Considering the massive computational effort to calculate the VI approach, we developed a new processing strategy, where only a 2D pressure field like for the thin layer approach and the height of the centre of mass of the atmospheric column is needed. First results look promising, especially for the low degrees, but further investigations need to be carried out.

In the results presented here the atmospheric tides (S1 and S2) were not modelled, although they have an impact on the orbiting satellite, as many other forces, too. They will be included in the processing of AGC in the next version to be available at <http://ggosatm.hg.tuwien.ac.at/>.

## Acknowledgements

We would like to thank the Austrian Science Fund (FWF), which supports the project GGOS Atmosphere (P20902), and the ECMWF for providing the meteorological data. Further to Jean Paul Boy and Pascal Gegout for making available the elastic Load Love numbers. We thank Frank Flechtner (GFZ) for providing the predicted and actual (release 04 version) GRACE errors and for valuable discussions and also the Institut für Astronomische und Physikalische Geodäsie (IAPG) of TU München for their constant support.

## References

- [1] Boy J. P., Chao B. F., 2005: Precise evaluation of atmospheric loading effects on Earth's time-variable gravity field, *Journal of Geophysical Research*, Vol. 110, B08412, doi: 10.1029/2002JB002333
- [2] Boy J. P., Gegout P., Hinderer J., 2002: Reduction of surface gravity data from global atmospheric pressure loading, *Geophysics Journal International*, Vol.149, pp. 534-545
- [3] Farrell W. E., 1972: Deformation of the Earth by Surface Loads, *Reviews of Geophysics and Space Physics*, Vol.10, No.3, pp. 761-797
- [4] Flechtner F., 2007: AOD1B Product Description Document for Product Releases 01 to 04 (rev. 3.1, April 13, 2007)
- [5] Gruber Th., Peters Th., Zenner L., 2009: The Role of the Atmosphere for Satellite Gravity Field Missions, *Observing our Changing Earth*, International Association of Geodesy Symposia 133, ed. by M. Sideris, Springer-Verlag Berlin Heidelberg
- [6] Schuh H., Schindelegger M., Wijaya D.D., Böhm J., Salstein D., 2010: Memo: A method for the calculation of global reference pressure (GRP), available at:

[http://ggosatm.hg.tuwien.ac.at/LOADING/REFPRES/global\\_reference\\_pressure\\_memo.pdf](http://ggosatm.hg.tuwien.ac.at/LOADING/REFPRES/global_reference_pressure_memo.pdf)

- [7] Swenson S., Wahr J., 2002: Estimated Effects of the Vertical Structure of Atmospheric Mass on the Time-Variable Geoid, *J. Geophys. Res.*, 107, 2194, doi:10.1029/2000JB000024
- [8] Torge W., 1989: *Gravimetry*, Walter de Gruyter-Berlin-New York, ISBN: 3-11-010702-3
- [9] Zenner L., Gruber T., Beutler G., Jäggi A., Flechtner F., Schmidt T., Wickert J., Fagiolini E., Schwarz G., Trautmann T., 2011: Using Atmospheric Uncertainties for GRACE De-Aliasing – First Results, *Geodesy for Planet Earth*, International Association of Geodesy Symposia, Springer
- [10] Zenner L., Gruber T., Jäggi A., Beutler G., 2010: Propagation of atmospheric model errors to gravity potential harmonics – Impact on GRACE De-Aliasing, *Geophysical Journal International*, 182(2), pp. 797-807
- [11] Velicogna I., Wahr J., Van den Dool H., 2001: Can Surface Pressure be used to remove atmospheric contributions from GRACE data with sufficient accuracy to recover hydrological signals? *Journal of Geophysical Research*, Vol. 106, No. B8, pp. 16415-16434

## Contacts

**Dipl.-Ing. Maria Karbon:** Advanced Geodesy, Institute of Geodesy and Geophysics, TU Wien, Gusshausstr. 27-29, 1040 Wien, Austria.

E-mail: maria.karbon@tuwien.ac.at

**MSc.Dr. techn. Dudy Darmawan Wijaya,** Advanced Geodesy, Institute of Geodesy and Geophysics, TU Wien, Gusshausstr. 27-29, 1040 Wien, Austria.

E-mail: wijaya@mars.hg.tuwien.ac.at

**Dipl.-Ing. Michael Schindelegger,** Advanced Geodesy, Institute of Geodesy and Geophysics, TU Wien, Gusshausstr. 27-29, 1040 Wien, Austria.

E-mail: michael.schindelegger@tuwien.ac.at

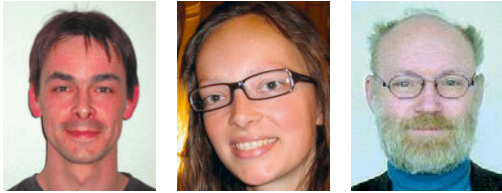
**Assistant Prof. Dipl.-Ing. Dr. techn. Johannes Böhm,** Advanced Geodesy, Institute of Geodesy and Geophysics, TU Wien, Gusshausstr. 27-29, 1040 Wien, Austria.

E-mail: johannes.boehm@tuwien.ac.at

**o. Univ. Prof. Dr.-Ing. Dr. h.c. Harald Schuh,** Advanced Geodesy, Institute of Geodesy and Geophysics, TU Wien, Gusshausstr. 27-29, 1040 Wien, Austria.

E-mail: harald.schuh@tuwien.ac.at

## Regional Ionosphere Models for Improving GNSS Navigation



*Sandro Krauss, Andrea Maier and Günter Stangl*

### Kurzfassung

Alle Signale von Satellitennavigationssystemen erfahren durch die Atmosphäre eine Laufzeitverzögerung. Von den verschiedenen Einflüssen ist jener der Ionosphäre am stärksten. Als dispersives Medium verzögert sie die Signale frequenzabhängig. Deswegen können Empfänger mit zwei oder mehr Frequenzen durch Bildung von Linearkombinationen die Verzögerung großteils eliminieren. Allerdings besteht der überwiegende Teil der Empfänger aus solchen, die nur die GPS-Frequenz L1 nutzen, weil die Empfängerkosten wesentlich geringer sind. Im Fall von Einfrequenzempfängern kann durch die Verwendung von Ionosphärenmodellen eine Verbesserung der Positionierung erzielt werden. Die Modelle reichen von statischen globalen bis zu lokalen, die nahezu in Echtzeit berechnet werden. Durch die Übermittlung von Korrekturdaten via EGNOS kann die Genauigkeit der Empfänger von L1-Code von mehreren Metern bis zu einem Meter oder gar darunter gesteigert werden. Auf Grund der derzeit schwachen Sonnenaktivität ist der Fehlereinfluss durch die Ionosphäre eher gering. Deshalb wurden Daten von GPS-Permanenzstationen während eines extremen Events des letzten Sonnenzyklus analysiert. Als Testgebiet wurde eine Region mittlerer Breite in Österreich gewählt, weil dort die Stationen eine relativ lange Zeitreihe besitzen. Es kann gezeigt werden, dass während hoher Sonnenaktivität die regionalen Modelle eine Verbesserung in der Positionierung gegenüber einem globalen Modell erzielen.

**Keywords:** Austria, GPS, ionosphere, OEGNOS

### Abstract

GNSS signals experience significant delays when travelling through the atmosphere. The major source of the delay is due to the ionosphere which is a dispersive medium. Receivers with two or in future more frequencies can eliminate most of this influence by computing an ionosphere-free combination of frequencies. The major part of navigation receivers, however, uses only L1-signals and thus needs external corrections to improve the positions degraded by the ionosphere. This article will give an overview to which extent positions determined by means of L1-signals can be improved if different ionosphere models, ranging from global to local ones, are applied. The corrections can be transmitted in near real-time by e.g. an EGNOS server which provides those data in order to reduce the standard error of several meters to a sub-meter level for L1 code receivers. The reduction of ionospheric delay becomes especially important during the maximum of a solar cycle. For this reason, the models have been applied to data gathered from permanent stations during extreme events of the last solar maximum. The mid-latitude region of Central Austria was chosen as a regional testbed with permanent stations providing a long time series. It can be shown that with increasing solar activity, regional models improve positions slightly better compared to a global model.

**Schlüsselwörter:** Österreich, GPS, Ionosphäre, OEGNOS

### 1. Introduction

When the Global Positioning System (GPS) was designed, the introduction of the two frequencies L1 and L2 should reduce the effect of the ionosphere onto positioning, at least for military users. Additionally, ionosphere parameters of the Klobuchar model [6] are transmitted together with the broadcast ephemeris and can be used by any receiver. Thereby ionospheric time-delay, examined over one day, strongly reflects a cosine curve, which has been mathematically modelled by Klobuchar. Thus it is possible to model the daily variations which have a total electron

content (TEC) maximum at early afternoon (14:00 LT) and a quite constant minimum during night. Nevertheless it has to be noted that the Klobuchar model can only correct about 50-70% of the ionospheric delay. Thus there is a need of modelling the ionosphere more accurate than the transmitted global model can do. Especially for receivers which either use range corrections from another station at distances of 1000 km and more by Differential GPS (DGPS) or want to correct their position by more adequate models like the European Geostationary Navigation Overlay Service (EGNOS [4]), the inclusion of the current ionospheric conditions is important.

The ionospheric delay of a transmitted signal with a frequency  $f$  (L1 = 1575.42 MHz) can be computed according to [5] by

$$\Delta IONO = \frac{40.3}{f^2} TEC .$$

Thereby the TEC is defined as the total number of electrons ( $N_E$ ) per  $m^2$  along the path  $s$ ,

$$TEC = \int N_E(s) ds$$

and is measured in TEC Units (1 TECU =  $10^{16}$  electrons/ $m^2$ ). Implicitly each delay is also a function of time because the number of electrons is not constant in space and time. Using more than one frequency, assuming constant electron numbers within the travelling time, the TEC can either be determined or its influence on the distance measurement can be eliminated by forming linear combinations. The impact of one TECU is equivalent to a distance of about 0.16 m for the C/A code which is in the same range as the wavelength of L1 (about 0.19 m).

However, the natural variations of the ionosphere are much larger than 1 TECU and may reach some hundreds of TECUs during extreme events. On this assumption we determined global and regional ionosphere models and investigated their impact on the station coordinates. In order to validate the results, a comparison with models from the Center for Orbit Determination in Europe (CODE) has been made. The research covers time periods of high solar activity as well as the present time where less solar activity is noticeable. Finally, the regional models were computed in near real-time and the results are provided to the Austrian EGNOS data server (OEGNOS, [7]) for an improvement of the position accuracy provided by the EGNOS service.

## 2. Ionosphere Models

When modelling the ionosphere it is important that the parameters adapt very quickly in time and cover special regions of the ionosphere, which may deviate from predicted models. For example, rapid amplitude and phase fluctuations, known as scintillations, arise quite locally and on short term. Other interferences arise from travelling disturbances which are running from the North Pole through channels to mid-latitudes. Not to forget solar outbursts and geomagnetic storms, which have an impact on the whole northern hemisphere. Therefore, models require current measurements with good resolution in time and space. For the present study

GPS measurements were used to determine the parameters of several ionosphere models. All of them were produced using the Bernese GNSS Software 5.1 [2] either in a post processing or in a near real-time mode. This software package offers the possibility to determine ionosphere models based on a Taylor series or spherical harmonics.

### 2.1 Global Ionosphere Model (GIM)

The models described in Sections 2.1 and 2.2 are based on the so called Single Layer Model (SLM), which assumes that all free electrons are concentrated in a thin shell of infinitesimal thickness. This assumption is necessary since it is nearly impossible to establish height dependent profiles of electron densities using ground based GPS observations [8]. However, by using data of low Earth orbiters (LEO) equipped with GPS receivers and spacecraft dedicated to measure the ionosphere parameters, like COSMIC/FOR-MOSAT and DEMETER, improved vertical profiles could be produced. Because those data are not easily accessible, especially not in real-time, the SLM provided by standard software will be regarded in the following.

The vertical TEC  $E$  can thus be represented as a function of geographic latitude  $\beta$  and sun fixed longitude  $s$ :

$$E(\beta, s) = \sum_{n=0}^{n_{\max}} \sum_{m=0}^n \tilde{P}_{nm}(\sin \beta) (a_{nm} \cos ms + b_{nm} \sin ms)$$

The maximum degree  $n_{\max}$  of the spherical harmonics expansion is set to 15.  $\tilde{P}_{nm}$  are the normalized Legendre functions and  $a_{nm}$ ,  $b_{nm}$  denote the coefficients of the spherical harmonics.

For the computation of a global ionosphere model, data from approximately 220 permanent GPS stations, mainly from the IGS network [3], contributed to the solution. To determine the ionospheric delay, zero difference smoothed code observations were processed limited to an elevation mask of  $10^\circ$ . Beside the representation with spherical harmonics, the GIM is also provided in the Ionosphere Exchange (IONEX) format with a spatial resolution of 5.0 degrees in longitude and 2.5 degrees in latitude, and a temporal resolution of two hours. The usage of the IONEX format, especially the interpolation methods between the grid-points, is described in [8].

### 2.2 Regional Ionosphere Model (RIM)

The regional models are basically determined with the same procedure as the previous global

model. The only difference is that the RIMs were determined with a higher temporal resolution of one hour and are spatially limited to a certain area. For the present study two different regions were evaluated.

The first selected area covers the European territory and comprises measurements of approximately 60 stations within the EUREF permanent network EPN [1]. The determination of the model is also based on spherical harmonics with  $n_{\max}$  equal 15 and the co-produced TEC map is aligned with the official product from CODE, having a spatial resolution of  $1^\circ \times 1^\circ$ . Hereafter this model is referred to as RIM-EUR.

When calculating ionosphere models in near real-time computations, the latency is a crucial factor. The computing time increases with the number of included stations. Therefore, the second area called RIM-AUT covers a much smaller region containing measurements from 16 GPS stations in Austria and the neighbouring countries (Figure 1). The reference point is located near the city of Rottenmann – the testbed area of the OEGNOS project (see chapter 3 for more details).

### 2.3 Taylor Series

The final model describes the ionosphere based on a Taylor series of degree and order 2 ( $n_{\max}$ ,  $m_{\max}$ ) instead of spherical harmonics. The coefficients are also derived from GPS zero difference observations

$$E(\beta, s) = \sum_{n=0}^{n_{\max}} \sum_{m=0}^{m_{\max}} E_{nm} (\beta - \beta_0)^n (s - s_0)^m .$$

$E_{nm}$  are the TEC coefficients of the Taylor series and  $\beta_0$ ,  $s_0$  the origin of the series which resides near the city of Rottenmann (blue mark in Figure 1). Finally,  $\beta$  denotes the geographic latitude of the intersection point of the receiver-to-satellite signal path with the ionospheric layer and  $s$  the sun-fixed longitude of the ionosphere pierce point. Due to the polynomial degree and order in the  $(\beta, s)$  domain the model is limited to a small area. Within the testbed this model was also implemented for near real-time processing.

### 2.4 Validation of the Models

The Klobuchar model was developed in the late 1980s using data from a period of high solar activity during solar cycle 20. Even if the parameters are changed by the GPS providers from time to time, the adaption to real ionosphere conditions is poor. Due to the fact that the model is to map the global ionosphere and that approximations to the geometrical calculations as well as constants are used, it only corrects about 50% of the ionospheric delay. The night-time constant, for example, is set to 5ns which is about 9 TECU. In fact, this variable is related to the sun activity and leads to deviations during solar quiet times (Figure 2, left side). Additionally there are many turbulent factors which cannot be predicted and have a major impact on the TEC behaviour (Figure 2, right side).

Within their routine analysis, CODE offers a regional ionosphere model covering Europe as well as global models with different latencies. Two predicted models are available with a validity of 24 and 48 hours. The rapid and final iono-

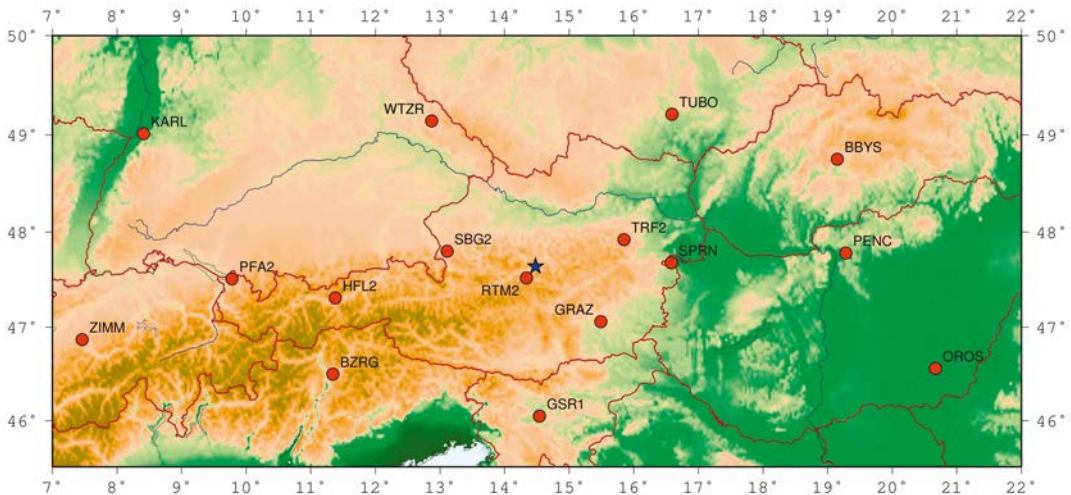


Fig. 1: Near real-time testbed RIM-AUT (Contributing stations are marked as circles and the central point near Rottenmann with a blue star)

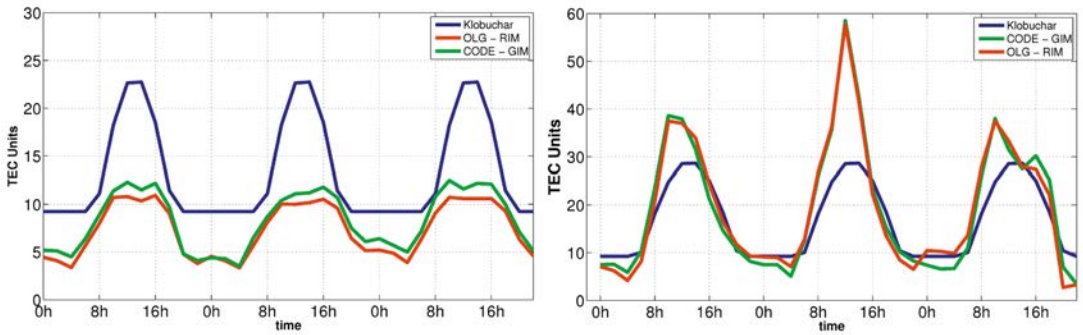


Fig. 2: Ionospheric time delay for station Rottenmann calculated using the Klobuchar model as well as the GIM and RIM during solar quiet times in 2006 (left) and the Halloween event in 2003 (right).

sphere products have a latency of one and four days, respectively. The regional European model is supplied once per month.

In order to validate our GIM and RIM-EUR solutions, a comparison with the final products from CODE was carried out. Figure 3 shows the differences between the solutions.

As expected, the main variations appear in oceanic regions and in areas where different stations were selected. Concerning the European continent the TEC differences in both models are only up to 1-2 TECU, which is the best achievable precision at present.

### 3. The OEGNOS Project

Comparisons between the different models, GIM, RIM and Taylor series, were carried out within the Austrian project OEGNOS [7]. Apart from the ionospheric correction, also the tropospheric delay has been computed and trans-

mitted. This project was led by the company TeleConsult Austria GmbH. The partners were the University of Technology in Vienna (Institute for Geodesy and Geophysics), the University Center of Rottenmann (UZR) and the Austrian Academy of Sciences (AAS, Space Research Institute). A substantial part of the project was financed by the Austrian research promotion agency FFG. One goal was to refine the corrections transmitted via EGNOS within Austria as a part of Central Europe [11]. Frequently, the direct line-of-sight to the EGNOS satellite is masked in Alpine regions. Therefore a terrestrial server was developed computing regional ionosphere and troposphere corrections and adding them to the range corrections to be transmitted in the RTCM format. The AAS generated the GIM, RIM and Taylor series based models and investigated their influence on the positioning. The University of Technology Vienna provided ionospheric cor-

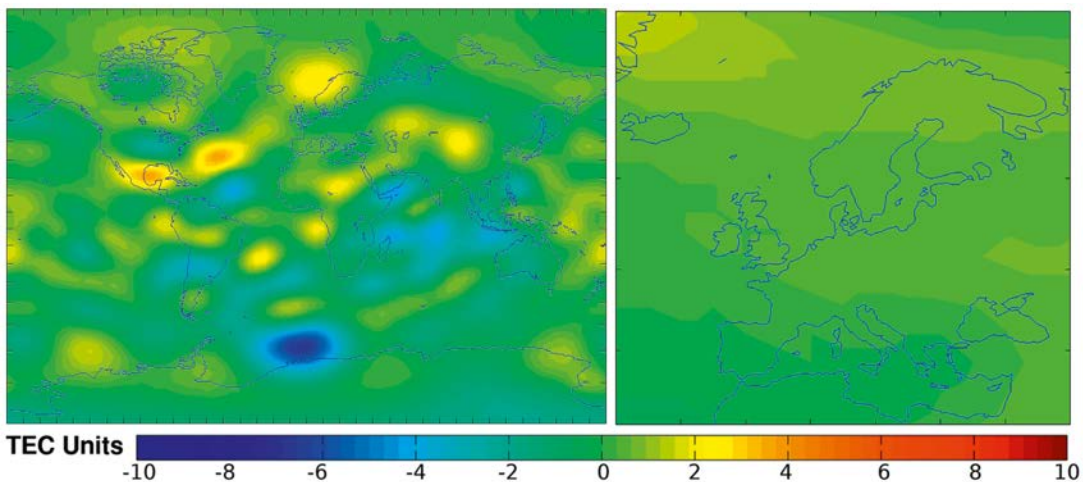


Fig. 3: Differences between TEC maps from CODE and our solutions (left GIM, right RIM-EUR), 6<sup>th</sup> June 2008 (14:00 LT)



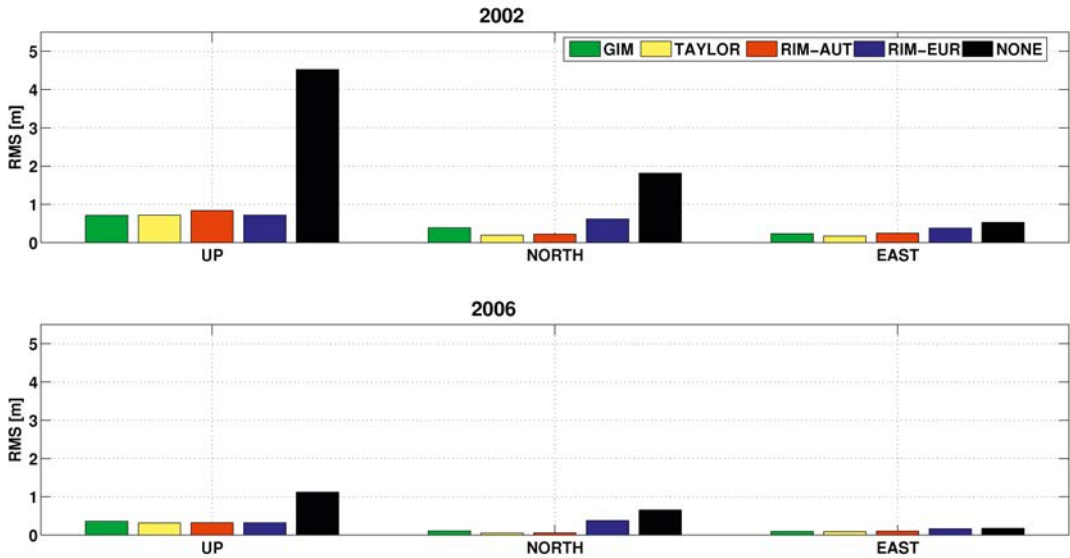


Fig. 4: RMS values of coordinate differences based on a two-week analysis for 2002 and 2006 including 16 contributing stations

rections in real-time based on decoded EGNOS messages, predicted TEC maps and modified Klobuchar coefficient models. UZR and TeleConsult designed and operated the server system and established the communication. Finally, the TeleConsult performed field tests under various conditions and used different models to check the impact in practice.

#### 4. Comparison of Different Ionosphere Models Concerning Station Coordinates

As mentioned before, the majority of the GPS receivers can only make use of the single frequency L1. Therefore, the following results are based on a precise point positioning (PPP) using just the L1 frequency.

##### 4.1 Post Processing Approach

In the last years the solar activity was rather low. In order to compare the models also during high solar activity, calculations for a certain time period in 2002 have been performed additionally. At that time the solar cycle 23 was nearly at the maximum. The post processing analysis based on daily GPS observations was set up for two weeks in 2002 (high solar activity) and 2006 (low solar activity).

In order to identify the effects of different ionosphere models, the obtained coordinates are compared to reference coordinates (ITRF2000 epochs 2002.0 and 2006.0 respectively,

phase baseline network from post processing, EPN+AMON [10]), which have an accuracy of 1–2 centimetres.

As we can see in Figure 4, all applied models reduce the error in the coordinates by 75 % during solar quiet and 85 % in solar active times, compared to results where no ionosphere model was used. In doing so, no model shows a significant improvement compared to the others depending on the time of day. In solar quiet times a different model selection has a maximum influence of 0.15 m on the positioning. During solar maxima, however, it becomes more important to use the optimal model.

##### 4.1.1 Impact of Extreme Solar Events on Position Solutions

Extreme solar flares can cause extraordinary ionospheric effects which in turn cause a degradation of the accuracy of positions determined by GPS. The so-called Halloween event in 2003, when two of the largest solar flares occurred (28<sup>th</sup> October, 4<sup>th</sup> November), was chosen to demonstrate these effects.

Observations recorded by 11 Austrian permanent GPS stations from 27<sup>th</sup> October to 6<sup>th</sup> November were used to calculate the stations local up, north and east coordinates. Figure 5 shows the coordinate differences in the up component using various ionospheric models and the respective values without any corrections.

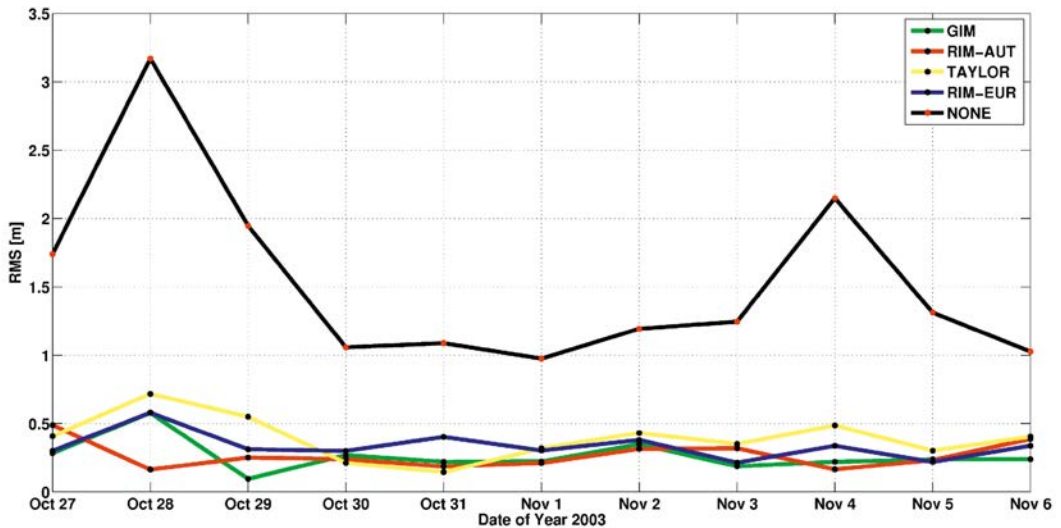


Fig. 5: Mean coordinate differences for up-direction (27<sup>th</sup> October – 6<sup>th</sup> November 2003)

The differences in north and east are considerably smaller.

The extreme solar flares are well distinguishable from the differences of the modelled and unmodelled values. The first peak indicates the solar flare at the end of October which is significantly higher than the differences induced by the second flare at beginning of November. It is clearly visible that even during extreme ionospheric conditions the application of any ionospheric model results in height differences considerably smaller than one meter.

#### 4.2 Near Real-Time Approach

Compared to the post processing scheme, several aspects had to be considered for near real-time operation. First of all the entire determination sequence had to be automated. Secondly, we had to use ultra-rapid orbits from IGS and a change from daily to hourly GPS data was mandatory. Also the inclusion of the latest state concerning antenna, receiver and satellite information had to be ensured. As an additional feature an email notification service was implemented which automatically sends an error report to the operator in case of an incomplete computation. After collection of the hourly data from the contributing GPS stations, the complete parameter estimation process was finished within 10 minutes after every clock hour. Afterwards, the model parameters were automatically transferred via ftp to the OEGNOS server, where the delivered TEC information was

transformed to vertical delays and furthermore mapped to the desired elevation of the signal by the University of Technology in Vienna. This range correction was finally forwarded to the OEGNOS server.

As previously mentioned, the global and European models from CODE are not suitable for near real-time computations due to their latency. Thus, we replaced them with the predicted ionosphere models from CODE for the final evaluation of the different models.

During the project duration in 2009 and 2010 a very low solar activity was predominate, and therefore differences between the predicted, and the calculated models are in the range of 10 centimetre (Table 1). Concerning the large RMS values it must be noted that Table 1 shows the absolute differences between the PPP solutions based on hourly data and a “true” phase solution (ITRF2005, phase baseline network from post processing, EPN+AMON). During this time a predicted model may be sufficient when the near real-time calculation fails or communication line was truncated. Nevertheless, it has to be emphasized that in case of increasing solar activity or an extreme solar event, the variations are significantly higher.

Finally it should be mentioned that there are fall-back strategies in case that the processing is stopped or the communication line is blocked. Under normal conditions the choice follows the priority starting with the RIM-AUT to the model based on a Taylor series and the predicted GIM

of CODE. If neither of these models is available the static Klobuchar model is used.

	UP [m]	NORTH [m]	EAST [m]
no model applied	1.41	0.88	0.93
Predicted model	1.14	0.49	0.85
Regional model	1.03	0.47	0.79
Taylor Series	1.05	0.50	0.83

**Tab. 1:** RMS of coordinate differences between a PPP solution for station Rottenmann over two weeks in 2009 and a 'true' phase solution

## 5. Conclusions

In case sub-meter accuracy by positioning with GPS and other navigation systems is required, the effect of the ionosphere must be compensated. If using single frequency receivers external support by ionosphere corrections is necessary. While predicted, global and regional models do not differ significantly in periods of low solar activity the use of a model which is created in near real-time by a regional cloud of permanent stations may improve positioning by a decimetre or more. The improvement seems to be moderate for a testbed in the mid-latitude which was presented here, but the gain will be much higher in regions where the impact of the ionosphere is larger like in polar and near-equatorial regions. The work presented in this article demonstrates that regional models of the ionosphere can be used in positioning services with an additional benefit. Sun eruptions like those occurred in October 2003 (Halloween event) demonstrated that a regional ionosphere model is more adaptive than a static global one or one which is computed days afterwards.

## Acknowledgement

The project OEGNOS was supported by the Austrian Federal Ministry for Transport, Innovation and Technology (BMVIT) within the Austrian Space Application Program (ASAP) which is handled by the Austrian research promotion agency, FFG. The authors want to thank the funding authorities as well as the project partners for their excellent cooperation.

## References

- [1] Bruyninx C., (2004), *The EUREF Permanent Network: a multi-disciplinary network serving surveyors as well as scientists*, Geoinformatics, Vol 7, pp. 32-35.
- [2] Dach R., Hugentobler U., Fridez P., Meindl M., (2007), *Bernese GNSS Software Version 5.0.*, Astronomical Institute, University of Bern.
- [3] Dow J.M., Neilan R.E., Rizos C., (2009), *The International GNSS Service in a changing landscape of Global Navigation Satellite Systems*, *Journal of Geodesy* 83:191–198, DOI: 10.1007/s00190-008-0300-3.
- [4] European Union (2010), *EGNOS Homepage*, <http://ec.europa.eu/enterprise/policies/satnav/egnos/>.
- [5] Hofmann-Wellenhof B., Lichtenegger H., Collins J., (2001), *GPS Theory and Practice* 5th revised edition, Springer Wien NewYork.
- [6] Klobuchar J.A., (1987), *Ionospheric Time-Delay Algorithm for Single Frequency GPS Users*, *IEEE Transactions on Aerospace and Electronic Systems*, 23, 325-331.
- [7] *OEGNOS Homepage*, <http://www.oegnos.at/>
- [8] Schaer S, Gurtner W, Feltens J (1998): IONEX: The IONosphere Map EXchange Format Version 1, February 25, 1998. In: Proceedings of the 1998 IGS Analysis Centers Workshop, ESOC, Darmstadt, Germany, 9–11 February 1998, p. 233–247.
- [9] Schaer S. (1999), *Mapping and Predicting the Earth's Ionosphere using the Global Positioning System*, PhD Thesis, University of Berne
- [10] Titz H, Höggerl N, Imrek E, Stangl G. (2009), *Realisierung und Monitoring von ETRIS89 in Österreich*, *Österreichische Zeitschrift für Vermessung & Geoinformation (VGI)*, Heft 2/09
- [11] Wasle E., Kemetinger A., (2011), *Die Verfügbarkeit und Genauigkeit von EGNOS steigern*, *Österreichische Zeitschrift für Vermessung & Geoinformation (VGI)*, Heft 4/10.

## Contacts

Dipl.-Ing. Sandro Krauss, Space Research Institute, Austrian Academy of Sciences, Schmiedlstrasse 6, 8042 Graz; Austria.

E-mail: sandro.krauss@oeaw.ac.at

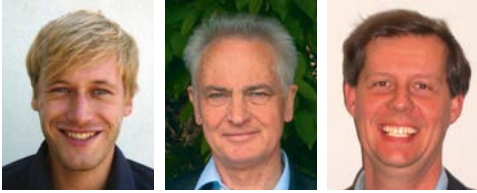
Dipl.-Ing. Andrea Maier, Space Research Institute, Austrian Academy of Sciences, Schmiedlstrasse 6, 8042 Graz; Austria.

E-mail: andrea.maier@oeaw.ac.at

Dipl.-Ing. Mag. Dr. phil. Günter Stangl, Federal Office of Metrology and Surveying, Space Research Institute, Austrian Academy of Sciences, Schmiedlstrasse 6, 8042 Graz; Austria.

E-mail: guenter.stangl@oeaw.ac.at

## Active tectonic deformation at the transition from the European and Pannonian domain monitored by a local GNSS network.



*Gregor Möller, Ewald Brückl and Robert Weber*

### Kurzfassung

Tektonische Prozesse, die zur Bildung der Alpen, Karpathen und Dinariden, sowie der Entstehung des Pannonische Beckens führten, sind auch heute noch aktiv. Der Übergang von der Europäischen Plattform und den Ostalpen hin zum Pannonischen Becken ist davon in besonderer Weise betroffen. Deformationsanalysen von GPS-Netzen bestätigen die anhaltende laterale Extrusion von Teilen der Ostalpen hin zum Pannonischen Becken. Erdbeben und rezente Deformationen konzentrieren sich entlang NE-SW streichender, sinistraler Seitenverschiebungen (Mur-Mürz Störung und Störungssysteme im südlichen Wiener Becken). Dieser Bereich ist auch das Untersuchungsgebiet von ALPAACT (Seismological and geodetic monitoring of **AL**pine-**PA**nnonian **ACT**ive **T**ectonics). Das geodätische Monitoring der aktiven Tektonik erfolgt durch ein lokales GNSS Netz, das sich von der Böhmisches Masse im Norden bis hin zum Steirischen Becken im Süden erstreckt und somit den Bereich der aktiven Störungen gut überdeckt. Die insgesamt 23 Stationen gehören entweder dem IGS-Netz, oder regionalen RTK-Positionierungsdiensten (ÖBB, Wien-Energie, BEWAG, EVN) an. Bislang wurden Daten der Jahre 2007 und 2008 mit der Software Bernese 5.0 unter Berücksichtigung präziser Bahninformation reprozessiert. Die Lösung ist über drei IGS-Stationen in ITRF2000 eingebunden. Für eine geodynamische Interpretation wurden die Geschwindigkeiten auf die Station Graz-Lustbühel (GRAZ) bezogen. Die Streuung der einzelnen Geschwindigkeitsvektoren ist groß und ein systematischer Anteil nicht unmittelbar erkennbar. Die mittlere Geschwindigkeit der südlich des Störungssystems Mur-Mürztal und Wiener Becken gelegenen Stationen gegenüber den nördlich davon gelegenen beträgt 1.1 mm/Jahr und ist ungefähr NE orientiert (Azimuth = 55°). Diese Werte entsprechen nahezu exakt einem kinematischen Modell der Ostalpen, das aus der Struktur der Lithosphäre abgeleitet und mittels regionaler geodätischer Deformationsmodelle kalibriert wurde. Die in der Arbeit präsentierten Ergebnisse sind wegen der geringen Relativbewegungen und kurzen Beobachtungsdauer trotz dieser guten Übereinstimmung nur als vorläufig anzusehen. Eine Beobachtungsdauer von mindestens 10 Jahren wird angestrebt.

**Schlüsselwörter:** ALPAACT, Mur-Mürztal, Wiener Becken, GNSS, Deformationsanalyse

### Abstract

Tectonic processes which led to the generation of the Alps, Carpathians, Dinarides, and the Pannonian basin are still on work. In particular they affect the transition zone from the European platform over the Eastern Alps to the Pannonian basin. GPS network solutions confirm the ongoing lateral extrusion of East Alpine crustal blocks directed to the Pannonian basin. Earthquakes and neo-tectonic deformations are concentrated along NE-SW oriented sinistral strike-slip faults (Mur-Mürz faults and Vienna transfer fault system). This area is the target of ALPAACT (Seismological and geodetic monitoring of **AL**pine-**PA**nnonian **ACT**ive **T**ectonics). The geodetic monitoring of active tectonics in this area is realized by a local GNSS network, which extends from the Bohemian Massif in the north to the Styrian basin in the south and spreads out over the active fault zone. The total of 23 stations belongs either to the IGS network or to regional RTK-positioning services (ÖBB, Wien-Energie, BEWAG, EVN). So far GNSS observation data from the years 2007 and 2008 were reprocessed using the Bernese software 5.0 and precise orbits. The solution is tied to the ITRF2000 by three IGS stations. For a geodynamic interpretation the velocities are referenced to the station Graz-Lustbühel (GRAZ). The individual velocity vectors scatter considerably and a systematic trend cannot be recognized directly. The mean velocity of the stations south of the Mur-Mürz valley and the Vienna basin transfer fault system, relative to the stations located in the north, amounts to 1.1 mm/year. Its orientation is about NE (azimuth = 55°). This result fits nearly perfectly the prediction of a kinematic model which was derived from the structure of the lithosphere and calibrated by regional geodetic deformation models. Due to the low relative velocities and the short observation period, these results should be considered as preliminary. Hence efforts will be made to achieve a geodetic monitoring over a time period of ten years.

**Keywords:** ALPAACT, Mur-Mürz valley, Vienna basin, GNSS, deformation analysis

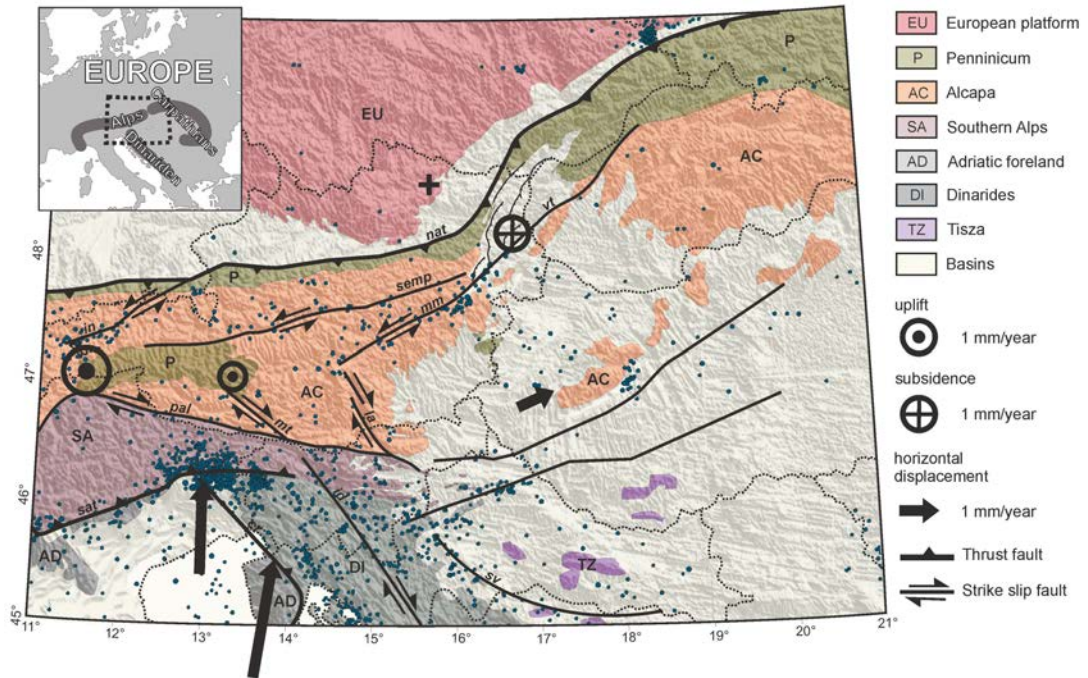


Fig. 1: Tectonic units and structures [7], seismicity (epicentres as blue dots according NEIC catalogue 1973-2008), and crustal deformations, horizontal velocities after [17], vertical velocities referenced to location marked by a bolt cross after [20].

## 1. Introduction

The transition zone from the European to the Pannonian domain is an area of active tectonic deformation. The most relevant process is the ongoing tectonic extrusion of parts of the Eastern Alps towards the Pannonian basin and the Carpathians [1]. Seismic activity, as an indicator of active tectonics, concentrates on a fault system which follows the Mur-Mürz valley (Styria) and the south-eastern boundary of the Vienna basin. The observation of strain and stress accumulation along these faults is of high importance for the estimation of a seismic hazard; especially for the estimation of the maximum credible earthquake in the capital Vienna and its highly populated and developed surrounding area [2]. The project ALPAACT (Seismological and geodetic monitoring of ALpine-PANnonian ACTive Tectonics<sup>1</sup> aims a detailed investigation of active tectonic processes in this area. The high precise estimation of earthquake locations is achieved by a densification of the existing seismic network [3]. Further, these accurate seismic data enable the correlation of the hypocentre location and the

focal mechanisms with the pattern of faults. Geodetic monitoring is essential to correlate tectonic deformation with the seismic stress relief. On the basis of long term observations the partitioning of a slip to different fault systems and to continuous deformation can be estimated. In this paper we give an overview of the tectonic setting of the study area and of previous work on this theme. In addition, the local GNSS network, the reprocessing and results from an observation period of 20 months are described. A preliminary interpretation is presented.

## 2. Geodynamic processes and tectonic setting

The Alpine orogen, its bifurcation into the Western Carpathians and Dinarides, as well as the Pannonian basin give evidence of young geological processes. The opening of the Atlantic during Jura (~170 Ma ago) may be considered as the initiation, and some of these processes are still on work, however, with decreasing intensity. The Seafloor spreading of the Penninic Ocean (Alpine Tethys) ended about 130 Ma and subduction of this ocean initiated ~80 Ma ago, with the European plate representing a passive margin. At the same time the Adriatic micro-plate

<sup>1</sup> <http://info.tuwien.ac.at/geophysik/research/alpdynamics/alpaaact.htm>

started to move independently from Africa to the north, following the trench suction force of the subducting Penninic lithosphere [4], [5], [6]. The collision between Europe and Adria took place about 35 Ma ago [7]. During Miocene the retreat of the remaining Alpine Thetys into the Carpathian embayment led to the development of the Pannonian Basin and finally the Carpathians [8]. Subduction of the Adriatic continental mantle to the west and the east formed the Apennines and Dinarides [9], [10], [11]. Major blocks of the East Alpine and former Western Carpathians extruded laterally to the east into the Carpathian embayment [1], [12], [13]. These units experienced large extension and created the Pannonian basin before their final collision with the Paleozoic European platform and the formation of the Western Carpathians [14].

Figure 1 shows the mayor tectonic units of the Eastern Alps and their surrounding areas. The Bohemian Massif represents the European platform in the north. In the south, Istria represents the part of the Adriatic plate, which was scarcely affected by the Alpine orogenesis. The Molasse basin in the north and the Venetian and Po plain in the south are typical forland basins, generated by the lithospheric load of the Alps. The Flysch belt in the north of the Alps witnesses the occurrence of turbidity currents, which were deposited at the southern margins of the Penninic Ocean. Molasse und Flysch have been widely overthrust by the Northern Calcareous Alps and the Greywacke units. The later form the Eastern Alps together with the crystalline East Alpine nappes and carbonate units in the south. Ophiolitic units derived from the Penninic Ocean have been exhumed within tectonic windows. In the Tauern window even a gneissic core of European provenience is exposed. The Periadriatic line divides the Eastern and Southern Alps. In contrast to the Eastern Alps the vergence of folding is mainly southward directed in the Southern Alps [9], [15]. At the South Alpine thrust fault (SAT) the Adriatic foreland and the Dinarides thrust under the South Alpine units.

The thrusting of Flysch over Molasse and the Northern Calcareous Alps over Flysch at the northern front of the Eastern Alps, as well as the back thrusting of the South Alpine units over the Adriatic foreland and the Dinarides are directly connected to the collision and continuing convergence between the European and Adriatic plates. During the extrusion of ALCAPA units (Eastern Alps-Western Carpathians – Pannonian units) to the east large dextral strike-slip move-

ments occurred along the Periadriatic line and the Mid-Hungarian fault zone. Sinistral strike-slip faults in the north (Inntal, SEMP, MM) and conjugate dextral strike-slip faults in the south (Mölltal – Idria, Lavant – Sava) are related to this extensional tectonic process. The Vienna basin is bound by the sinistral Vienna basin transfer fault in the south – east and was generated by a pull-apart mechanism. Normal faults within this basin compensate for the extension in the basin.

### 3. Active tectonics of the study area

Seismic activity is an indicator of current brittle deformation of the Earth's crust related to active tectonic processes. Earthquakes gather at and around active fault systems. Their magnitudes are related to the size of the rupture surface and the seismic slip. Information about the orientation of the rupture surface and the slip vector can be derived from the radiation pattern (fault plain solution). Epicentres of earthquakes with magnitudes three and higher (NEIC 1973-2008), are superimposed on Figure 1. The area of highest seismicity is the Friuli district in the Southern Alps. Hypocenter locations and focal mechanisms correspond to back-thrusting of the Southern Alps and strike slip movements. Another area of relatively high seismicity is the Mur-Mürz fault and the southern Vienna basin. Focal plane solutions indicate mostly a SW-NE oriented left-lateral strike slip with little dip slip components [16]. Distinct stripes of high seismicity follow the Dinaric thrust belt. The Periadriatic line shows weak seismicity with the exception at its transition to the Mid-Hungarian fault zone.

Figure 1 contains also a compilation of geodetically observed horizontal displacements [17], [18], [19] and elevation changes [20]. These data provide a large scale picture of crustal movements and deformation. The EU platform is considered as fix. The arrows correspond to an Euler pole between 46°–47° N and 8°–10° E and indicate movements approximately to the north with rates between 2.5–3.5 mm/year [17], [18]. North of the South Alpine thrust belt and south of Tauern window is a zone of high compressional strain [17]. This zone extends with decreasing strain to the E and SE, covers the Dinarides, and ceases to the Pannonian basin. Data from dense GPS networks crossing the Alps at the latitude of the Friuli district confirm the regional data and the significant N-S compression in the Southern Alps [21]. E to NE oriented velocities of ~ 1 mm/year of the Pannonian basin indicate that the tectonic escape is an ongoing process. A multi-net-

work GPS combined solution [22] confirms this general deformation pattern and reveals additionally N-S directed extension due to a gravitational collapse within the Tauern window. Besides this extension the Tauern window shows still an uplift rate of ~1 mm/year, the Vienna basin subsides up to 1 mm/year [20].

Plate boundaries of oceanic lithospheres are well defined by the topography of the sea floor, the pattern of magnetic anomalies, the distribution of hypocentres, and geodetically observable deformations. In contrast to the situation on oceans, continental plate boundaries find their expression as >100 km wide fault systems. For example, the fault system related to the plate boundary between Europe and Adria in the central area of the Eastern Alps (Tauern window) reach from the NAT to the SAT which are separated by a distance of ~150 km. However, a clear and well defined identification of a continental plate boundary (especially a destructive plate boundary connected to convergence) can be achieved if the structure of the Moho disconti-

nuity is considered. The interpretation of the data from the seismic experiments CELEBRATION 2000 and ALP 2002 [23], [24] and the integration of results from earlier studies in the Western Alps [25], revealed a fragmentation of the Moho and the uppermost mantle into an EU and AD plate and a newly inferred PA fragment. These three plates (EU, AD, PA) form a triple junction SE of the eastern border of the Tauern window (Figure 2). PA' represents a transition zone from the thick crust under the Dinarides (> 40 km) to the thin and extended crust of the Pannonian basin (< 25 km). We do not further consider this subdivision and include PA' into PA.

Brückl et al. [26] developed a kinematic model (Figure 2) of the relative velocities between AD, EU, and PA under the assumption of a stable triple junction AD-EU-PA, pure strike-slip between PA and EU near the triple junction and the large scale geodetically observed N-S convergence of 3.0 mm/year between AD and EU and 1.0 mm/year eastward extrusion of PA relative to AD. According to this model the conver-

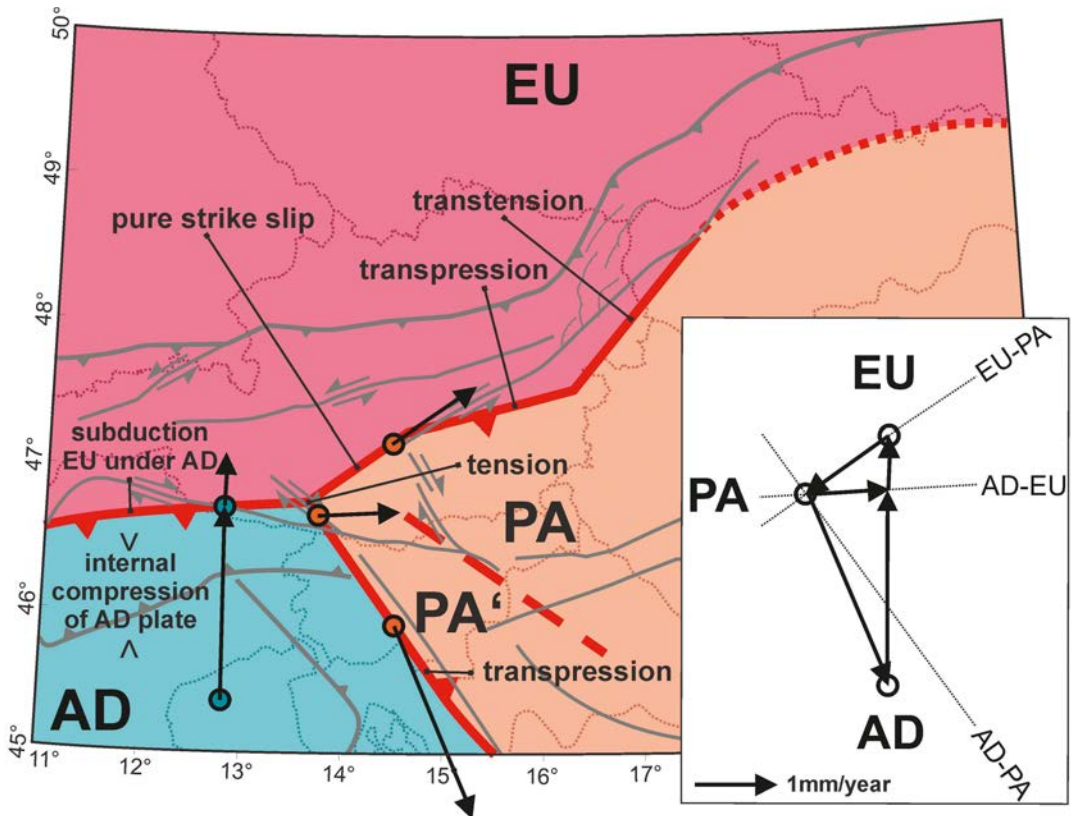


Fig. 2: Kinematic model based on Moho fragmentation red bold lines) into European (EU), Adriatic (AD), and Pannonian plate (PA, PA'); inset shows velocity triangle at the triple junction AD-EU-PA (after Brückl et al., 2010); velocity arrows show the relative velocities of AD to EU, PA to EU, and PA (PA') to AD.

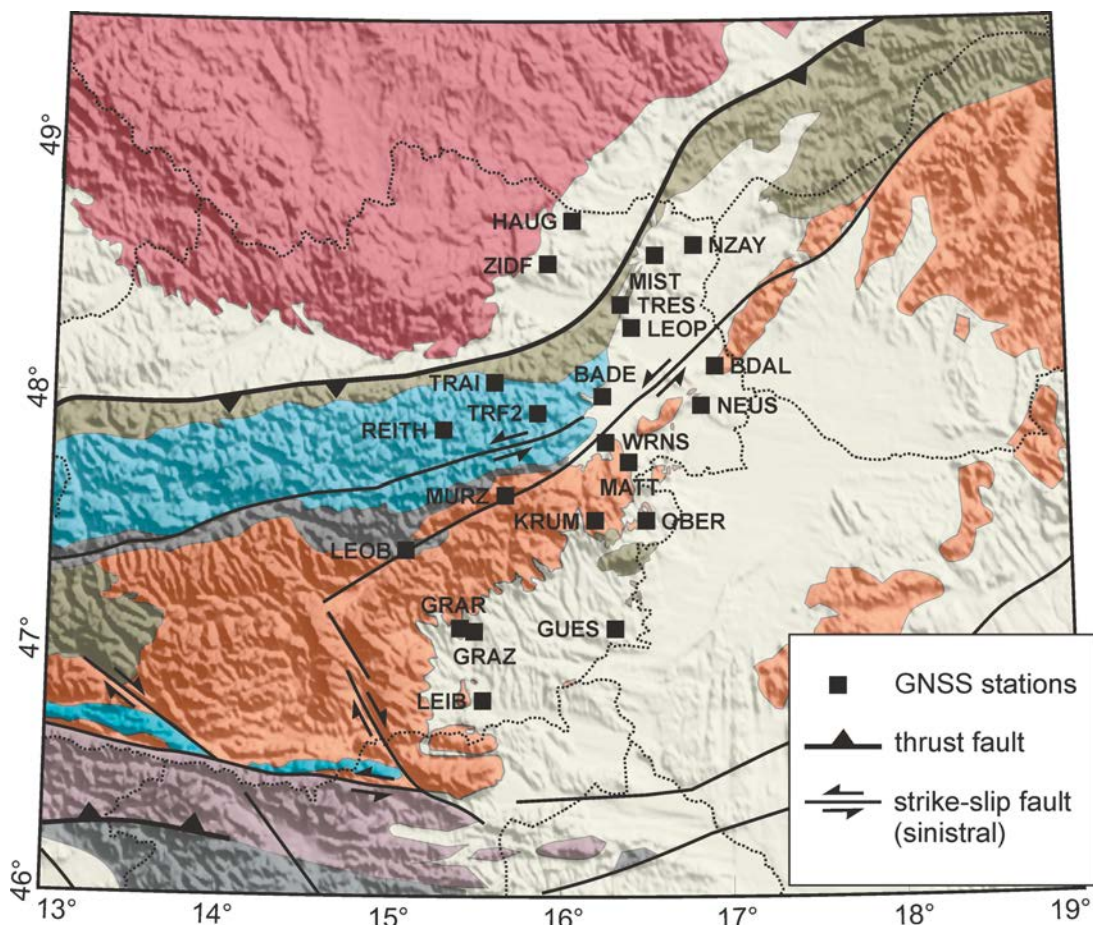


Fig. 3: Location of GNSS stations superimposed on geological map and DTM.

gence between AD und EU can be partitioned into 0.6 mm/year overthrust of AD mantle over EU mantle and 2.4 mm/year compression within the most northern part of AD. At the triple junction PA withdraws from AD to the east by 1.0 mm/year. This extension is being compensated probably by the ongoing extrusion of the Tauern window. South of the compression zone within the Southern Alps the relative velocity between AD and PA changes to dextral transpression with a total amount of 2.5 mm/year. The pure sinistrale strike-slip movement between EU und PA near the triple junction amounts to 1.2mm with an azimuth of 54°. The total amount and the direction of the relative velocity of PA versus EU are preserved further to the NE. However, because of the changing strikes of the MM fault and the Vienna basin transfer fault there is a change to transpression at the MM fault and to transtension along the Vienna basin transfer fault.

#### 4. GNSS stations, data, and reprocessing

In the framework of project ALPAACT observation data of 23 GPS permanent stations obtained in the period Jan 2007 until October 2008 has been reprocessed. These stations belong either to the IGS-network, established for providing high quality GNSS products (e.g. precise satellite orbits and clock corrections) and monitoring geodynamic processes on a global scale (e.g. IGS station network) or to operational regional RTK-positioning services (GNSS sites operated by the Austrian railways (ÖBB) as well as the Austrian power supply companies Wien-Energie, BEWAG and EVN).

As shown in Figure 3 the stations are grouped along the Mur-Mürz and the Vienna basin transfer faults. The most northern stations are located at the Bohemian Massif and the Molasse zone. In the southeast the GNSS network reached into the Styrian basin and to the Pannonian basin. The



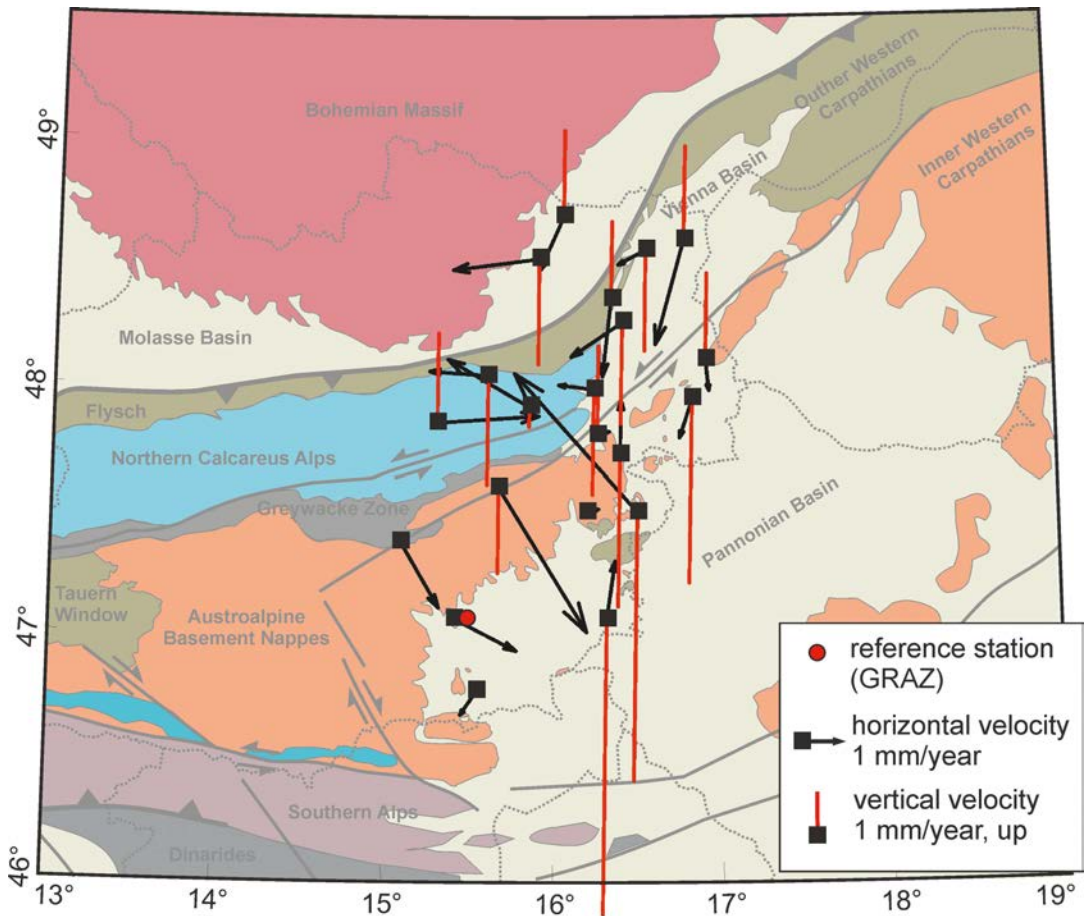


Fig. 4: Horizontal and vertical velocities relative to GRAZ (Graz Lustbühel).

total range of the network covers therefore a wide transition zone from the EU and the PA plate.

Daily station coordinates covering a span of almost 2 years (period from Jan, 1<sup>st</sup>, 2007 until Oct 30<sup>th</sup>, 2008) were calculated by means of a classical network approach to obtain station velocities with respect to the ITRF2000 velocity field. The processing was performed with Bernese Software 5.0 [27]. The solution was tied to the ITRF2000 (epoch 1997.0) frame by relatively tight constraints on the coordinates ( $\sigma = \pm 0.1$  mm) of the IGS reference stations Graz and Mattersburg (indicated in the graphics and attached tables by their labels GRAZ, MTBG) as well as the Hungarian station at Penc (PENC). This most eastern station Penc is situated on the PA plate but was not depicted in (Figure 3) to maintain clarity of the map.

Precise orbit information (Rapid Products) provided by the IGS (International GNSS Service)

was introduced. Observations down to 5 degree elevation were processed and the tropospheric delay was mapped to zenith by the well known dry and wet Niell Mapping Functions. Tropospheric zenith delay parameters were estimated with 2h time resolution by limiting large temporal variations due to relative constraints of  $\pm 2$ mm between subsequent parameters. Utilizing the ionosphere-free linear combination of the dual frequency data ambiguity resolution has been carried out by means of the narrow lane strategy. The formal errors of the resulting daily site coordinates are at the 0.1–0.4mm level, which suggest at least an accuracy of 2–3 mm in plane and about 3–5mm in the height component. In a final step the normal equations of the individual daily solutions were stacked while constraining the ITRF2000 velocities of stations GRAZ, PENC and MTBG tightly ( $\sigma = \pm 0.1$  mm/year). This procedure resulted in a reference coordinate set

and a residual station velocity field with respect to the ITRF2000 velocity field.

A problematic issue are equipment changes. Antenna changes at the stations PENC (in the period from 25.06.2007 till 12.07.2007) and MTBG (10.11.2008) caused artificial jumps in the reference station coordinates and therefore affected the derived velocities of all stations. For both stations these jumps have been carefully corrected by introducing suitable antenna phase centre correction information. These antenna changes can affect the quality of the estimated height component and the subsequently derived height velocities but usually do not affect the horizontal velocities.

In case of missing observation data from at least one reference station the accuracy of the calculated coordinate solution is degraded. Especially in 2008 the days (DOY 001, 133, 230-231, 271, 280-286) are affected by this data-shortage. These daily solutions were excluded from the estimation of the site velocities. Finally, the calculated velocity vector of station Trafelberg (TRFB), which is part of the APOS network (operated by the Austrian Federal Agency for Survey & Metrology) has been derived from a short observation span of 8 months starting in March 2008 until October 2008.

## 5. Results, preliminary interpretation, and discussion

Figure 4 illustrates the horizontal and vertical velocity field obtained by the rotation of the derived velocity information to the local plane. The displayed vectors have to be interpreted as station velocities with respect to the ITRF2000 velocity field (station velocities determined in the ITRF2000 where the velocity of station GRAZ was subtracted). Table 1 depicts the corresponding numerical information.

Histograms of the horizontal and vertical velocity components are shown in Figure 5. The horizontal velocities  $>4$  mm/year at stations OBER and MURZ and the vertical velocities  $<-6$  mm/year at stations GUES and OBER are classified as outliers and not further considered. Mean and standard deviation of the total amount of the horizontal velocities relative to GRAZ are  $1.4 \pm 0.8$  mm/year, the directions scatter considerably. The corresponding vertical velocities amount to  $-0.5 \pm 2.4$  mm/year.

In standard geodetic reference systems all stations belong to the EU plate. However, according to the results of large scale GPS

campaigns [17], [18] and the new picture of the structure of the Moho discontinuity the stations are distributed over EU, PA, and the plate boundary zone between EU and AD (see Figure 5 and Table 1). We investigate two models to describe the horizontal velocity field in a cartesian coordinate system.

First we assume rigid plate motion and model the observed horizontal velocity data by a rotation around the centroid of the GNSS stations (model A). The location of the centroid is fixed by subtracting an average velocity vector from all data. The angle of rotation around the centroid of the stations is determined by minimizing the squared sum of the horizontal velocity residual. Figure 6a shows the calculated and the residual horizontal velocities (= observed minus calculated velocity). The average residual horizontal velocity is reduced to 1.3 mm/year by the translation and by a subsequent anti-clockwise rotation with  $\Omega = 4$  nrad/year.

The second model (model B) considers the fragmentation of the lithosphere into an EU and PA plate. The stations close to the SEMP, Mur-Mürz, and Vienna basin transfer faults (BADE, LEOB, MURZ, WRNS) are not further considered because they are located in the high seismicity area of this active fault system (Figure 1) and an assignment to different plates is not possible. We must be aware that the assumption of a narrow continental plate boundary between EU and PA is inherent in model B. Figure 6b shows the calculated and the residual velocities (= observed minus calculated velocity). The EU plate is fixed by subtracting the average horizontal velocities of the stations located on this plate. The average relative horizontal velocity of PA versus EU is 1.1 mm/year with an azimuth of  $\alpha = 55^\circ$ . The average of the residual horizontal velocities is 1.2 mm/year. For model B it makes sense to look also at the vertical velocities. According to our data PA subsides relative to EU with a velocity of  $0.6 \pm 1.2$  mm/year. Modelling the vertical velocities by this subsidence of PA relative to EU the standard deviation of the residuals is reduced not significantly by less than 0.1 mm/year.

The models A and B reduced the L1 norm of the observed horizontal velocities only slightly. A decision between the two models or their refinement is not possible on the basis of the existing data which cover a time span of only 22 month. The average residual horizontal velocities ( $\sim 1.2$  mm/year) and the standard deviation of the residual vertical velocities after removing the

long	lat	station	location	ve[mm/a]	vn[mm/a]	vu[mm/a]	plate
15.61	48.06	TRAI	Traisen	-1.5	0.1	-2.8	EU
15.31	47.88	REIT	Reith	2.6	0.2	2.3	EU
16.80	48.61	NZAY	Neusiedl/Zayer	-0.7	-2.7	2.4	EU
15.86	47.93	TRFB	Traffelberg	-2.1	1.2	-0.5	EU
16.36	48.37	TRES	Tresdorf	-0.2	-2.0	2.0	EU
15.92	48.63	ZIDF	Ziersdorf	-2.2	-0.3	-2.7	EU
16.07	48.70	HAUG	Haugsdorf	-0.6	-1.4	2.2	EU
16.42	48.27	LEOP	Leopoldau	-1.3	-0.9	-2.6	EU
16.57	48.57	MIST	Mistelbach	-0.7	-0.4	-2.6	EU
15.68	47.61	MURZ	Mürzzuschlag	2.3	-3.7	-2.2	Fault
15.09	47.39	LEOB	Leoben	1.0	-1.7	-0.1	Fault
16.25	48.00	BADE	Baden	-0.9	0.1	-2.7	Fault
16.27	47.82	WRNS	Wiener Neustadt	0.3	0.1	2.3	Fault
16.92	48.12	BDAL	Bad Deutschaltenburg	0.1	-0.8	2.2	PA
16.50	47.51	OBER	Oberpullendorf	-3.2	3.5	-6.9	PA
15.55	46.78	LEIB	Leibnitz	-0.4	-0.6	-0.1	PA
15.49	47.07	GRAZ	Graz (Lustbühel)	0	0	0	PA
16.32	47.07	GUES	Güssing	0.2	1.5	-7.6	PA
15.42	47.07	GRAR	Graz	1.6	-0.8	0.1	PA
19.28	47.78	PENC	Penc, Hungary	0.7	-2.2	1.5	PA
16.84	47.96	NEUS	Neusiedl	-0.3	-1.0	-4.7	PA
16.40	47.74	MTBG	Mattersburg	0.0	1.4	-3.9	PA
16.20	47.50	KRUM	Krumbach	0.3	0.1	0.2	PA

Tab. 1: Approximate reference station coordinates in ITRF2000 and station velocities (north, east, up) tied to the velocity of GRAZ in ITRF2000; last column shows assignment of stations to EU and PA and fault zone according kinematic model B (see text).

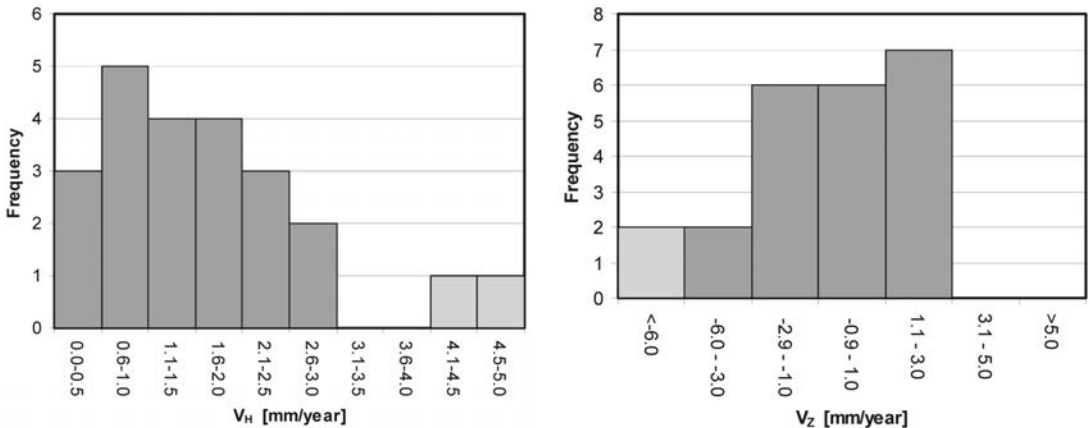


Fig. 5: Frequencies of observed horizontal and vertical velocities relative to GRAR; Values deemed as outliers are marked in light grey.

mean values for the EU and PA plates (2.5 mm/year) may be regarded as an upper bound of the total observational error, including local technical and geological site effects. Comparing the results with the kinematic model presented in Figure 2 we find a surprisingly high agreement. The active fault systems SEMP, MM, and the Vienna basin transfer fault are sinistral strike-slip faults. Model A indicates a counter-clockwise rotation which corresponds to the rotation of sinistral simple shear. An even better agreement is given between model B and the kinematic model. These two models yield nearly the same magnitude of the relative horizontal velocity between EU and PA (1.1 mm/year, respectively 1.2 mm/year). The azimuth of the vector is  $55^\circ$  for model B and  $54^\circ$  for the kinematic model (Figure 2). Considering the ratios between model parameters and observational errors we must be aware that this nearly perfect agreement is accidental. Only a considerably longer observation period could validate this interpretation.

## 6. Conclusion

The Mur-Mürz strike-slip fault and the Vienna basin transfer fault area has been selected to observe actual tectonic deformations due to ongoing lateral extrusion processes at the transition from the Eastern Alps to the Pannonian basin and Western Carpathians. Data from 23 GNSS stations in this area, covering a period of 22 months, were processed, taking advantage of precise orbit information and accurate atmospheric corrections. The mean horizontal velocity relative to the ITRF station GRAZ (Graz Lustbühel) and its standard deviation is  $1.4 \pm 0.8$  mm/year. Data from the stations OBER (Oberpullendorf) and MURZ (Mürzzuschlag) yield horizontal velocities  $> 4$  mm/year and are classified as outliers. The corresponding values of the vertical velocities are  $-0.5 \pm 2.4$  mm/year. The vertical velocities for OBER and GUES (Güssing) are outliers ( $> 6$  mm/year) and not further considered.

In spite of the highly scattered directions of the relative velocities two reasonable geodynamic conceptions were applied to model the observed horizontal velocities. Model A assumes a rigid plate motion and a counter-clockwise rotation of  $\sim 4$  nrad was derived. Model B follows the kinematic model derived from the Moho structure and a partitioning of the area into an EU, AD, and PA plate (Brückl et al., 2010). A nearly perfect agreement of the approximately NE movement of PA versus EU follows from the available data.

Also the counter-clockwise rotation derived from model A and the sinistral strike-slip movement according to model B have the same polarity of the relative movement. However, the reduction of the data variance by the two models is very low (26 % for the more appropriate model B). Time series longer than 10 years would be necessary to decide between different models, or to refine the geophysical model. Public data from GNSS stations neighbouring our investigation area should also be considered in the future.

Considering the length of GNSS time series in the area of interest we argue for "permanent" observations. Earthquakes  $M > 5$  may occur with an average occurrence interval of  $\sim 50$  years along the Mur-Mürz or Vienna basin transfer fault<sup>2</sup>. The seismological observation will continue by ZAMG or further research projects. In order to deepen our understanding of seismicity in this area high resolution and continuous geodetic monitoring is indispensable, for example to estimate seismic slip deficits and seismic hazards [2]. Another point is the spatial resolution of the GNSS network. In order to confine zones by geodetic observations we should at least keep the density of stations. Furthermore, we have to expect outliers in our data, not only because of instrumental problems, "geological noise" (very local movements in the range of mm/year) and velocities of stations near the fault zones (Mur-Mürz, Vienna basin transfer, SEMP) may be also an issue, so far not considered sufficiently.

## Acknowledgements

We acknowledge gratefully the funding of the Project ALPAACT by the Austrian Academy of Sciences. We further say our thanks to Johanna Brückl, who compiled the geological maps and prepared figures.

## References

- [1] Ratschbacher L., Frisch W., Linzer H.-G. and Merle O.: Lateral extrusion in the Eastern Alps, Part 2.: Structural analysis, *Tectonics*, 10, 2, 257-271, 1991
- [2] Hinsch R. and Decker K.: Seismic slip rates, potential subsurface rupture areas and seismic potential of the Vienna Basin Transfer Fault, *Int J Earth Sci (Geol Rundsch)*, DOI 10.1007/s00531-010-0613-3, 2010
- [3] Apoloner M.-T., Brückl E., Brückl J., Loderer W., Mertl S. and Schurr B.: Location performance of the ALPAACT seismic network, *Geophysical Research Abstracts*, Vol. 13, EGU2011-6950-1, 2011
- [4] Le Pichon X., Bergerat F. and Roulet M.-J.: Plate kinematics and tectonics leading to the Alpine belt formation: A new analysis, in: *Processes in Continental Lithospheric*, 1988

<sup>2</sup> <http://www.zamg.ac.at/erdbeben>

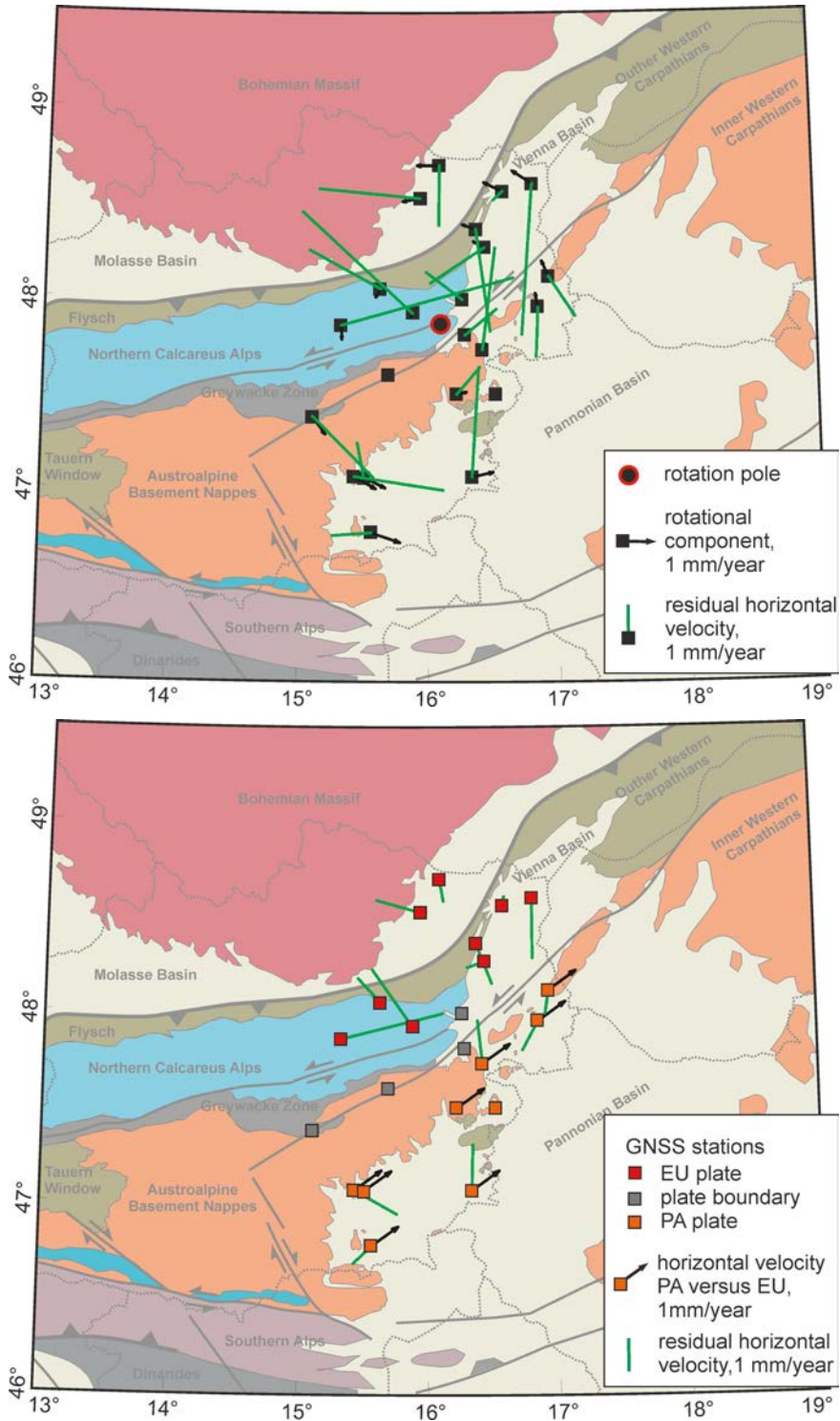


Fig. 6: Interpretation of observed horizontal velocity field; a) modelling by a rotation with the centroid of all stations as rotation pole; b) modelling by translation of stations located on PA relative to stations located on EU; stations located on or near the Mur-Mürz, SEMP, and Vienna basin transfer faults are excluded.

- [5] *Stampfli G.M. and Kozur H.W.*: Europe from the Variscan to the Alpine cycles. in *European Lithosphere dynamics*, In: *European Lithosphere Dynamics*, D.G., Gee, R.A. Stephenson, (Ed.), *Geolog. Soc. London Memoirs*, 32, London, pp. 129-145, 2006
- [6] *Handy M. et al.*: Reconciling plate-tectonic reconstructions of Alpine Tethys with the geological-geophysical record of spreading and subduction in the Alps, *Science Reviews*, doi: 10.1016/j.earscrev.2010.06.002, 2010
- [7] *Schmid S.M., Fügenschuh B., Kissling E. and Schuster R.*: Tectonic map and overall architecture of the Alpine orogen, *Eclogae Geologicae Helvetiae*, 97, 93-117, 2004
- [8] *Royden L.H.*: Evolution of retreating subduction boundaries formed during continental collision, *Tectonics*, 12 (3), 629-638, 1993
- [9] *Doglioni C. and Carminati E.*: The effects of four subductions in NE Italy, *Mem. Sci. Geol.*, 54, ISSN 0391-8602, 1-4, 2002
- [10] *Pamić J., Tomljenović B. and Balen D.*: Geodynamic and petrogenetic evolution of Alpine ophiolites from the central and NW Dinarides: an overview, *Lithos*, 65, 113-142, 2002
- [11] *Horváth F., Bada G., Szafián P., Tari G., Ádám A. and Cloething S.*: Formation and deformation of the Pannonian basin: constraints from observational data, in: *European Lithosphere Dynamics*, edited by D.G. Gee and R.A. Stephenson, *Geological Society London Memoir*, 32, pp. 129-145, London, 2006
- [12] *Linzer H.-G., Decker K., Peresson H., Dell'Mour R. and Frisch W.*, *Balancing lateral orogenic float of the Eastern Alps*, *Tectonophysics*, 354, 211-237, 2002
- [13] *Decker K. and Peresson H.*: Tertiary kinematics in the Alpine-Carpathian-Pannonian system: links between thrusting, transform faulting and crustal extension, In: *Oil and Gas in Alpidic Thrustbelts and Basins of Central and Eastern Europe*, Wessely G. and Liebl W. (Ed.), *EAGE, Spec. Publ.*, 5, 69-77, 1996
- [14] *Ustaszewski K., Schmid S.M., Fügenschuh B., Tischler M., Kissling E. and Spakman W.*: A map-view restoration of the Alpine-Carpathian-Dinaridic system for the Early Miocene, *Swiss J. Geosci.*, 101, Supplement 1, 273-294, 2008
- [15] *Castellarin A., Nicolich R., Fantoni R., Cantelli L., Sella M. and Selli L.*: Structure of the lithosphere beneath the Eastern Alps (southern sector of the TRANSALP transect), *Tectonophysics*, 414(1- 4) , 259-282, doi:10.1016/j.tecto.2005.10.013, 2006
- [16] *Reinecker J. and Lenhardt W.A.*, *Present-day stress field and deformation in eastern Austria*, *Int. Journ. Earth Sciences*, 88, 532-530. 1999
- [17] *Grenerczy G. and Kenyeres A.*: Crustal deformation between Adria and the European platform from space geodesy, in the Adria microplate: GPS geodesy, tectonics and hazards, edited by Pinter N., Grenerczy G., Weber J., Stein S. and Medak D., *NATO Science Series IV: Earth and Environmental Sciences*, 61, pp. 321-334, Springer, 2006
- [18] *Weber J., Vrabec M., Stopar B., Pavlovic-Preseren P. and Dixon T.*: The PIVO-2003 Experiment: A GPS Study of Istria Peninsula and Adria Microplate motion, and active tectonics in Slovenia, in *The Adria microplate: GPS geodesy, tectonics and hazards*, edited by Pinter N., Grenerczy G., Weber J., Stein S. and Medak D.: *NATO Science Series IV: Earth and Environmental Sciences*, 61, Springer, Wien, New York, 321-334, 2006
- [19] *Haslinger C., Kraus S. and Stangl G.*: The Intra-Plate Velocities of GPS Permanent Stations of the Eastern Alps, *VGI*, 95 (2), ISSN 0029-9650, 2006
- [20] *Höggerl N.*: Bestimmung von rezenten Höhenänderungen durch wiederholte geodätische Messungen, in: *Die Zentralanstalt für Meteorologie und Geodynamik 1851–2001*, edited by Hammerl Ch., Lenhardt W., Steinacker R. and Steinhauser P., *Leykam, Graz*, ISBN 3-7011-7437-7, 2001
- [21] *Völksen C. and Gerlach C.*: Geodätische Forschung in den Alpen. 16. Internationale Geodätische Woche Obergurgl 2011, *Proceedings*. Editors Grimm-Pitzinger/Weinold, Wichmann, Berlin, ISBN 978-3-87907-505-8, 226-229, 2011
- [22] *Caporali A., et al.*: Surface kinematics in the Alpine-Carpathian-Dinaric and Balkan region inferred from a new multi-network GPS combination solution, *Tectonics*, 474, doi:10.1016/j.tecto.2009.04.35, 2009
- [23] *Behm M., Brückl E., Chwatal W. and Thybo H.*: Application of stacking techniques to 3D wide-angle reflection and refraction seismic data of the Eastern Alps, *Geophys. J. Int.*, 170(1), 275-298, doi:10.1111/j.1365-246X.2007.03393.x., 2007
- [24] *Brückl E., Bleibinhaus F., Gosar A., Grad M., Guterich A., Hrubcova P., Keller R., Majdanski M., Sumanovac F., Tiira T., Yliniemi J., Hegedüs E., Thybo H.*: Crustal structure due to collisional and escape tectonics in the Eastern Alps region based on profiles Alp01 and Alp02 from the ALP 2002 seismic experiment, *J. Geophys. Res.*, 112, B06308, doi:10.1029/2006JB004687, 2007
- [25] *Waldhauser F.R., Kissling E., Ansorge J. and Mueller St.*: Three-dimensional interface modelling with two-dimensional seismic data: The Alpine crust-mantle boundary, *Geophys. J. Int.*, 135, 264-278, 1998
- [26] *Brückl E., Behm M., Decker K., Grad M., Guterch A., Keller G.R. and Thybo H.*: Crustal structure and active tectonics in the Eastern Alps, *Tectonics*, 29, doi:10.1029/2009TC002491, 2010
- [27] *Dach R., Hugentobler U., Fridez P., Meindl M.*: *Bernese GPS Software Version 5.0*. Astronomical Institute University of Berne, Switzerland, 2007

## Contacts

Dipl.-Ing. Gregor Möller, Institute of Geodesy and Geophysics, Vienna University of Technology, Gusshausstrasse 27-29, 1040 Vienna, Austria.  
E-mail: gregor.moeller@tuwien.ac.at

Em.O.Univ.Prof. Dipl.-Ing. Dr.phil. Ewald Brückl, Institute of Geodesy and Geophysics, Vienna University of Technology, Gusshausstrasse 27-29, 1040 Vienna, Austria.  
E-mail: ebrueckl@mail.tuwien.ac.at

a.o. Prof. Dipl.-Ing. Dr. Robert Weber, Institute of Geodesy and Geophysics, Vienna University of Technology, Gusshausstrasse 27-29, 1040 Vienna, Austria.  
E-mail: robert.weber@tuwien.ac.at

## Ray-traced tropospheric slant delays in VLBI analysis



Vahab Nafisi, Matthias Madzak, Johannes Böhm, Harald Schuh and Alireza A. Ardalan

### Abstract

Modeling troposphere delays is a major source of error in the analysis of observations from space geodetic techniques, such as Very Long Baseline Interferometry (VLBI). Numerical weather models (NWM) have been continuously improving with regard to spatial and temporal resolution as well as advances in data assimilation and thus provide valuable datasets for atmospheric research. The improved accuracy of NWMs have made ray-tracing a suitable technique to estimate the slant total delays for the observations in the neutral atmosphere, i.e. mainly in the troposphere. We have developed a direct ray-tracing method for estimating those slant delays for radio signals using data of the European Centre for Medium-range Weather Forecasts (ECMWF) which is based on the solution of the Eikonal equation. We show results for a two-week campaign of continuous VLBI sessions in 2008 (CONT08), where we applied ray-traced delays to the observed delays and analyzed the repeatability of baseline lengths in comparison to a standard approach with zenith delays and mapping functions. We find that on average, baseline length repeatabilities are similar if residual zenith delays and gradients are estimated. On the other hand, as expected, ray-traced delays perform better if residual zenith delays and gradients are not solved for in VLBI analysis.

**Keywords:** Ray-tracing, CONT08, Tropospheric delay, Refractivity

### Kurzfassung

Die Modellierung der troposphärischen Laufzeitverzögerung ist eine der Hauptfehlerquellen für die Auswertung von Beobachtungen geodätischer Weltraumverfahren wie der Very Long Baseline Interferometry (VLBI). Numerische Wettermodelle wurden in den vergangenen Jahren hinsichtlich ihrer räumlichen und zeitlichen Auflösung sowie bezüglich ihrer Genauigkeit verbessert, und dadurch eignen sie sich sehr gut für die Atmosphärenforschung. Zum Beispiel können numerische Wettermodelle dafür verwendet werden, Strahlverfolgung (Ray-tracing) zu rechnen, um die troposphärische Laufzeitverzögerung zu bestimmen. Wir haben einen Algorithmus für direktes Ray-tracing entwickelt, um diese Laufzeitverzögerungen von Signalen im Radiowellenbereich mit Hilfe von Wetterdaten des European Centre for Medium-Range Weather Forecasts (ECMWF) zu berechnen, wobei der Ray-tracing Algorithmus auf einer Lösung der Eikonal-Gleichung basiert. Gezeigt werden Ergebnisse in Form von Wiederholbarkeiten der Basislinienlängen einer zweiwöchigen kontinuierlichen VLBI-Beobachtungskampagne im Jahr 2008 (CONT08). Die erhaltenen Basislinienlängen, abgeleitet mit Verwendung der Laufzeitverzögerungen aus Ray-tracing, werden mit jenen verglichen, die Laufzeitverzögerungen eines Standardansatzes verwenden. Der Standardansatz beschreibt die Modellierung der schrägen Laufzeitverzögerung als Produkt einer Zenitlaufzeitverzögerung und einer Projektionsfunktion. Die erhaltenen Wiederholbarkeiten zeigen ähnliche Werte für die beiden Modellierungsmöglichkeiten, wenn Zenitlaufzeitverzögerungen und Gradienten in der Auswertung mitgeschätzt werden. Allerdings werden bessere Ergebnisse mit Ray-tracing erzielt, wenn diese beiden Größen in der Ausgleichung nicht geschätzt werden.

**Schlüsselwörter:** Strahlverfolgung, CONT08, Troposphärische Laufzeitverzögerung, Refraktivität

### 1. Introduction

The troposphere is a composition of dry gases and water vapor, which imposes a time delay of propagating electromagnetic waves. Furthermore, an inhomogeneous medium causes an electromagnetic (EM) wave to propagate along a curved path, which is called the bending effect. Because of these two effects on space geodetic observations, the observed distances will be longer than the straight line distances between the receiver and transmitter in vacuum. In this

paper, the combination of both effects will be called the total delay.

Tropospheric delay modeling has always been an important issue in space geodetic data analysis. As described by the IERS Conventions 2010 (Petit and Luzum, 2010 [1]) a priori hydrostatic zenith delays are usually determined from the surface pressure as suggested by Saastamoinen (1972 [2]), which are then mapped down to the elevation of the observation with the hydrostatic mapping function (Davis et. al., 1985 [6]),

while wet zenith delay parameters are estimated with the wet mapping function as partial derivative. Tropospheric gradient effects are estimated to account for the azimuthal asymmetry of the delays (Chen and Herring, 1997 [3]). Modern mapping functions such as the Vienna Mapping Functions 1 (VMF1; Böhm et al., 2006a [4]) and the Global Mapping Functions (GMF, Böhm et al., 2006b [5]) are based on numerical weather models (NWMs). In particular with the VMF1, the variability of the coefficients with respect to location of the site and time of observation is accounted by 6-hourly meteorological data sets provided by the European Centre for Medium-range Weather Forecasts (ECMWF).

NWMs have been continuously improving with regard to their spatial and temporal resolution as well as with regard to advances in data assimilation. This enhanced accuracy of NWMs has made ray-tracing a promising technique to determine the total delay.

This paper discusses the application of the ray-tracing method for calculating total tropospheric delays in VLBI analysis. In Section 2 we introduce the refractivity of moist air. In Section 3 the ray-tracing method will be discussed, which is developed for total delay computations in two dimensions. In Section 4 we show some results about applying ray-traced delays in CONT08 VLBI analysis. Outlook and concluding remarks from this research are summarized in Section 5.

## 2. Refractive index of moist air

For a medium, the refractive index  $n$  is defined as the ratio of the velocity of an electromagnetic wave in vacuum to the speed of propagation in this medium as stated in Equation (1)

$$n = \frac{c}{v}, \quad (1)$$

where  $c$  and  $v$  are phase velocities in vacuum and in the medium, respectively. The refractive index of a signal in moist air is slightly different from unity, and  $(n-1)$  is small. Therefore, it is more convenient to introduce and use another parameter named refractivity  $N$  with  $N = (n-1) \times 10^6$ . The refractivity  $N$  of moist air is expressed as (Davis, 1986 [7])

$$N = k_1 \frac{p}{T} + \left( k_2' \frac{e}{T} + k_3' \frac{e}{T^2} \right) Z_v^{-1} = N_h + N_{nh}, \quad (2)$$

where  $k_2'$  is

$$k_2' = k_2 - k_1 \frac{R_d}{R_v} \quad (3)$$

and  $Z_v$  is the water vapor compressibility factor, which in normal conditions is close to one (Kleijer, 2004 [11]).

The parameters  $p$ ,  $T$ , and  $e$  are total pressure, temperature, and water vapor pressure, respectively. Additionally, we need the gas constants for dry air ( $R_d$ ) and water vapor ( $R_v$ ). The parameters  $k_1$ ,  $k_2$  and  $k_3$  are refractivity coefficients; for these investigations we have used the 'best average' coefficients suggested by Rüeiger (2002 [8]), which are  $k_1 = 77.6890 \times 10^{-2} \text{K/hPa}$ ,  $k_2 = 71.2952 \times 10^{-2} \text{K/hPa}$ , and  $k_3 = 375.463 \times 10^3 \text{K}^2/\text{Pa}$ .

## 3. Total tropospheric delay

The total delay can be defined as the difference between the propagation time of a specific wave in a real medium (in our case the troposphere), and in vacuum. In ideal conditions, which means without any dispersion, the path of the ray between the receiver and the source of the wave (a quasar in VLBI) will be a straight line.

$$S = \int_V ds. \quad (4)$$

On the other hand, due to variations in the tropospheric refractive index, the real path of the ray is defined as

$$L = \int_T n(r, \theta, \lambda, t) ds, \quad (5)$$

where  $r$  is the radial distance,  $\theta$  is the co-latitude, and  $\lambda$  is the longitude ( $0 \leq \theta \leq \pi$ ,  $0 \leq \lambda \leq 2\pi$ ).  $n(r, \theta, \lambda, t)$  describes the dependency of refractivity on the position of the site and also on the time of observation. Using Equations (4) and (5) and considering refractivity instead of index of refractivity, the total tropospheric delay reads as

$$\Delta\tau = 10^{-6} \int_T N(r, \theta, \lambda, t) ds + \left( \int ds - S \right). \quad (6)$$

The first term of Equation (6) represents the signal delay along the path, which causes the excess of the path. The second term denotes the so-called geometric delay. The first term inside the bracket is along the curved path  $T$ . Note that the bending effect is not synonymous with the geometric delay, since the along-path delay is evaluated along the bent ray path. Inserting Equation (2) into Equation (6), we have

$$\Delta\tau = 10^{-6} \int_T N_h(r, \theta, \lambda, t) ds + \left( \int ds - S \right) + 10^{-6} \int_T N_{nh}(r, \theta, \lambda, t) ds + \left( \int ds - S \right) \quad (7)$$

$$\Delta\tau = \Delta\tau_h + \Delta\tau_{nh} + \Delta\tau_b. \quad (8)$$



Equation (8) shows the different components of the signal delay due to tropospheric propagation effects, i.e. the hydrostatic ( $\Delta\tau_h$ ) and non-hydrostatic ( $\Delta\tau_{nh}$ ) parts as well as the bending effect  $\Delta\tau_b$ , which depends on total refractivity. The propagation path is also determined by the total refractivity. The total tropospheric delay can be determined by direct ray-tracing using the well known Eikonal equation, which can be expressed as (Wheeler 2001 [9])

$$|\nabla L_i|^2 = n(r, \theta, \lambda, t)^2. \quad (9)$$

In this equation  $\nabla L_i$  shows the components of the ray directions and  $L$  is the optical path length. Equation (9) is a partial differential equation of the first order for  $n(r, \theta, \lambda, t)$  and it can be expressed in many alternative forms. In the 3D case there are seven partial derivative equations, and six of them must be solved simultaneously and the seventh equation is Equation (5) (Cerveny, 2005 [10]). Tropospheric ray-tracing mainly deals with the determination of total delays along the ray path and thus one parameter of interest is the arc-length along the ray. The final output of this equations system will be the position of any point along the trajectory of the ray. In addition we must mention that our method is developed in orthogonal spherical coordinates, which is more suitable and meaningful for our purpose, but ray-tracing systems can be expressed and solved in any curvilinear coordinate system, including non-orthogonal systems.

Equation (9) can be easily reduced to 2D ray-tracing by neglecting out of plane components of the ray path. In this case, we assume that the ray will stay in a plane of constant azimuth.

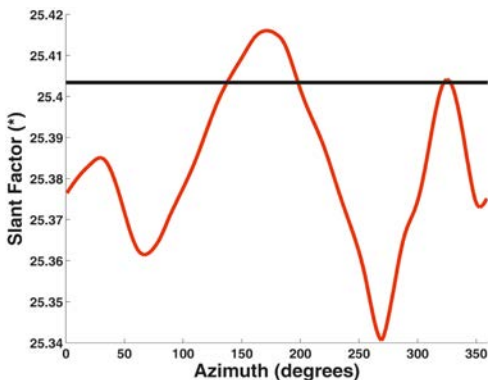


Fig. 1: Slant factors for 5 degrees elevation using the ray-tracing package (red) and VMF1 (black) for the station Tsukuba, on 18 August 2008. (\*) Ray-traced slant factors are multiplied by the nominal value 2.5 m.

For our ray-tracing system we use pressure level data from the European Centre for Medium-range Weather Forecasts (ECMWF). The resolution of the dataset is 0.5 degrees and 25 pressure levels have been interpolated and extrapolated to provide reasonable incremental step sizes for solving the Eikonal Equation (9) as well as the numerical integration in Equation (7). Coordinates of the site, time of the observation and outgoing elevation angle and azimuth of the ray are other important inputs to a typical ray-tracing software. Outputs of this method are the total delays of the observations, which are used as an input to the VLBI software. Figure 1 shows the slant factors (slant total delays divided by zenith total delays) from ray-tracing as well as for VMF1.

#### 4. Data analysis using CONT08 observations

The ray-traced tropospheric delays are included in the analysis of VLBI observations of CONT08, a two-week VLBI campaign in August 2008. For this purpose the Vienna VLBI Software (VieVS) has been adopted to read external files with the ray-traced delays. The criterion for the validity of this approach is the baseline length repeatability, i.e., the standard deviation of baseline lengths in the case of CONT08. The results are compared to those of a standard approach where a priori total delays are set up as the sum of hydrostatic and wet slant delays, each of them being the product of the zenith delay derived from data of the ECMWF and the respective VMF1 (Böhm et al., 2006a [4]). Thus in both cases, ray-tracing and ECMWF/VMF1, the a priori delays include the wet part, and if residual zenith delays are estimated the wet VMF1 is used as partial derivative with ECMWF/VMF1 and the wet Global Mapping Function (GMF, Boehm et al., 2006b [5]) with ray-tracing. We have considered three cases:

##### 4.1 Estimating zenith delays and gradients

Figure 2 shows the baseline length repeatabilities for all baselines of the CONT08 experiment using the two models. Gradients are estimated in the analysis as well as wet zenith delays

For 31 of all 55 baselines the repeatability is better if using ECMWF/VMF1. The maximum degradation using ray-traced delays instead of ECMWF/VMF1 is 2.4 mm whereas the mean degradation is  $0.6 \text{ mm} \pm 0.6 \text{ mm}$ . On the other hand the remaining 24 baselines show a smaller (better) repeatability using ray-traced delays: the maximum improvement is 2.2 mm with an average of  $0.5 \text{ mm} \pm 0.6 \text{ mm}$ . Station TIGO is part

of the two baselines showing the maximum improvement and the maximum degradation. This cannot be explained and further investigations must be done. However, the smaller number of observations at TIGO can be a contributing reason.

#### 4.2 Estimating zenith delays, not estimating gradients

Another analysis was carried out without estimating gradients. Since ray-tracing solves the Eikonal equation, atmospheric asymmetry is already taken into account in this method. On the other hand the model ECMWF/VMF1 calculates the total delay as a product of zenith delays and mapping functions and therefore does not consider the azimuthal asymmetry of the atmosphere. Repeatabilities are shown in Figure 3.

Baselines shorter than about 6000 km show clearly better results using ray-tracing instead of ECMWF/VMF1. In total, 36 of 55 baselines show smaller repeatabilities using ray-traced delays compared to delays from the second model. The benefit becomes smaller for longer baselines and, for most baselines longer than about 9000 km, ECMWF/VMF1 models the tropospheric path delay more accurately than ray-tracing. The differences of repeatabilities of the two models increase without estimating gradients.

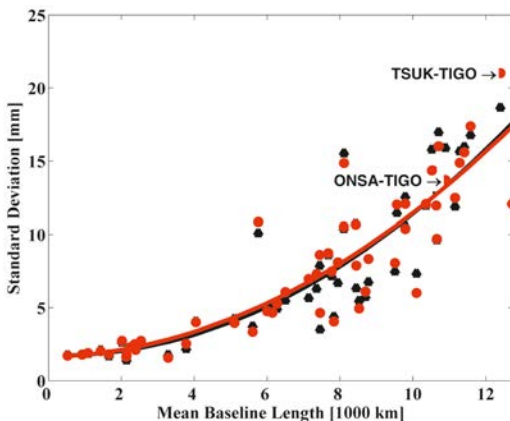


Fig. 2: Baseline length repeatabilities for CONT08 using ray-traced delays (black plus signs) and delays from the ECMWF/VMF1 (red triangles) versus baseline lengths. The solid lines show least squares polynomial curves of second order for both models for better comparability. Residual zenith delays and gradients are estimated. Two baselines showing the maximum degradation (Tsukuba-TIGO) and the maximum improvement (Onsala-TIGO), respectively, if ray-traced delays were used, are marked separately (arrows).

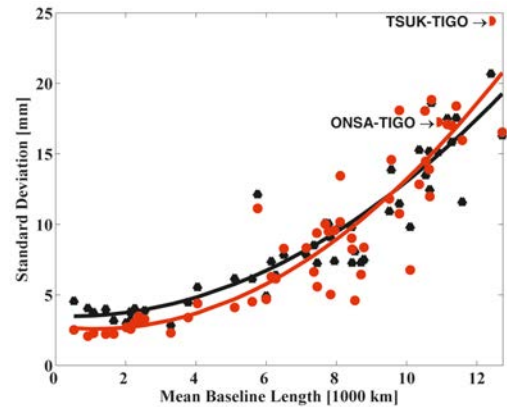


Fig. 3: Baseline length repeatabilities for CONT08 using ray-traced delays (black plus signs) and delays from ECMWF/VMF1 (red triangles) versus baseline lengths. Residual zenith delays were estimated, but no gradients. The solid lines show least squares polynomial curves of second order for both models.

#### 4.3 Neither estimating zenith delays, nor estimating gradients

Wet zenith delays are usually estimated in the analysis as mentioned before. As both models already contain the wet part in their total delay, the additional estimation of a residual zenith delay might be unnecessary. However, in a third run baseline length repeatabilities are obtained without estimating gradients and without estimating residual zenith delays (Figure 4).

Repeatabilities increase significantly for both models compared to the results displayed in

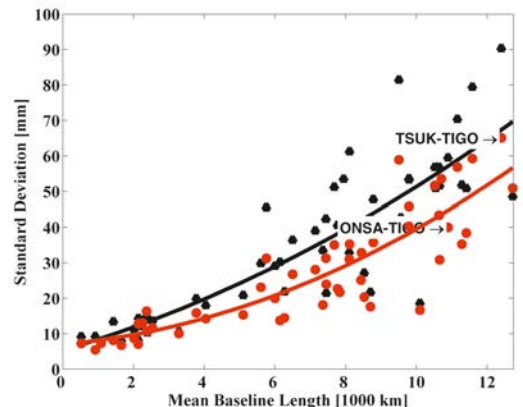


Fig. 4: Baseline length repeatabilities for CONT08 using ray-traced delays (black plus signs) and delays from ECMWF/VMF1 (red triangles). No gradients and no wet zenith delays were estimated in the analysis. The solid lines show least squares polynomial curves of second order for both models.

Figure 3. This shows clearly that residual zenith delays should be estimated also when using ray-traced delays. With ray-traced delays results are better compared to ECMWF/VMF1: 50 of 55 baselines (91%) show smaller standard deviations with ray-tracing. The mean improvement using ray-traced delays instead of ECMWF/VMF1 is 9.5 mm.

## 5. Concluding remarks

Ray-traced delays, obtained from the equation system shown in Section 3, were used to correct VLBI observations for the influence of the troposphere. Their quality was assessed by comparing baseline length repeatabilities for CONT08 to those derived from a standard approach with elevation-dependent mapping functions. The conclusions are: (1) On average, ray-traced delays yield an accuracy similar to the standard approach. However, taking a closer look, at some stations ray-traced delays provide better tropospheric corrections, whereas at other stations the corrections are worse compared to standard elevation-dependent models. To find the reason, more investigations need to be carried out. (2) In both cases the additional estimation of gradients and residual zenith delays is considered necessary since it improves the results.

## Acknowledgments

We like to thank the International VLBI Service for Geodesy and Astrometry (IVS) (Schlüter and Behrend 2007 [12]) for coordinating the CONT08 campaign.

J. Böhm thanks the Zentralanstalt für Meteorologie und Geodynamik (ZAMG) for granting access to data of the ECMWF.

V. Nafisi thanks the Austrian Science Fund (FWF) for supporting this research under project P20902-N10 (GGOS Atmosphere). V. Nafisi would also like to acknowledge the Iran Ministry of Science, Research and Technology (MSRT) and the University of Isfahan for funding part of his research at Vienna University of Technology.

## References

- [1] Petit, G. and B. Luzum, (Eds.) (2010). *IERS Conventions (2010)*. Frankfurt am Main: Verlag des Bundesamts für Kartographie und Geodäsie, Frankfurt, ISBN 1019-4568, IERS Technical Note 36, pp. 179.
- [2] Saastamoinen, J. (1972). *Atmospheric correction for the troposphere and stratosphere in radio ranging of satellites*. In *The Use of Artificial Satellites for Geodesy*, eds. S. W. Henriksen, A. Mancini, and B. H. Chovitz, Vol. 15 of *Geophysical Monograph Series*, American Geophysical Union, Washington, D.C., ISBN 0-87590-015-1, 247–251.
- [3] Chen, G. and T.A. Herring (1997), *Effects of atmospheric azimuthal asymmetry on the analysis of space geodetic data*. *J. Geophys. Res.*, 102(B9), 20489–20502.
- [4] Böhm, J., B. Werl, and H. Schuh (2006a), *Tropospheric mapping function for GPS and very long baseline interferometry from European Center for Medium-range Weather Forecasts operational analysis data*. *J. Geophys. Res.*, 111, B02406, doi:10.1029/2005JB003629.
- [5] Böhm, J., A. Niell, P. Tregoning, and H. Schuh (2006b), *The Global Mapping Function (GMF): A new empirical mapping function based on data from numerical weather model data*. *Geophys. Res. Lett.*, 33, L07304, doi:10.1029/2005GL025546.
- [6] Davis, J.L., T. A. Herring, I. I. Shapiro, A. E. E. Rogers, and G. Elgered (1985), *Geodesy by radio interferometry: Effects of atmospheric modeling errors on estimates of baseline length*, *Radio Science*, Vol. 20, No. 6, pp. 1593–1607.
- [7] Davis, J.L. (1986), *Atmospheric propagation effects on radio interferometry*. Ph. D. thesis, Harvard College Observatory, Massachusetts Institute of Technology, USA. <http://hdl.handle.net/1721.1/27953>
- [8] Rüeeger, J.M. (2002). *Refractive index formulae for radio waves*. FIG XXII International Congress, International Federation of Surveyors (FIG), Washington, D.C., [http://www.fig.net/pub/fig\\_2002/Js28/JS28\\_rueger.pdf](http://www.fig.net/pub/fig_2002/Js28/JS28_rueger.pdf).
- [9] Wheelon, A.D. (2001), *Electromagnetic scintillation : Geometrical optics*. Cambridge University Press, pp 455.
- [10] Cerveny V. (2005), *Seismic ray theory*, Cambridge University Press, New York, pp 713.
- [11] Kleijer F., (2004), *Tropospheric Modeling and Filtering for Precise GPS Leveling*, PhD Thesis, TU Delft, pp. 262. [http://enterprise.lr.tudelft.nl/publications/files/ae\\_kleijer\\_20040413.pdf](http://enterprise.lr.tudelft.nl/publications/files/ae_kleijer_20040413.pdf)
- [12] Schlüter W, Behrend D (2007) *The International VLBI Service for Geodesy and Astrometry (IVS): current capabilities and future prospects*. *J Geodesy*, 81(6–8): 379–387. doi:10.1007/s00190-006-0131-z.

## Contacts

**Vahab Nafisi**, Institute of Geodesy and Geophysics, Vienna University of Technology, Austria; Department of Surveying and Geomatics Engineering, College of Engineering, University of Tehran, Iran; Department of Surveying Engineering, Faculty of Engineering, The University of Isfahan, Iran.

E-mail: vahab.nafisi@tuwien.ac.at, nafisi@eng.ui.ac.ir

**Matthias Madzak**, Institute of Geodesy and Geophysics, Vienna University of Technology, Austria.

E-mail: matthias.madzak@tuwien.ac.at

**Johannes Böhm**, Institute of Geodesy and Geophysics, Vienna University of Technology, Austria.

E-mail: johannes.boehm@tuwien.ac.at

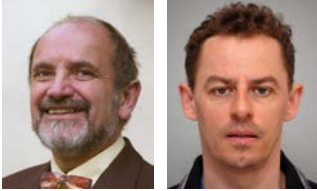
**Harald Schuh**, Institute of Geodesy and Geophysics, Vienna University of Technology, Austria.

E-mail: harald.schuh@tuwien.ac.at

**Alireza A. Ardalan**, Department of Surveying and Geomatics Engineering, College of Engineering, University of Tehran, Iran.

E-mail: ardalan@ut.ac.ir

## 20 years of International Comparison of Absolute Gravimeters (ICAG) at the Bureau International des Poids et Mesures (BIPM) in Paris with participation of the BEV



*Diethard Ruess and Christian Ullrich*

### Abstract

Since 1987 the BEV (Federal Office of Metrology and Surveying) has been operating the absolute gravimeter JILAg-6 which is used for basic measurements to determine or review fundamental gravity stations in Austria and abroad. These stations are the base of the Austrian gravity reference system. A few stations are part of international projects like UNIGRACE [1] or ECGN [2]. The BEV maintains the national standard for gravimetry in Austria, which is validated and confirmed regularly by international comparisons. All these applications require high accuracy and a precise description of the measurement uncertainty. Such campaigns have been organised eight times in an interval of approximately 4 years at the BIPM in Sévres/Paris since 1981. This paper gives an overview of the uncertainty of the measurements reached by the Austrian Absolute Gravimeter and assessed by the international comparisons of absolute gravimeters (ICAG). The history and the results of these ICAGs and especially the performance of the Austrian absolute gravimeter JILAg-6 at these ICAGs are described in detail below. Since 2010 the absolute gravity measurements in Austria have been continued with the new absolute gravimeter FG5 (manufacturer Micro-g Solutions Inc., USA).

**Keywords:** Absolute gravimetry, metrology, international comparisons, JILAg, FG5, uncertainty

### Kurzfassung

Das BEV (Bundesamt für Eich- und Vermessungswesen) betreibt seit 1987 in der Abteilung V1 das Absolutgravimeter JILAg-6 und ab 2010 das Absolutgravimeter FG5, das im Bereich Grundlagenvermessung für die Neubestimmung und regelmäßige Überprüfung von Fundamentalpunkten der Schwere im In- und Ausland eingesetzt wird. In Österreich bilden diese Punkte die Grundlage des Referenzsystems Schwere. Einige dieser Stationen sind Bestandteil internationaler Projekte wie z.B. UNIGRACE [1] und ECGN [2]. Darüber hinaus wird das Gerät im Eichwesen als Normal für die Schwerebestimmung verwendet. All diese Anwendungen erfordern eine hohe Genauigkeit und eine präzise Angabe der Messunsicherheit, die nur durch internationale Messvergleiche gewährleistet werden kann. Diese Vergleichskampagnen wurden seit 1981 insgesamt acht Mal im zeitlichen Abstand von ca. 4 Jahren an dem Bureau International des Poids et Mesures (BIPM) in Sévres/Paris veranstaltet. Dieser Artikel gibt einen Überblick über die erreichte Messunsicherheit des österreichischen Absolutgravimeters anhand der bei den internationalen Absolutgravimeter Vergleichskampagnen (ICAG) erzielten Ergebnisse. Die Geschichte und Resultate dieser Vergleichsmessungen und speziell das Abschneiden des österreichischen Absolutgravimeters JILAg-6 werden genau beschrieben. Seit 2010 werden die Absolutschweremessungen in Österreich mit dem neuen Absolutgravimeter FG5 (Hersteller Micro-g Solutions Inc., USA) fortgesetzt.

**Schlüsselwörter:** Absolutgravimetrie, Metrologie, Internationale Vergleiche, JILAg, FG5, Messunsicherheit

### 1. Introduction

The surveying part of the BEV has a very long tradition of gravity measurements dating back to the late 19<sup>th</sup> century. Absolute free-fall gravity measurements using the Italian instrument IMG6 [3] started in Austria in 1980. These measurements formed the beginning of a new gravity reference network in Austria, based on absolute gravity values which replaced the gravity level of the European Calibration Line used before. In 1986 the first Austrian absolute gravity meter

JILAg-6 was bought by seven Austrian scientific institutes and operated by the BEV [4]. The new instrument was used to stabilize the Austrian gravity reference network (OeSGN) as well as for scientific investigations in gravity changes. From that time on more than 70 absolute gravity stations were installed in Austria and neighbouring countries and some of them have been regularly monitored [5]. Since 1987 the BEV has been operating the absolute gravimeter JILAg-6 which is used for basic measurements to deter-

mine or monitor fundamental gravity stations in Austria and abroad. A few stations are part of international projects like UNIGRACE [1] or ECGN [2]. As a national metrology institute (NMI) the Metrology Service of the BEV maintains the national standards for the realisation of the legal units of measurement and ensures their international equivalence and recognition. Thus the BEV maintains the national standard for gravimetry in Austria, which is validated and confirmed regularly by international comparisons. Such campaigns have been organized eight times in an interval of approximately 4 years at the BIPM in Sèvres/Paris since 1981. All these applications require high accuracy and a precise description of the measurement uncertainty. Due to the fact that the JILAg-6 gravimeter can not achieve the high technical standards required nowadays a new absolute gravimeter was purchased in 2010 by the BEV together with ZAMG (Central Institute for Meteorology and Geodynamics, Vienna). Since then the measurements have been continued with the new absolute gravimeter FG5-242 (manufacturer Micro-g Solutions Inc., USA).

The International Comparisons of Absolute Gravimeters (ICAGs) have been organized by the Working Group on Gravimetry of the Consultative Committee on Mass (CCM WGG) and Study Group 2.1.1 on Comparison of Absolute Gravimeters (SGCAG) of Sub-Commission 2.1 of the International Association of Geodesy (IAG) and the Bureau International des Poids et Mesures (BIPM) in Sèvres/Paris, France. To determine the precision and measurement uncertainty of transportable gravimeters, you need constant environmental conditions during the campaign. All known kinds of errors arising during the abso-

lute gravity measurements were examined and documented in a technical report. Since 1989 the Austrian absolute gravimeter JILAg-6 participated six times in the ICAGs at the BIPM in Paris (figure 1) and two times in the ECAG in Luxembourg. The results of these ICAGs and especially the performance of the Austrian absolute gravimeter JILAg-6 are reported in this paper.

## 2. Description of the International Comparisons of Absolute Gravimeters (ICAGs)

From 1981 to 2009 the Bureau International des Poids et Mesures (BIPM) in Sèvres organized the ICAGs. These ICAGs are carried out systematically every 3-5 years with the intention to set up the World Gravimetric Basestation network [6]. The dates are: 1981 (1.ICAG), 1985 (2.ICAG), 1989 (3.ICAG), 1994 (4.ICAG), 1997 (5.ICAG), 2001 (6.ICAG), 2005 (7.ICAG) and 2009 (8.ICAG).

Most of the absolute gravimeters participating in the ICAGs are of the “free – fall type” and only a few use the “fall and rise” method. The principle is similar to the legendary experiment of Galileo Galilei who used the free fall at the Leaning Tower of Pisa in the 16<sup>th</sup> century to calculate earth gravity acceleration.

A freely falling reflective test mass is dropped in a vacuum. This causes optical fringes to be detected at the output of an interferometer. This signal is used to determine the local gravitational acceleration. The absolute determination of the gravity acceleration arises from the use of physical primary standards of highest accuracy: a Rubidium standard for the time measurement and an Iodine stabilized laser for the measurement of the distance. At every station a few hundred to thousand drops were performed to calculate the gravity from the average of all drops.

The gravity value is determined by an absolute gravimeter at the so-called effective height (or actual height)  $h$  over the pillar, on which the gravimeter is mounted. Its magnitude  $h$  depends on the type of instrument and on the manner in which it is mounted. For JILA type gravimeters  $h$  was on an average of 84 cm and for FG5 gravimeters on an average of 128 cm. In order to compare the absolute gravimeters, it is necessary to reduce the measured gravity values to one. Therefore high precision ties were performed with relative gravimeters as well as gradient measurements calculated over the drop distance from relative measurements. The result of

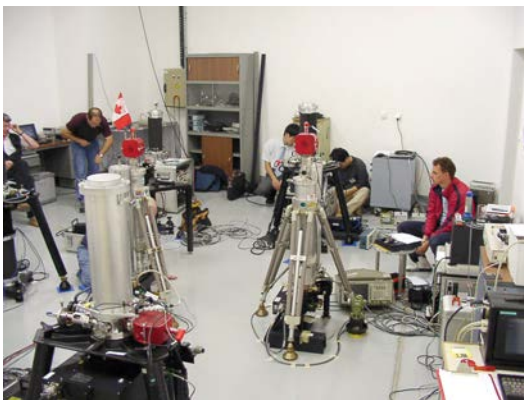


Fig. 1: Absolute gravimeters during the ICAG 2005 at BIPM, site B: In front right the JILAg-6 AG around FG5 instruments and the Canadian JILAg-2 (with the Canadian flag)

every single ICAG is the Comparison Reference Value (CRV).

Comparing the measurement results of absolute gravimeters of the highest metrological quality in the ICAGs at the BIPM as well as in the "Regional Comparisons of Absolute Gravimeters" (RCAG) is currently the only way to test the measurement uncertainty in absolute g-measurements and to determine the offsets of individual gravimeters with respect to the Comparison Reference Value (CRV). The CRVs in the ICAGs are the g-values from different absolute gravimeters obtained at one or more gravity station at the BIPM.

In 1986 the first Austrian absolute free fall gravimeter JILAg-6 was purchased in cooperation with seven scientific Austrian institutes (ZAMG, GBA, UNI Vienna, TU Graz (2), MUL, OeAW) and was operated by the BEV (staff: Ruess & Ullrich) [4], [5]. Regular monitoring measurements using the absolute gravimeter are carried out at the stations of the Austrian Gravity Network (ÖSGN) [15] and stations abroad (Europe) which are a valuable contribution to a common gravity reference system [5]. Up to 2009 the absolute gravity measurements were performed by the absolute gravimeter JILAg-6 and continued from 2010 onwards with the latest series of the absolute gravimeter FG5-242 (manufacturer Micro-g Solutions Inc., USA).

### 3. Detailed history and results of every single ICAG

#### 1<sup>st</sup> and 2<sup>nd</sup> ICAG:

The first international comparison was carried out in 1981 in Sévres and produced five independent determinations from seven instruments (all that were available at the time). The second ICAG was carried out in 1985 and brought seven independent determinations from eight instruments. As a result of the second ICAG several instruments were found to show notable systematic errors which occasionally reached a few tens of  $\mu\text{Gal}$ . This circumstance and the intention to set up in the nearest future the World Gravimetric Basestation Network with 3-5  $\mu\text{Gal}$  (1 Gal =  $1\text{cm/s}^2$ ) precision lead to the resolution to carry out comparisons systematically every four years [6].

#### 3<sup>rd</sup> ICAG:

In autumn of 1989 ten countries participated in the 3<sup>rd</sup> ICAG. Austria was part of the campaign for the first time. These countries were: Austria, Canada, Finland, Germany, USA, and

France with instruments of the JILA type (USA) and different types of instruments from China, Italy, Japan and USSR. On six different pillars 19 independent absolute determinations were conducted with approx. 44,000 drops [6]. The 3<sup>rd</sup> ICAG was the start of absolute gravity comparisons on a grand scale. From the 3<sup>rd</sup> ICAG onwards one and the same Austrian absolute gravimeter JILAg-6 participated non-stop in all six following ICAGs from 1989 to 2009. Since the BIPM cannot simultaneously accommodate and provide normal conditions for operation of such a large number of instruments during the ICAGs, it was decided to carry out the measurements in groups [6].

The complete error was determined as the squared sum of the incidental error and the sum of the systematic errors obtained from engineering-physical calculations and specialised laboratory research carried out by the holders of the instruments [7]. The known systematic error for all instruments was 4.3  $\mu\text{Gal}$  in this case. The complete square error of the determination of the absolute gravity value by one instrument reached  $\pm 7.1 \mu\text{Gal}$  at this ICAG. The JILAg-6 performed two measurements at point A2 and A8. Referenced to point A (50 cm over pillar) the final results were [6]:

1. measurement JILAg-6:	980 925 985.4 $\mu\text{Gal}$
2. measurement JILAg-6:	980 925 980.6 $\mu\text{Gal}$
All measurements (CRV):	980 925 976.5 $\mu\text{Gal}$
	( $\sigma = \pm 7.6 \mu\text{Gal}$ )

The average deviation of the Austrian JILAg-6 was: + 6.5  $\mu\text{Gal}$ .  
(1  $\mu\text{Gal} = 10 \text{nm/s}^2$ )

#### 4<sup>th</sup> ICAG 1994:

Eleven absolute gravimeters (some 25 were in use world-wide at that time) were operated at five sites and then compared by means of a high-precision gravity network. Since gravity is space- and time-dependent, this comparison series tried to minimize the "space" and "time" required for the measurements. Therefore each AG was allowed to occupy the assigned observation point for five days. Due to the large number of instruments, interchange of observation points was not considered [8]. This was the first time the FG5 absolute gravimeter type took part in this ICAG and FG5 AG's are nowadays the world's most widely used AGs.

The results have indeed shown that there is a systematic unsuspected error (comparator circuit) of approx. 10  $\mu\text{Gal}$  between FG5 and JILAg instruments and therefore the final results were

corrected accordingly. This error detection underlines the importance of comparisons of AGs.

The results demonstrate that absolute gravimetry can be carried out to an accuracy of 3  $\mu\text{Gal}$  to 4  $\mu\text{Gal}$  which represents a substantial improvement since the first international comparison (1981: 10  $\mu\text{Gal}$ ).

The final mean g value at BIPM site A0 at 90 cm was [8]:

$$g = 980\,920\,710.2 \mu\text{Gal} (\sigma = \pm 3.3 \mu\text{Gal}).$$

For the Austrian AG JILAg-6 we get transferred from pillar A8 to A0:

$$g = 980\,925\,706.0 \mu\text{Gal}, \text{ which is an average deviation of } -4.2 \mu\text{Gal}.$$

**5<sup>th</sup> ICAG 1997:**

High accuracy of gravity measurements becomes increasingly important when observations are made at a site where GPS or GLONASS observing systems are operating. Therefore the task of the ICAG is to provide an experimentally based estimation of the level of accuracy of absolute gravimeters [9].

Fifteen absolute gravimeters participated in this comparison. Ideally a large number of gravimeters are ideal for a better determination of the accuracy of the gravity value. On the other hand, including more instruments also increases the chances of obtaining an erroneous determination of gravity, e.g. relative gravity ties. The

transfer contributes 1-2  $\mu\text{Gal}$  to the scatter of the data from the complete group of gravimeters. As there are a limited number of absolute gravity sites at the BIPM, not all instruments were able to measure at all of them [9].

The mean gravity value obtained at Station A (0.9m) at the BIPM was:

$$g = 980\,925\,707.8 \mu\text{Gal} \text{ with a standard uncertainty of } 2.8 \mu\text{Gal}.$$

This is consistent with the results obtained during previous comparisons at this site.

For the Austrian AG JILAg-6 we got transferred to A0:

$$g = 980\,925\,702.6 \mu\text{Gal}, \text{ which is an average deviation of } -5.2 \mu\text{Gal}.$$

Taking the uncertainty of the mean for the last two comparisons we got:

$$1.1 \mu\text{Gal} \text{ for } 1997 \text{ and } 1.0 \mu\text{Gal} \text{ for } 1994 [9].$$

**6<sup>th</sup> ICAG 2001:**

Seventeen absolute gravimeters from twelve countries and one AG from the BIPM as well as seventeen relative gravimeters were used during this comparison. The primary objective of the ICAG 2001 was to determine the level of uncertainty for the absolute measurement of free-fall acceleration g on the ground and to try to improve the international uniformity of such measurements [10]. The increasing number of absolute gravimeters participating in the ICAGs

**Measurement results of the absolute gravimeters in the ICAGs in 1997, 2001 und 2005**

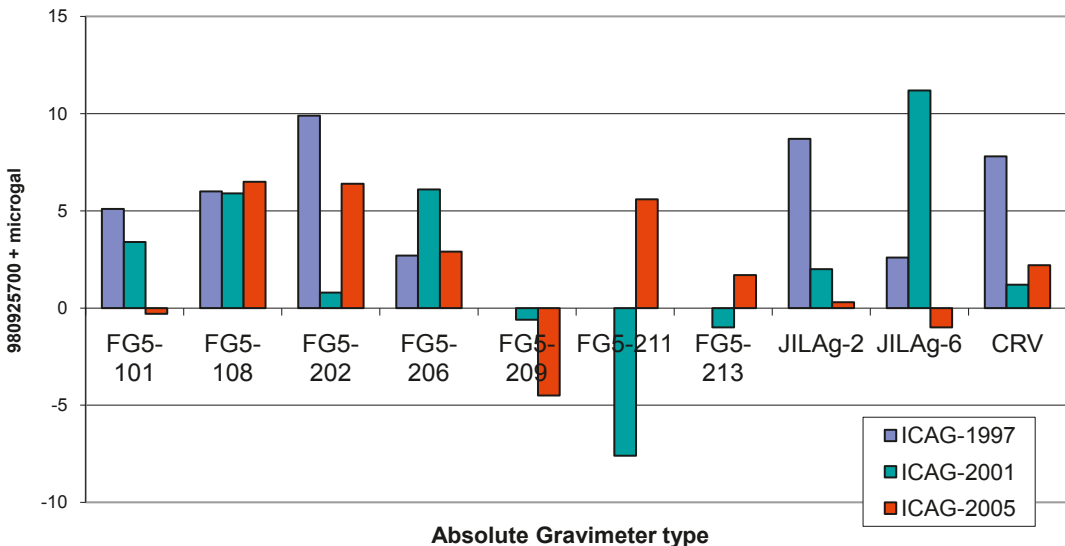


Fig. 2: The results of the ICAGs from 1997, 2001 and 2005 of different AGs [11]

requires the use of several sites at the BIPM micro network, so that these absolute measurements can be made within a relatively short time period. Therefore the sites B were created in a new building.

The  $g$  value obtained as a result of a combined adjustment of the weighted data of the absolute and relative measurements during ICAG-2001 at the point A.090 of the BIPM is:  $980\,925\,701.2 \mu\text{Gal}$  with a standard uncertainty of  $5.5 \mu\text{Gal}$ .

This value is  $6.6 \mu\text{Gal}$  lower than the CRV of ICAG-1997, which was a large discrepancy at this time. This testifies to the high potential of thoroughly maintained and properly operated gravimeters [10]. The Austrian AG JILAg-6 shows an opposite trend and we get transferred to A0:  $g = 980\,925\,711.3 \mu\text{Gal}$ , which is  $10.1 \mu\text{Gal}$  above the CRV.

### 7<sup>th</sup> ICAG 2005:

Nineteen absolute gravimeters carried out 96 series of measurements of free fall acceleration  $g$  at the sites of the BIPM gravity network (11 gravity stations). For the first time a complete list of uncertainties was presented. The organization, measurement strategy, calculation and presentation of the ICAG-2005 results were described in a technical protocol pre-developed for the comparison. The expanded uncertainty of each gravimeter was evaluated according to the ISO (International Standardization Organization) guide [12]. The combined uncertainty was evaluated from instrumental and site-dependent uncertainties [11].

The ICAG-2005 was organized in such a way that one could either take part in a pilot

study or a key comparison. The key comparison was organized to establish the equivalence of national measurement standards and the pilot study was addressed to geophysical institutes or services. Austria took part in the key comparison with the JILAg-6 absolute gravimeter. The CRV for the ICAG-2005 is at point A0.90:  $g = 980\,925\,702.2 \mu\text{Gal}$  (+/-  $0.7 \mu\text{Gal}$ ) [11].

For the Austrian AG JILAg-6 we got transferred to A0:  $g = 980\,925\,699.0 \mu\text{Gal}$ . The combined uncertainty of the JILAg-6 was calculated and estimated with approx.  $5 \mu\text{Gal}$ .

In figure 2 the results of the ICAGs from 1997, 2001 and 2005 of different AGs are shown [11]. The results of the JILA-type instruments do not disperse significantly more than the FG5 instruments.

### 8<sup>th</sup> ICAG 2009:

The very last ICAG at the BIPM was held in autumn 2009. A total of 63 measurements were made by 21 AGs of which 11 participated in the key comparison (like Austria) and 10 in the pilot study. In the ICAG 2009, five stations located at BIPM were used and each gravimeter measured at three of them. The final report is not yet finished and therefore the CRV 2009 can not be given here. But it is possible to compare the results of the measurements from the JILAg-6 at the same pillars with the last ICAG [11] (see table 1). The deviation of the JILAg-6 measurements at the ICAG2009 from the CRV from 2005 is on an average  $+8 \mu\text{Gal}$ .

The combined standard instrumental uncertainty of the JILAg-6 is estimated and calculated to be approximately  $6 \mu\text{Gal}$ . The main part of this error is due to electronically effects (electrostat-

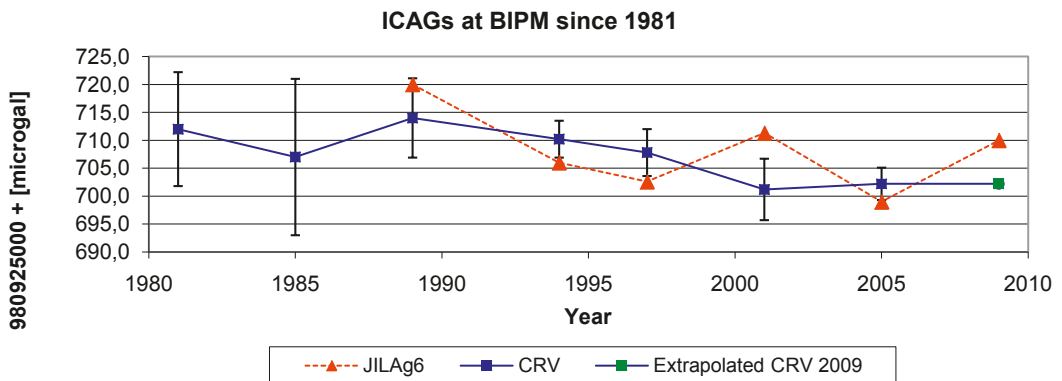


Fig. 3: Comparison Reference Value (CRV) plotted against results of JILAg-6 at the International Comparison of Absolute Gravimeters (ICAGs)



pillar	CRV-2005 [ $\mu\text{Gal}$ ]	JILAg-6 2005 [ $\mu\text{Gal}$ ]	JILAg-6 2009 [ $\mu\text{Gal}$ ]
B1	980 928 012.9	—	980 928 018.7
B2	980 927 997.2	980 928 001.0	980 928 011.4
B5	980 928 020.1	—	980 928 025.4

Tab. 1: CRV (Comparison Reference Value) of 2005 and results of JILAg-6 in 2005 and 2009 at ICAG

ic). Other (unknown) effects (due to the age of the JILAg-6) are estimated with  $3 \mu\text{Gal}$ .

The instrumental uncertainty value of approx.  $6 \mu\text{Gal}$  can also be derived from experimental comparison measurements on a very quiet station at laboratory environment conditions (Trafalberg, Austria).

Due to the bad measurement conditions (site dependent uncertainty) during the measurements of JILAg-6 at ICAG09 the combined uncertainty varies between 7 and  $9 \mu\text{Gal}$ .

#### 4. Overall results and interpretation of the ICAGs

Since 1981 the Bureau International des Poids et Mesures (BIPM) in Sèvres has organized ICAGs eight times now.

The Austrian absolute gravimeter JILAg-6 has participated non-stop in all six ICAGs from 1989 to 2009. In comparison: the Canadian JILAg-2 participated five times and the Finnish JILAg-5 participated four times. Concerning the follow-up models of the JILA: the FG5-108 of the BIPM and the FG5-101 of the BKG Germany participated five times from 1994 onwards. The IMGC absolute gravimeter (followed by IMGC2), a special device from Italy, participated non-stop in all ICAGs, but it shows major deviations from the CRV.

The result of every single ICAG is the Comparison Reference Value (CRV) and is referenced to a pillar and a special height: like A or B at the BIPM, 90 cm above the pillar.

In figure 3 the distribution of the CRV in comparison to the result of the Austrian absolute gravimeter JILAg-6 is shown (the CRV for ICAG-2009 was extrapolated).

The expanded uncertainty  $U$  is defined by the formula:

$$U = k u_c$$

where  $u_c$  is the combined uncertainty and  $k$  is the coverage factor. An expanded uncertainty defines an interval of the values of the measure and those have a specified coverage probability or level of confidence  $p$ . The usual value of 95% was chosen for such a probability in the case of ICAG-2005 [11]. The coverage factor  $k$  is used as a multiplier of

the combined standard uncertainty in order to obtain an expanded uncertainty. The values of  $k$  were obtained under the assumption that the resultant probability distribution is a Student's one and with the evaluation of effective degrees of freedom from the Welch-Satterthwaite formula [12].

The combined uncertainty  $u_c$  is the square root of the sum of the squared instrumental uncertainty, the site-dependent uncertainty and the experimental standard deviation. The expanded uncertainties are then used for the evaluation of the weight of each measurement result in the CRV calculation.

From the metrological point of view figure 4 is conclusive, which shows the deviation of the Austrian absolute gravimeter from the CRV. The standard deviation of the deviations is  $\sigma = \pm 6 \mu\text{Gal}$ . This value can be interpreted as well as measurement uncertainty. If we look back to the combined uncertainty estimation of the JILAg-6 from the technical protocol 2009 we will find a value of  $7.9 \mu\text{Gal}$ . So this value matches the measurement uncertainty of the JILAg-6. From experimental measurements at Trafalberg Observatory similar results were derived for the uncertainty of the JILAg-6 gravimeter.

#### 5. European Comparison of Absolute Gravimeters (ECAG)

Since 2003 the Luxembourg's European Center for Geodynamics and Seismology (ECGS) has organized the European Comparisons of Absolute Gravimeters (ECAGs). These ECAGs were held twice in 2003 and 2007 and the Austrian JILAg-6 participated in both comparisons. This was the first time in the history of geophysics and metrology that 15 absolute gravimeters were brought together in the same location for simultaneous observations [13]. The results for the Austrian JILAg-6 at the ECAGs were perfect: at ECAG-2003 the offset to the Comparison Reference Value (CRV) was  $2.0 \mu\text{Gal}$  and at ECAG-2007 the offset was  $-1.2 \mu\text{Gal}$  to the CRV [14].

#### 6. Future comparisons of absolute gravimeters

Absolute gravimeters have been compared in international campaigns (ICAGs) for more than 30

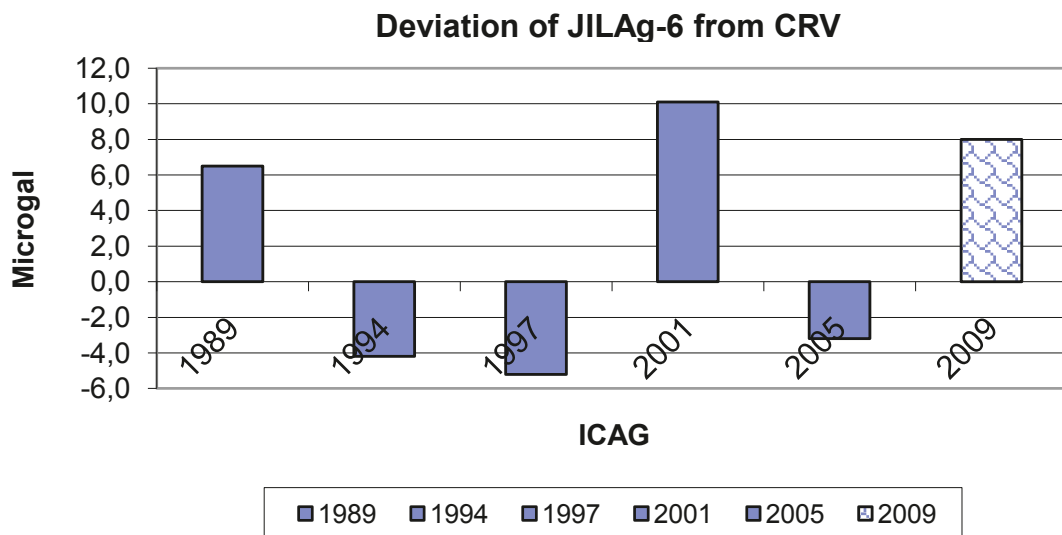


Fig. 4: Deviation of JILAg-6 from Comparison Reference Value (CRV)

years at the BIPM in a cooperation of metrological and geosciences institutions. After BIPM's decision to terminate the local support for the International Comparisons of Absolute Gravimeters, working groups of CCM and IAG came together to discuss the possibilities of continuing the comparisons.

The continuation of the CIPM (International Committee for Weights and Measures) Key Comparisons of Absolute Gravimeters and the official proposal by METAS (Switzerland) to be a pilot of CIPM KC in 2013 hosted by the laboratory in Walferdange (Luxembourg), as well as the proposals from the All-Russian D. I. Mendeleev Research Institute for Metrology (Russian Federation) and from the National Institute of Metrology (China) to host and pilot the CIPM KC on ab-

solute gravimetry in 2017 and 2021 respectively is under discussion.

The definitely next ECAG will be held in November 2011 in Luxembourg, and Austria will take part for the first time with its new absolute gravimeter FG5-242.

The BEV, together with its partners from the Central Institute for Meteorology and Geodynamics (ZAMG) and the University of Vienna - Institute of Meteorology and Geophysics (IMGW) is very much interested to contribute to the realization of a Global Absolute Gravity Reference Network. Therefore the BEV together with the ZAMG proposed the geophysical "Conrad Observatory" (COBS) on Traflberg (TRFB) for the RICAG (Regional International Comparison of Absolute Gravimeters; figure 5). This site is also a station of the ECGN project and the observatory features a specified laboratory for gravity observations with a stationary GWR superconducting gravimeter (SG). The laboratory is situated underground and securely anchored to the rocks, far away from industry and traffic and provides space for up to 10 absolute gravimeters simultaneously.

#### Summary

The Austrian absolute gravimeter JILAg-6 has been running since 1987 and has been used for a lot of gravity observations in Europe for establishing the absolute level of the gravity reference frame in Austria and abroad. Repeated observations at some selected stations should also give information about the stability of gravity or



Fig. 5: Comparison of three types of gravimeters (GWR, FG5, JILAg) in the gravity laboratory at the Conrad Observatory Traflberg of ZAMG

its changes. The precision and the uncertainty of these observations, respectively, can only be seen during comparisons with other absolute gravimeters. Therefore every four years a highly representative number of absolute gravimeters were gathered at the BIPM in Sèvres / France for comparison purposes. The achievement of the JLAG-6 instrument in the course of these comparisons is presented in this paper and also allows the estimation of the quality of basic gravity values.

## References

- [1] Ruess, D., 2002: Der Beitrag Österreichs an UNI-GRACE – Unification of Gravity Systems of Central and Eastern European Countries. VGI 3+4/2002, 129-139, Wien.
- [2] Ruess, D., 2005: Development of the European Combined Geodetic Network (ECGN) in Austria. Report on the Symposium of the IAG Subcommittee for Europe (EUREF), Vienna, Austria, 1 – 4 June 2005.
- [3] Marson, I., Steinhäuser P., 1981: Absolute Gravity Measurements in Austria. EOS, Trans. Am. Geoph. Un., Vol. 62, 258.
- [4] Ruess D., Steinhäuser P., Jeram G., Faller J., 1989: Neue Absolutschweremessungen in Österreich. Tagungsber. 5. Int. Alpengravimetrie-Kolloquium Graz 1989, Österr. Beitr. Zu Meteorol. U. Geophysik, 2, 95-110, Wien.
- [5] Ruess, D. 2001: Absolute Schweremessungen in Österreich seit 1987. Die Zentralanstalt für Meteorologie und Geodynamik 1851 – 2001, 150 Jahre Meteorologie und Geophysik in Österreich, pp. 590 – 607, Leykam, Graz 2001, ISBN 3-7011-7437-7.
- [6] Boulanger, Y., Faller J., Groten E., Arnaudov G., Becker M., Bernard B., Cannizzo L., Cerutti G., Courtie N., Feng Youg-Yuan, Fried J., Guo You-Guang, Hanada H., Huang Da-Lun, Kalish E., Kloppin F., Li De-Xi, Leord J., Mäkinen J., Marson I., Ooe M., Peter G., Röder R., Ruess D., Sakuma A., Schnüll N., Stus P., Scheglov S., Tarasük W., Timmen L., Torge W., Tsobokawa T., Tsuruta S., Vänskä A., Zhang Guang-Yuan, 1991: Results of the 3rd International Comparison of Absolute Gravimeters in Sèvres 1989. BGI, Bull. D'Inf. 68, 24 – 44.
- [7] Niebauer, T.M., Sasagawa, G.S., Faller, J.E., Hilt R., Kloppin, F., 1995: A new generation of absolute gravimeters. Metrologia, Vol. 32, Nb. 3, BIPM, Nov. 1995, pp 159-180.
- [8] Marson I., Faller J.E., Cerutti G., De Maria P., Chartier J.-M., Robertsson L., Vitushkin L., Friederich J., Krauterbluth K., Stizza D., Liard J., Gagnon C., Lothhammer A., Mäkinen J., Murakami M., Rehren F., Schnüll M., Ruess D., Sasagawa G. S., 1995: Fourth International Comparison of Absolute Gravimeters. Metrologia, Vol. 32, Nb. 3, BIPM, Nov. 1995, pp 137-144.
- [9] Robertsson, L., Francis, O., van Dam, T., Faller, J., Ruess, D., Delinte, J.-M., Vitushkin, L., Liard, C. Gagnon, Guo You Guang, Huang Da Lun, Fang Yong Yuan, Xu Jin Yi, G. Jeffries, J., Hopewell, H., Edge, R., Robinson, I., Kibble, B., Mäkinen, J., Hinderer, J., Amalvict, M., Luck, H. B., Wilmes, H., Rehren, F., Schmidt, K., Schnüll, M., Cerutti, G., Germak, A., Zabek, Z., Pachuta, A., Arnaudov, G., Kalish, E., Stus, Y., Stizza, D. J., Friederich, J., Chartier, J.-M. and Marson, I., 2000: Results from the Fifth International Comparison of Absolute Gravimeters, ICAG97; Metrologia 38, pp. 71-78, BIPM 2001, pp 71-78.
- [10] L. Vitushkin; M. Becker; Z. Jiang; O. Francis; T. M. van Dam; J. Faller; J.-M. Chartier; M. Amalvict; S. Bonvalot; N. Debeglia; S. Desogus; M. Diament; F. Dupont; R. Falk; G. Gabalda; C. G. L. Gagnon; T. Gattacceca; A. Germak; J. Hinderer; O. Jamet; G. Jeffries; R. Käker; A. Kopaev; J. Liard; A. Lindau; L. Longuevergne; B. Luck; E. N. Maderal; J. Mäkinen; B. Meurers; S. Mizushima; J. Mrlina; D. Newell; C. Origlia; E. R. Pujol; A. Reinhold; Ph. Richard; I. A. Robinson; D. Ruess; S. Thies; M. van Camp; M. van Ruymbeke; M. F. de Vilalta Compagni; S. Williams, 2001: Results of the Sixth International Comparison of Absolute Gravimeters, ICAG-2001. Metrologia, 2002, 39, n°5, 407-424.
- [11] Vitushkin, L., et. al., 2010: Results of the Seventh International Comparison of Absolute Gravimeters ICAG-2005 at the Bureau International des Poids et Mesures, Severs, in press.
- [12] Guide to expression of uncertainty in measurement, ISO, 1993.
- [13] O. Francis, T. van Dam, 2003: International Comparisons of Absolute Gravimeters in Walferdange (Luxembourg) of November 2003. Cahiers du Centre European de Geodynamique et de Seismologie, Vol. 26, 1-23.
- [14] O. Francis, T. van Dam, A. Germak, M. Amalvict, R. Bayer, M. Bilker-Koivula, M. Calvo, G.-C. D'Agostino, T. Dell'Acqua, A. Engfeldt, R. Faccia, R. Falk, O. Gitlein, M. Fernandez, J. Gjevestad, J. Hinderer, D. Jones, J. Kostelecky, N. Le Moigne, B. Luck, J. Mäkinen, D. McLaughlin, T. Olszak, P. Olsson, A. Pachuta, V. Palinkas, B. Pettersen, R. Pujol, I. Prutkin, D. Quagliotti, R. Reudink, C. Rothleitner, D. Ruess, C. Shen, V. Smith, S. Svitlov, L. Timmen, C. Ulrich, M. Van Camp, J. Walo, L. Wang, H. Wilmes and L. Xing: Results of the European Comparison of Absolute Gravimeters in Walferdange (Luxembourg) of November 2007. Gravity, Geoid and Earth Observation, Springer Berlin Heidelberg, Ed. Stelios, P. Mertikas, vol. 135, 31-35, 2010.
- [15] Ruess D., Gold W., 1996: The Austrian Gravity Base Net 1995. Austrian Contributions to the XXI. Gen. Ass. of IUGG. VGI 84, 3/96, 275-283, Wien.

## Contacts

Dr. Diethard Ruess, BEV - Federal Office of Metrology and Surveying, Department Control Survey, Head of V11 - Geophysics and Precise Levelling, Schiffamtsgasse 1-3, 1020 Vienna, Austria.

E-Mail: diethard.ruess@bev.gv.at

Mag. Christian Ullrich, BEV - Federal Office of Metrology and Surveying, Department Control Survey, V11 - Geophysics and Precise Levelling, Schiffamtsgasse 1-3, A-1020 Vienna, Austria.

E-Mail: christian.ullrich@bev.gv.at



## Automatic Registration of Laser Scanner Point Clouds with Genetic Algorithms

Stefan Schenk and Klaus Hanke

### Abstract

During a terrestrial laser scan, usually different scanning positions are necessary to avoid hidden parts on the object. The resulting scans are then merged into one single point cloud in a registration procedure. Usually artificial targets or approximate values are required to initiate the spatial transformation. We illustrate the theoretical background of a robust as well as automated registration approach without any prior knowledge of the scanner's position and attitude by using Genetic Algorithms. Then we discuss the results using the example of a cave survey, where the registration using artificial targets reached the limit of practicability.

**Keywords:** automatic registration, point clouds, Genetic Algorithms

### Kurzfassung

Im Zuge der Erfassung eines Objekts mittels terrestrischer Laserscanner sind im Allgemeinen mehrere Standpunkte notwendig, um Lücken in verdeckten Bereichen zu vermeiden. Die so erfassten Scans werden erst über eine gegenseitige Registrierung zu einer gemeinsamen Punktwolke vereinigt. Häufig werden zu diesem Zweck künstliche Passmarken / Passobjekte oder manuell erzeugte Näherungswerte für die räumliche Transformation verwendet. Die Autoren zeigen den theoretischen Hintergrund eines Ansatzes zur Registrierung von Scans mit Genetischen Algorithmen, der ohne Vorwissen über Standpunkt und räumliche Lage des Scanners auskommt und gleichzeitig zu robusten Ergebnissen führt. Der praktische Einsatz wird anhand der 3D-Erfassung eines bronzezeitlichen Bergbaustollens diskutiert, bei dem die Verwendung künstlicher Ziele an ihre Grenzen gestoßen war.

**Schlüsselwörter:** automatische Registrierung, Punktwolken, Genetische Algorithmen

### 1. Introduction

Surveying is an indispensable companion of every archaeological excavation (fig. 1). Modern documentation techniques allow for complete and precise data acquisition with laser scanners leading to full textured 3D models of the excavation and its artefacts [1]. As the recording and representation of such complex structures and surfaces needs scanning from several scan



Fig. 1: Typical point cloud acquisition with a terrestrial laser scanner and artificial target spheres

positions (for results see fig. 2), the single point clouds have to be registered to each other to be transformed into a common coordinate framework. Only after determining and applying the transformation parameters, the merging and final modelling of the point clouds can take place.

Generally the registration problem is solved by scanning additional spherical or cylindrical marks, at least three of which have to be visible also from other positions to guarantee a six parameter (relative) spatial transformation. These tie-features should be well distributed in space around the object and lead to a high effort for additional measurements. Figure 1 shows the complicated positioning of target spheres in a narrow pre-historic Bronze Age mining gallery. This gives an idea of the method's limit of practicability. Absolute orientation using control-features was not adopted in this case as the artificial marks were positioned as needed "on-the-fly" and the project did not require any georeferencing.

Another possibility to establish the registration is based on the manual assignment of assumed coincident points in the point clouds. However it is often hard to identify such points. Due to the fact that point clouds are discrete representa-

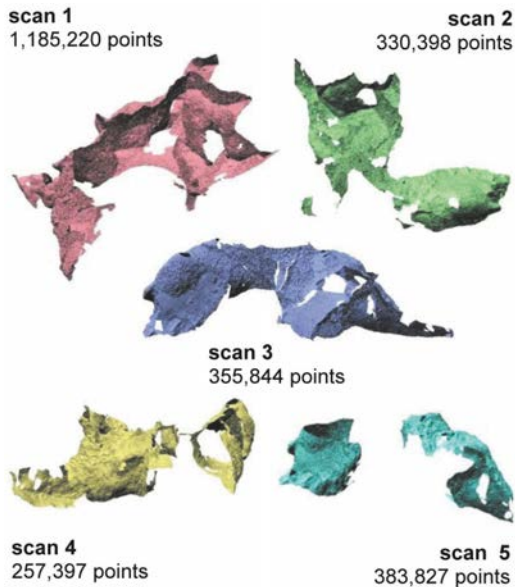


Fig. 2: Single scans of a prehistoric cave

tions of the original object's surface only, one can imagine that in most cases there won't even be any exact point-to-point correspondences.

As this procedure is, with a high number of single point clouds, very time-consuming and also fairly error-prone, we tried to develop a robust and automatic approach avoiding any manual interaction. Hereby we combine already well-established registration strategies such as coarse registration using features, the application of Genetic Algorithms as well as ICP-algorithms for fine registration.

Contrary to other popular approaches, however, we do not try to identify the position of the global optimum already after coarse registration. This is reasonable as, due to the necessary approximations during coarse registration, the correct solution may appear worse than those that are actually wrong. Thus we propose to introduce a Genetic Algorithm in between coarse and fine registration to both optimize and reduce the number of possible solutions at the same time.

Further we use imperfect and subdivided features to enhance the robustness of the registration of point clouds which are partially occluded and/or characterized by a significant noise level or imperfect geometry.

Summarized we elaborate the positive aspects of different approaches and try to minimize their drawbacks.

## 2. Related previous work

Mathematically, the process of point cloud registration can be seen as search for an optimal alignment between two point clouds  $X = (x_1, \dots, x_N)$  and  $Y = (y_1, \dots, y_N)$ . Sometimes point-to-point correspondences are already known or were manually established. Hereby  $X$  and  $Y$  do not contain the whole point clouds, but only the corresponding point pairs, meaning that each point  $x_i \in X$  has a corresponding point  $y_i \in Y$  with the same index. As stated in [2], the rigid-body transformation can be expressed as

$$m(x) := x' = t + R \cdot x \quad (1)$$

whereby each point  $x$  is transformed to a new position  $x'$  by applying a rotation  $R$  and a translation  $t$ , such that the sum of the squared Euclidean distances between  $X$  and  $Y$  is minimized:

$$\sum_{i=1}^N \|x'_i - y_i\|^2 \rightarrow \min \quad (2)$$

If at least three correspondences in two point clouds are known, the registration task can for instance be solved by using the closed-form solution presented in [3].

Similar to the manual identification of point correspondences, also automatic methods use the object's properties itself for the registration and typically also split the registration process into coarse and fine registration. For each of these steps a number of methods can be found in literature [4].

One of the main challenges during coarse registration is the efficient search of correspondences. Especially when registering bigger objects or outdoor scenes, point clouds contain a certain noise level, resulting from the limited instrument precision and/or the discretisation of rough or in small parts occluded object surfaces. In those cases some authors, e.g. [5] and [6], propose the use of features such as planes or also more complex geometric elements such as cylinders [7].

After roughly orientating the point clouds, fine registration improves their alignment further. Most popular approaches are based on the ICP (Iterative Closest Point) algorithm presented by [8] and [9]. [10] list different variations of the ICP-algorithm and evaluate their speed and solution quality.

As alternative to the already mentioned approaches, Genetic Algorithms (GAs) can be adapted for both coarse and fine registration. They prove more robust as they are better in detecting the global optimum and are able to

find solutions where other algorithms may fail. They are fairly well suited for the registration of free-form objects as shown for example in [11], [12] or [13]. Nevertheless, their major drawback is that they are computationally expensive.

### 3. Background information

In the following chapter we give some brief background information about basic principles used in this work.

#### 3.1 Genetic Algorithms

Genetic Algorithms (GAs) are adaptive heuristic search algorithms which are inspired by the principles of natural evolution. They are able to find solutions in large and complex search spaces where other algorithms may fail due to local optima. Genetic Algorithms are however known to be computationally expensive, which is especially true for the registration of point clouds. By using a Genetic Algorithm in between coarse and fine registration, the algorithm does not need to search the whole solution space and thus we can take advantage of its robustness and at the same time increase its practicability.

The registration concept discussed in this paper is not bound to a very specific Genetic Algorithm. A variety of algorithms was successfully tested; we found however that the Genetic Algorithm and parameters described in [12] behave quite well on our datasets. Thus our actual implementation is mainly based on [12] and works with randomly chosen subsets of single points from the point clouds.

Figure 3 shows a typical structure of a Genetic Algorithm. At the beginning a pool of random solutions is created, forming the so-called initial population. Note that these solutions can also be supplied by a preceding algorithm (e.g. an algorithm for coarse registration).

Each solution is represented as vector of parameters. Contrary to [12] we do not store it

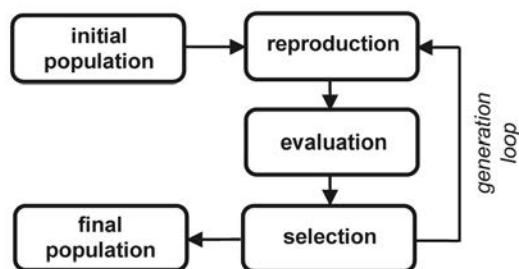


Fig. 3: Typical structure of a Genetic Algorithm

in the six-dimensional form  $[\alpha, \beta, \gamma, t_x, t_y, t_z]$  with the three Euler-angles  $\alpha, \beta, \gamma$  and  $t_x, t_y, t_z$  as the three elements of the translation vector  $\mathbf{t}$ , but follow the advice in [13] and use a unit quaternion  $\mathbf{q}$  for the homogenous representation of the rotation.

In the so called reproduction additional solutions are created by randomly applying the principles of mutation and crossover. Regarding mutation one already given solution is taken and altered by adding a small arbitrary rotation and translation. Crossover is adopted by selecting two existing solutions and interpolating them. For quaternions this can be done for example by applying a spherical linear interpolation (SLERP). The needed interpolation factor  $t$  is chosen randomly between 0 and 1.

After the number of solutions in the population was increased (typically doubled), the actual quality (fitness) of the single solutions is evaluated by a so-called fitness function. We are using the one stated in [12] which is based on the sum of the squared distances between corresponding points. To accelerate this step a kd-tree is used.

Based on their quality, a certain number of solutions is then selected for the next iteration (generation) adopting a binary tournament. Hereby solutions with higher quality have a better chance to be selected.

Due to the continuous repetition of reproduction, evaluation and selection, an optimization of the population can be achieved until a specified termination criterion is met (for instance a maximum number of iterations).

By reusing the fitness function, at the end the best solution can be identified within the final population.

#### 3.2 Imperfect features

When trying to identify features (e.g. edges, borders or planar patches) in point clouds, one may observe that the selection of detection thresholds can be decisive for the results. If point clouds are characterized by a significant noise level or imperfect geometry (such as rough surfaces or round borders and edges) or contain occluded parts (e.g. due to trees (see fig. 4)), features may emerge differently when applying feature detection to other point clouds also due to the different point of view.

In this sense the term "imperfect features" does not refer to a special feature type as such, but implies that features may be only approxi-

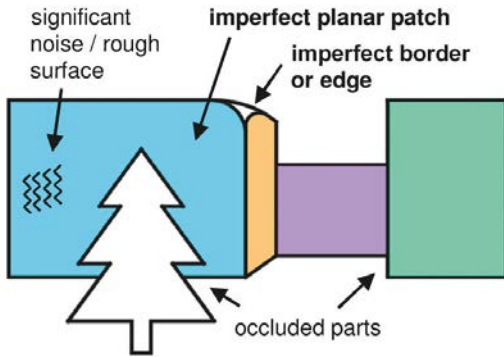


Fig.4: Imperfect features

mated, “partly correct” or even misrepresent the original object.

**3.3 Subdivided features**

Sometimes it may happen that due to unfavourable circumstances the needed feature correspondences can get rather poor for a “correct” registration. This is especially true with datasets where we can’t deny the presence of imperfect features. To overcome this we propose to subdivide larger features into smaller parts (see fig. 5) and work only with those which are not influenced by occlusion or other effects anymore.

In [5] the concept of subdividing point clouds into regular raster cells for fast plane detection was introduced. We evolve this idea not by subdividing the point clouds itself, but its features. Note that in this paper we mainly refer to subdivided planar patches, but the concept is applicable to other feature types as well.

By calculating the barycentre and principal axis of each planar patch we can establish an individual local coordinate system and use it for subdividing features into a regular grid (see fig. 5). For some features this will lead to similar grids (and therefore similar subdivided features) also

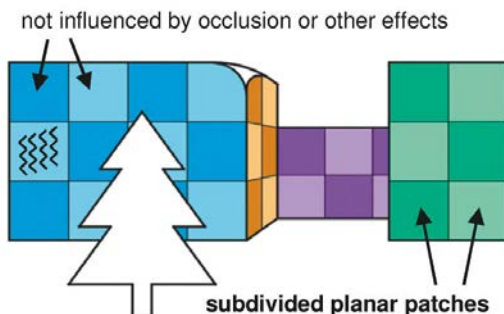


Fig. 5: Subdivided features

in other point clouds. Our algorithm is, however, able to handle also the other cases, where subdivision results in a differing grid. For more information about imperfect and subdivided features consult [14] or [15].

**4. Automatic registration**

One of the biggest challenges in point cloud registration is the huge amount of data, which is typically given as unsorted list of point-coordinates. Due to this, efficient strategies have to be used to achieve practically acceptable running times also for bigger objects.

Figure 6 shows the three main steps of the here presented registration strategy GAReg-ISF (Genetic Algorithm Registration with Imperfect and Subdivided Features) [14], exemplarily using coloured puzzle pieces to represent the single point clouds.

In a first step the point clouds are individually analysed and for all of them additional information such as normal vectors and features are identified. This is followed by the pair-wise registration of the possible point cloud combinations.

Afterwards a multi-view registration is employed where the results of the pair-wise registrations are used to align the point clouds to a globally consistent digital representation of the original object.

**4.1 Scan-analysis**

The so-called scan-analysis is the first step in GAReg-ISF. The main aim of scan-analysis is to reduce the millions of single points to distinctive areas (features) to increase the overall robustness of the registration process. Hereby geometrical features are identified out of the single point clouds; planes for instance proved to be rather robust against noise, outliers and small occlusions.

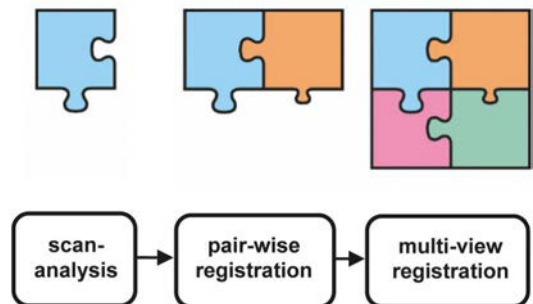


Fig. 6: Automatic registration strategy

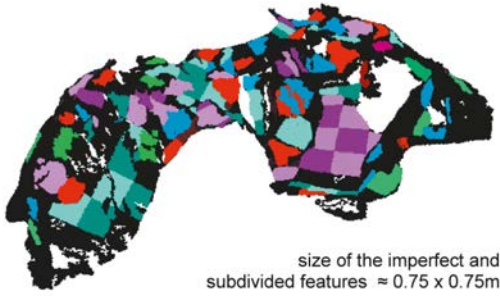


Fig. 7: Imperfect and subdivided planar patches

The results of a scan-analysis using imperfect and subdivided features can be seen in figure 7, illustrating scan 3 of a cave in Mauken near Brixlegg, Tyrol, Austria.

**4.2 Pair-wise registration**

The information resulting from scan analysis is processed during pair-wise registration; hereby respectively two point clouds are aligned with each other.

First of all coarse registration using imperfect and subdivided features takes place, traditionally followed by fine registration. Figure 8, however, shows the enhanced approach of GAReg-ISF, where a third step right in between coarse and fine registration is introduced by using a Genetic Algorithm. Hereby, valid solutions resulting from coarse registration mark possible locations (schematically represented as bubbles in fig. 8) of the global optimum in the search space. This is done by taking the solutions of coarse registration as initial population for the Genetic Algorithm. When one or eventually even several solutions have been identified by the algorithm, a pair-wise fine registration can be employed using an accordingly higher degree of details.

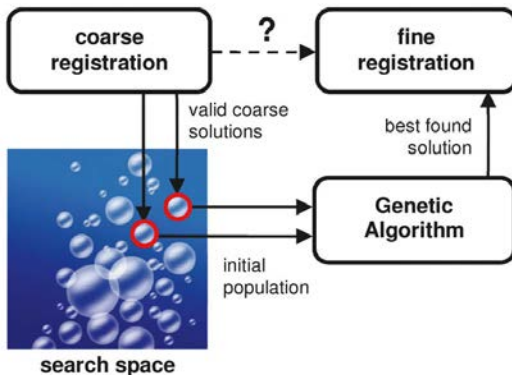


Fig. 8: Enhanced pair-wise registration

**4.2.1 Coarse registration**

The principal target of coarse registration is the approximately correct alignment of two point clouds. The huge data volume and the very often missing information about the spatial relationship between the single point clouds prove particularly challenging in this step.

As stated in [6], three linearly independent planes  $\epsilon_i, \epsilon_j, \epsilon_k$  (see figure 9a) in each point cloud are necessary to form a valid registration. In some cases it is however difficult or simply not possible to gather enough corresponding planes in each point cloud for registration.

An additional consideration is presented in [16]: Hereby also the barycentre of each planar patch is used for the registration process, which means that only two planar patches need to be visible and detectable in each point cloud. The same strategy can be adapted also to imperfect and subdivided features with the barycentres  $r_i$  and  $r_j$  as shown in figure 9b.

To keep computational efforts within an acceptable range, several hierarchical comparisons are carried out.

At the beginning, all possible combinations of (yet not subdivided) planar patch pairs from one point cloud with all of such of the other point cloud have to be considered. A lot of wrong com-

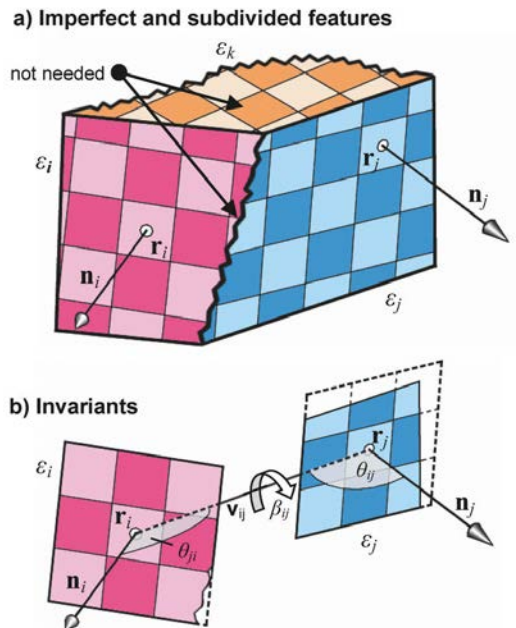


Fig. 9a-b: Invariants of the imperfect and subdivided features for efficient correspondence detection



binations can however be eliminated by checking the minimal and maximal spatial distance of the (yet not subdivided) planar patch pairs as well as the angle between normal vectors [16] and the difference of mean intensity information.

For the remaining correspondences their subdivided planar patches are now used. Figure 9b shows four invariants, stated in [11] and [4], which enable an efficient search strategy. The invariants between two subdivided features with the barycentres  $\mathbf{r}_i$  and  $\mathbf{r}_j$  correspond to the distance  $\|v_{ij}\|$  between the barycentres, the pair-wise relative orientations  $\theta_{ij}$  and  $\theta_{ji}$ , as well as a twist angle  $\beta_{ij}$ .

It is quite obvious that in most cases still a lot of wrong correspondences will result from the above mentioned rough comparison. For further limitation, the local neighbourhoods of the features are now included into the search process. This is done by comparing also the eight nearest subdivided planar patches around  $\mathbf{r}_i$  and  $\mathbf{r}_j$  (fig. 9b). The remaining combinations of subdivided planar patch pairs can then be used to create a list of rough pair-wise alignments of the point clouds. After sorting out similar solutions these are supplied as initial population to a Genetic Algorithm.

#### 4.2.2 Genetic Algorithm

The use of a Genetic Algorithm in GAReg-ISF has different reasons. First of all it is able both to optimize and reduce the number of solutions provided by the coarse registration. This way the probability of missing the “correct” solution can be decreased. At the same time the Genetic Algorithm is able to correct the allowed approximations resulting from the concept of imperfect and subdivided features and from coarse registration.

A well balanced optimization carried out with a Genetic Algorithm is most of the times characterized by the convergence of a population towards the global optimum. Such a convergence on the basis of the translation  $\mathbf{t}$  of a dataset used in [15] is shown in figure 10 a-c. Note that in this case the translation is dimensionless as the dataset used in this example was temporary scaled to unit size during the registration process. Through the implementation of an additional “taboo-search” also more than one solution can be found by repeating the procedure. This was successfully tested registering two synthetic doubly-symmetric planar patches with two graves (forming an X), where the algorithm was able to find all four solutions[14].

#### 4.2.3 Fine registration

To conclude the pair-wise matching process, an ICP-algorithm (see [8], [9] and [10]) is employed for fine registration. In this step we use an ICP-algorithm for the alignment of only two point clouds, whereas after multi-view registration an algorithm is applied which supports the simultaneous alignment of more than two point clouds.

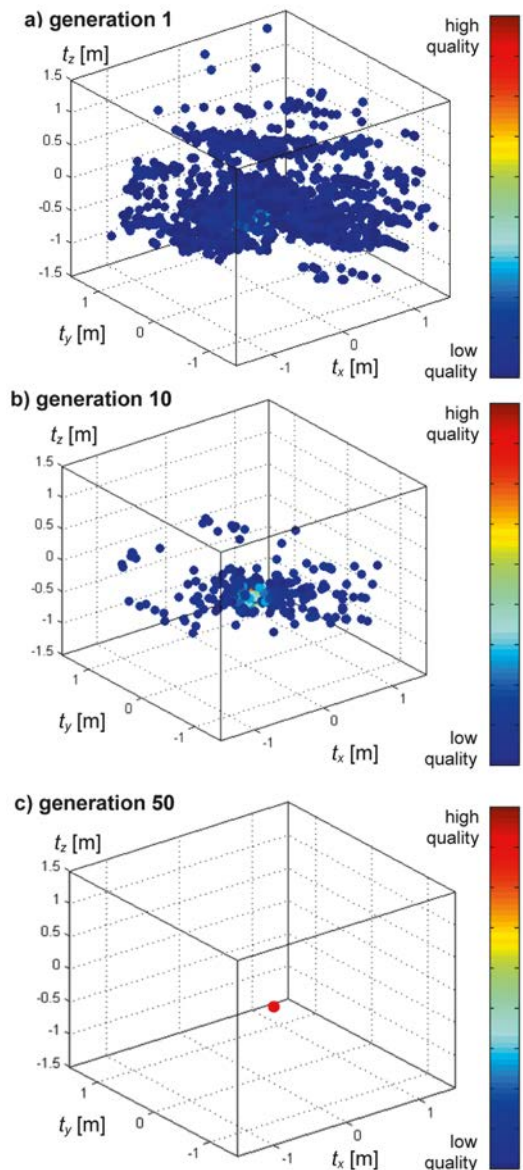


Fig. 10a-c: Convergence of the solutions

### 4.3 Multi-view registration

In most cases several point clouds need to be registered in order to create a preferably complete digital representation of an object.

This is particularly challenging as often not only one but several pair-wise registration results can seem feasible. Figure 11 shows different solutions resulting from the pair-wise registration of the same two point clouds (represented as puzzle pieces).

Thereby contradicting solutions (fig. 11a) seem to be detectable more easily as apparently correct (but wrong) solutions (fig. 11b). Both cases are however quite similar, because the actual surface contradictions are limited to areas of direct contact. As proposed in [17], a visibility consistency check can help to identify wrong alignments.

To differentiate between locally (fig. 11c) and globally correct solutions (fig. 11d), solutions showing a larger overlap are preferred. Note that in this case a solution is called "globally correct" if it leads to the result expected by the user (see fig. 12).

According to [18], at the beginning of the multi-view registration the results of the pair-wise regis-

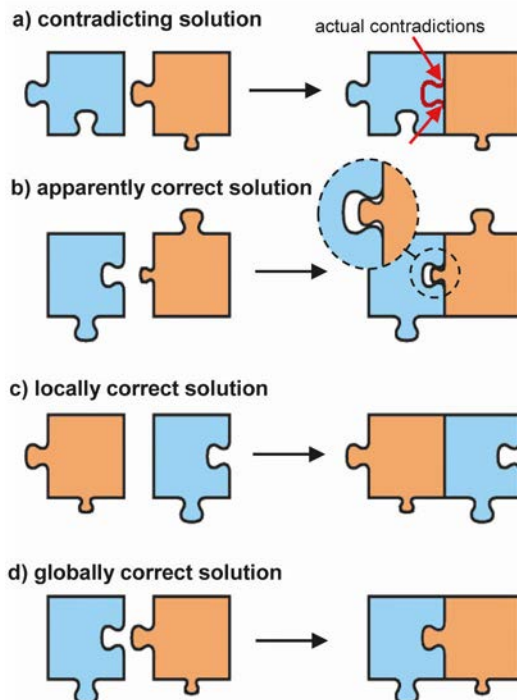


Fig. 11a-d: Different solutions resulting from pair-wise registration

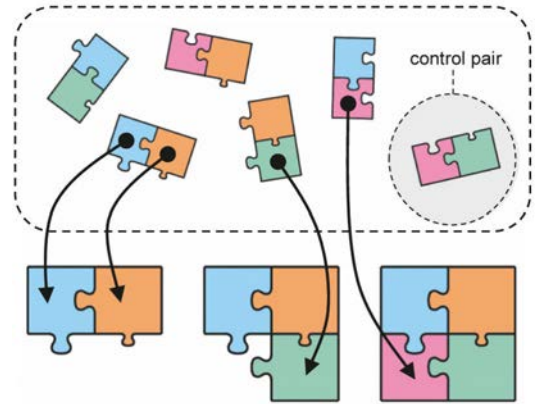


Fig. 12: Multi-view registration

tration are sorted according to their quality. The best solution is fixed and iteratively the next pair is added until all point clouds are aligned (fig. 12). After each iteration step the point clouds are realigned so that a globally consistent representation of all views can be ensured.

### 5. Experimental results

To explore the potentials and limits of GAReg-ISF, a number of experiments have been carried out [15]. The cave in Mauken is definitely among those cases that are not characterized by ideal conditions for a registration method using planes. Nevertheless, we were able to represent even such complex surfaces by using imperfect and subdivided features (fig. 7).

For the feature extraction and for the ICP-algorithm 100,000 randomly chosen points were used, whereas for the Genetic Algorithm 3,000 were taken.

The point clouds were registered twice using two independent methods: the classical registration with artificial spheres (as tie-features) and the automatic registration approach GAReg-ISF. As the local coordinates of the sphere centres were already gathered for each station during the classical approach, they can also be transformed according to the transformation parameters calculated with GAReg-ISF. This makes it possible to compare the resulting coordinates of the sphere centres for both approaches. Table 1 illustrates the standard deviations of the sphere centres as well as the spatial distances between the averaged centres.

As noticed even the classical registration using artificial spheres shows certain deviations. This is probably due to the scanner's limited accuracy

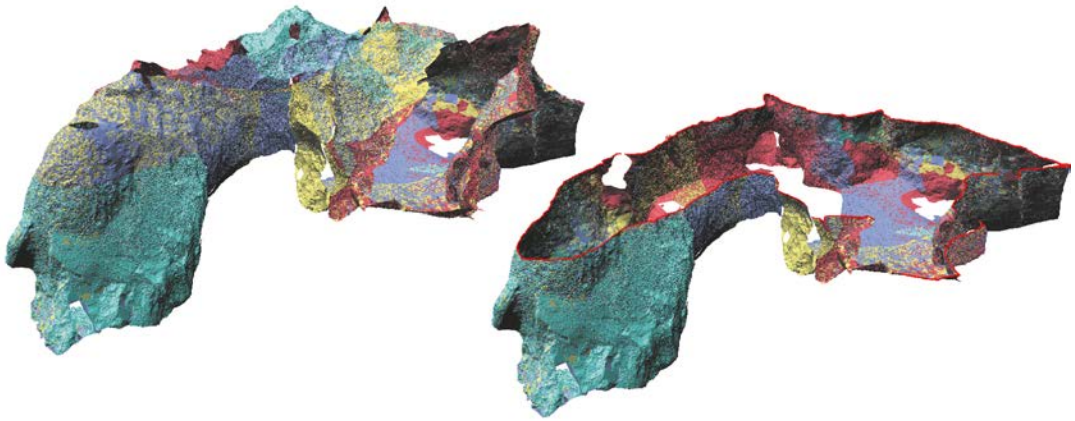


Fig. 13a-b: Exterior view and horizontal section of the registered scans

and minor displacements of the spheres in the course of the measuring. The same displacements also influence the results of GAReg-ISF, though actually working without spheres.

For both methods the maximal standard deviation can be found in x-direction of sphere 3 as well as the maximal spatial distance with 1.6 mm. Overall these results are absolutely satisfying. Figure 13 shows different views of the five registered point clouds of the Mauken cave.

sphere	station	std. dev. of sphere centres						spatial distance [mm]
		target spheres			GAReg-ISF			
		X mm	Y mm	Z mm	X mm	Y mm	Z mm	
1	1,3,4,5	0.9	0.6	0.4	0.3	0.8	0.5	1.0
2	1,2,3,4	1.6	2.1	0.1	0.8	2.8	1.1	0.6
3	1,2,5	2.6	0.7	0.1	3.7	2.0	1.2	1.6
4	1,2,3,4,5	0.6	1.7	0.3	1.5	1.1	0.6	1.5

Tab. 1: Comparison of the sphere centres resulting from the registration with artificial spheres and GAReg-ISF

**6. Conclusion**

In the mentioned cave project, the classical registration approach using artificial spheres has reached its limits as it was hard to select useful positions for the single spheres. Thus we used the fully automatic registration approach GAReg-ISF and evaluated the spatial difference of the

results by applying the calculated transformation parameters to locally known target sphere coordinates. We showed that GAReg-ISF is able to reach results of comparable accuracy as the classical registration using artificial spheres in complex surroundings by rendering at the same time the overall registration workflow more efficient.

**Acknowledgements**

The dataset discussed in this paper was provided by the FWF special research program HiMAT (History of Mining Activities in the Tyrol). Twelve institutes of different scientific fields from natural sciences, humanities to engineering are taking part in this consortium. The entire project is mainly funded by the Austrian Science Funds, the regional authorities of Tyrol, Salzburg und Vorarlberg as well as the Autonomous Province Bolzano/South-Tyrol (Italy).

**References**

- [1] Hanke, K., Moser, M., Grimm-Pitzinger, A., Goldenberg, G. & Toechterle, U. (2008): Enhanced potential for the analysis of archaeological finds based on 3D modeling. In: IAPRS, The International Archives of Photogrammetry, Remote Sensing and Spatial Information Sciences, XXXVII, Part B5, pp. 187-192
- [2] Hofer, M. & Pottmann, H. (2003): Orientierung von Laserscanner-Punktwolken. In: Vermessung & Geoinformation 91, pp. 297-306
- [3] Horn, B. K. P. (1987): Closed-form solution of absolute orientation using unit quaternions. In: Journal of the Optical Society of America 4 (4), pp. 629-642
- [4] Salvi, J., Matabosch, C., Fofi, D. & Forest, J. (2007): A review of recent range image registration methods with accuracy evaluation. In: Image and Vision Computing 25 (5), pp. 578-596
- [5] von Hansen, W. (2006): Robust automatic marker-free registration of terrestrial scan data. In: IAPRS, The International Archives of Photogrammetry, Remote Sensing and Spatial Information Sciences, XXXVI, Part 3, pp. 105-110

- [6] Brenner, C., Dold, C. & Ripperda, N. (2008): Coarse orientation of terrestrial laser scans in urban environments. In: ISPRS Journal of Photogrammetry and Remote Sensing 63 (1), pp. 4-18
- [7] Rabbani, T., Dijkman, S., van Den Heuvel, F. & Vosselman, G. (2007): An integrated approach for modelling and global registration of point clouds. In: ISPRS Journal of Photogrammetry and Remote Sensing 61 (6), pp. 355-370
- [8] Besl, P. & McKay, N. (1992): A method for registration of 3D shapes. In: IEEE Transactions on Pattern Analysis and Machine Intelligence 14 (2), pp. 239-256
- [9] Chen, Y. & Medioni, G. (1992): Object modeling by registration of multiple range images. In: Image and Vision Computing 10 (3), pp. 145-155
- [10] Rusinkiewicz, S. & Levoy, M. (2001): Efficient variants of the ICP algorithm. In: 3DIM 2001. Proceedings of the 3rd International Conference on 3-D Digital Imaging and Modeling, pp. 145-152
- [11] Brunnström, K. & Stoddart, A. J. (1996): Genetic algorithms for free-form surface matching. In: Proceedings of the 13th International Conference on Pattern Recognition
- [12] Silva, L., Bellon, O. R. P. & Boyer, K. L. (2005): Robust range image registration using genetic algorithms and the surface interpenetration measure: World Scientific (Series in Machine Perception and Artificial Intelligence, 60)
- [13] Lomonosov, E., Chetverikov, D. & Ekárt, A. (2006): Pre-registration of arbitrarily oriented 3D surfaces using a genetic algorithm. In: Pattern Recognition Letters 27 (11), pp. 1201-1208
- [14] Schenk, S. (2010): Automatische Registrierung von Punktwolken. Genetische Algorithmen mit genäherten und unterteilten Merkmalen. Dissertation. Universität Innsbruck
- [15] Schenk, S. & Hanke, K. (2009): Genetic Algorithms for Automatic Registration of Laser Scans with Imperfect and Subdivided Features (GAReg-ISF). In: Photogrammetrie - Fernerkundung - Geoinformation (2009/1), pp. 23-32
- [16] He, W., Ma, W. & Zha, H. (2005): Automatic registration of range images based on correspondence of complete plane patches. In: 3DIM 2005. Proceedings of the 5th International Conference on 3-D Digital Imaging and Modeling, pp. 470-475
- [17] Huber, D. F. & Hebert, M. (2003): Fully automatic registration of multiple 3D data sets. In: Image and Vision Computing 21 (7), pp. 637-650
- [18] Pulli, K. (1999): Multiview registration for large data sets. In: 3DIM'99. Proceedings of the 2nd International Conference on 3-D Digital Imaging and Modeling, pp. 160-168

#### Contacts

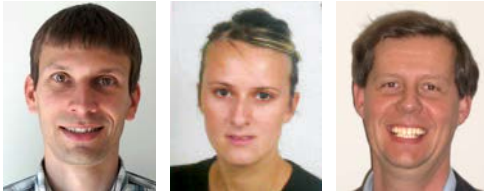
Dipl.Ing. Dr.techn. Stefan Schenk, Surveying and Geoinformation Unit, University of Innsbruck, Technikerstrasse 13, A 6020 Innsbruck, Austria.

E-Mail: stefan.schenk@student.uibk.ac.at

Univ.Prof. Dipl.Ing. Dr.techn. Klaus Hanke, Surveying and Geoinformation Unit, Head, University of Innsbruck, Technikerstrasse 13, A 6020 Innsbruck, Austria.

E-Mail: klaus.hanke@uibk.ac.at

## Precise Point Positioning – Towards Real-Time Applications



*Gottfried Thaler, Ana Karabatic and Robert Weber*

### Abstract

Precise Point Positioning (PPP) denotes a GNSS (Global Navigation Satellite System) based positioning technique, where dual-frequency code and phase measurements from a single receiver are used to calculate precise site coordinates at the sub-decimeter level. The data processing relies on precise satellite orbits and clock correction information determined from observation data of a global reference station network provided by organizations such as the International GNSS Service (IGS). Typically, the ionospheric delay is almost completely eliminated by means of the ionosphere-free linear combination, while the tropospheric delay and the receiver clock bias are estimated parameters along with the site coordinates.

Introduced for the first time about 14 years ago the PPP technique was mainly used in post-processing applications. Barriers for a more intense use of PPP were a lack of accurate real-time orbit and clock products, the still poor knowledge of receiver and satellite calibrations biases and last, but not least, long coordinate filter convergence times due to complex or incomplete integer ambiguity fixing. However, to meet the increasing demand of upcoming real-time (RT) applications IGS has initiated a real-time working group to investigate the feasibility of real-time GNSS data distribution and the generation of derived products such as precise clock corrections and orbits. Scientific organizations and companies operating reference stations can participate in the working group either by delivering their data-streams via a central service or by providing real-time GNSS products.

This article deals with the contributions of the Institute of Geodesy and Geophysics, Technical University of Vienna (TUW) to the IGS Real-Time Working Group and with the quality of PPP positioning obtained using the RT-data stream established at our institute. Aside from the positioning aspect the potential of PPP to derive related products such as tropospheric delays to contribute to weather forecast models is discussed. Finally prospects as well as current barriers of PPP in view of the upcoming new GNSS systems and signals are highlighted.

**Keywords:** GNSS, Precise Point Positioning, IGS Real-Time Working Group

### Kurzfassung

Mit Precise Point Positioning (PPP) wird eine GNSS- (Global Navigation Satellite System) basierte Positionierungstechnik bezeichnet, welche unter Nutzung von 2- Frequenz Code- und Phasenbeobachtungen eines einzelnen Empfängers die Berechnung präziser Stationskoordinaten mit sub-dm Genauigkeit erlaubt. Die Datenprozessierung stützt sich dabei auf präzise Satellitenbahn- und Uhrinformation welche von Organisationen wie dem International GNSS Service (IGS) aus Daten eines globalen Netzwerkes berechnet und bereitgestellt wird. Die ionosphärische Verzögerung wird bei PPP im Allgemeinen durch Bildung der ionosphärenfreien Linearkombination eliminiert, die troposphärische Verzögerung und der Stationsuhrfehler werden als Parameter neben den Koordinaten geschätzt.

Seit rund 14 Jahren wird PPP als Punktbestimmungstechnik eingesetzt, vor allem geeignet für Postprozessierung Applikationen. Als Hindernis für die verstärkte Nutzung erwiesen sich die echtzeitnahe Verfügbarkeit von präziser Bahn- und Uhrinformation, eine bis heute unzulängliche Kenntnis der Empfänger- und Satellitenhardwarekalibrierung („calibration biases“) und nicht zuletzt die lange Konvergenzzeit der Koordinatenlösung. Um der stark steigenden Nachfrage nach in Echtzeit verfügbaren Beobachtungsdaten und Bahn- und Uhrprodukten zu begegnen, wurde von IGS die Real-Time Working Group ins Leben gerufen. Die Arbeitsgruppe setzt sich aus Forschungsinstituten aber auch kommerziellen Unternehmen zusammen, welche einerseits GNSS Referenzstationen betreiben oder Echtzeitprodukte aus deren Beobachtungen ableiten.

Dieser Artikel beschäftigt sich vorrangig mit dem Beitrag des Instituts für Geodäsie und Geophysik (TU-Wien) zur IGS Real-Time Working Group und mit der erreichbaren Positionierungsgenauigkeit bei Nutzung der intern berechneten und bereitgestellten Echtzeit-Korrekturdatenströmen. Neben dem Positionierungsaspekt wird auch kurz auf das Potenzial der ebenfalls mittels PPP geschätzten troposphärischen Signalverzögerungen eingegangen. Der Beitrag schließt mit einem Ausblick auf Stärken aber auch Problembereiche von PPP in Hinblick auf die demnächst verfügbaren neuen Navigationssysteme und Signale.

**Schlüsselwörter:** GNSS, Precise Point Positioning, IGS Real-Time Working Group

## 1. Introduction

Precise Point Positioning (PPP) is a positioning technique that uses undifferenced single- or dual-frequency pseudorange and carrier phase observations of a single receiver along with the precise satellite orbit and clock error information to achieve a few centimeter-level precision (see [1], [6], [10]). The concept of PPP was first introduced in the 1970's by R.R. Anderle, and was characterized as a single station positioning with fixed precise orbit solutions and Doppler satellite observations [7]. Nevertheless, the relative positioning mode has dominated the field of GPS data processing until the late 1990's, when the Jet Propulsion Laboratory (NASA) showed that the achievable precision of PPP can be comparable to that from relative positioning and implemented this new technique in their GIPSY/OASIS-II GPS processing software [10]. Consequently, the achievable positioning accuracy for a static receiver provided by PPP is at the cm-level accuracy with 24 hours of observations for a static receiver [2].

In contrast to relative positioning, in PPP no regional network correlations will be introduced and no reference station data is explicitly required for data processing. Aside from the fact that this makes PPP cost effective, the technique also allows to check the consistency of the introduced orbit, clock and atmosphere error models irrespective of environmental station biases propagated by differencing techniques.

The PPP dual-frequency functional model for code and phase reads

$$P_{if} = \rho - c(\Delta t^S - \Delta t_R) + \Delta \rho_{Trop} \quad (1)$$

$$\Phi_{if} = \rho - c(\Delta t^S - \Delta t_R) + \Delta \rho_{Trop} + \lambda_{if} b_{if} \quad (2)$$

where  $P_{if}$  stands for the ionosphere-free combination of pseudorange measurements and  $\Phi_{if}$  is the ionosphere-free combination of carrier phase measurements in metric units. The term  $\rho$  denotes the geometric distance between the satellite and the receiver antenna and  $c$  is the speed of light.  $\Delta t^S$  and  $\Delta t_R$  are the satellite and the receiver clock errors respectively, and  $\Delta \rho_{Trop}$  denotes the tropospheric delay. The phase equation (Eq. (2)) contains in addition the ionosphere-free effective carrier phase wavelength  $\lambda_{if}$  and the ambiguity parameter  $b_{if}$ . This ambiguity parameter  $b_{if}$  contains instrumental biases, and is therefore no longer an integer number not even in the zero-difference basic phase observables on L1 and L2. Remaining effects such as phase wind-up, relativity corrections, tidal corrections, phase antenna center variations, etc., have to be introduced through appropriate models.

Dependency of PPP on precise IGS (International GNSS Service) orbit and clock products [4] restricts the use of this technique to post-processing applications, since the latency of these products is at least 17 hours after the observed epoch in the case of the IGS "rapid" products. Real-time applications, on the other hand, rely on broadcast information or precise

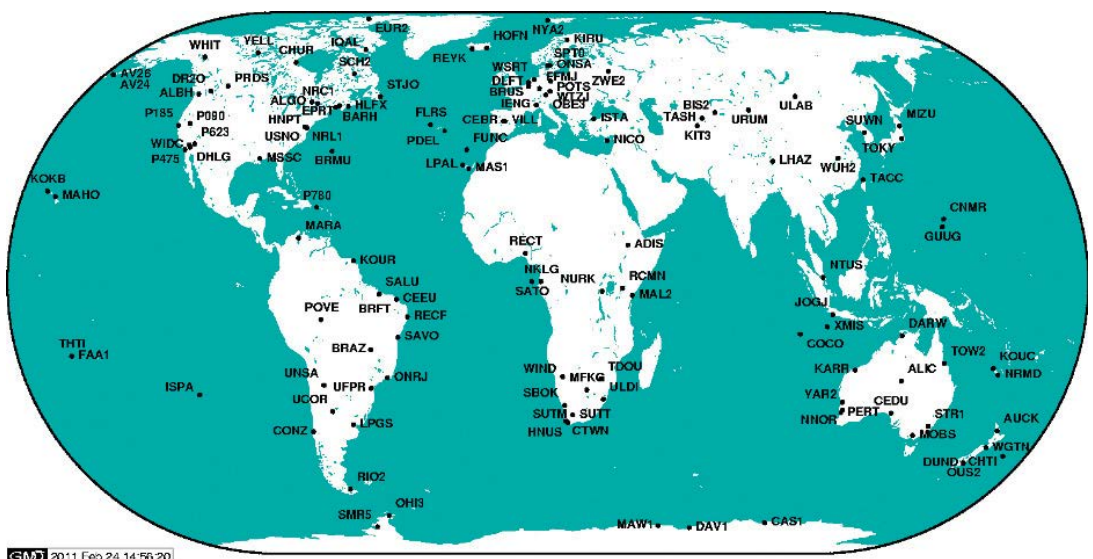


Fig. 1: RTIGS station network

predictions. While the GNSS broadcast messages are unsuitable for single point positioning at the sub-meter level, the IGS products have sub-dm orbit accuracy but the accompanying clock corrections are still at the 2-4 ns level after a 6 hours prediction period. These range errors map directly into the PPP solution. Therefore the IGS has investigated potential improvements of orbit and clock correction product generation for RT purposes and established an appropriate Working Group focusing on GNSS real-time data flow and product development in 2002.

After the successful Data and Analysis Center Workshop “Towards Real-Time Network,” in Ottawa, Canada in April 2002, the main goal of the IGS Real-Time Working Group (RTWG), led by Mark Caissy of National Resources Canada, was to establish a global GNSS station network (the RTIGS network) consisting of stations which are delivering their observation data in real-time (at most a delay of a few seconds) to central processing facilities, and subsequently to potential users. The data transmission is performed using the internet and the User Datagram Protocol (UDP). Nowadays (2011) this global real-time station network consists of approximately 80 stations (see Fig. 1).

In parallel, appropriate real-time PPP software has to be developed to investigate the potential of RT-PPP. These software packages are mainly developed by private companies or research institutes, and few of them are publicly available. Examples are the software BNC (BKG Ntrip Client) developed by the Federal Agency of Cartography and Geodesy (BKG - Bundesamt für Kartographie und Geoinformation [11]) in Germany, or an open-source program package RTKLib developed at the Tokyo University of Marine Science and Technology. Both packages process broadcast ephemeris corrections for satellite orbits and clocks provided in the RTCMv3 format.

## 2. Software RTIGU-Control

Besides establishing RT products one task of the IGS RTWG is to monitor the quality of the issued IGU (IGS ultra-rapid) products. This is of special interest as IGU clock corrections experience a considerable degradation in quality with increasing prediction periods, and there is a need for a quick detection of outliers. For that purpose the Institute for Geodesy and Geophysics of the Technical University of Vienna (TUW) contributes to the RTWG by developing the software RTIGU-Control [8]. Based on the software RTIGS Mul-

ticast Receive (RTIGSMR) provided by NRCAN [12] and by introducing the RTIGS network observations, RTIGU-Control is able to calculate orbits and clock corrections for the whole GPS satellite constellation in “near” real-time (delay of approximately 15 – 20 seconds). RTIGSMR is already able to decode and prepare the incoming real-time observations for further use and serves as a development platform for creating RTIGU-Control. The three main features of RTIGU-Control can be summarized as followed:

- monitoring of the predicted IGU products, especially the predicted satellite clock corrections;
- calculation of individual daily RTIGU-Control clock and orbit products (TUW-products) for later comparison with other RTIGS center products; and
- assisting real-time positioning applications by providing real-time satellite orbit and clock correction data (see Sec. 3).

The functionality of RTIGU-Control shall be briefly described below. The program calculates, in a first step, the real-time clock corrections and clock drifts with respect to GPS time for the GPS satellites and tracking stations by means of carrier-smoothed observations. This may be regarded as an initial step of an iterative process, because the calculated clock corrections are based on the predicted IGU orbits. A subsequently applied Kalman Filter step (kinematic approach) introduces again the carrier-smoothed observations, this time correcting for the clock corrections of step 1 to calculate the positions and velocities of the satellites. Although the procedure is not totally independent of the IGU solution it still performs a consistency check of the IGU predictions. Clock corrections and orbit information are loaded every 30s to clock – RINEX and SP3 – files. Results and comparisons to IGU products are displayed online on the operator screen but also stored in clock RINEX and SP3 file formats, e.g. for validation of the performance of the IGU-predicted products. Furthermore the established orbit and clock parameters are used to calculate corrections to the broadcast ephemeris, which can finally be fed into a real-time PPP algorithm. The calculation scheme of RTIGU-Control for one epoch is displayed in Fig. 2. The following general steps are performed.

**Carrier-smoothing:** The carrier-smoothing algorithm is based on a weighting procedure of temporal phase differences together with

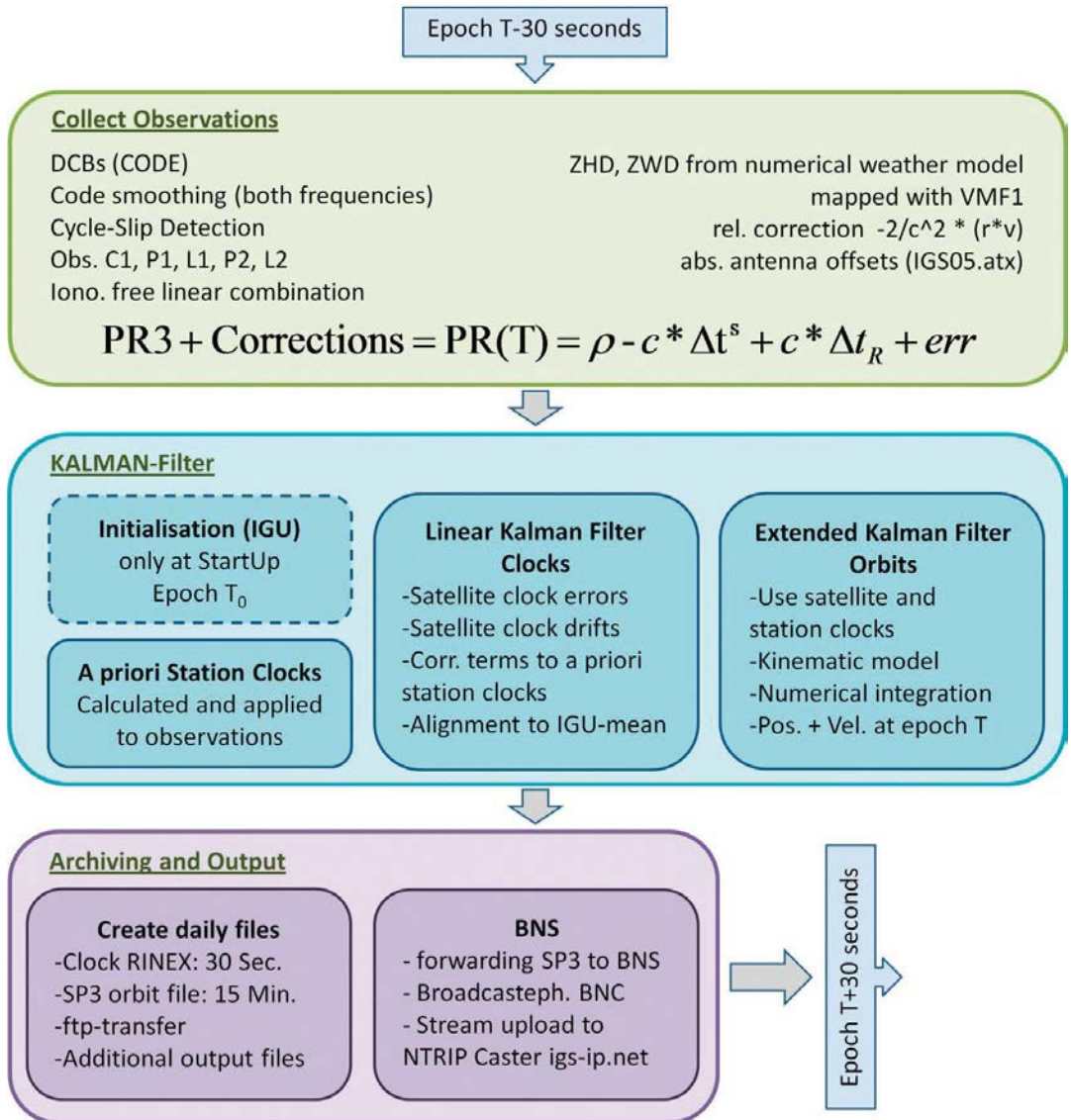


Fig. 2: RTIGU-Control calculation scheme

raw code observations [5]. Code DCBs (Differential Code Biases) provided by the IGS Analysis Center CODE are applied to the observations at both frequencies. Also, cycle-slip detection is performed within this calculation step.

**Ionosphere-free linear combination:** The smoothed pseudoranges (PRs) at both frequencies are merged by means of the ionosphere-free linear combination (PR3) to reduce the ionospheric delay of the signals.

**Apply corrections:** The tropospheric delay is corrected using gridded ZHD (zenith hydrostatic delay) and ZWD (zenith wet delay) information

calculated from numerical weather models (predictions). They are mapped into the specific elevation using the VMF1 mapping function [3]. The 2<sup>nd</sup> order relativistic effect is applied and the absolute antenna offsets (IGS05.atx) are included. Additionally solid earth tide corrections are applied to the fixed coordinates of the reference stations.

**Linear Kalman Filter - clocks:** Within this calculation step the satellite clock corrections with respect to GPS Time as well as their linear drifts are calculated. Because of the unpredictable behavior of most station clocks, approximate a



priori values are calculated by introducing the satellite clock corrections of the previous epoch. The filter solely estimates correction terms to these a priori station clock corrections. The mean of all satellite clock corrections is aligned to the IGU clock mean (reference).

**Extended Kalman Filter - orbits:** Introducing again the observations corrected for the satellite and station clock errors, the orbits of the satellites are estimated. The kinematic model that is used considers the attraction due to the central term for earth gravitation plus the oblateness (J2) of the Earth. The predicted values are generated using a numerical integration process. After this step the positions, as well as the velocities, of all available satellites are obtained. The clock estimation has been separated from the orbit estimation to limit the required processing time of each processing step. In general, and in case of available adequate computer power, it is advisable to estimate all parameters in a single step which allows for proper stochastic modeling.

**Archiving and streaming:** All calculated results are coded in clock RINEX and SP3 orbit files for further analysis and stored on the ftp server of the Institute. Additionally SP3 files containing the calculated orbits and clocks are generated every epoch and forwarded to BNS (see Sec. 3).

**3. Data Flow and PPP Field Test**

Typically real-time PPP applications make use of continuously available observation and broadcast information data from a GNSS receiver together with actual corrections to satellite orbit and clock parameters. To perform the task of calculating corrections to the broadcast ephemerides and satellite clock errors use is made of the software BNC (BKG NTRIP Client) and BNS (BKG NTRIP State Space Server) provided by the BKG as well as the real-time orbit and clock information calculated by RTIGU-Control. BNC receives the GPS broadcast information from the NTRIP-Caster igs-ip.net and forwards it to BNS. RTIGU-

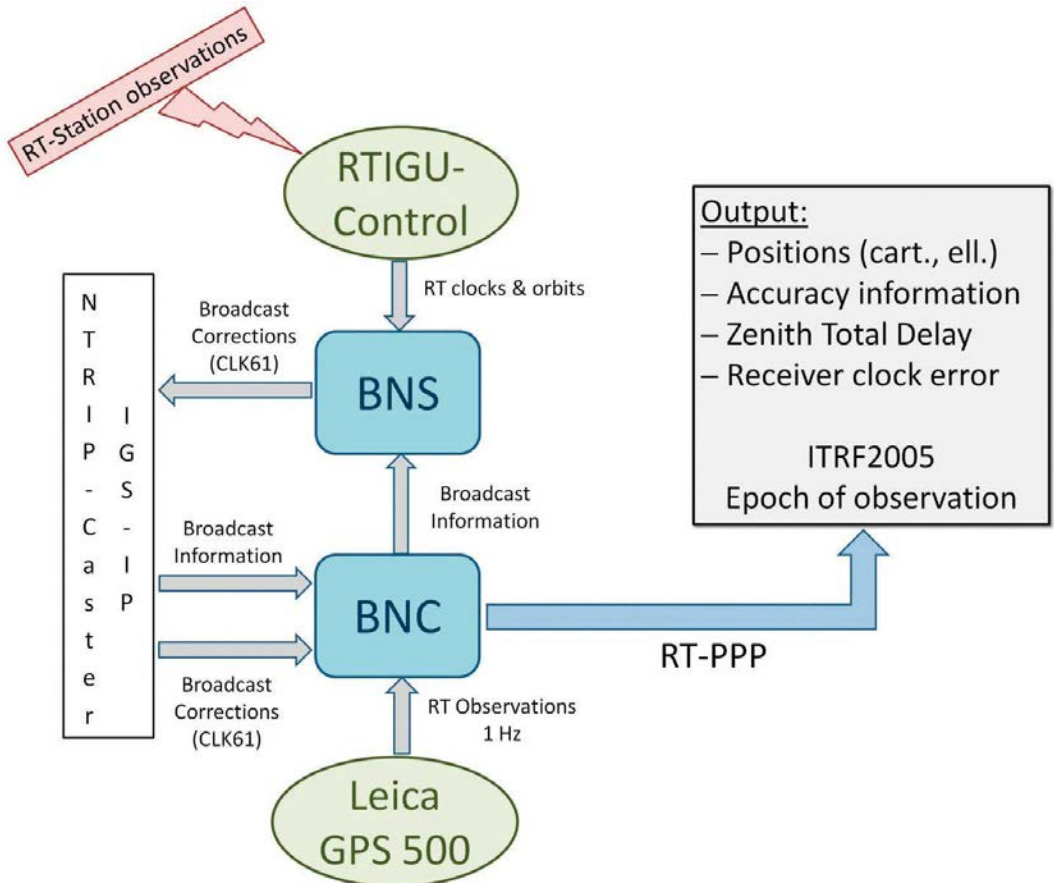


Fig. 3: Processing scheme of the RT-PPP experiment

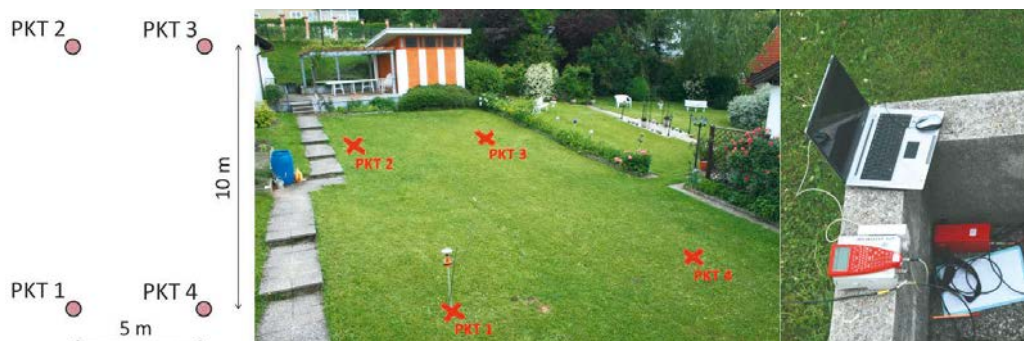


Fig. 4: Setup of the RT-PPP test scenario

Control calculates the satellite orbits and clock errors and forwards them in SP3 file format to BNS.

BNS calculates the correction terms to the broadcast ephemerides and clock errors using the forwarded data sets and delivers these corrections in a RTCMv3 format back to the NTRIP-Caster within the correction data stream CLK61. Finally, besides various other correction data streams provided by several other institutions, this CLK61 stream applied to the underlying broadcast information is used within the built-in real-time PPP client of BNC to calculate site coordinates. The processing scheme is shown in Fig. 3.

To study the achievable accuracy using RTIGU-Control products with RT-PPP, both static as well as a kinematic test scenario were set up [9]. Current observation data were collected by a Leica GPS 500 receiver. The test area comprised four static points forming a rectangle with dimensions of approximately 5 to 10 meters. The Leica GPS 500 receiver was connected to a AT502 Antenna and delivered measurements with a data rate of 1Hz to the serial port of the notebook

where BNC was installed. The broadcast information and the correction data stream CLK61 were received via WLAN from the NTRIP-Caster igs-ip.net. Parallel to the RT-PPP solutions calculated by BNC, the raw observation data were stored for post-processing. An external power supply unit completed the necessary equipment (see Fig. 4).

After initializing the RT-PPP algorithm at PKT 1 static measurements were carried out at PKT 2 – PKT 4 for about half an hour at each point. Afterwards several kinematic tests were carried out, for example one kinematic trajectory described a “figure eight”, another one involved moving randomly between the four points.

Tab. 1 shows the schedule of the different tasks performed in RT-PPP experime

The RT-PPP results were recorded within the log file of BNC, the raw measurements as RINEX v2.11 observation file. The reference coordinates of PKT1 – PKT4 were calculated by means of the Leica GeoOffice (LGO) software using the static observations together with rapid IGS products and observations from a nearby reference station. The kinematic trajectories and the static

Measurement time (MESZ) Date: June,12th 2010	Measurement scenario	BNC RT-PPP (kin.)	LGO Baseline	NRCan PPP (kin.)	Comments
12:11 – 13:43	Static, PKT 1	X	X	X	Initialising RT-PPP
13:45 – 14:23	Static, PKT 2	X	X	X	
14:26 – 15:57	Static, PKT 3	X	X	X	
14:59 – 15:32	Static, PKT 4	X	X	X	
From 15:35	Kinematic	X	—	X	figure eight
From 15:37	Kinematic	X	—	X	random movement
From 15:42	Kinematic	X	—	X	loop

Tab. 1: Tasks and schedule of the RT-PPP test scenarios

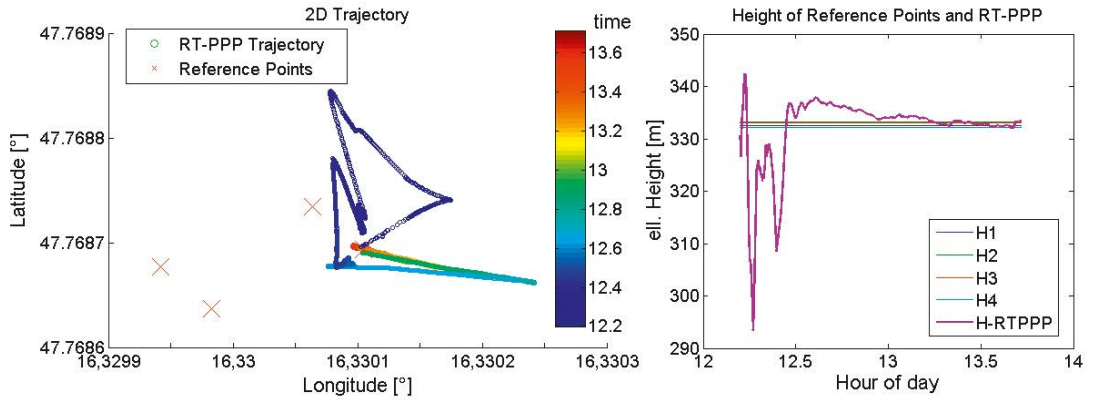


Fig. 5: Initialization step at PKT 1

observations were processed using the online kinematic PPP service of National Resources Canada (NRCAN). Finally, these reference solutions were then compared with the achieved RT-PPP solutions.

The convergence time of the BNC PPP algorithm is typically 30 to 45 minutes, but depends also on the quality of the broadcast corrections and the ratio between code and phase measurement noise set by the user. In the worst case, if the quality of the broadcast corrections is extremely bad, the coordinate solution does not converge. Fig. 5 shows the convergence process at PKT 1 for the horizontal position as well as for the height component. The change in the horizontal position with time is color-coded, which means position solutions during the initialization period are plotted with blue circles, positions obtained after convergence of the filter algorithm are plotted with red circles. The heights of the reference points are plotted as horizontal lines. Convergence was achieved about 45 minutes after initialization.

After the convergence of BNC's PPP algorithm at PKT 1 and at the other three corner points of the test rectangle (PKT 2 – PKT 4) RT-PPP measurements were carried out and afterwards compared with the reference position, and additionally with the kinematic solutions of NRCAN online PPP service. As an example the solutions obtained from NRCAN and by RT-PPP at PKT 3 are shown in Fig. 6.

The horizontal positions it has to be pointed out that the point clouds obtained from both solutions are clearly separated in space. The coordinate rms. of the NRCAN point cloud is about 10 cm with an offset to the reference position (red "X") of 10 cm in the southwest direction. In the case of RT-PPP the rms. of about 15 cm is slightly larger with an offset of 25 cm in the south-east direction of the reference position. Another clearly visible detail is that the solutions show an artificial movement with time (color-coded) which can be related to the changing satellite geometry. The offset can be caused by differences in orientation of the introduced orbit represen-

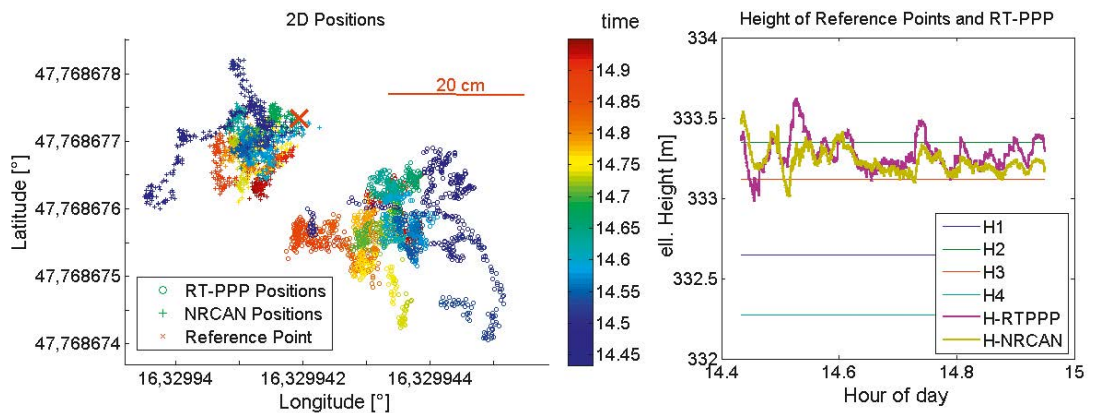


Fig. 6: Reference, NRCAN and RT-PPP solutions for PKT 3

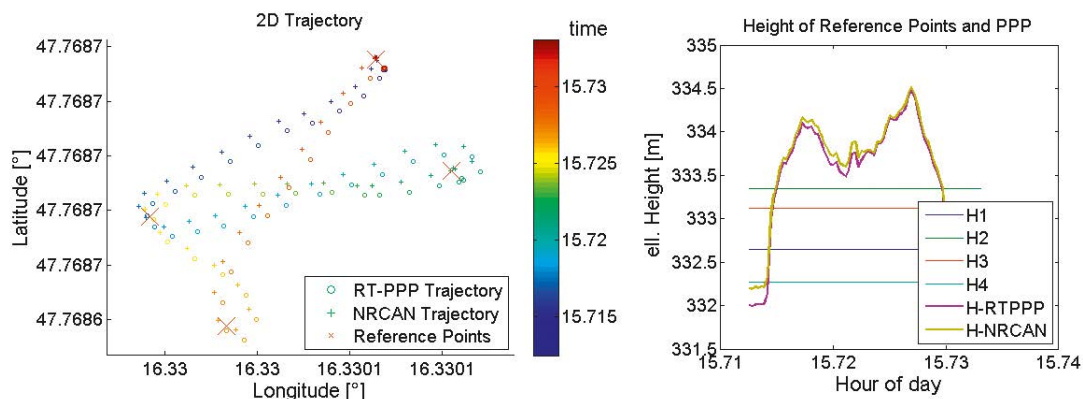


Fig. 7: Results of the kinematic test scenario "loop"

tations, on the one hand real-time orbit information and on the other a precise IGS orbit product for post-processing, well aligned to the underlying reference frame. The height time series of both PPP solutions are very similar. In most cases the RT-PPP solution are a few cm above the NRCAN solution. Both PPP solutions show a bias of approximately 10-15 cm compared to the reference height. This may be caused in both cases by an insufficient modeling and estimation of the tropospheric path delay.

As a final example, the results of the kinematic "loop" experiment are shown in Fig. 7.

Starting at PKT 4, PKT 3 was circled. Afterwards the receiver was moved along the diagonal of the rectangle until PKT 1 was reached. From there the receiver was moved back to PKT 3 and further on to PKT 2. Finally the chosen path led back to PKT 4 along the other diagonal of the rectangle. In Fig. 7 the horizontal plot contains again the reference positions of the corner points, the trajectory of the NRCAN solution obtained from post-processing and the real-time trajectory from BNC obtained with the RTIGU-Control broadcast corrections. Similar to the static experiment one can see an offset of approximately 30 cm in the southeast direction of the RT-PPP solution from the reference position (and also with respect to the NRCAN solution). This offset remains constant over the whole observation period of the kinematic test. This would be an indicator of a stable number (and geometry) of visible satellites, although the elevation mask characteristics are significantly changing during the movement of the antenna. A check of the raw observation data confirmed that no change in the number of tracked satellites took place during this experiment.

The conducted RT-PPP experiment confirms that using the real-time orbit and clock correction data-stream obtained from RTIGU-Control for real-time PPP algorithms such as the one used by the BNC software can provide positioning accuracies of 20 – 30 cm in horizontal position as well as height. Therefore, this technique can be integrated into various global navigation applications.

#### 4. Summary and Prospects

PPP has become a valid alternative to network-based GNSS processing, at least for a number of post-processing applications. Currently real-time PPP solutions still suffer from extended coordinate filter convergence times compared to differential techniques, as well as having a limited positioning accuracy at the 10-20 cm-level, primarily caused by missing calibration information preventing integer ambiguity fixing. Nevertheless, there are a number of applications, aside from exclusive positioning tasks, which can be addressed using PPP. In this context "near" real-time troposphere monitoring can be mentioned as an example. The tropospheric delay is a parameter of the PPP process and the variation of atmospheric humidity is of great interest to meteorology. PPP data from a dense reference station network can be processed in short time frames which allows computation of tropospheric delays within a couple of minutes, hence contributing to weather forecasting. For details see [6].

The set of new signals provided by next generation and modernized GNSS programs will allow for improved ambiguity resolution techniques. In terms of PPP these signals will offer the opportunity to choose less noisy ionospheric-free linear combinations and allow for the modeling of higher order ionospheric effects. However, the

use of new GNSS signal for PPP will only be possible if the accompanying systematic inter-system biases can be determined to high accuracy.

## References

- [1] *Anderle, R.J. (1976)*: Point positioning concept using precise ephemeris. In: Satellite Doppler positioning; Proceedings of the International Geodetic Symposium, Las Cruces, N. Mex., October 12-14, 1976. Vol. 1. (A77-47370 22-43) Las Cruces, N. Mex., New Mexico State University, pp. 47-75.
- [2] *Bisnath, S. & Gao, Y. (2008)*: Current state of Precise Point Positioning and future prospects and limitations. In Proceedings of IUGG 24th General Assembly (in press).
- [3] *Böhm J., Werl B., & H. Schuh (2006)*: Troposphere mapping functions for GPS and Very Long Baseline Interferometry from European Center for Medium-Range Weather Forecasts operational analysis data. *Journal Geophysical Research*, 111, B02406, doi: 10.1029/2005JB003629.
- [4] *Dow, J., Neilan, R. & Rizos, C. (2009)*: The International GNSS Service in a changing landscape of Global Navigation Satellite Systems. *Journal of Geodesy*, Vol. 83, pp. 191-198.
- [5] *Hofmann-Wellenhof B., Lichtenegger H. & Wasle E. (2008)*: GNSS – Global Navigation Satellite Systems, GPS, GLONASS, Galileo and more. Springer Verlag, Wien, New-York, ISBN 978-3-211-73012-6.
- [6] *Karabatic, A. (2011)*: Precise Point Positioning – an alternative technique for ground based GNSS troposphere monitoring. PhD thesis, Vienna Technical University, Institute of Geodesy and Geophysics, Vienna, Austria (in press).
- [7] *Kouba, J. & Heroux, P. (2001)*: Precise Point Positioning using IGS orbit and clock products. *GPS Solutions*, Vol. 5, pp. 12-28.
- [8] *Thaler, G. (2011)*: Orbit- und Uhrberechnung der GPS-Satellitenkonstellation basierend auf Echtzeit-Beobachtungsdaten des RTIGS-Stationsnetzwerks. PhD thesis, Vienna Technical University, Institute of Geodesy and Geophysics, Vienna, Austria (in press).
- [9] *Thaler, G., Karabatic, A. & Weber, R. (2010)*: Consistency check of improved real-time clock and orbit products by means of PPP. In proceedings of ENC GNSS 2010, October 19-21, 2010, Braunschweig, Germany.
- [10] *Zumberge, J., Heflin, M., Jefferson, D., Watkins, M. & Webb, F. (1997)*: Precise point positioning for the efficient and robust analysis of GPS data from large networks. *Journal of Geophysical Research*, Vol. 102, pp. 5005-5017.
- [11] *Bundesamt für Kartographie und Geoinformation BKG, GNSS Data Center*: <http://igs.bkg.bund.de/ntrip/ntriphompage>
- [12] *National Resources Canada, Geodetic Survey Division (NRCan, GSD)*: [http://www.geod.nrcan.gc.ca/index\\_e.php](http://www.geod.nrcan.gc.ca/index_e.php)

## Contacts

Dipl.-Ing. **Gottfried Thaler**, WIEN ENERGIE Stromnetz GmbH, Abteilung NTDG - digitales Grundplanwerk, Mariannengasse 4 – 6, 1095 Vienna, Austria.

E-Mail: [gottfried.thaler@wienstrom.at](mailto:gottfried.thaler@wienstrom.at)

Dr. **Ana Karabatic**, Vienna Technical University, Institute of Geodesy and Geophysics, Gußhausstraße 27-29, 1040 Vienna, Austria

E-Mail: [ana.karabatic@tuwien.ac.at](mailto:ana.karabatic@tuwien.ac.at)

a.o. Prof. Dipl.-Ing. Dr. **Robert Weber**, Vienna Technical University, Institute of Geodesy and Geophysics, Gußhausstraße 27-29, 1040 Vienna, Austria.

E-Mail: [robert.weber@tuwien.ac.at](mailto:robert.weber@tuwien.ac.at)

## Estimating platform kinematics using multi-antenna GNSS



Andreas Wieser and Roland Aschauer

### Abstract

The position, velocity, and attitude of a moving platform can be determined in realtime using GNSS with three or more antennas rigidly mounted on the platform. Objects shading satellite signals and causing multipath effects are a major concern for practical applications. In this contribution we derive the observation equations relating the platform parameters directly to the undifferenced pseudo-range, carrier-phase, and Doppler observations. We demonstrate that this approach is superior to deriving the platform kinematics from the kinematics of the individual GNSS antennas because it yields higher redundancy and offers a useful option for mitigating multipath effects created by the platform itself.

**Keywords:** GNSS, platform, attitude, positioning, multipath

### Kurzfassung

Position, Geschwindigkeit und Orientierung einer bewegten Plattform können mit Hilfe von drei oder mehr auf der Plattform fix montierten GNSS Antennen in Echtzeit bestimmt werden. Eine Herausforderung stellen dabei Plattform-Aufbauten dar, welche die Satellitensignale abschatten und Mehrwegeeffekte verursachen. Wir leiten in diesem Beitrag die Beobachtungsgleichungen her, welche die gesuchten Plattform-Parameter direkt mit den undifferenzierten Pseudostrecken-, Trägerphasen- und Dopplerbeobachtungen verknüpfen. Die Schätzung unter Verwendung dieser Beobachtungsgleichungen ist der Bestimmung der Plattform-Kinematik aus den Trajektorien der einzelnen GNSS Antennen überlegen, weil die Redundanz höher ist und sich eine praktische Möglichkeit zur Reduktion der negativen Auswirkungen von Mehrwegeeffekten und Abschattungen durch die Plattform selbst ergibt.

**Schlüsselwörter:** GNSS, Plattform, Lage, Positionierung, Mehrwegeeffekte

### 1. Introduction

Applications like mobile mapping, guidance and control of construction machines, hydrographic surveying or guidance of a slip form require the position and spatial orientation of a moving platform to be estimated accurately and reliably. The Institute of Geodesy and Geophysics at the Vienna University of Technology has established a research focus on platform navigation with particular interest in kinematic positioning and attitude determination at the centimeter and sub-degree level. Experimental investigations are carried out using a mobile robot which the Institute acquired lately (Fig. 1).

While GPS has initially been established for positioning, navigation and timing, it was an obvious idea to derive also the attitude i.e., spatial orientation, of a platform from GPS once relative positions of nearby antennas could be estimated with mm to cm accuracy, see e.g. [6]. In a PhD thesis carried out at the Stanford University, Clark Cohen developed a multiplexing receiver for attitude determination and related the attitude to the single-difference carrier-phase observations collected by a single receiver connected to several

GPS antennas [2]. This allowed estimating platform attitude directly from the GPS observations rather than computing it through a Helmert transformation. This approach also avoided the problem of handling the time offset between multiple non-synchronized receivers. Subsequently, optimum configurations of multi-antenna arrays for attitude determination were studied and found to be 4 antennas arranged in a tetrahedron [10]. By taking the time derivatives of the attitude equations given in [2], Ueno et al. [11] developed



Fig. 1: Autonomous robot equipped with multi-sensor system for kinematic positioning and mobile mapping

equations for estimating attitude rate directly from single-differenced Doppler observations.

Less attention has been paid to the simultaneous estimation of highly accurate position, velocity and attitude (PVA), and its potential benefit for effective mitigation of platform multipath and obstruction effects. However, these are of major importance for applications like the ones mentioned above and are the motivation for this contribution. A major challenge when using multi-antenna GNSS for platform PVA determination in applications to construction and surveying engineering is the selection of suitable antenna locations on the platform (machine). These locations cannot be freely chosen such as to provide optimum GNSS signal reception and data quality. Usually, they are restricted to parts of the platform where the antennas can be rigidly mounted but do not mechanically interfere with normal operation of the machine.

The antennas will therefore typically be subject to obstruction of satellite signals by parts of the platform. This affects the redundancy and the geometry negatively and thus impairs precision and reliability. However, these parts of the platform will typically also act as signal reflectors, see Fig. 2, and thus cause multipath effects which may be as large as about 5 cm at the individual carrier-phase observation level. The effect on the estimated coordinates may be of similar magnitude. This impairs the accuracy of the results and may be a significant challenge for quality control in the context of reliability and of outlier detection. The effect is even worse if the reflector is cylindrically or spherically shaped (see Fig. 2b). All satellite signals which are not obstructed may then be subject to (strong) multipath effects.

Furthermore, reflecting objects on the platform are usually close to the receiving antenna. The multipath error consequently oscillates with a period of several minutes up to half an hour or even more unless the platform exhibits significant attitude changes at shorter time scales. This can be derived from the well-known equations describing multipath error oscillations, see e.g. [4]. So, the multipath effects are virtually stationary and cannot be mitigated significantly by averaging over a few epochs or by filtering. Thus they are a significant challenge for machine guidance, platform navigation and similar applications.

A potential solution is the use of specially designed antennas with high attenuation close to the antenna horizon, see [1]. However, this will not be successful for near-boresight reflected signals

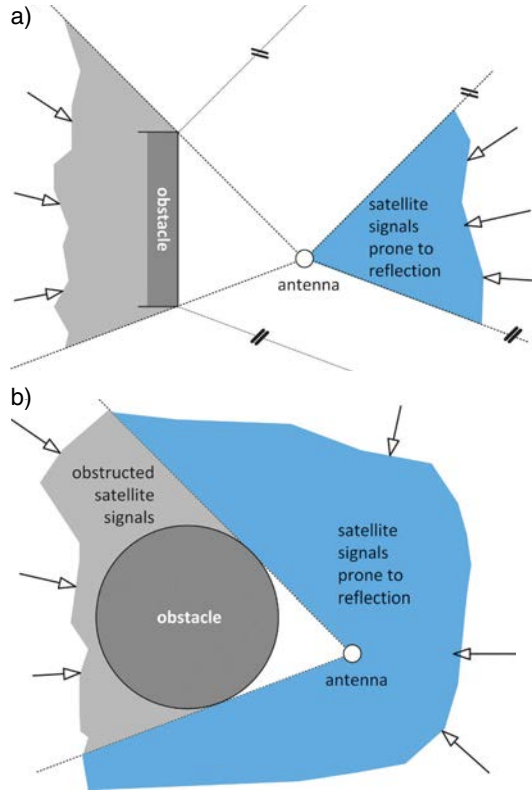


Fig. 2: Signal obstruction and reflection caused by a planar obstacle (a) and by a spherical obstacle (b) in the vicinity of a GNSS antenna; satellite (sender) assumed at infinite distance in direction of shaded areas.

(e.g. with high elevation satellites) and it will introduce an unwanted reduction of signal strength and availability of clear signals. We consider the use of suitably tuned microwave absorbing material (e.g. foam) a more suitable means for preventing reflections at the platform from reaching the GNSS antennas, see Fig. 3. If the absorbing screens are properly shaped and mounted, they will not introduce additional signal obstruction and thus not deteriorate the satellite availability further. However, they will avoid near-field multipath effects of the satellite signals actually received. The drawback is that the position and velocity of the individual antennas may not be observable from the GNSS observations anymore because of the signal obstruction. On the other hand, it is not necessary to estimate the *individual* antenna positions for the applications mentioned above. Instead, three or more antennas rigidly connected to the same platform can be used to collect raw data for estimating the position and velocity of the arbitrarily chosen platform origin. Band the plat-

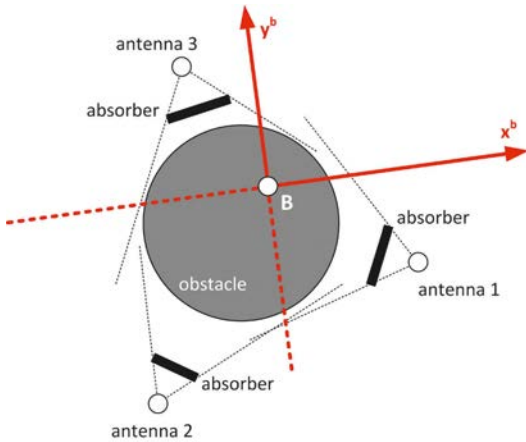


Fig. 3: Multi-antenna arrangement with microwave absorbing screens (absorbers) and platform coordinate frame (b-frame)

form attitude i.e., the orientation of the platform coordinate axes with respect to an earth fixed frame instead. Due to the lever arm of the individual antennas it is necessary to include the attitude rate as a nuisance parameter if the platform velocity is estimated.

In the following we will derive the observation equations linking the platform PVA to the undifferenced GNSS observations taking into account that there is no difference between GPS and any other GNSS as far as these equations and their practical applicability are concerned. We assume that raw GNSS observations from a nearby reference station are available and that double differenced (DD) pseudorange and carrier phase observations involving this reference station are used along with undifferenced Doppler observations obtained at the platform. (There is no practical benefit from using Doppler observations obtained at the stationary reference site or from processing DD Doppler observations.) In comparison with the previously published approaches based on single difference measurements obtained at the platform, this approach allows fully exploiting any potential redundancy, in particular when processing a maximum set of linearly independent DD observations rather than DD observations obtained using a reference-station/rover-station scheme. A useful algorithm for finding such a maximum set of DD can be found in [8].

When deciding whether individual terms need to be taken into account or may be neglected, we will consider terms negligible if they affect the carrier-phase and Doppler observation by less than 0.5 mm and 0.5 mm/s, respectively.

In correspondence with the applications mentioned above we will assume that the platform moves with a speed of less than 10 m/s, rotates with a rate of less than 0.6 rad/s (180° within 5 s) and that the lever arms are less than 10 m in length. Nevertheless, we will also indicate how the results relate to larger platforms or faster moving ones and are thus applicable to other applications than the ones mentioned above.

**2. Coordinate systems and transformations**

The locations of the GNSS antennas with respect to the platform, i.e., their coordinates expressed in the right-handed Cartesian “body-frame” (b-frame), are assumed to be known. The transformation of these coordinates to the earth-centered-earth-fixed frame (e-frame), e.g. ITRF2005, can be expressed as follows:

$$\mathbf{X}_i^e = \mathbf{X}_B^e + \mathbf{C}_b^e \mathbf{X}_i^b \tag{2.1}$$

with

$\mathbf{X}_i^e, \mathbf{X}_i^b$  ... coordinates of antenna  $i$  expressed in e- and b-frame, respectively,

$\mathbf{X}_B^e$  ... coordinates of origin of b-frame expressed in e-frame, and

$\mathbf{C}_b^e$  ... b-frame to e-frame rotation matrix.

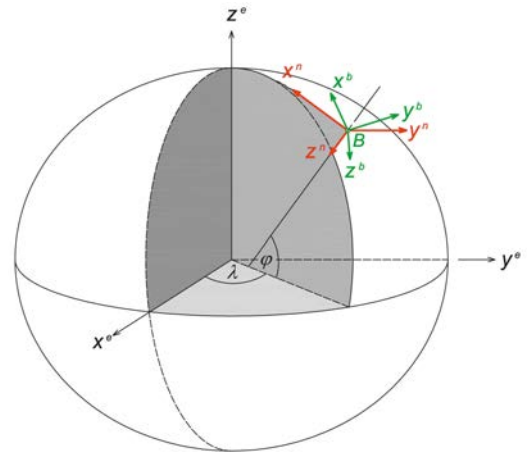


Fig. 4: Earth-centered-earth-fixed frame (e), navigation frame (n), and body (b) frame

For convenience, the b-frame to e-frame rotation matrix is split into a rotation with respect to the local level frame (n-frame) and a rotation of the local level frame with respect to the e-frame, see e.g. [5, §1.5 and § 5]:



$$\mathbf{C}_b^e = \mathbf{C}_n^e \mathbf{C}_b^n \quad (2.2)$$

with

$$\mathbf{C}_n^e = \begin{bmatrix} -\sin \varphi_B \cos \lambda_B & -\sin \lambda_B & -\cos \varphi_B \cos \lambda_B \\ -\sin \varphi_B \sin \lambda_B & \cos \lambda_B & -\cos \varphi_B \sin \lambda_B \\ \cos \varphi_B & 0 & -\sin \varphi_B \end{bmatrix} \quad (2.3)$$

where  $\varphi_B$  and  $\lambda_B$  indicate the ellipsoidal coordinates of the b-frame origin, and the axes of the n-frame point towards North, East and Down, as visualized in Fig. 4. The attitude of the platform can be described conveniently using yaw ( $\alpha$ ), pitch ( $\chi$ ) and roll ( $\eta$ ) which represent angles of sequential rotation according to

$$\mathbf{C}_b^n = \mathbf{R}_3(-\alpha) \mathbf{R}_2(-\chi) \mathbf{R}_1(-\eta), \quad (2.4)$$

where  $\mathbf{R}_k(\theta)$  is a rotation matrix describing the counter-clockwise rotation of a right-handed coordinate system about its  $k$ -th axis, see Fig. 5. If the platform is only slightly tilted, the yaw angle equals approximately the geodetic azimuth of the  $x^b$ -axis.

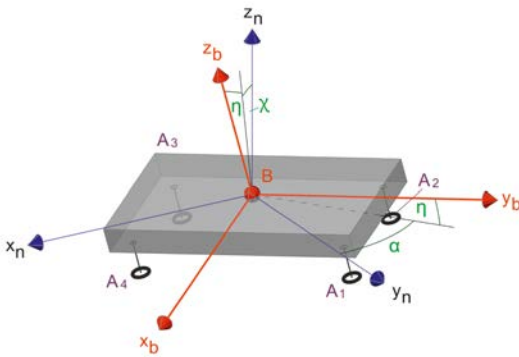


Fig. 5: Relative orientation of platform with respect to n-frame, expressed using pitch ( $\chi$ ), roll ( $\eta$ ) and yaw ( $\alpha$ ) angles ( $z^n$ -axis in reality pointing downwards; view is upside down for graphical reasons).

### 3. Position and attitude

The one-way carrier phase measurement between the receiving antenna  $i$  and the satellite  $j$ , can be expressed in units of meters as

$$\phi_i^j = \lambda \cdot \Phi_i^j = \rho_i^j - \lambda \cdot N_i^j + \dots \quad (3.1)$$

with

$$\rho_i^j = \|\mathbf{X}_j^e - \mathbf{X}_i^e\| = \sqrt{(\Delta \mathbf{X}_{ij}^e)^T \cdot \Delta \mathbf{X}_{ij}^e} \quad (3.2)$$

and

$\Phi_i^j$  ... carrier phase observation (in cycles)

$\lambda$  ... wavelength (in m/cycle)

$N_i^j$  ... one-way carrier phase integer ambiguity (in cycles)

In this equation, almost all terms which are treated identically with platform positioning as with individual point positioning or which are irrelevant for the present discussion, have been omitted for clarity. Without further discussion it is assumed that the Sagnac correction is properly applied to the satellite position such that eq. (3.2) actually represents the geometric distance between the satellite and the receiver expressed in the e-frame. A comprehensive discussion of the entire observation equation can be found in [7], [9] or other standard textbooks on GPS.

The non-linear measurement equations (3.1) are linearized at a suitable approximation in order to estimate the unknown parameters using linear estimators based on a chosen optimization criterion like maximum likelihood or minimum mean square error. This linearization yields the linearized observation equations

$$\underbrace{\phi_i^j - (\phi_i^j)_o}_{=: y_{\phi_i^j}} = \underbrace{\frac{\partial \phi_i^j}{\partial (\mathbf{X}_i^e)^T} \cdot d\mathbf{X}_i^e}_{\dots + \varepsilon_i^j + O^2} + \underbrace{\frac{\partial \phi_i^j}{\partial N_i^j} \cdot dN_i^j}_{=: e_{\phi_i^j}} + \dots \quad (3.3)$$

with the carrier phase measurement  $(\phi_i^j)_o$  computed from the assumed or predicted values of all parameters, and the original error term lumped together with the neglected higher order terms  $O^2$  into the residual  $e$ . From eq. (3.2) one can easily derive that the partial derivative with respect to the coordinates of the receiving antenna is the negative receiver to satellite unit vector expressed in the e-frame i.e.,

$$\frac{\partial \phi_i^j}{\partial (\mathbf{X}_i^e)^T} = -(\mathbf{a}_{ij}^e)^T. \quad (3.4)$$

The derivative with respect to the integer ambiguity is just the negative wavelength but does not need to be discussed any further here, because ambiguity resolution in the model derived here is carried out using the usual strategies and is thus not within the scope of the paper. However, as stated above, we aim at estimating the coordinates of the platform origin rather than those of the individual antennas. So, instead of the usual derivative with respect to  $\mathbf{X}_i^e$  we need the one with respect to  $\mathbf{X}_B^e$ . We can easily obtain it tak-

ing into account eq. (2.1) and applying the chain rule:

$$\frac{\partial \phi_i^j}{\partial (\mathbf{X}_B^e)^T} = \frac{\partial \phi_i^j}{\partial (\mathbf{X}_i^e)^T} \cdot \frac{\partial \mathbf{X}_i^e}{\partial (\mathbf{X}_B^e)^T}. \quad (3.5)$$

The first term on the right hand side is the usual derivative w.r.t. antenna position as given in eq. (3.4). The second term on the right hand side is a  $3 \times 3$  matrix which can be computed from eq. (2.1), e.g. by calculating each of the nine elements of the matrix separately. The result can be written in compact form using the Kronecker-product  $\mathbf{A} \otimes \mathbf{B} = [a_{ij} \mathbf{B}]$  which creates copies of the second matrix scaled by the elements of the first, and the  $\text{vec}$  operator which creates a column vector by stacking the columns of a matrix starting with the leftmost one:

$$\frac{\partial \mathbf{X}_i^e}{\partial (\mathbf{X}_B^e)^T} = \mathbf{I} + \left[ \mathbf{I}_3 \otimes (\mathbf{C}_b^n \mathbf{X}_i^b)^T \right] \cdot \frac{\partial \text{vec} \mathbf{C}_n^e}{\partial (\mathbf{X}_B^e)^T}. \quad (3.6)$$

The second term on the right hand side of this equation arises from the fact that the b-frame to e-frame rotation matrix given in eq. (2.2) also depends on  $\mathbf{X}_B$  via the ellipsoidal coordinates used in eq. (2.3). The partial derivatives of  $\mathbf{C}_n^e$  w.r.t.  $\mathbf{X}_B$  can best be calculated numerically when needed. However, the magnitude of the term in brackets is the length of the lever arm. The elements of the right most term correspond to the rotation of the North-, East- and Down-axes as one moves along the ellipsoid. These elements do not exceed about  $1/(6.3 \times 10^6)$  rad/m. The combined effect of the whole term is negligible if it is less than 0.5 mm (i.e. half the standard deviation of high-precision carrier phase measurements). We easily find that this is the case if the product of lever arm and error of the approximate/predicted position is bounded by:

$$\|\mathbf{X}_i^b\| \cdot \|d\mathbf{X}_B^e\| \leq 3 \cdot 10^3 \text{ m}^2. \quad (3.7)$$

This is certainly the case for the scenarios described in section 1. So we have with sufficient accuracy:

$$\frac{\partial \mathbf{X}_i^e}{\partial (\mathbf{X}_B^e)^T} = \mathbf{I} \quad (3.8)$$

and

$$\frac{\partial \phi_i^j}{\partial (\mathbf{X}_B^e)^T} = -(\mathbf{a}_{ij}^e)^T. \quad (3.9)$$

The measurement also includes information on the attitude of the platform if the antenna phase

center does not coincide with the platform origin, i.e. if  $\mathbf{X}_i^b \neq \mathbf{0}$ . This attitude must necessarily be estimated along with the platform position. So, we also need the derivatives of the carrier phase measurements w.r.t. the attitude parameters. It is possible to estimate corrections of the assumed approximate yaw, pitch and roll values directly. However, it is easier to follow an approach well known from inertial navigation, see e.g. [5, §5.3], and introduce an additional rotation matrix such that

$$\mathbf{C}_b^e := \delta \mathbf{C}_\psi \cdot (\mathbf{C}_b^e)_o \quad (3.10)$$

with

$$\delta \mathbf{C}_\psi := \mathbf{R}_3(\psi_3) \mathbf{R}_2(\psi_2) \mathbf{R}_1(\psi_1), \quad (3.11)$$

$$(\mathbf{C}_b^e)_o := \mathbf{C}_n^e \cdot \mathbf{C}_b^n(\alpha_o, \chi_o, \eta_o). \quad (3.12)$$

The sequential rotations about the first, second and third axis on the right hand side of eq. (3.11) are modeled using rotation matrices of the same type as explained in section 2. Eq. (3.12) defines an approximation of the entire b-frame to e-frame rotation matrix computed from fixed values of yaw, pitch and roll (e.g. the predicted values), and from the actual position of the b-frame origin. We assume that this approximation differs from the true rotation by less than 2 deg. This is achievable in practical applications either by iterated adjustment or by suitable prediction using a Kalman Filter. So, the second matrix on the right hand side of (3.12) will be treated as a fixed term subsequently, while the entire b-frame to e-frame rotation (3.10) depends on the unknown location and the unknown additional rotations  $\psi_1, \psi_2, \psi_3$ .

Once the values of these angles and of the platform coordinates have been estimated, the corresponding b-frame to e-frame rotation matrix

$$\hat{\mathbf{C}}_b^e := \mathbf{R}_3(\hat{\psi}_3) \cdot \mathbf{R}_2(\hat{\psi}_2) \cdot \mathbf{R}_1(\hat{\psi}_1) \cdot \mathbf{C}_n^e(\hat{\mathbf{X}}_B^e) \cdot \mathbf{C}_b^n(\alpha_o, \chi_o, \eta_o) \quad (3.13)$$

can be computed. After left-multiplication of this matrix by  $[\mathbf{C}_n^e(\hat{\mathbf{X}}_B^e)]^T$  the yaw, pitch and roll angles  $\hat{\alpha}, \hat{\chi}, \hat{\eta}$  can be extracted from the resulting matrix using the parameterization as of eq. (2.4). This shows that it is actually not necessary to estimate these angles directly. The advantage of the proposed approach is a considerable simplification of the required terms if the  $\psi_i$  are small, i.e. if the prediction of yaw, pitch and roll is accurate, as will be shown next.

For small  $\psi_k$  we may write

$$\delta \mathbf{C}_\psi \approx \mathbf{I} - \Psi, \quad \Psi = \begin{bmatrix} 0 & -\psi_3 & \psi_2 \\ \psi_3 & 0 & -\psi_1 \\ -\psi_2 & \psi_1 & 0 \end{bmatrix} \quad (3.15)$$

and thus

$$\mathbf{C}_b^e \approx (\mathbf{I} - \Psi) \cdot (\mathbf{C}_b^e)_o. \quad (3.16)$$

The error of this approximation is on the order of  $\psi^2$  (e.g.,  $10^{-3}$  if the predicted attitude has an error of about 2 deg). This is not negligible for calculating the carrier-phase measurement or for carrying out actual transformations using eq. (2.1); so these steps need to be carried out using eq. (3.11). However, eq. (3.16) is sufficiently accurate for estimating the attitude errors. For this purpose, the angles  $\psi_k$  are collected in a  $3 \times 1$  vector  $\boldsymbol{\psi}$ , and the related partial derivatives needed for parameter estimation in a linearized model are obtained from (2.1) with (3.16) as:

$$\frac{\partial \mathbf{X}_i^e}{\partial \boldsymbol{\psi}^T} = \begin{bmatrix} 0 & -Z_o & Y_o \\ Z_o & 0 & -X_o \\ -Y_o & X_o & 0 \end{bmatrix} \text{ with } \begin{bmatrix} X_o \\ Y_o \\ Z_o \end{bmatrix} := (\mathbf{C}_b^e)_o \cdot \mathbf{X}_i^b \quad (3.17)$$

Using (3.17), (3.4) and the definition of the vector cross product  $\times$  one can easily verify that

$$\frac{\partial \phi_i^j}{\partial \boldsymbol{\psi}^T} = \frac{\partial \phi_i^j}{\partial (\mathbf{X}_i^e)^T} \cdot \frac{\partial \mathbf{X}_i^e}{\partial \boldsymbol{\psi}^T} = -(\mathbf{a}_{ij}^e \times [(\mathbf{C}_b^e)_o \cdot \mathbf{X}_i^b])^T \quad (3.18)$$

The error of these partial derivatives is on the order of  $\psi^2 \cdot \|\mathbf{X}_i^b\|$  and is negligible for parameter estimation if

$$\psi^2 \cdot \|\mathbf{X}_i^b\| \cdot |\boldsymbol{\psi}| = |\boldsymbol{\psi}^3| \cdot \|\mathbf{X}_i^b\| \leq 5 \times 10^{-4} \text{ m} \quad (3.19)$$

i.e., if the error of the predicted attitude is less than about 2 deg.

The linearized observation equations of the pseudorange measurements  $P_i^j$  do not differ from those of the carrier-phase measurements as far as the relation to platform position and attitude is concerned. Thus eqs. (3.9) and (3.18) also hold for the pseudorange measurements if  $\phi$  is replaced by  $P$ . Using these partial derivatives for computing the elements of the measurement matrix (and the usual ones with respect to other parameters like clock errors, atmospheric corrections or ambiguities, as needed), the platform position and orientation can be estimated from pseudorange or carrier-phase observations, e.g. using the Least-Squares method within a Gauß-Markov-Model (GMM) for the static case

or a Kalman Filter for kinematic processing. Of course, the linearized equations using the above partial derivatives can easily be transformed into those of the DD observations by pre-multiplication with a DD-operator matrix. For illustration, we will show a numeric example in section 5.

#### 4. Velocity and attitude rate

The one-way Doppler measurement between the receiving antenna  $i$  and the satellite  $j$ , can be expressed in units of m/s as

$$D_i^j = [\dot{\mathbf{X}}_i^e - \dot{\mathbf{X}}_j^e]^T \mathbf{a}_{ij}^e \cdot (1 - \delta t_i) \pm \dots \quad (4.1)$$

with

$\dot{\mathbf{X}}_i^e$  ...receiver velocity expressed in e-frame (in m/s)

$\dot{\mathbf{X}}_j^e$  ...satellite velocity expressed in e-frame with Sagnac correction applied (in m/s)

$\delta t_i$  ...receiver clock drift (in s/s)

Again, the focus is on those terms of the observation equation which require different treatment than in the single-antenna case. So, all other terms have been omitted in eq. (4.1). A comprehensive derivation of the entire Doppler observation equation suitable for obtaining estimated receiver velocity at the mm/s level is given in [12].

The linearized observation equation is computed using the following sufficiently accurate derivatives, see e.g. [12, p. 73]:

$$\frac{\partial D_i^j}{\partial (\dot{\mathbf{X}}_i^e)^T} = (\mathbf{a}_{ij}^e)^T (1 - \delta t_i) \quad (4.2)$$

$$\frac{\partial D_i^j}{\partial (\mathbf{X}_i^e)^T} = \frac{(\dot{\mathbf{X}}_j^e - \dot{\mathbf{X}}_i^e)^T}{\|\dot{\mathbf{X}}_j^e - \dot{\mathbf{X}}_i^e\|} \cdot (\mathbf{I} - \mathbf{a}_{ij}^e \cdot (\mathbf{a}_{ij}^e)^T) \quad (4.3)$$

However, in the present context we do not estimate the velocity of the individual antenna but rather that of the platform. So we need to apply again the chain rule i.e.,

$$\frac{\partial D_i^j}{\partial \mathbf{p}^T} = \frac{\partial D_i^j}{\partial (\dot{\mathbf{X}}_i^e)^T} \cdot \frac{\partial \dot{\mathbf{X}}_i^e}{\partial \mathbf{p}^T} + \frac{\partial D_i^j}{\partial (\mathbf{X}_i^e)^T} \cdot \frac{\partial \mathbf{X}_i^e}{\partial \mathbf{p}^T} \quad (4.4)$$

to calculate the derivation of eq. (4.1) with respect to the velocity and position of the platform, the attitude and the attitude rate (any one of those

represented by  $\mathbf{p}$  in eq. 4.4). The last partial derivative on the right hand side has already been computed above for  $\mathbf{p} = \mathbf{X}_B^e$  (eq. 3.8) and  $\mathbf{p} = \boldsymbol{\psi}$  (eq. 3.17); it is  $\mathbf{0}$  for the other two vectors  $\mathbf{p} = \mathbf{X}_B^e$  and  $\mathbf{p} = \boldsymbol{\psi}$ .

From (2.1) and (3.10) we obtain by differentiating w.r.t. time and taking into account that the antenna is fixed on the platform:

$$\dot{\mathbf{X}}_i^e = \dot{\mathbf{X}}_B^e + \delta\dot{\mathbf{C}}_\psi \cdot (\mathbf{C}_b^e)_o \cdot \mathbf{X}_i^b + \delta\mathbf{C}_\psi \cdot \dot{\mathbf{C}}_n^e \cdot \mathbf{C}_b^e(\alpha_o, \chi_o, \eta_o) \cdot \mathbf{X}_i^b \quad (4.5)$$

The term including  $\dot{\mathbf{C}}_n^e$  affects the Doppler observation by less than

$$\left\| \dot{\mathbf{X}}_B^e \cdot \left\| \mathbf{X}_i^b \right\| / R \leq 1.6 \cdot 10^{-5} \text{ m/s} \quad (4.6)$$

where  $R$  is the radius of curvature of the earth, and the maximum dimension and speed of the platform as defined in sec. 1 have been used for computing the numeric value. This term is negligible for all practical purposes considered herein. So, we have with sufficient accuracy

$$\dot{\mathbf{X}}_i^e = \dot{\mathbf{X}}_B^e + \delta\dot{\mathbf{C}}_\psi \cdot (\mathbf{C}_b^e)_o \cdot \mathbf{X}_i^b \quad (4.7)$$

and consequently

$$\frac{\partial \dot{\mathbf{X}}_i^e}{\partial (\dot{\mathbf{X}}_B^e)^T} = \mathbf{I} \quad (4.8)$$

The Doppler observation depends on  $\mathbf{X}_B^e$  via  $\mathbf{C}_n^e$  which is part of  $(\mathbf{C}_b^e)_o$ . However, the effect on the linearized observation equation is negligible (less than 0.5 mm/s) if

$$\left| \dot{\boldsymbol{\psi}} \cdot \left\| \mathbf{X}_i^b \right\| \cdot \left\| d\mathbf{X}_B^e \right\| \leq 3 \cdot 10^3 \text{ m}^2/\text{s} \quad (4.9)$$

which is clearly the case for the scenarios considered herein, since a prediction of the platform position with sufficiently low error  $d\mathbf{X}_B^e$  (less than 500 m) can easily be found. So, we have with sufficient accuracy:

$$\frac{\partial \dot{\mathbf{X}}_i^e}{\partial \mathbf{X}_B^e} = \mathbf{0} \quad (4.10)$$

The term including the time derivative of  $\delta\mathbf{C}_\psi$  in eq. (4.7) is neither negligible for computing the reduced observation nor for computing the partial derivatives. These can be written conveniently as

$$\frac{\partial \dot{\mathbf{X}}_i^e}{\partial \boldsymbol{\psi}^T} = \left( \mathbf{I}_3 \otimes [(\mathbf{C}_b^e)_o \cdot \mathbf{X}_i^b]^T \right) \cdot \frac{\partial \text{vec}(\delta\dot{\mathbf{C}}_\psi)}{\partial \boldsymbol{\psi}^T} \quad (4.11)$$

where  $\delta\dot{\mathbf{C}}_\psi$  and its derivation w.r.t.  $\boldsymbol{\psi}$  needs to be computed from the correct equation (3.11) rather than from (3.15), i.e. from

$$\begin{aligned} \delta\dot{\mathbf{C}}_\psi = & \mathbf{R}_3(\boldsymbol{\psi}_3)\mathbf{R}_2(\boldsymbol{\psi}_2) \begin{bmatrix} 0 & 0 & 0 \\ 0 & -\sin\boldsymbol{\psi}_1 & \cos\boldsymbol{\psi}_1 \\ 0 & -\cos\boldsymbol{\psi}_1 & -\sin\boldsymbol{\psi}_1 \end{bmatrix} \cdot \dot{\boldsymbol{\psi}}_1 + \\ & + \mathbf{R}_3(\boldsymbol{\psi}_3) \begin{bmatrix} -\sin\boldsymbol{\psi}_2 & 0 & -\cos\boldsymbol{\psi}_2 \\ 0 & 0 & 0 \\ \cos\boldsymbol{\psi}_2 & 0 & -\sin\boldsymbol{\psi}_2 \end{bmatrix} \mathbf{R}_1(\boldsymbol{\psi}_1) \cdot \dot{\boldsymbol{\psi}}_2 + \\ & + \begin{bmatrix} -\sin\boldsymbol{\psi}_3 & \cos\boldsymbol{\psi}_3 & 0 \\ -\cos\boldsymbol{\psi}_3 & -\sin\boldsymbol{\psi}_3 & 0 \\ 0 & 0 & 0 \end{bmatrix} \mathbf{R}_2(\boldsymbol{\psi}_2)\mathbf{R}_1(\boldsymbol{\psi}_1) \cdot \dot{\boldsymbol{\psi}}_3 \end{aligned} \quad (4.12)$$

Since the dependence of the velocity vector of the antenna on the attitude rate is also via  $\delta\dot{\mathbf{C}}_\psi$  we obtain in complete analogy

$$\frac{\partial \dot{\mathbf{X}}_i^e}{\partial \boldsymbol{\psi}^T} = \left( \mathbf{I}_3 \otimes [(\mathbf{C}_b^e)_o \cdot \mathbf{X}_i^b]^T \right) \cdot \frac{\partial \text{vec}(\delta\dot{\mathbf{C}}_\psi)}{\partial \boldsymbol{\psi}^T} \quad (4.13)$$

Also this expression needs to be evaluated using the strict equation (4.11) rather than one obtained from the approximation (3.15). However, the columns of the 9x3 matrix  $\partial \text{vec}(\delta\dot{\mathbf{C}}_\psi) / \partial \boldsymbol{\psi}^T$  are simply obtained from the matrices preceding  $\dot{\boldsymbol{\psi}}_1, \dot{\boldsymbol{\psi}}_2, \dot{\boldsymbol{\psi}}_3$  in eq. (4.12) by vectorizing.

Finally, we get the required partial derivatives of the Doppler observations with respect to the unknown parameters of the platform by inserting the respective intermediate results into (4.4). This yields:

$$\frac{\partial D_i^j}{\partial (\mathbf{X}_B^e)^T} = \frac{(\dot{\mathbf{X}}_j^e - \dot{\mathbf{X}}_i^e)^T}{\left\| \mathbf{X}_j^e - \mathbf{X}_i^e \right\|} \cdot \left( \mathbf{I} - \mathbf{a}_{ij}^e \cdot (\mathbf{a}_{ij}^e)^T \right) \quad (4.14)$$

$$\frac{\partial D_i^j}{\partial (\dot{\mathbf{X}}_B^e)^T} = (\mathbf{a}_{ij}^e)^T (1 - \delta i_i) \quad (4.15)$$

$$\begin{aligned} \frac{\partial D_i^j}{\partial \boldsymbol{\psi}^T} = & (\mathbf{a}_{ij}^e)^T \left( \mathbf{I}_3 \otimes [(\mathbf{C}_b^e)_o \cdot \mathbf{X}_i^b]^T \right) \cdot \\ & \cdot \frac{\partial \text{vec}(\delta\dot{\mathbf{C}}_\psi)}{\partial \boldsymbol{\psi}^T} (1 - \delta i_i) \end{aligned} \quad (4.16)$$

$$\begin{aligned} \frac{\partial D_i^j}{\partial \boldsymbol{\psi}^T} = & (\mathbf{a}_{ij}^e)^T \left( \mathbf{I}_3 \otimes [(\mathbf{C}_b^e)_o \cdot \mathbf{X}_i^b]^T \right) \cdot \\ & \cdot \frac{\partial \text{vec}(\delta\dot{\mathbf{C}}_\psi)}{\partial \boldsymbol{\psi}^T} (1 - \delta i_i) \end{aligned} \quad (4.17)$$

When deriving (4.16) the contribution by the product of (4.3) and (3.17) has been neglected because it is too small. Further simplifications are

possible if it can be assured that the predicted coordinates are accurate to within a few meters – (4.14) is negligible then –, if the receiver exhibits a low oscillator frequency offset (unlike some low-cost receivers) – in this case,  $\delta\dot{t}_i$  is negligible in the above equations –, and if the predicted values of  $\psi$  are exactly 0 (i.e., if yaw, pitch and roll as used in eq. (3.12) are updated in case the estimated or predicted value of  $\psi$  were non-zero without such an update) – (4.16) can then be expressed using

$$\frac{\partial \text{vec}(\delta\dot{\mathbf{C}}_{\psi}^b)}{\partial \psi^T} = \begin{bmatrix} 0 & 0 & 0 & \dot{\psi}_2 & -\dot{\psi}_1 & 0 & \dot{\psi}_3 & 0 & \dot{\psi}_1 \\ -\dot{\psi}_2 & 0 & 0 & \dot{\psi}_1 & 0 & 0 & 0 & \dot{\psi}_3 & -\dot{\psi}_2 \\ -\dot{\psi}_3 & 0 & 0 & 0 & -\dot{\psi}_3 & 0 & \dot{\psi}_1 & \dot{\psi}_2 & 0 \end{bmatrix}^T \tag{4.18}$$

and (4.17) can be replaced by

$$\frac{\partial D_i^j}{\partial \psi^T} = -\mathbf{a}_{ij}^e \times [(\mathbf{C}_b^e)_o \cdot \mathbf{X}_i^b] (1 - \delta\dot{t}_i) \tag{4.19}$$

### 5. Numeric example

For demonstration, we briefly analyze the situation shown in Fig. 6. We will predict the precision of the position, velocity and attitude of the platform as estimated on an epoch-by-epoch basis using single-frequency GPS DD carrier-phase observations and undifferenced Doppler observations. Three GPS antennas (A1, A2, A3) are mounted on a nearly horizontal platform, and a fourth GPS antenna is setup about 100 m east at a stationary reference site (REF). All antennas track satellites at elevations higher than 15 deg.

When evaluating a single epoch of data here, we assume that the carrier-phase integer ambiguities have already been resolved and that the pseudorange observations are only used for data pre-processing. So, the parameter vector contains 15 elements, namely the e-frame coordinates and velocities of B, the attitude corrections  $\psi_k$  and their rate (as nuisance parameters), and the receiver clock

drift of the three platform receivers (no Doppler observations are used at REF). The actual GPS satellite distribution on Feb 1, 2011, 1:30 UTC as seen in Vienna, Austria has been arbitrarily chosen for demonstration purposes. Two scenarios are distinguished: (a) the antennas are not affected by any signal obstruction (obstacle in Fig. 6 is lower than the antennas), (b) the obstacle is 2 m higher than the antennas and thus causes significant but different obstruction to each platform antenna.

The observation matrices of the undifferenced carrier-phase and Doppler observations of a single epoch are set up using the partial derivatives derived in sec. 3 and 4. The undifferenced observations are assumed to be uncorrelated, to have standard deviations proportional to  $1/\sin E$ , and to have a standard deviation of 2 mm and 2 mm/s, respectively, in zenith direction. Double differencing of the carrier-phase observations and the associated variance propagation are taken into account properly by multiplication of the original observations and observation matrix with a DD operator matrix before estimating the unknown parameters using weighted least squares adjustment.

The satellite visibility for scenario (b) and about half an hour of data is shown in Fig. 7. The epoch actually processed lies within this period. The grey shading indicates obstructed portions of the sky. Obstructed satellites are shown in grey color; their data are not used when evaluating scenario (b). It is clear from this figure that the position of antenna A3 could not be estimated individually (less than 4 satellites available), and that the geometry for estimating the positions of the other two platform antennas is rather poor. This is also confirmed by the DOP values reported in Tab. 1. These values represent the RDOP, see [3], i.e. the trace of the cofactor matrix of the coordinates estimated in relative mode. Using all available data to estimate the origin of the platform rather than the individual antenna, we obtain a DOP of 6.4, which is not excellent, but better than any of the individual site's DOP. Furthermore, only the combination of the data allows obtaining an estimate of the platform position at all, in this case.

If the obstacle on the platform does not cause any GPS signal obstruction, the satellite visibility at each of the platform antennas is identical to the one at the reference station (Fig. 7, top left). In this case, the RDOP is 5.8 when determining each one of the platform antennas individually with REF as reference station, see Tab. 1. This

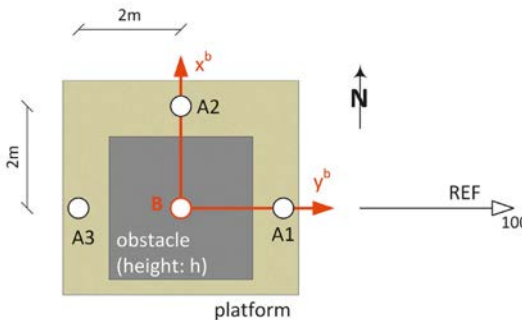


Fig. 6: Setup used for numeric example

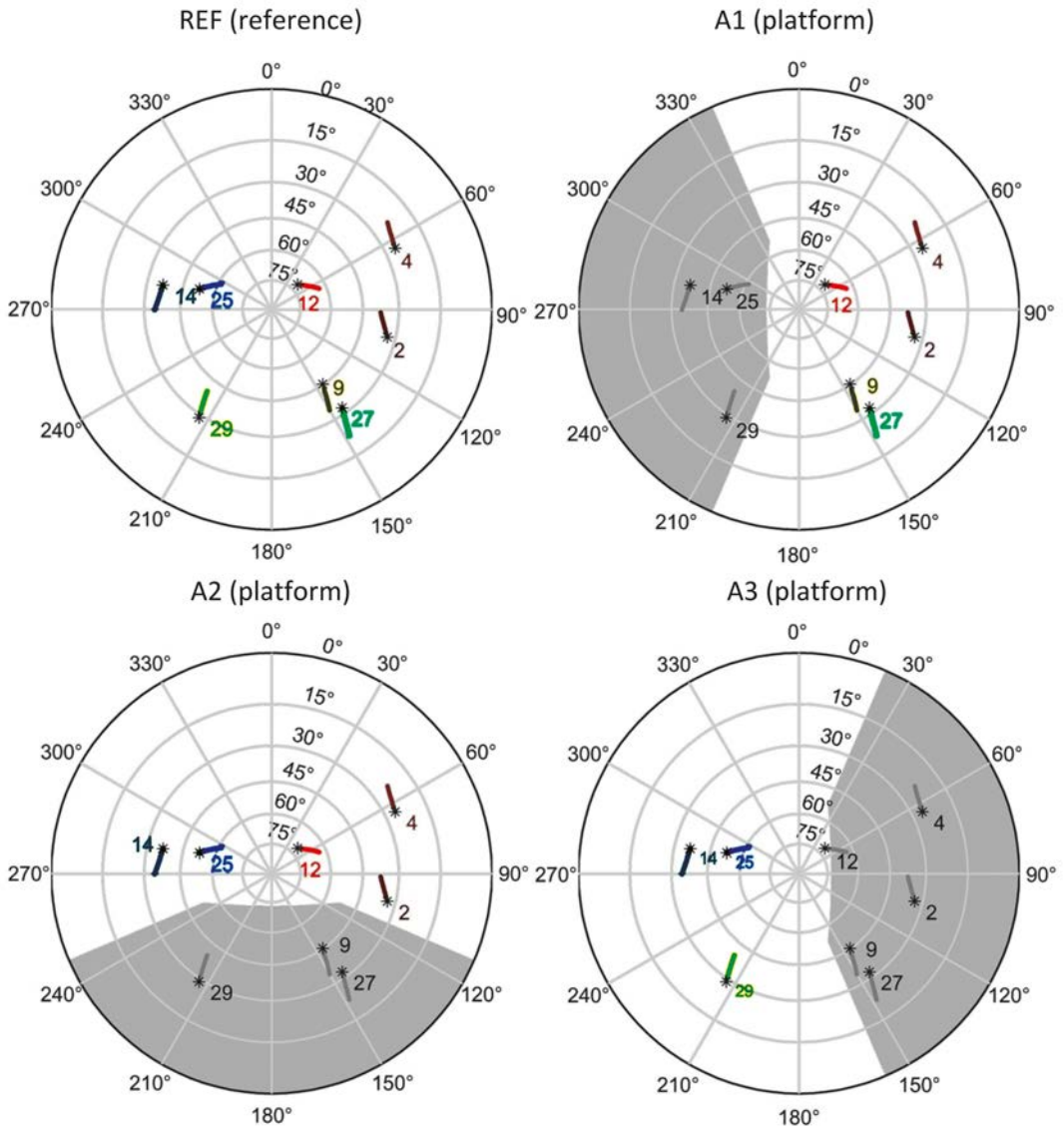


Fig. 7: Satellite visibility at the reference station and at the three antenna sites on the platform as used for the numeric example, scenario (b) i.e., with obstruction

indicates that the satellite distribution is not ideal even without obstruction (however, it is a real situation). The DOP value reduces to 4.9 if all data are combined to estimate the position of the platform origin directly which indicates significantly better precision.

The predicted standard deviation of all estimated parameters except the clock drift is given in Tab. 2 for both scenarios. The values refer to the direct estimation of the 15 states mentioned above and give an impression of

the attainable precision, even in a suboptimum case like the one chosen. While the standard deviations of the estimated coordinates and velocities are virtually independent of platform size (and the results of the numeric examples are thus also valid for the robot shown in Fig. 1), the standard deviations of the attitude and attitude rates scale linearly with antenna separation (if the obstruction masks remain unaltered).

Of course, the measures of precision do not reflect the reliability, in particular the magnitude

Point ID	No obstacle	With obstacle
A1	5.8	13.4
A2	5.8	8.4
A3	5.8	$\infty$
B (platform origin)	4.9	6.4

Tab. 1: DOP values indicating relative precision of 3D-coordinates (based on elevation dependent variances of the one-way observations)

of potentially undetected gross errors (minimum detectable biases) and their effect on the estimates (external reliability). An analysis of these values shows that errors between 10 and 20 mm (e.g., typical multipath effects) would go unnoticed with most of the observations, and even larger errors with some of them, in particular in the scenario with obstruction. The corresponding effect on the coordinates reaches about 15 mm in the case without obstruction but exceeds 50mm in the other case.

This shows that multipath suppression e.g. by microwave absorbing screens as proposed in sec. 1 may be very useful in case reflections at parts of the platform are likely. Only such means would allow practically achieving accuracies like the standard deviations given in Tab. 2. Furthermore, in reality one would try to apply 4 rather than 3 antennas, and carry out parameter estimation using a Kalman Filter if the platform is kinematic, or static processing in a Gauß-Markov model if the platform is static within measurement precision. This increases the redundancy, reduces the standard deviation of the results, increases the probability of correctly detecting and identifying outliers, and reduces the impact of potentially missed outliers. The equations derived above are applicable to both processing schemes and to all GNSS, not only to GPS.

**6. Conclusion and outlook**

We have presented observation equations of GNSS carrier-phase and Doppler observations for direct estimation of platform position, velocity and attitude. The derived terms refer to the

undifferenced observations and can thus easily be used for any linear combinations of observations, including single- and double-differences of equal types of observations.

Often, objects on a platform simultaneously cause signal obstruction and multipath effects thus deteriorating both precision and accuracy of the results obtained using GNSS antennas on the platform. However, the combined processing of data from multiple antennas – and potentially the shading of multipath signals using microwave absorbing material – may allow mitigating this problem. This was demonstrated above using a numeric example where the platform state can be estimated precisely from the data of three platform antennas using the proposed algorithm.

The derived equations can be used without any modification for processing GPS pseudorange observations and corresponding observations obtained from other/future GNSS. Currently, the algorithms are being extended by dynamic models of the platform and are being implemented in a Kalman Filter software for subsequent experimental validation using the mobile robot shown in Fig. 1. These experiments will also include the use of microwave absorbing foam for multipath mitigation. Further investigations also comprise proper handling of time lags between non-synchronized receivers. Such lags have not been considered above, because the data output epochs of typical geodetic GPS receivers are synchronized to GPS time at the micro-second level or better and the lags are therefore negligible with respect to the applications and assumptions discussed above. However, the use of low-cost equipment might be attractive for certain applications, but such receivers may synchronize only loosely with a common time basis and consequently, the lags of the individual receivers on the platform need to be taken into account.

	Position [mm]			Attitude [0.1 deg]			Velocity [mm/s]			Rotation rate [0.01 deg/s]		
	<i>N</i>	<i>E</i>	<i>U</i>	$\eta$	$\chi$	$\alpha$	<i>N</i>	<i>E</i>	<i>U</i>	$\dot{\psi}_1$	$\dot{\psi}_2$	$\dot{\psi}_3$
No obstacle	3.8	2.3	8.7	1.3	2.1	0.5	2.0	1.3	5.1	0.2	0.4	0.2
With obstacle	4.7	4.8	11.0	2.5	3.2	1.0	3.4	3.3	8.5	0.3	0.6	0.3


Tab. 2: Standard deviation ( $1\sigma$ ) of estimated parameters for the two scenarios discussed in the text (*N*: North, *E*: East, *U*: Up)

## References

- [1] *Boccia L, Pace P, Amendola G, Di Massa G (2008)*: Low multipath antennas for GNSS-based attitude determination systems applied to high-altitude platforms
- [2] *Cohen CE (1992)*: Attitude Determination Using GPS. PhD Dissertation, Stanford University, California, USA, 184p
- [3] *Goat C (1988)*: Investigation of an alternate method of processing global positioning survey data collected in kinematic mode. In: Groten E, Strauß R (Eds) GPS-Techniques Applied to Geodesy and Surveying. Lecture Notes in Earth Sciences 19, Springer, Berlin, pp93-106
- [4] *Georgiadou Y, Kleusberg A (1988)*: On carrier signal multipath effects in relative GPS positioning. ManuscriptaGeodaetica 13, pp 172-179
- [5] *Jekeli C (2001)*: Inertial Navigation Systems with Geodetic Applications. Walter de Gruyter, Berlin – New York, 352p
- [6] *Kleusberg A (1995)*: Mathematics of Attitude Determination with GPS. GPS World, Innovation Column, September, pp 72-78
- [7] *Leick A (2004)*: GPS Satellite Surveying. John Wiley & Sons, Hoboken, 435p
- [8] *Saalfeld A (1999)*: Generating basis sets of double-differences. Journal of Geodesy 73, pp 291-297
- [9] *Teunissen P, Kleusberg A (1998)*: GPS for Geodesy. 2<sup>nd</sup>ed, Springer Verlag, Berlin - Heidelberg - New York, 650p
- [10] *Ueno M, Santerre R, Babineau S (1997)*: Impact of antenna configuration on GPS attitude determination. In: Proc 9th World Congress International Association of Institutes of Navigation (IAIN), Amsterdam, The Netherlands, 18-21 November, 8p
- [11] *Ueno M, Santerre R, Kleusberg A (1999)*: Direct determination of angular velocity using GPS. Journal of the Royal Institute of Navigation 53(2), pp 371-379
- [12] *Wieser A (2007)*: GPS based velocity estimation and its application to an odometer. Engineering Geodesy - TU Graz, Shaker Verlag, Aachen, ISBN 978-3-8322-6460-4

## Contacts

Univ. Prof. DI Dr. **Andreas Wieser**, Vienna University of Technology, Institute of Geodesy and Geophysics, Gußhausstraße 27-29/1283, 1040 Vienna, Austria.  
E-Mail: andreas.wieser@tuwien.ac.at

**Roland Aschauer**, BSc, Unionstraße 47/9, 4020 Linz.  
E-Mail: e0526796@student.tuwien.ac.at 





## Dynamic strain measurements using embedded fiber optic sensors

*Helmut Woschitz and Fritz K. Brunner*

### Abstract

Engineering geodetic monitoring has reached a very high level of maturity and provides information with millimetre accuracy. However, these measurements have low data rates and are naturally limited by the surface of the objects, e.g. buildings. The use of embedded sensors, especially fiber optical sensors (FOS), can provide important information about the inside behaviour of an object, even continuously. This information is used in structural health monitoring (SHM) to assess the health state of a building, which is a rather new but significant development. Several fiber optic (FO) instruments are commercially available. They offer high precision, e.g. some micrometres or even some nanometres for measuring changes in length, and high data rates, e.g. 1 kHz. In this paper, two FO measuring systems for dynamic strain measurements are presented and two novel applications are described.

**Keywords:** fiber-optic measurement systems, dynamical measurements, long gauge SOFO sensors, FBG sensors

### Kurzfassung

Das ingenieurgeodätische Monitoring hat einen hohen Reifegrad erreicht und liefert großräumige Informationen mit Millimeter-Genauigkeiten. Allerdings liegen diese Messungen zumeist nur niederfrequent vor und können auch nur an der Oberfläche der Objekte (z.B. Bauwerke) durchgeführt werden. Im „Structural Health Monitoring“ (SHM) werden Sensoren in das Bauwerk integriert, womit Informationen aus dem Inneren eines Objektes zugänglich werden. Dafür gibt es auch mehrere faseroptische Sensoren (FOS) mit wichtigen Vorteilen, z.B. elektromagnetische Immunität, geringe Größe, Multiplexing, hohe Messpräzisionen und Abtastraten von mehreren 100 Hz. Daher wurden 2001 am Institut für Ingenieurgeodäsie der TU Graz als neues Forschungsthema FOS und deren Anwendungen für die Ingenieurgeodäsie aufgegriffen. In der vorliegenden Arbeit werden zwei FOS beschrieben und deren Anwendung in zwei neuen Projekten vorgestellt. Mit beiden Systemen können Längenänderungen zwischen zwei Ankerpunkten mit sehr hoher Präzision und relativ hohen Abtastraten bestimmt werden.

**Schlüsselwörter:** Faseroptische Messsysteme, dynamische Messungen, langarmige SOFO Sensoren, FBG Sensoren

### 1. Introduction

Geodetic monitoring of structures and the determination of deformations has reached a high level of maturity considering the instrumental as well as the analysis developments. Here structures stands for large civil engineering structures like bridges or dams, and natural objects like slopes. But classical geodetic instruments rarely provide high data rates. For example, geodetic deformation surveys with total stations are usually carried out at certain repeat times, e.g. annually for dams or with periods of some hours or even minutes for individual monitoring projects. During the past 20 years GPS measurements have been used to continuously measure deformations with very high precision of several millimetres. However, all geodetic measurements are restricted by the surface of a structure and thus the results rather describe the external deformation of a structure, [1]. But on a global scale – global refers here to the structure and its surroundings – the geodetic data are extremely

important as they are the sole source of information about the integral behaviour of a structure.

The use of embedded sensors can overcome the barrier of the structure's surface for geodetic measurements. Embedding sensors is of course possible during the construction of a new building otherwise the sensors have to be applied to the structure's surface. For this purpose fiber optic sensors (FOS) have emerged as the most useful sensor type. FOS have also unique properties, e.g. electromagnetic immunity, long term stability, small dimensions or multiplexing availabilities. The optical fibers can be used as sensors as well as for the transmission of the signals which allows the analysis unit to be quite distant to the measurement site. The generic term for deformation studies is Structural Health Monitoring (SHM), and the civil engineering aspects are treated under the term Civil Structural Health Monitoring (CSHM). The international organisation for CSHM is ISHMII (International Society for Structural Health Monitoring of Intelligent Infrastructure). ISHMII is

about to launch its international journal (JCSHM) published by Springer Verlag, [2]. Two recent book releases clearly indicate that SHM using embedded fiber optic sensors has also reached a mature level, [3] and [4].

A few years ago the Department of Engineering Geodesy and Measurement Systems (EGMS) of the Graz University of Technology started a serious build-up of FOS equipment and practical applications. This initiative started with the investigation of a monolithic concrete deck using embedded FOS of the SOFO type and geodetic measurements, [5]. Recognising the unique capability of geodetic measurements to provide global data, the proposal has been made to combine sporadic geodetic with continuous FOS measurements for an advanced health monitoring system of structures, [6]. Recently a study of a fiber optical tiltmeter was completed, [7], and a novel calibration facility of FOS has been developed. However, in this contribution two applications of FOS will be presented where dynamical measurements of strain values are essential. In the first application, long gauge fiber optic sensors (5 m length) were used for the measurement of a large geotechnical structure, in the second Fiber-Bragg-Grating sensors (5 mm length) were used to determine the deformations inside of a rather small structural element.

## 2. Dynamical long gauge fiber-optic SOFO system

### 2.1 Principle

The SOFO measurement system (produced by Smartec, Switzerland) works with low-coherent light and two separate interferometers, [8]. The SOFO sensor is the first interferometer and consists of two monomode glass fibers which are laid out in a protective hose. One fiber which is under tension is the measurement fiber (red, fig. 1), and the other fiber, the reference fiber, is loosely spun between the anchors (green, fig. 1). Thus the temperature compensated change of the length between the anchors can be measured. The sensor may be stretched about +1.5% and shortened by -0.5% during deformation. It can be embedded in the material of the structure and may be operated by the SOFO Static or the SOFO Dynamic reading unit, [9]. For the SOFO Dynamic a Mach-Zehnder interferometer, [10], is used for the demodulation of the signal. Fig. 1 shows the principal components of the system.

The phase-modulator located in one branch of the Mach-Zehnder interferometer can be

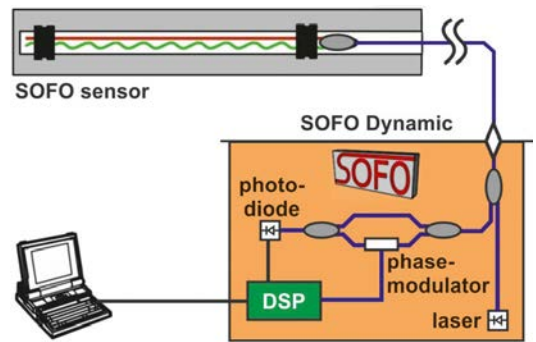


Fig. 1: Schema of the SOFO Dynamic system using a Mach-Zehnder interferometer and a DSP (digital signal processor) unit, after [10]

operated with 50 kHz. Up to 8 SOFO sensors can be used simultaneously by splitting the light of the laser-diode and dedicating a Mach-Zehnder interferometer to each sensor. Smartec claims a resolution of 10 nm and 1 kHz which is fully confirmed by our own experiments, [11]. The use of a phase-modulator in the Mach-Zehnder interferometer realises a high frequency resolution of length changes, however, only relative distance changes can be measured. Using the same sensors but another reading unit (SOFO Static), absolute measurements may be performed (2  $\mu\text{m}$  precision, approx. 0.1 Hz).

### 2.2 Application: Large Strain-Rosette

On alpine slopes, deep-seated gravitational creep is a frequently observed phenomenon. However, the causes and mechanisms of these landslides are insufficiently understood for the prediction of motions. Thus we have developed a GPS monitoring system, [12], and use this system since 1999 for monitoring the landslide "Gradenbach", Austria.

The GPS monitoring results show that the motion of the mass movement is not uniform but rather intermittent, i.e., periods of accelerated motions (velocities up to 2 m/year) are followed by quiescent periods, [13]. However, GPS surveys are not sufficiently precise and fast enough to allow for a detailed study of this pattern of motions. But very precise dynamic measurements of the local strain situation could yield an insight into the geomechanics of this behaviour of a landslide which is required for the prediction of the landslide's motions. Therefore, we have developed an embedded strain rosette for dynamic in-situ measurements of local distance changes. The concept and the results of a test installation were shown in [14]. The strain rosette consists of three 5 m

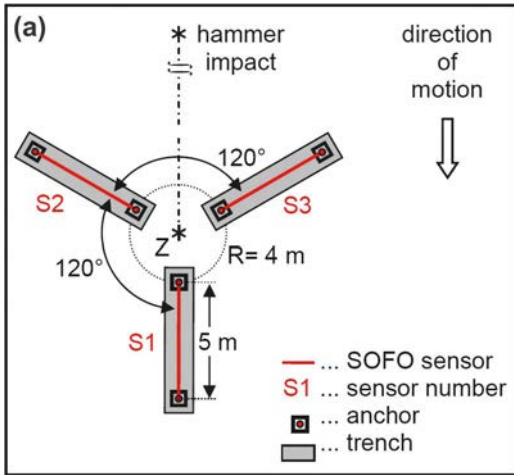


Fig. 2: (a) Schema of the strain rosette, (b) sensor S2 whilst embedding

long extensometers at a separation of 120° in orientation. The extensometers are long gauge fiber optical sensors of the SOFO type.

Fig. 2a shows a schema of the strain-rosette. Each sensor was embedded in a separate trench at a depth of about 2 m (fig. 2b), where it was attached to two concrete anchors of 0.5 m length and 0.3 m diameter. The main challenge of embedding the sensors was their proper connection with the rock material, [15].

At the landslide area, mass movements cause micro-earthquakes, which occur approximately once a week and have duration of less than 0.1 s (E. Brückl, personal communication). The exact

relationship between these micro-earthquakes and the mass movement is rather unknown. It is one of the purposes of the strain rosette to detect possible strain waves associated with the Gradenbach deep-seated mass movement.

In order to investigate the capability of the strain rosette to measure strain waves, artificial excitations were used. The strain variations were generated by hammer (5 kg) impacts to the ground and data were acquired with the SOFO Dynamic reading unit with a sampling frequency of 1 kHz. First experiments have shown very small signal amplitudes, e.g. 0.14 μm for hammer impacts 5 m away from the strain rosette's centre Z. With increasing distance, they even get smaller due to energy dissipation and absorption in the soil and they quickly get down to the noise level of the measuring system. Thus, at each point, 16 consecutive hammer impacts were performed and the signals were time-stacked. The experiment comprised hammer impacts at various distances and orientations from Z. Fig. 3 shows the signals (relative movement  $dL$  of the anchors of sensor S1) of the 16 impacts carried out at a position 155 m away from Z and their averaged signal.

The noise level of the system is  $s_{dL} = 0.4$  nm and at this distance the amplitudes of the signal

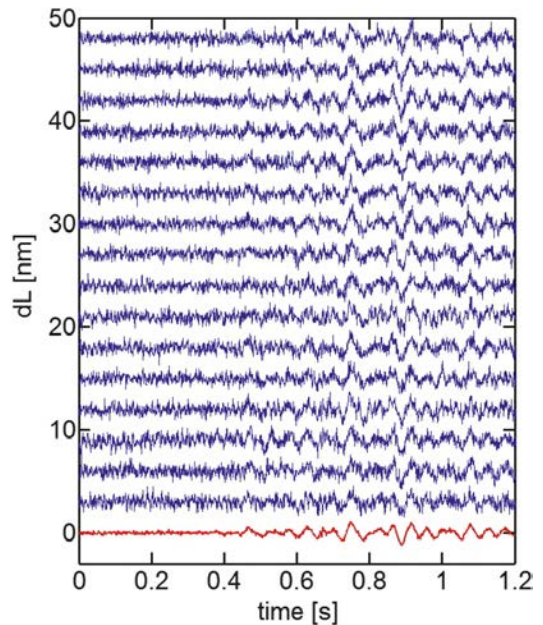


Fig. 3: Strain variations generated by 16 consecutive hammer impacts (blue line, time stacked and shifted for 3 nm to each other) and their mean (red) measured with sensor S1 at a distance of 155 m away from the strain rosette's centre

are as small as about 1 nm. This highlights the very high resolution of the measured strain variations using the SOFO Dynamic reading unit and the strain rosette. Other experiments have confirmed the high reproducibility of the signals which is in the nanometre range.

Using this highly sensitive measuring system, we now hope to find the signals of the rare micro-earthquakes. However, until now, we could only detect a regional earthquake (magnitude  $M_L = 1.4$ ; epicentre in Serbia; signal amplitudes at strain-rosette of 0.3 nm), see [15].

### 3. Fiber-Bragg-Grating Sensors

#### 3.1 Principle

The principle of Fiber-Bragg-Gratings (FBG) sensors is shown in fig. 4. A light-source emits band limited light, which is transmitted into the direction of the FBG using an optical fiber. The FBG consists of periodic changes ( $10^{-6} < \Delta n < 10^{-2}$ ) of the core's refractive index  $n$ , see [16] for example. The FBG reflects one portion of the light ( $\lambda_B$ ) which corresponds to

$$\lambda_B = 2n\Lambda_B \tag{1}$$

where  $n$  is the refractive index and  $\Lambda_B$  is the grating period.

The remaining parts of the light are transmitted along the fiber until they meet another FBG, where another portion of light is reflected. This allows to place several tens or even more than hundred sensors on one single fiber. The reflected signal travels back and is split by an optical coupler into two parts, with one part travelling to the spectrometer. There, its wavelength  $\lambda_B$  is detected. If strain is applied to the FBG, primarily the grating period  $\Lambda_B$  will change and as a consequence,  $\lambda_B$  of the reflected light

will be shifted. Thus, the applied strain can be determined with a resolution of about  $1 \mu\epsilon$  by measuring the wavelength shift  $\Delta\lambda_B$ . The unit micro-strain [ $\mu\epsilon$ ] is commonly used in FOS applications and equivalent to the well-known [ppm] in geodesy:

$$1 [\mu\epsilon] = \frac{\Delta L}{L} \cdot 10^{-6} \tag{2}$$

The Bragg-wavelength  $\lambda_B$  also depends on  $n$ , see eq. (1), and thus  $\lambda_B$  is also sensitive to temperature. If absolute strain values are necessary, the measurements must be corrected for temperature induced wavelength shifts. For this purpose, a FBG-based temperature sensor may be used, where the grating is shielded against mechanical strain. The strain and temperature sensitivities of a typical FBG sensor are ([17], p. 127):

$$\frac{1}{\lambda_B} \cdot \frac{\Delta\lambda}{\Delta\epsilon} = 0.78 \cdot 10^{-6} / \mu\epsilon \tag{3}$$

$$\frac{1}{\lambda_B} \cdot \frac{\Delta\lambda}{\Delta t} = 6.678 \cdot 10^{-6} / K$$

The sensitivities given in eq. (3) are reduced for  $\lambda_B$  because of the dispersive characteristics of glass and they may vary for different fiber types. Using a modern instrument with an optical resolution of 1 pm, strain and temperature may be acquired with a resolution of  $0.8 \mu\epsilon$  and 0.1 K respectively.

Several instruments are commercially available. Some of them provide sampling rates up to several kHz and allow the simultaneous measurement of all connected FBGs. There is also a variety of FBG based sensors available, either ready-for-use sensors in standard applications or bare fiber sensors for most flexibility in special applications.

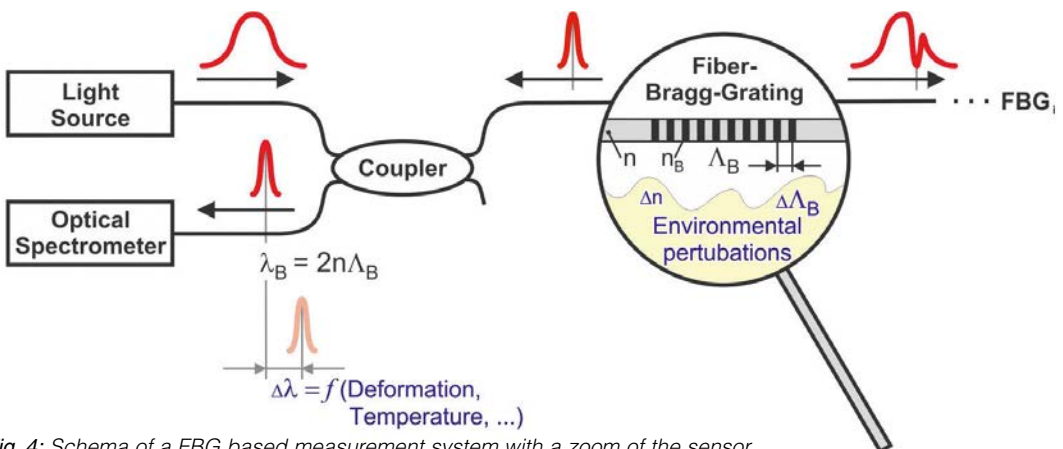


Fig. 4: Schema of a FBG based measurement system with a zoom of the sensor

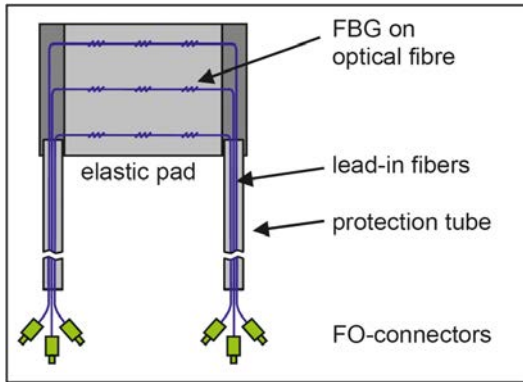


Fig. 5: Schema of the rail-strain-pad

### 3.2 Application: Rail-Strain-Pad

Elastic pads are used in railway engineering to reduce the stress in the roadbed and track components. In Austria, these pads need to be replaced after very short time spans (every 2.5 to 4 years, [18]), especially in the alpine regions. The reason for the short replacement time is rather unknown. Thus, investigations should be performed with strain measurements inside the elastic pad during the passage of trains. As the pads are rather small (e.g.  $160 \times 150 \times 7 \text{ mm}^3$ ), FOS appeared to be the only suitable sensor type. The optical fiber has small dimensions (e.g. 0.25 mm diameter) and when using FBG sensors, several sensors can be integrated into one single pad. However, the signals of individual sensors must not overlap in order to separate them correctly. Because of the large horizontal deformation during a train passage (about 2 % to 3 %), three sensors placed on a single fiber. Using three fibers and an instrument with several input lines, it was possible to integrate 9 sensors into one elastic rail-strain-pad, see fig. 5.

Draw tower gratings, [19], of 5 mm length were used, as this FBG sensor type provides a higher mechanical resistance compared to recoated sensors. In order to get the most reliable results, the fibers were integrated into the material matrix of the elastic pad during its production.

For testing and calibration purposes, the rail-strain-pad was put on a test facility used for applying pressure. The passage of a passenger train (heavy engine, 6 wagons, velocity of 140 km/h) was simulated, loading the pad by the corresponding known vertical forces. Fig. 6a shows these forces, which vary in between 18 kN (i.e. the clamping force of the rail clamps which hold the rail at the sleepers) and 65 kN. Exemplarily, the strain measured by the three sensors A to C on the middle fiber (see fig. 6b) is shown in figs. 6c-e.

Note that the FBG sensors are arranged eccentrically inside this rail-strain-pad. The measured strain values are quite different for the three sensors, indicating that the strain distribution inside the pad is quite nonlinear. Sensor A, which is the outmost of the three sensors, shows the largest strain values (up to  $1500 \mu\epsilon$ ). Sensor C, which is 10 mm closer to the pad's centre, provides strain values that are smaller by a factor of 7. In the central region of the pad (sensor B), even negative strain ( $-20 \mu\epsilon$ ) appears, indicating that the pad is compressed in this region. This performance was previously unknown.

It is now one of the next goals to compute the forces applied to the rail-strain-pad using the

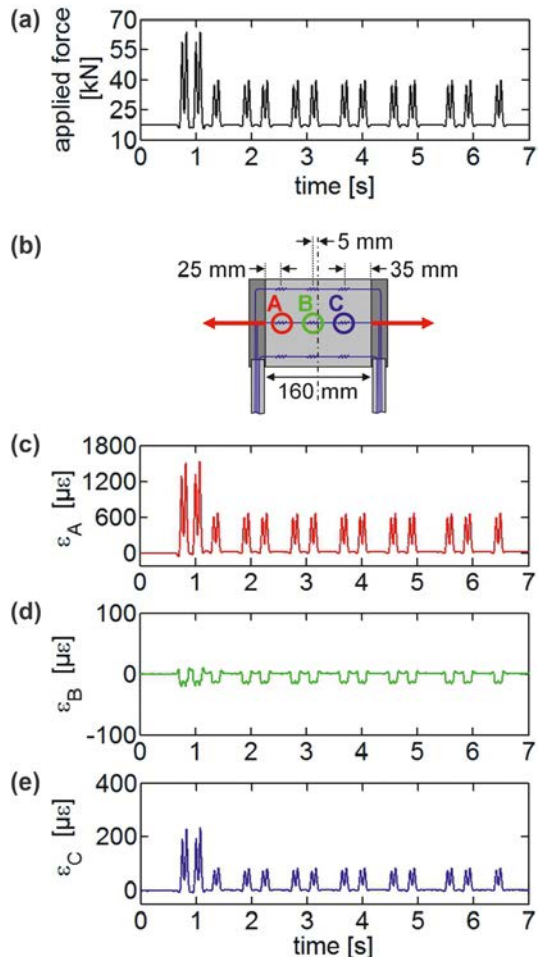


Fig. 6: Simulation of a train passage with (a) the vertical forces applied by a test facility, (b) the location of the FBG sensors inside the rail-strain-pad and the strain measured by (c) sensor A, (d) sensor B and (e) sensor C

FBG signals and individual calibration functions for each sensor. First results were already shown in [20].

#### 4. Outlook

Two novel examples of embedded FOS for the dynamic measurement of strain are presented: (i) large strain rosette and (ii) rail-strain-pad. The large strain rosette consists of three 5 m long SOFO sensors which are embedded in the rock material of a landslide mass. The attainable precision is better than  $2 \mu\epsilon$  with 1 kHz. The strain rosette will now be used to study the Gradenbach landslide in order to detect precursors of accelerated and decelerated motions of the landslide. The rail-strain-pad was developed for the study of forces acting on the elastic pad during train passages. Here the fiber optical sensors FBG are embedded in the pad and the results of this study will be used in a new the design of the pad's material.

These two examples show the implantation of FOS in existing structures of different size, and the latter the embedding of the FOS when the structure is being built up. Both examples have shown the potential of the fiber optic instruments used, especially for dynamic measurements. SHM is a growing discipline with many new applications and thus new FO instruments with enhanced performance or even new functionality will be available in the future.

#### Acknowledgements

The strain rosette shown in this paper is part of a research project funded by the Austrian Academy of Sciences as part of the Austrian contribution to ISDR. The development of the rail-strain-pad was supported by the FFG in cooperation with Getzner Werkstoffe GmbH (DI P. Burtscher, DI M. Dietrich).

#### References

- [1] Brunner FK, Woschitz H (2011): Über die Erweiterung des ingenieurgeodätischen Monitorings. Allg. Verm. Nachrichten, in press.
- [2] ISHMII (International Society for Structural Health Monitoring of Intelligent Infrastructure), [www.ishmii.org](http://www.ishmii.org)
- [3] Karbhari VM, Ansari F (Eds.) (2009): Structural health monitoring of civil infrastructure systems. Woodhead Publishing Ltd., 552 pages
- [4] Boller C, Chang FK, Fujino Y (2009): Encyclopedia of Structural Health Monitoring. John Wiley and Sons Ltd., 5 Volumes, 2709 pages
- [5] Lienhart W (2007): Analysis of Inhomogeneous Structural Monitoring Data. Series "Engineering Geodesy – TU Graz", Shaker Verlag, Aachen, Germany, 269 pages
- [6] Brunner FK (2009): Faseroptische Sensorik: Ein Thema für die Ingenieurgeodäsie. Öst. Z. f. Vermessung & Geoinformation 97: 335 – 342

- [7] Macheiner K (2010): Development of a fiber optic tiltmeter for static and kinematic applications. Series "Engineering Geodesy – TU Graz", Shaker Verlag, Aachen, Germany, 239 pages
- [8] Inaudi D, Elamari A, Pflug L, Gisin N, Breguet J, Vurpillot S (1994): Low-coherence deformation sensors for the monitoring of civil-engineering structures. Sensors and Actuators A 44: 125-130
- [9] Glišić B, Inaudi D (2007): Fibre optic methods for structural health monitoring. Wiley, 262 pages
- [10] Inaudi D, Glisic B, Posenato D (2004): High-speed demodulation of long-gauge fibre optic strain sensors for dynamic structural monitoring. In Boller C, Staszewski WJ (eds.) 'Structural Health Monitoring 2004, Proc. 2nd Europ. Workshop on Structural Health Monitoring', München, DEStech publ., 485-491
- [11] Woschitz H, Macheiner K, Brunner FK (2011): In-situ Strainmessungen mit langarmigen faseroptischen Sensoren. Allg. Verm. Nachrichten, in press.
- [12] Brunner FK, Zobl F, Gassner G (2003): On the Capability of GPS for Landslide Monitoring. Felsbau 21: 51-54
- [13] Brückl E, Brunner FK, Kraus K (2006): Kinematics of a deep-seated landslide derived from photogrammetric, GPS and geophysical data. Engineering Geology 88: 149-159
- [14] Brunner FK, Woschitz H, Macheiner K (2007): Monitoring of deep-seated mass movements. CD-Proc. 3rd Int. Conf. on Structural Health Monitoring of Intelligent Infrastructure (SHMII-3), Nov.13-16, 2007, Vancouver, Canada
- [15] Woschitz H, Brunner FK (2008): Monitoring a deep-seated mass movement using a large strain rosette. 13th Int. Symp. on Deformation Measurement and Analysis, May 12-15, 2008, Lisbon, Portugal
- [16] Kashyap R (2010): Fiber Bragg Gratings. 2nd ed., Academic Press, San Diego, 614 pages
- [17] Yu FTS, Yin S (2002): Fiber Optic Sensors. Marcel Dekker Inc., New York, 494 pages
- [18] Auer F (2005): Optimierter Zwischenlagenwechsel bei den ÖBB. ZEVrail Glasers Analen 129: 440-443
- [19] Chojetzki C, Klaiberg T, Ommer J, Rothardt M, Betz D (2004): Faser-Bragg-Gitter für Hochtemperaturanwendungen. Technisches Messen 71: 555-652
- [20] Woschitz H (2010): Entwicklung eines Rail-Strain-Pads unter Verwendung von Faser-Bragg-Gitter-Sensoren. In Wunderlich T (ed.) Beiträge zum 16. Internationalen Ingenieurvermessungskurs München 2010. Wichmann: 171-182

#### Contacts

Dr. Helmut Woschitz, Engineering Geodesy and Measurement Systems, Graz University of Technology, Steyrergasse 30, A-8010 Graz, Austria.  
E-Mail: [helmut.woschitz@tugraz.at](mailto:helmut.woschitz@tugraz.at)

Univ.Prof. Dr. Fritz K. Brunner, Engineering Geodesy and Measurement Systems, Graz University of Technology, Steyrergasse 30, A-8010 Graz, Austria.  
E-Mail: [fritz.brunner@tugraz.at](mailto:fritz.brunner@tugraz.at)

# Leica Viva TS15

## Die schnellste bildbasierte Totalstation



... let us inspire you

### Leica Viva TS15 & Leica Viva SmartPole – Bilder sagen mehr als Messungen

- Integrierte hochauflösende Weitwinkelkamera
- Bisher unerreichte Displayqualität
- Bildbasierte Aufnahme- und Skizzierfunktionen
- Direkte logische Zuordnung der Bilder zu Punkten Linien oder Flächen
- Innovative Leica Viva SmartWorx Software
- Kombinierbar mit Leica Viva GNSS als SmartPole- oder SmartStation-Lösung
- ▶ Bildunterstützte Messungen
- ▶ Auch bei stärkster Sonneneinstrahlung
- ▶ Papierlose, wetterunabhängige Feldskizzen
- ▶ Keine nachträgliche zeitaufwendige Zuordnung im Büro notwendig
- ▶ Einfache und selbsterklärende Bedienung
- ▶ Flexibler und produktiver dank optimiertem Messablauf

**Leica Geosystems Austria GmbH**  
Gudrunstraße 179, A-1100 Wien  
Tel. 01/98 122-0, Fax 01/98 122-50  
lgs.austria@leica-geosystems.com  
[www.leica-geosystems.at](http://www.leica-geosystems.at)

- when it has to be **right**

**Leica**  
Geosystems